CONTINUUM AND MOLECULAR MODELING OF SYNAPTIC VESICLE DOCKING AND FUSION

A Dissertation

Presented to the Faculty of the Graduate School

of Cornell University

In Partial Fulfillment of the Requirements for the Degree of

Doctor of Philosophy

by

Pankaj Singh

August 2018

CONTINUUM AND MOLECULAR MODELING OF SYNAPTIC VESICLE DOCKING AND FUSION

Pankaj Singh, Ph. D.

Cornell University 2018

Transmission of neural information starts by the fusion of a synaptic vesicle inside a neuron with the membrane of the neuron. This fusion process mainly consists of two steps. First one is docking which is to bring the vesicle into the proximity of neuron membrane, against the repulsive forces from electrostatics and hydration. The forces necessary to overcome this repulsion are provided by a family of proteins known as SNARE. Second step is fusion pore formation, which leads to the release of the neurotransmitter, for its collection by the next neuron. We have studied the process of synaptic vesicle fusion using Continuum and CG molecular models. Continuum models of the vesicle and neuron membrane are used to understand the deformation and forces in the membrane system in response to the SNARE and repulsive forces. In another study, a CG-model of SNARE is combined with continuum model of the membranes to analyze the deformation and forces during docking. Our calculations show that about 4-7 SNARE complexes are needed to "dock" the vesicle. Using a continuum model, we estimated the docking time of a synaptic vesicle under the effect of hydrodynamics. We found out that it is the nature of the force generated by the docking machinery which governs it. We have also developed a CG model incorporating lipid bilayer membrane and SNARE complexes to better understand the dynamics of the fusion process.

BIOGRAPHICAL SKETCH

Pankaj Singh was born in Jhansi, Uttar Pradesh, India in 1988. He grew up in the city of Aligarh, Uttar Pradesh, 90 miles south east of Indian national capital, New Delhi. He is a Ph.D. candidate in the Field of Theoretical and Applied Mechanics in the Department of Mechanical and Aerospace Engineering at Cornell University. He is advised by Prof. Chung-Yuen Hui from Cornell University and Prof. Anand Jagota from Lehigh University. He loves to think about theoretical and computational techniques applied to mechanical systems. His research focus has been on continuum and molecular modeling of synaptic vesicle fusion during neurotransmission. He holds a Dual Bachelor-Masters of Technology in Mechanical Engineering from Indian Institute of Technology, Kanpur in the year 2012. He really enjoys outdoors, while hiking or biking. His favorite bike ride is 90 miles loop of Cayuga Lake.

Dedicated to Pitaji.

ACKNOWLEDGMENTS

I would like to express my sincerest regards to my advisor, Prof. Chung-Yuen Hui for his invaluable guidance and support during my years at Cornell University. His enthusiasm and curiosity towards mechanics, dedication towards research and an excitement for life have always been an inspiration for me. This dissertation would not have been possible without his mentorship which provided me with best possible guidance and immense support to grow into an independent researcher. His welcoming nature to discuss things beyond academics has made him special for all of his students. I always cherished his homemade dinners several times a year, group lunches, food and travel stories. He has been more than a mentor for me and I will always look up to him as an ideal human being, with the strongest work ethics and excitement for life.

I am extremely thankful to Prof. Anand Jagota, Prof. Jim Jenkins, Prof. Paulette Clancy and Prof. Fernando Escobedo for being on my special committee and guiding me through my research and academics. I would like to thanks Prof. Jagota for inviting to work in his lab during the Spring'14 and helping me throughout my research continuously. I would also like to thank our collaborator Prof. Maria Bykhovskaia for her immense help in giving us biological insight all through this research work. I am extremely grateful to have work together with Dr. Nicole Fortoul on joint research article and projects. I would also like to thank Dr. Marcia Sawyer for her invaluable help and suggestions on dealing with administrative matters.

I am also thankful to my fellow research group members: Jing, Feng, Snow, Abhishek, Tianshu, Jingyi, Haibin and Zezhou, who have always been extremely supportive and provided with invaluable ideas and suggestions, making me realize the power of thinking out aloud and discussing ones thoughts. Being around them certainly made me much better researcher and improved how I approached problems and came up with a solution. I am lucky to have had such amazing research group members as good friends, which made our discussions more free flowing.

I am greatly thankful to my long list of friends in Ithaca. Friends from the Indian community: Abhishek, Samanvya, Nikunj, Maneet, Arjun, Macha, Avik, Ved, Chaitanya, Shreyas, Ritika, Kritka, Arzoo, Chaitali, Gauri, Aniket, Ashesh, Ayush, Ritesh, Himanshu, Pooja and Rohil, friends from Gamma Alpha: Ian, Allie, Eric, Sam, Shaun, Zach, Aditya, Diego, Rachel, Sarah, Kevin, Tim, David, Kalay, Christine, Leilah and Mane, friends from the Cornell Outing Club: Kath, Emily, Kendra, Bhuvanesh and Connor, friends from Lehigh University: Jack, Tyler, Sarah, Sam, Steph and Akshaya. I am lucky to have shared some of the most memorable moments of my graduate life with them.

I am forever indebted to my parents: Jai Devi and Teeran Singh, to go away from the norm to give me their love and unwavering support for this Ph.D. I am extremely thankful for my sister Moon, who always has been wiser than me and came in to rescue when I needed the support most. I am eternally grateful to my girlfriend Lauren, for being that calmest spot in my life whenever things went crazy. She always had faith in me and everyday inspired me to be better than what I was yesterday. I

would like to thank Gabuzzi family for their affection towards me and to make me feel welcomed into their lives.

I would like to acknowledge the sources of financial support that have made my graduate studies possible. I am thankful to the department of Mechanical and Aerospace Engineering for providing me Research Fellowships and Teaching Assistantships. I am also thankful for the support from National Institute of Health (Award Number: R01 MH099557) towards a major financial assistance during my entire Ph.D.

TABLE OF CONTENTS

BIOGRPAHICAL SKETCH …… iv

ACKNOWLEDGEMENTS ……... vi

TABLE OF CONTENTS ……..... ix

LIST OF FIGURES ……... xiv

CHAPTER 1. INTRODUCTION …… 1

1.1. Neurotransmission ……... 1

1.2. Synaptic vesicle fusion …… 2

1.2.1. Lipid bilayer membrane structures: Synaptic vesicle and neuron plasma membrane …….. 4

1.2.2. SNARE complex ……... 6

1.3. Role of SNARE on Vesicle docking …… 8

1.4. Synaptic Vesicle Fusion ……... 9

1.5. Organization ……... 10

1.6. Bibliography ..…… 13

CHAPTER 2. A CONTINUUM MODEL OF DOCKING OF SYNAPTIC VESICLE TO PLASMA MEMBRANE ……... 17

2.1. Abstract …….. 18

2.2. Introduction …… 19

2.3. Geometry and model …….. 21

2.3.1. Governing equations for the vesicle membrane …….. 24

2.3.2. Governing equations for the plasma membrane …….. 28

2.4. Results …… 29

2.5. Effect of Hemi-fusion …… 45

2.6. Summary and Conclusion …….. 47

Bibliography …… 49

Appendix A2 ……... 56

CHAPTER 3. COARSE-GRAINED MODEL OF SNARE MEDIATED DOCKING

…….. 120

3.1. Abstract …… 121

3.2. Introduction …….. 122

3.3. Materials and methods ……. 125

3.3.1. All Atom simulations ….……... 125

3.3.2. SNARE Coarse-Grained model …… 126

3.3.3. Continuum model of the vesicle and plasma membrane …….. 135

3.3.3.1. Governing equations for the continuum membrane model and their solution ……..……..……..…….. 140

3.4. Results ……..……..……..……..…….. 142

3.4.1. Force-displacement response of the vesicle-membrane interaction .. 142

3.4.2. SNARE force-separation curve ……..……..……. 143

3.4.3. Combined SNARE and vesicle-membrane results ……... 145

3.5. Discussion and conclusion ……..……..……... 152

Bibliography …….. 156

Appendix A3 ……. 167

CHAPTER 4. HYDRODYNAMICS GOVERN THE PRE-FUSION DOCKING TIME OF SYNAPTIC VESICLE ……..……..…….. 203

4.1. Abstract ……..……..……..……..…… 204

4.2. Introduction ……..……..……..……..…….. 204

4.3. Materials and methods ……..……..……..……... 206

4.3.1. Model: Geometry, fluid flow and membrane mechanics …….. 207

4.3.2. Lubrication theory ……..……..……..……... 208

4.3.3. Elastic deformation of the plasma membrane: Calculation of w ….. 209

4.3.4. Numerical solution ……..……..……..…….. 210

4.4. Results ……..……..……..……..…….. 210

4.4.1. Undeformable plasma membrane limit ……..……... 210

4.4.2. Deformable membrane ……..……..……..… 213

4.4.3. Different force model ……..……..……..….. 219

4.5. Conclusions ……..……..……..……..…….. 221

Bibliography …….. 223

Appendix A4 ……. 233

CHAPTER 5. COARSE-GRAINED MODELING OF SYNAPTIC VESICLE FUSION ……..……..……..……..……. 276

5.1. Abstract ……..……..……..……..…… 277

5.2. Introduction ……..……..……..……..…..… 278

5.3. Model ……..……..……..……..……... 281

5.3.1. Lipid membrane ……..……..……..……..… 283

5.3.2. SNARE coarse grained model ……..……..…….. 287

5.3.2.1. Bonded interactions ……..……..……... 287

5.3.2.2. Non-bonded interactions ……..……..……... 288

5.4. Results ……..……..……..……..…….. 290

5.4.1. Membrane fusion under the effect of an indenter ……. 290

5.4.2. SNARE mediated synaptic vesicle fusion …… 295

5.5. Summary and Conclusion ……..……..……..…….. 300

Bibliography …….. 302

Appendix A5 ……. 308

CHAPTER 6. CONCLUSION AND FUTURE WORK ……..……... 344

6.1. Discussion ……..……..……..…… 344

6.2. Future work ……..……..……..…….. 347

Bibliography ……..……..……..……..…….. 349

LIST OF FIGURES

1.1 Schematic of synaptic vesicle fusion (Image ref: J.H. Hurst et al, J. Clin. Invest., 2013, kennesaw.edu) ……..……..……..……. 3

1.2 Lipid bilayer and single lipid molecule (Image ref: Wikipedia) ……. 5

1.3 SNARE complex: a) along with synaptic vesicle and plasma membrane b) its constituent proteins (Image ref: Wikipedia) ……..……..…….. 6

1.4 Synaptic vesicle docking ……..……..……..……... 8

1.5 Synaptic vesicle fusion ……..……..……..…..…… 9

2.1 Schematic of the axisymmetric model. Inset shows the deformed structure under the effect of SNARE-machinery force and electrostatic interaction. …… 24

2.2 (a) Arc length and tangent angle over the membrane, (b) Forces and moment along a cut in the membrane. ……..……..……..……... 26

2.3 Deformed geometry for different force magnitudes. The thick lines represent the plasma membrane and the thin lines represent the vesicle. The inset shows the zoomed-in section near the load application point (shown as •). The parameters of the analysis are: load application point, $\bar{S}_0 = \pi / 6$, pretension in plasma membrane, $\bar{T}_0 = 1$ and vesicle pressure. $\bar{p}_0 = 1$. ……..……..……. 32

2.4 Separation between the two C-termini (of Syx and Syb) of SNARE-machinery with the strength of the line force. ……..……..…… 33

2.5 Tension along the arc length for the vesicle (a) and the plasma membrane (b). The inset in (b) shows the location of force on the vesicle and the plasma membrane in the undeformed configuration. ……..……..…... 34

2.6 Maximum tension in vesicle and compression in plasma membrane as the load is increased for different surface charge densities. …… 35

2.7 Deformed geometry of the membranes under varying force location, while keeping its magnitude the same. The inset shows the location of the force application point ($\bullet$) on the deformed geometry for different cases. The parameters are: line force magnitude, $\bar{F} = 20$, pretension in plasma membrane, $\bar{T}_0 = 1$ and vesicle pressure. $\bar{p}_0 = 1$. …….. 36

2.8 Tension along the arc length of the vesicle (a) and the plasma membrane (b), when the location of the SNARE-machinery force is varied. Inset in (b) shows the different locations of the SNARE-mechanism. ……... 37

2.9 Maximum tension in the vesicle and the plasma as the location of the force is varied ……. 38

2.10 Maximum tension in the vesicle and plasma as the magnitude of force supplied by the SNARE-machinery is increased for different locations of the SNARE-machinery. ……. 38

2.11 Deformed geometry of the membranes as the pretension in the plasma membrane is varied. Inset shows the location ($\bullet$) of the force on the deformed

geometry. The parameters are: load application point, $\bar{s}_0 = \pi / 6$, line force magnitude $\bar{F} = 20$, and vesicle pressure, $\bar{p}_0 = 1$. 40

2.12 Tension in the vesicle and compression in the plasma membrane along the arc length for two different values of pretension. 41

2.13 Maximum tension in the vesicle and maximum compression in the plasma membrane (on the left axis) and minimum separation between the vesicle and the plasma membrane (on the right axis) as pretension is varied 42

2.14 Deformed geometry of the membranes as the osmotic pressure in the plasma membrane is varied. Inset shows the location ($\bullet$) of the force on the deformed geometry. The parameters are: load application point, $\bar{s}_0 = \pi / 6$, pretension in plasma membrane, $\bar{T}_0 = 1$ and line force magnitude $\bar{F} = 20$ 43

2.15 Tension in the vesicle and compression in the plasma membrane along the arc length for three different values of osmotic pressure. 44

2.16 Maximum tension in the vesicle and plasma membrane as the magnitude of pressure across the vesicle is increased 45

3.1 The AA (*left*) and CG (*middle*) representations of the SNARE bundle are shown. Both models include helices Syb, Syx, SN1, and SN2 with each helix contributing one residue to the ionic layer (*beads*): R56, Q226, Q53, and Q174 respectively. The C-terminal ends of Syb and Syx play an integral role in the fusion process in that they attach to the vesicle (Syb) and plasma membrane (Syx). The ENM spring network (*right*) that maintains the individual helical

structure is shown for Syb and Syx where the thick lines represents the Cα backbones and the thin lines represent ENM springs. The Miyazawa and Jernigan contacts between Syb and Syx are also represented (*dotted lines*). (*B*) The spectra used to compare the fluctuations of the AA and CG models are shown for Syb. Values for ks of 0.0963 N/m and Rc of 20 Å were used for the CG model. The inset shows 10 snapshots of Syb during the corresponding AA simulation. (*C*) Mean distance for different values of parameter *A* along with snapshots of the SNARE bundle. The original crystal is represented by the black line. The version chosen for simulation is marked by the black circle. …….. 130

3.2 (*A*) A schematic of the axisymmetric model in the undeformed configuration, showing the location of SNARE and direction of force applied. (*B*) The repulsive forces (shown by the dotted lines) act on the deformed configuration of the vesicle as does the SNARE force, *F*. (*C*) The figure shows the convention for shear force (*Q*), in-plane tension (*T*), and moment (*M*) acting on the cross-section of the membrane a location (*S*), where (S) is the tangent angle in the undeformed configuration measured from the vertical. (*D*) Example of a deformed vesicle-plasma membrane complex for a 20-nm diameter vesicle docked by 15 SNAREs …… 138

3.3 (*A*) Force versus SNARE end separation for the vesicle-membrane system for different numbers of SNAREs for the hydration repulsion case. (*B*) The force during separation of the ends of the SNARE bundle using λ of 0.30 for the CG model of SNARE along with snapshots of the SNARE bundle at the corresponding C-terminal end separation. The end separation is defined as the

distance between the Syb and Syx C-terminal beads. Syb, Syx, the ionic layer residues (*beads*), and the C-terminal residues (*beads with arrows*) that are attached to pulling beads are shown in each SNARE snapshot. The purple arrows correspond to the direction along which the C-terminal beads are being pulled. (*C*) The force as a function of Syb-Syx C-terminal distance is shown for the vesicle-membrane (the exponentially decreasing curves) and SNARE. One (*solid line*), two (*dash line*), and three (*dash-dot line*) SNAREs are shown in this plot. Intersections between the vesicle-membrane and SNARE force-displacement responses represent equilibrium states. There are a number of instabilities represented by load-drops. These correspond to separation of individual layers and have been so labeled. …… 145

3.4 *A*) Energy as a function of SNARE end separation when repulsion between the vesicle and plasma membrane is dominated by hydration repulsion. The energetic contributions from SNARE (attractive), hydration (repulsive) and the total (their sum) are shown. The hydration repulsion has been shifted vertically by -17 kT for clarity. (*B*) Contour plot of total energy as a function of SNARE end separation distance for different numbers of SNAREs under hydration repulsion. Circles correspond to global energy minima representing the equilibrium SNARE end separation for a given number of SNAREs. Vesicle radius is 20 nm. (*C*) Contour plot of total energy as a function of SNARE end separation distance for different numbers of SNAREs under electrostatic repulsion for a fixed charge of -0.025 C/m2 on the vesicle and the membrane in the limit of high tension in the vesicle and plasma membrane. For this case, minimum lateral separation between the SNARE bundles has been increased

from 3 nm to 4nm. (*D*) The structure of SNARE corresponding to the case shown in Fig. 4 *B*, number of SNAREs=1. Syb, Syx, SN1, SN2 are shown with the ionic layer residues indicated as large beads. *(E*) The same structure as in Fig. 4 *D* but showing only Syb and Syx for clarity. All contacts for residues within 2σ of each other are indicated with thin lines ……... 151

4.1 Synaptic vesicle docking mediated by ribbon structure and SNARE proteins, (b) the driving force is represented by single force acting on the south pole of the vesicle (c) deformed plasma membrane under hydrodynamic and driving force, horizontal arrows indicate direction of fluid flow ……... 196

4.2 Traverse time of the vesicle for a constant force ……. 201

4.3 Traverse time of the vesicle versus number of SNAREs using eq. 4.10. *m* governs the rate of decay of SNARE force with distance. …….. 202

4.4 Traverse time with varying decay exponent, for $n = 1$ ……. 204

4.5 Traverse time with varying number of SNAREs ……. 205

4.6 Traverse time with varying number of pretension, for number of SNAREs (a) $n = 1$ (b) $n = 2$ and (c) $n = 3$ ……. 207

4.7 Traverse time of synaptic vesicle vs. a) number of SNARE complex when $F_{1max} = 17\ pN$ b) F_{1max} when number of SNARE complexes, $n = 1$ …… 209

5.1 Schematic for SNARE mediated synaptic vesicle fusion a) side view of pre-fusion geometry b) simplified membrane geometry c) a side view close up of

pre-fusion geometry d) post-fusion and fusion pore formation. …….. 281

5.2 FENE and harmonic bonds in a lipid molecule …….. 285

5.3 Bending stiffness calculation of lipid membrane using the methodology proposed by Hu et al. [29]. F_x is the force exerted by the lipid membrane on the yz face of the simulation box and is scaled with $\frac{\epsilon^{lipid}}{\sigma^{lipid}}$, the coefficients b_i's are the coefficients in the expansion, L_x and L_y are the length of the membrane along x and y directions, k_B is the Boltzman Constant and T is the temperature. …….. 286

5.4 Schematic of membrane fusion under the effect of indenters ……. 292

5.5 Critical separation between the membranes for hemifusion to occur……... 293

5.6 Fusion pore formation in membranes under in-plane tension ……. 294

5.7 SNARE protein mediated synaptic vesicle fusion a) side view (yz plane) b) top view (xy plane) …… 297

5.8 (a) A closer look at the fusion pore from the top vesicle side (xy plane) (b) View of the red slice of the fused membranes along x axis (c) View of the green slice of the fused membranes along y axis ...…… 300

Introduction

1.1 Neurotransmission

In the body of living organisms, the neural information is transmitted across the nervous system by the process of neurotransmission. The nervous system is a network of specialized cells called neurons. Neural information is transmitted from a neuron to its neighbor in the network by electric impulses and chemical transfer. The chemical transfer involves transportation of neurotransmitter and is synchronized by an electric impulse commonly known as an action potential. The neurotransmitters are packed inside nanometer scale sacs known as synaptic vesicles. These vesicles are fused to the base of the neuron to release the neurotransmitter towards the next neuron in the network.

The process of neurotransmission is a crucial step in the functioning of the nervous system. An improper neurotransmission can lead to various neurological disorders. For example, GABA (**g**amma-**A**mino**b**utyric **a**cid) is associated with the regulation of neurotransmission of Glutamate, which is a key neurotransmitter associated with anxiety. The malfunctioning of GABA receptors at the interface between two neurons is believed to be the cause behind anxiety [1]. In the case of brain injuries it has been reported that the level of calcium ions in the neurons goes up, which will result in improper action potential and hence poor neurotransmission [2]. Huntington's disease involves an excessive release of the neurotransmitter Glutamate and reduced release of Dopamine at the synapse. Glutamate and Dopamine interplay governs the motor control in living organisms [3]. A reduction on Dopamine release is the major cause

behind Parkinson's disease. This reduction is caused by the blockage of dopamine receptors in the neurons [4].

Despite its importance, neurotransmission is not well understood. The length scale involved in the process of neurotransmission is of the order of $\sim 20nm$, which is the radius of the synaptic vesicle [5]. The time scale associated with the neurotransmission is few nano-seconds [6]. The lacks of simultaneous spatial and temporal resolution at nanometer and nanosecond level respectively pose a huge obstacle in visualizing neurotransmission.

In this thesis we used a simulation based approach to study neurotransmission and more specifically synaptic vesicle fusion. Coarse Grained Molecular Dynamics (CGMD) simulation techniques capture the role of molecular interaction in the fusion process. Continuum mechanics based models provide additional insight on a coarser scale. n this work, we employed both approaches to study synaptic vesicle fusion.

In the next section, we will give a more detailed description of the synaptic vesicle fusion process.

1.2 Synaptic vesicle fusion

Synaptic vesicle fusion is the exocytosis process by which neurons exchange the neurotransmitter between them. As shown in Fig. 1.1, when a neural signal is received by neuron 1, also known as presynaptic neuron, that signal has to be passed along to the neuron 2, the postsynaptic neuron. The neural signal travels down the body of presynaptic neuron in form of an electric impulse referred to as, action potential. This action potential then reaches the synapse, which is the interface between two neighboring neurons. It needs to be emphasized that the neurons are not in direct

contact with each other – they are separated by a gap known as synaptic cleft which is approximately $20nm$ wide [7].

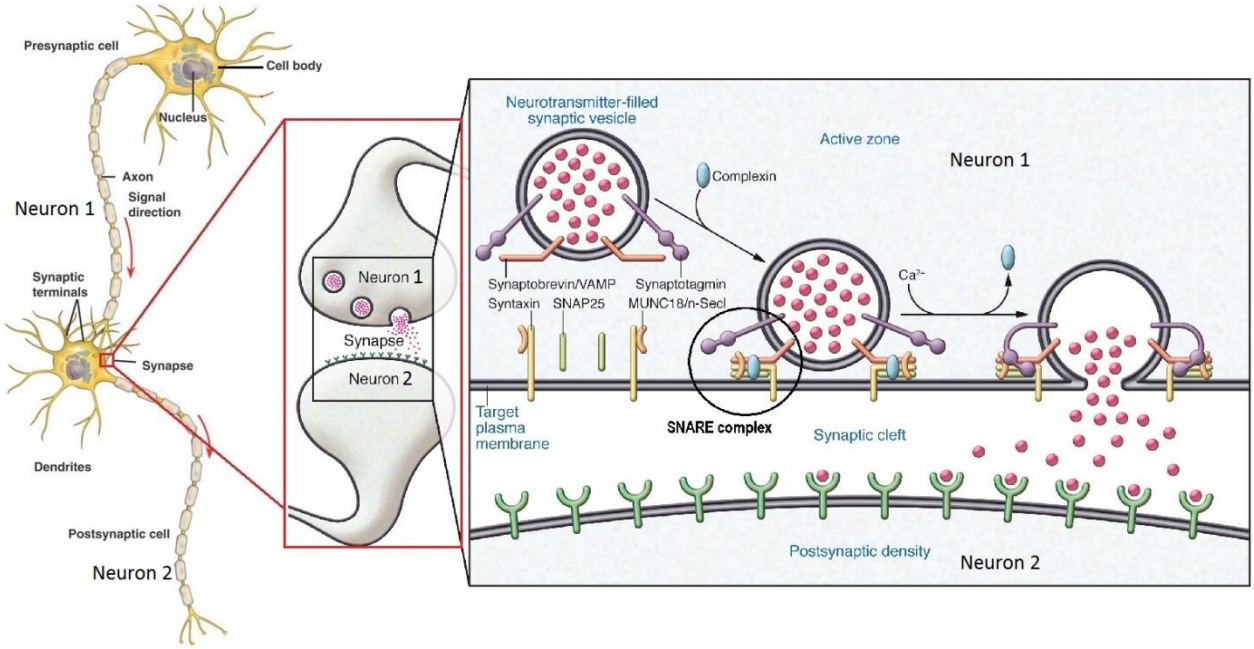

Fig 1.1: Schematic of synaptic vesicle fusion (Image ref: J.H. Hurst et al, J. Clin. Invest., 2013, kennesaw.edu)

The base of the presynaptic neuron has prepackaged sacs of neurotransmitters, known as synaptic vesicles with a radius of $20nm$. These vesicles wait at the base of the neuron for an action potential to trigger the fusion process. The machinery which drives the fusion process is a protein complex known as *SNARE* (**S**oluble **N**SF [*N*-ethylmaleimide *S*ensitive *F*usion protein] **A**ttachment Protein **Re**ceptor). The role of the SNARE protein complex in fusion can be broken down into two major steps:

1) To position the vesicle into the proximity of neuron plasma membrane and this step is known as priming of synaptic vesicles or docking;

2) Upon the arrival of action potential, the SNARE complex undergoes changes in conformation, which leads to fusion pore formation, allowing the release of the neurotransmitter into the synaptic cleft.

Before diving into the details of the synaptic vesicle fusion, we will describe the different components of synaptic vesicle fusion.

1.2.1 Lipid bilayer membrane structures: Synaptic vesicle and neuron plasma membrane

The surfaces of synaptic vesicles and neuron are composed mostly of lipid bilayers. The lipid bilayer membrane is an omnipresent biological element playing an extremely important role in various biological processes. Lipid membranes along with specific set of proteins regulate the essential cell processes like exocytosis, endocytosis, cell division, signaling etc. Lipid molecules are the basic building blocks of the lipid membranes. These molecules are amphiphilic in nature, due to the presence of a hydrophilic head and hydrophobic tails as shown in Fig. 1.2. When exposed to an aqueous medium, they tend to form interesting structure in order to minimize their free energy. The goal of these structures is to keep the hydrophobic tails away from water. As shown in Fig. 1.2, bilayer membranes are one of many geometric structures which result under this criterion of energy minimization.

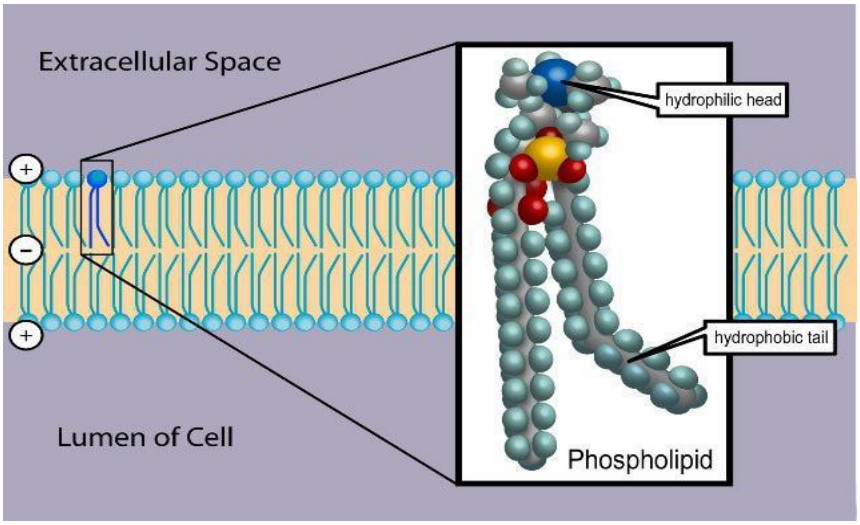

Fig 1.2: Lipid bilayer and single lipid molecule (Image ref: Wikipedia)

The synaptic vesicle is roughly a spherical structure of radius $\sim 20nm$. The presence of neuro-transmitters inside the vesicles creates an osmotic pressure across the synaptic vesicle membrane. This pressure is about $0.3Osm$ [8] at room temperature. This osmotic pressure creates an in-plane tensile stress in the membrane comparable to its rupture strength of $\sim 10mN/\mathrm{m}$ [9], [10]. The SNARE complex positions and further regulates the in-plane tension. Specifically, the SNARE complex can imposed additional tension on the membrane, so a fusion pore can be formed to release its contents.

In contrast, the neuron plasma membrane is a relatively larger structure. Relative to the synaptic vesicle, it can be modeled as flat surface as there is no significant osmotic pressure across this membrane.

1.2.2 SNARE complex

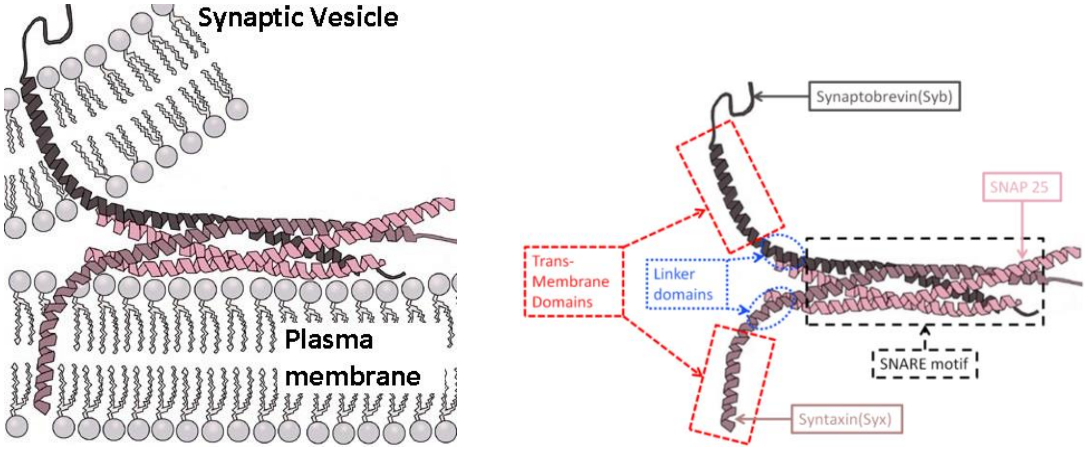

Fig 1.3: SNARE complex: a) along with synaptic vesicle and plasma membrane b) its constituent proteins (Image ref: Wikipedia)

A SNARE (**S**oluble **N**SF **A**ttachment Protein **Re**ceptor) complex is a tightly bound bundle of four proteins helices which is attached to the synaptic vesicle and neuron plasma membrane, as shown in fig 1.3a. Its role is to drive synaptic vesicle fusion. The four protein helices are contributed by three different proteins of SNARE family and they are listed below:

1. **Synaptobrevin (Syb)**

   This is a protein which is anchored to the lipid bilayer membrane of the synaptic vesicle and also known as v-SNARE or VAMP (**V**esicle **A**ssociated **M**embrane **P**rotein) [11], [12]. It contributes one SNARE motif to the SNARE complex bundle. Fig. 1.3b shows that the helix of this protein can be divided into three parts:

   a. SNARE motif

The part of the helix which is contributed towards the SNARE complex formation.

b. Linker domain

A small portion of the helix which connects the SNARE domain with the Trans-Membrane Domain. It is believed that it changes its conformation from unstructured (ribbon like) to structured (helical) upon arrival of action potential at the synapse [13]–[15].

c. Trans-Membrane Domain (TMD)

The TMD is a helical domain of the Syb which extends into the membrane of the synaptic vesicle and acts as an anchor for it [16]. Due to the hydrophobic nature of the TMD it is stable within the hydrophobic core of the lipid bilayer membrane.

2. Syntaxin (Syx)

Syx is the SNARE protein which contributes one SNARE motif (called t-SNARE) in the SNARE complex. It is anchored to the neuron plasma membrane by a similar hydrophobic TMD as that of Syb. Together SNAP-25 and Syx are known as t-SNAREs, means that they are attached to the target membrane or neuron plasma membrane. It has a very similar structure to that of Syb as shown in fig. 1.3b, with a SNARE motif, a linker domain and a TMD. The linker domain of Syx is also believed to change its conformation from unstructured to structured, upon the arrival of action potential at synapse [17].

3. SNAP-25

SNAP-25 contributes two SNARE motifs in the SNARE bundle. The two helices are called SN1 and SN2. The unstructured sequence of SNAP-25 between SN1 and SN2 is anchored to the top of the plasma membrane [18]. This domain of SNAP-25 is adsorbed on the surface of the plasma membrane due to palmitoylation of few amino acids.

1.3 Role of SNARE on Vesicle Docking

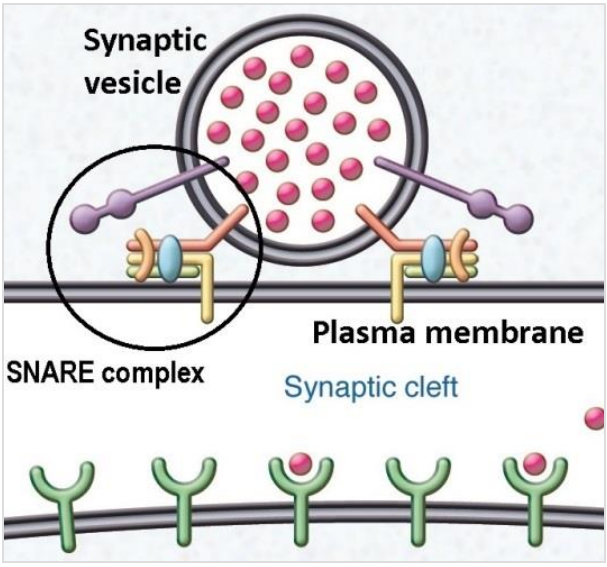

Fig 1.4: Synaptic vesicle docking

A synaptic vesicle which is tightly packed with neurotransmitter migrates towards the neuron plasma membrane. Upon which the v-SNARE anchored to the lipid membrane of the synaptic vesicle finds a t-SNARE group on the neuron plasma membrane. These v-SNARE and t-SNARE zips together to form the SNARE complex. This zippering process closes the gap between the two lipid membrane structures and results in docking as shown in Fig. 1.4. Specifically, the zippering of the SNARE motifs provides energy to counter the repulsive effects of following interactions:

1. The lipid molecules have a hydrophilic head, which can be charged or polar. This gives rise to electrostatic repulsion between the two lipid membrane structures.
2. Due to the polar/charged nature of the lipid heads, the water molecules are hydrogen bonded with lipid heads. The resistance against breaking the hydrogen bonds is known as hydration pressure.
3. Hydrodynamic forces can affect the docking process. A pressure gradient is required to create an outward flow of fluid in between the two membranes. This allows for the molecular rearrangements in the opposing lipid membranes, setting the environment for the synaptic vesicle fusion.

1.4 Synaptic Vesicle Fusion

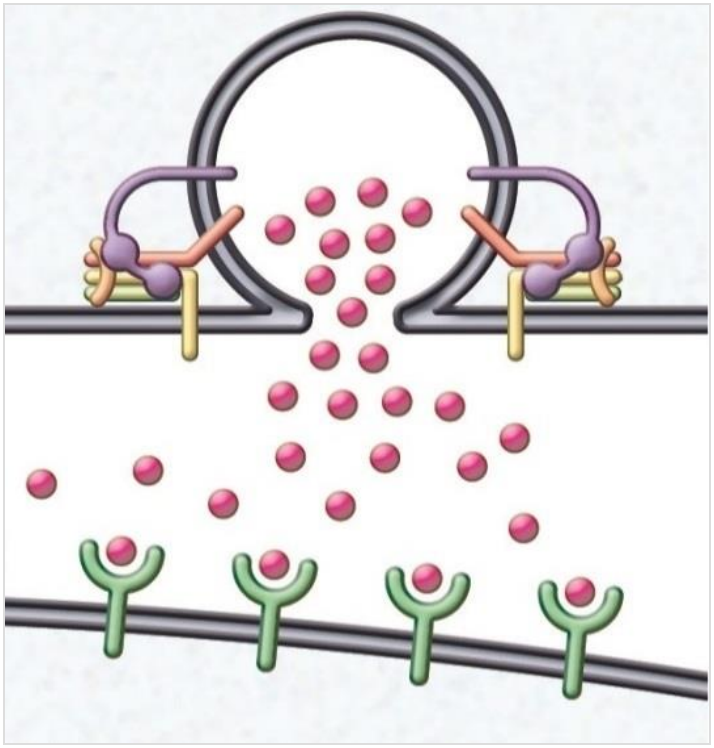

Fig 1.5: Synaptic vesicle fusion

When the action potential arrives at the synapse, the docked vesicle is brought closer to the neuron membrane. The arrival of action potential initiates several conformational changes in the docked synaptic vesicle. One of these changes takes place in the linker domain of Syb and Syx. The unstructured linker domain where bending stiffness is negligible becomes helical and this stiffening straightens the entire helix of Syb/Syx from its initial bent state. In this straighten state, these helices minimizes their elastic free energy [19].

The process of helical straightening brings the two lipid membranes further close to each other. This squeezes the water out and the molecular rearrangements in the lipid bilayer structures lead to formation of a fusion pore. The pathway from two lipid membranes to a fusion pore is a debatable topic [20]–[23]. The intermediate stages of this process are believed to be a stalk and a hemifused diaphragm. The hemifused diaphragm then ruptures to release the contents of the synaptic vesicle into the cleft. In some other observations, it has been proposed that next stage after stalk formation is fusion pore formation. Another topic of debate in this area lies in answering the question of how many SNARE complexes are needed for a successful synaptic vesicle fusion [24].

1.5 Organization

In this work we will talk about the approaches which have been incorporated in understanding the synaptic vesicle fusion. We have used a combination of continuum mechanics and CGMD models to simulate various aspects of the synaptic vesicle fusion.

In chapter 2, we have used a continuum mechanics model to understand the deformation and in-plane tension in the synaptic vesicle and neuron plasma membrane. This is in response to the external force acting on the membrane structures due to SNARE complexes and the electrostatic repulsion. From the deformed membrane shape we can locate the point at which the lipid membranes are closest to each other. This location is the probable site for stalk fusion and subsequently the fusion pore.

In Chapter 3, we have used the continuum model developed in chapter 2 along with a CGMD model of SNARE complex to answer the highly debatable question of how many proteins are needed to dock a synaptic vesicle. The SNARE complex force has to compete against the electrostatic repulsion and hydration pressure. A vesicle is assumed to be docked, if the shortest gap between the two membranes is $\sim 2nm$ [reference needed]. Based on our calculation 4-8 SNAREs complexes are sufficient to dock the synaptic vesicle at $\sim 2nm$ away from the neuron plasma membrane.

In chapter 4, we looked into the role of hydrodynamics in the synaptic vesicle docking. During the docking the physiological fluid has to be squeezed out from the gap between the vesicle and neuron plasma membranes. We have used a lubrication theory to compute the traverse time of synaptic vesicle under the effect of SNARE forces. Based on the experimental studies [25], it takes $\sim 250m\sec$ to dock a synaptic vesicle and it requires the force from the SNARE complex to decay rapidly as the gap closes.

Chapter 5 looks into the CGMD simulation of SNARE mediated membrane fusion and pore formation. The CGMD SNARE model used in [19] is implemented along with a CGMD lipid bilayer model [26]. The simulation studies inclined towards the possibility of stalk and subsequently a pore is formed. The simulation is still under the parameter tuning for interaction between SNARE and lipid bilayer membrane CGMD models.

Bibliography

[1] R. B. Lydiard, “The role of GABA in anxiety disorders.,” *J. Clin. Psychiatry*, vol. 64 Suppl 3, pp. 21–27, 2003.

[2] I. Fineman, D. A. Hovda, M. Smith, A. Yoshino, and D. P. Becker, “Concussive brain injury is associated with a prolonged accumulation of calcium: a 45Ca autoradiographic study,” *Brain Res.*, vol. 624, no. 1–2, pp. 94–102, 1993.

[3] V. M. André, C. Cepeda, and M. S. Levine, “Dopamine and Glutamate in Huntington’s Disease: A Balancing Act,” *CNS Neurosci. Ther.*, vol. 16, no. 3, pp. 163–178, 2010.

[4] S. Hisahara and S. Shimohama, “Dopamine Receptors and Parkinson’s Disease,” *Int. J. Med. Chem.*, vol. 2011, pp. 1–16, 2011.

[5] S. Castorph, D. Riedel, L. Arleth, M. Sztucki, R. Jahn, M. Holt, and T. Salditt, “Structure parameters of synaptic vesicles quantified by small-angle X-Ray scattering,” *Biophys. J.*, vol. 98, no. 7, pp. 1200–1208, 2010.

[6] V. Kiessling, S. Ahmed, M. K. Domanska, M. G. Holt, R. Jahn, and L. K. Tamm, “Rapid fusion of synaptic vesicles with reconstituted target SNARE membranes,” *Biophys. J.*, vol. 104, no. 9, pp. 1950–1958, 2013.

[7] L. P. Savtchenko and D. A. Rusakov, “The optimal height of the synaptic cleft,” *Proc. Natl. Acad. Sci.*, vol. 104, no. 6, pp. 1823–1828, 2007.

[8] L. Qu, Y. Akbergenova, Y. Hu, and T. Schikorski, “Synapse-to-synapse variation in mean synaptic vesicle size and its relationship with synaptic morphology and function,” *J. Comp. Neurol.*, vol. 514, no. 4, pp. 343–352,

2009.

[9] K. Olbrich, W. Rawicz, D. Needham, and E. Evans, “Water Permeability and Mechanical Strength of Polyunsaturated Lipid Bilayers,” *Biophys. J.*, vol. 79, no. 1, pp. 321–327, 2000.

[10] W. Rawicz, B. A. Smith, T. J. McIntosh, S. A. Simon, and E. Evans, “Elasticity, Strength, and Water Permeability of Bilayers that Contain Raft Microdomain-Forming Lipids,” *Biophys. J.*, vol. 94, no. 12, pp. 4725–4736, 2008.

[11] T. J. Siddiqui, O. Vites, A. Stein, R. Heintzmann, R. Jahn, and D. Fasshauer, “Determinants of synaptobrevin regulation in membranes,” *Mol Biol Cell*, vol. 18, no. 6, pp. 2037–2046, 2007.

[12] J. Han, K. Pluhackova, D. Bruns, and R. A. Böckmann, “Synaptobrevin transmembrane domain determines the structure and dynamics of the SNARE motif and the linker region,” *Biochim. Biophys. Acta - Biomembr.*, vol. 1858, no. 4, pp. 855–865, 2016.

[13] J. F. Ellena, B. Liang, M. Wiktor, A. Stein, D. S. Cafiso, R. Jahn, and L. K. Tamm, “Dynamic structure of lipid-bound synaptobrevin suggests a nucleation-propagation mechanism for trans-SNARE complex formation,” *Proc. Natl. Acad. Sci.*, vol. 106, no. 48, pp. 20306–20311, 2009.

[14] M. Bowen and A. T. Brunger, “Conformation of the synaptobrevin transmembrane domain,” *Proc. Natl. Acad. Sci.*, vol. 103, no. 22, pp. 8378–8383, 2006.

[15] D. H. Kweon, C. S. Kim, and Y. K. Shin, “Regulation of neuronal SNARE

assembly by the membrane," *Nat Struct Biol*, vol. 10, no. 6, pp. 440–447, 2003.

[16] A. Stein, G. Weber, M. C. Wahl, and R. Jahn, "Helical extension of the neuronal SNARE complex into the membrane," *Nature*, 2009.

[17] M. Lindau, B. A. Hall, A. Chetwynd, O. Beckstein, and M. S. P. Sansom, "Coarse-grain simulations reveal movement of the synaptobrevin C-terminus in response to piconewton forces," *Biophys. J.*, vol. 103, no. 5, pp. 959–969, 2012.

[18] S. Gonzalo, W. K. Greentree, and M. E. Linder, "SNAP-25 is targeted to the plasma membrane through a novel membrane- binding domain," *J. Biol. Chem.*, vol. 274, no. 30, pp. 21313–21318, 1999.

[19] N. Fortoul, P. Singh, C. Y. Hui, M. Bykhovskaia, and A. Jagota, "Coarse-grained model of SNARE-mediated docking," *Biophys. J.*, vol. 108, no. 9, pp. 2258–2269, 2015.

[20] L. V Chernomordik and M. M. Kozlov, "Mechanics of membrane fusion," *Nat. Struct. Mol. Biol.*, vol. 15, no. 7, pp. 675–683, 2008.

[21] Y. Kozlovsky, L. V. Chernomordik, and M. M. Kozlov, "Lipid Intermediates in Membrane Fusion: Formation, Structure, and Decay of Hemifusion Diaphragm," *Biophys. J.*, vol. 83, no. 5, pp. 2634–2651, 2002.

[22] K. Katsov, M. Muller, and M. Schick, "Field theoretic study of bilayer membrane fusion. I. Hemifusion mechanism," *Biophys J*, vol. 87, no. 5, pp. 3277–3290, 2004.

[23] K. Katsov, M. Müller, and M. Schick, "Field theoretic study of bilayer membrane fusion: II. Mechanism of a stalk-hole complex.," *Biophys. J.*, vol. 90, no. 3, pp. 915–26, 2006.

[24] M. K. Domanska, V. Kiessling, A. Stein, D. Fasshauer, and L. K. Tamm, "Single vesicle millisecond fusion kinetics reveals number of SNARE complexes optimal for fast SNARE mediated membrane fusion," *J. Biol. Chem.*, vol. 284, no. 46, pp. 32158–32166, 2009.

[25] D. Zenisek, J. a Steyer, and W. Almers, "Transport, capture and exocytosis of single synaptic vesicles at active zones.," *Nature*, vol. 406, no. 6798, pp. 849–854, 2000.

[26] I. R. Cooke, K. Kremer, and M. Deserno, "Efficient tunable generic model for fluid bilayer membranes," Feb. 2005.

Chapter 2

Synaptic vesicle docking is an extremely crucial step during the neurotransmission process. A neurotransmitter filled synaptic vesicle is made fusion ready and positioned in the proximity of the neuron plasma membrane. Docking is mediated by the proteins of SNARE family. These proteins zip together to form a SNARE complex. This complex serves as the clamping mechanism for the docking. The constituent proteins are attached to both neuron plasma membrane and synaptic vesicle at one end. The other end of these proteins is the initiation site for the zippering. This zippering provides the necessary force needed for clamping to dock the vesicle and competes against the electrostatic force. This electrostatic force originates due to the charge present on the lipid membranes. A force balance between the clamping force and electrostatic forces determine the deformation and stress in the membranes.

In this chapter we present a continuum mechanics based theory to estimate the state of the system under a prescribed clamping force. The system is assumed to be an axis-symmetric model, in which the synaptic vesicle is modeled as a sphere, whereas the neuron plasma membrane is modeled as a circular disc. The size of the circular is chosen to be much larger than the size of the synaptic vesicle ($\sim 20nm$). This assumption is made based on the cryo-electron images of the synapse. The neuron plasma membrane is nearly flat compared to the synaptic vesicle. To mimic the far field, a constant line load is applied on the edge of the neuron plasma membrane. The clamping force of the SNARE complex is distributed over a circular line on the synaptic vesicle and the neuron plasma membrane.

The model predicts the location of the closest proximity between the vesicle and plasma membrane occurs near the location where proteins are anchored to the membranes. This suggests that the fusion of the membranes gets initiated at location away from the bottom of the synaptic vesicle. At this location the in-plane tension in the membrane of vesicle is significantly high compared to the rest of the surface of the vesicle. One other important finding indicates that if the location of the load application is moved away from the center the more SNARE complexes need to be employed in order to maintain a similar distance of closest proximity between the two membranes. We also study the effect of surface charge, osmotic pressure and the far field pretension in the neuron plasma membrane on the deformation in the system.

2.1 Abstract

Neurotransmitter release from neuronal terminals is governed by synaptic vesicle fusion. Vesicles filled with transmitters are docked at the neuronal membrane by means of the SNARE machinery. After a series of events leading up to the fusion pore formation, neurotransmitters are released into the synaptic cleft. In this paper, we study the mechanics of the docking process. A continuum model is used to determine the deformation of a spherical vesicle and a plasma membrane, under the influence of SNARE-machinery forces and electrostatic repulsion. Our analysis provides information on the variation of in-plane stress in the membranes, which is known to affect fusion. Also, a simple model is proposed to study hemi-fusion.

2.2 Introduction

Neuronal transmitters are packed into vesicles and released from synaptic terminals by fusion of the vesicles with the plasma membrane. Synaptic vesicle fusion is mediated by the protein complex termed the SNARE. Details of the mechanism are still unclear, since it occurs at the microsecond scale, and thus it is difficult to capture the process using current imaging techniques. The release of transmitters into the synaptic cleft involves two major steps: 1) docking of vesicle on the plasma membrane, and 2) membrane fusion and subsequently pore opening. The central role in this entire mechanism is played by a specialized group of proteins termed the SNARE (soluble N-ethylmaleimide-sensitive-factor attachment protein receptor) complex [1–4]. More specifically, the process involves two transmembrane proteins Synaptobrevin 2 (Syb), Syntaxin 1 (Syx) and a protein SNAP-25 [5]. Syb is attached at one end to the vesicle by embedding a hydrophobic trans-membrane domain [6] into the vesicle membrane. It is hence referred to as "v-SNARE". The protein Syx embeds a transmembrane domain [7], and the protein SNAP-25 is anchored with a palmitoyl chain [8], onto the plasma membrane. The proteins attached to the target membrane are termed as "t-SNAREs". When a vesicle is near the plasma membrane, t-SNAREs form an acceptor site for the v-SNARE leading to the formation of the SNARE complex [9,10]. This SNARE complex consists of four helices (contributed by the Syb, Syx and SNAP-25), zippered into a tight bundle. It has been suggested that several SNARE complexes are involved in the docking process and the zippering action of these SNAREs provides a force to counter the repulsive electrostatic force between the membranes. Gao et al.[11] using optical tweezers controlled pulling experiments, found that the SNARE-

machinery generates forces of an order of 2-20 pN, depending on the level of zippering. Recently, calculations of the electrostatic repulsion between the vesicle and the membrane suggested that the repulsive force changes strongly with distance between the vesicle and membrane, and is on the order of 100-200 pN for a separation of 1nm between a typical synaptic vesicle and plasma membrane [12].

Synaptic vesicle and plasma membranes are bilayers made up of relatively long amphipathic lipid molecules, with their hydrophilic heads in the aqueous solution on either side of their bilayer and the hydrophobic tails in the interior. Lipid membranes are generally regarded as two dimensional fluids that, from modeling point of view, conserve their area during deformation [13,14]. Because the outer surface of the bilayer usually carries a net negative charge, considerable force is required to overcome the electrostatic repulsion between the vesicle and plasma membranes to dock the former. It has been hypothesized that the energy released during the SNARE zippering is utilized to overcome the energy barrier of the electrostatic interaction [15].

Coarse-grained continuum models for the contact mechanics of vesicle membranes have been studied by various authors [16–28]. Recently, Blount et al. [29], analysed the problem of a pressurized cylindrical vesicle interacting with a rigid substrate under a potential which has short range repulsion and long range attraction. Our approach in this work is similar, except that our vesicle is spherical, our substrate is a lipid membrane and the attractive potential is replaced by the zipping force exerted by the SNARE-machinery, which is modeled as a concentrated line load acting on both

membranes. Electrostatic repulsion between the membranes is modeled using the Debye-Huckel theory [12].

2.3 Geometry and Model

The geometry is shown schematically in Fig 2.1. We use a cylindrical coordinate system (r,θ,z) with θ the angle of revolution about z axis. To simplify the calculation, we assume axisymmetry; that is, we model the docking process by prescribing a circle of line forces of magnitude F on a spherical vesicle of radius R (see Fig 2.1) as well as on the plasma membrane. These forces represent the zipping of the SNARE-machinery and counter the repulsive electrostatic forces between them. As shown in Fig 2.1, the line force acts along a latitude of the undeformed vesicle and is constrained to remain normal to the deformed surface. The location of the latitude is specified by the arc length S_0 of a cross-section in the reference configuration, which is taken to be a spherical vesicle. Because the plasma membrane is very large compared to the vesicle radius, its reference configuration is taken to be a flat circular membrane of radius L under pretension T_0. We allow two different types of line forces acting on the plasma membrane. Both sets of forces act on a circle of radius S_0 and have the same magnitude F. The first set is assumed to be always normal to the deformed plasma membrane, while the second set is always directed opposite to the force on the vesicle (Fig 2.1).

The double layer model of charged surfaces in electrolytes has been successfully used to model the electrostatics near the lipid bilayers [30,31]. In this work, we follow the

double layer model used by Bykhovskaia et al. [12] where electrostatic repulsion between the vesicle and plasma membrane is determined by the solution of Debye-Huckel (DH) equation. McIntosh et al. [32] observed that when the gap between the membranes is greater than 1 nm, the DH equation predicts membrane interactions consistent with their experiments. For membrane separation below 1 nm, which is close to the Debye length $l_D \approx (0.67\text{nm})$ in our system, hydration repulsion, van der Waals attraction, and nonlinearity in the electrostatics come into play. Thus, as long as the gap between the membranes is greater than the Debye length, the solution of the DH equation should give a reasonable description of the electrostatics. It will be shown in the results section that, for the issues addressed in this manuscript, the separation between the membranes is always greater than twice the Debye length, ensuring that our electrostatics is consistent with the DH approximation. In our model, the electrostatic interaction between curve surfaces is calculated by the Derjaguin approximation [33], which assumes that locally the surfaces are flat, so interaction between two material points on the different membranes separated by a distance of δ (see Fig. 2.1, figure on right) can be described by determining the force per unit area between two infinite parallel planes separated by the same distance. The DH equation, appropriate for this geometry is given by eq. 2.1a. The repulsive force per unit area between the two planes, F_e, is obtained by solving eq. 2.1a using the constant charge boundary conditions (eq. 2.1b). Details of solution are given in Supplementary information (see eq. A2.105).

$$\frac{\partial^2 \varphi}{\partial z^2} = \frac{\varphi(z) - \varphi_0}{l_D^2},$$

$$-\varepsilon\varepsilon_0 \left.\frac{\partial \varphi}{\partial z}\right|_{z=0} = \sigma_{pm}, \quad \varepsilon\varepsilon_0 \left.\frac{\partial \varphi}{\partial z}\right|_{z=\delta} = \sigma_v \qquad \text{2.1a-c}$$

$$F_e = \frac{\sigma_v^2 + \sigma_{pm}^2 + 2\sigma_v\sigma_{pm}\cosh(\delta / l_D)}{2\varepsilon\varepsilon_0 \sinh^2(\delta / l_D)}$$

where $\sigma_v (= -0.025\,\mathrm{C/m^2})$ and $\sigma_{pm} (= -0.070\,\mathrm{C/m^2})$ are the surface charge densities of the vesicle and plasma membrane respectively, $l_D (= 0.67nm)$ is the Debye length, $\varepsilon (= 80)$ is the relative permittivity of water and ε_0 is the permittivity of vacuum. Our choice of surface charge densities above is based on the work of Bykhovskaia et al. [17]. It is about 2 to 3 times higher than those reported by Pekker et al. [34]. However, as noted later (see Fig. 2.6), the tension profile between membranes is insensitive to the magnitude of charge densities within this range. We also check that the equilibrium distances between the membranes are also not very sensitive to the magnitude of charge densities within this range (see Fig. A2.5).

The membranes are deformed by the zipping force of the SNARE complexes and electrostatic repulsion force. We model this deformation using continuum theory. The strain energy densities W of both membranes are given by,

$$W = cH^2 \qquad \text{2.2}$$

where H is the mean curvature and $c \approx 10 - 20k_BT$ is the bending rigidity of the lipid bilayer [35].

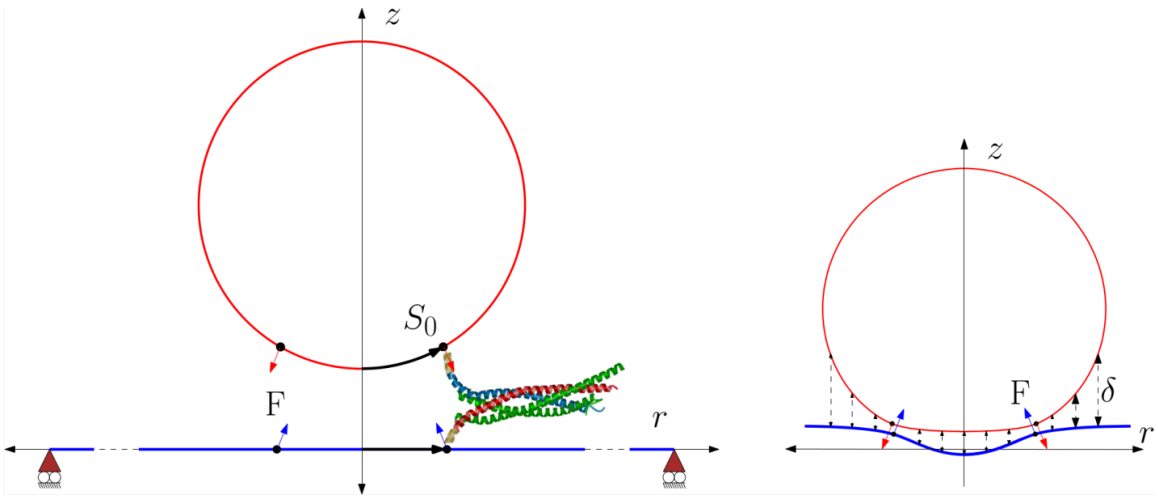

Fig 2.1: Schematic of the axisymmetric model. Inset shows the deformed structure under the effect of SNARE-machinery force and electrostatic interaction.

2.3.1 Governing equations for vesicle membrane

In the following, we use the formulation of Jenkins [17,36] and Long et al. [37] to derive the governing equations for the deformation of the spherical vesicle and the flat plasma membrane. The undeformed configuration of the vesicle is a sphere of radius R with arc-length in a cross-section denoted by S, whereas the plasma membrane occupies the interior of a circle of radius $L >> R$. We introduce the notation ϕ to denote the angle made by the tangent to a point on the cross-section of the deformed membrane in the (r,z) plane with the z axis (see Fig 2.1a). The osmotic pressure of the vesicle is denoted by p_0. The forces acting on the vesicle and plasma membrane due to SNARE complexes (several SNARE complexes can be attached to a vesicle, and the forces due to these vesicles are distributed uniformly on a closed circular arc on the vesicle) are denoted by F and $-F$ respectively (see Fig 2.1). Forces are resolved into a normal (F_n) and tangent component (F_t) with respect to the deformed

vesicle and plasma membrane. The electrostatic interaction force F_e is given by eq. 2.1 and is assumed to act in the z direction.

The equations describing the deformation involve the angle ϕ, the mean curvature H, the deformed arc length ξ, the deformed coordinates of a generic material point (r,z), which has an arc length coordinate S in the undeformed configuration. The force variables relevant to the calculation involve the shear force Q and, d an integration constant which determines the tension T in the membranes.

To reduce the number of parameters in our simulations we introduce normalized variables which are indicated by a horizontal bar. All distances are normalized by R, the radius of the vesicle. Since the bending rigidity c has units of energy, we use it to normalize force per unit length quantities, i.e., the out of plane shear, Q and in-plane tension T is normalized by c/R^2. Also, force per unit area quantities, p_0, F_e, F_t and F_n are made dimensionless by dividing with c/R^3. These variables are summarized in eqs. 2.3, below.

$$\begin{aligned}
&\bar{S} = \frac{S}{R}, \quad \bar{r} = \frac{r}{R}, \quad \bar{z} = \frac{z}{R}, \quad \bar{H} = RH, \quad \bar{\xi} = \frac{\xi}{R}, \\
&\bar{Q} = \frac{QR^2}{c}, \ \bar{d} = \frac{dR^2}{c}, \\
&\bar{p}_0 = \frac{p_0 R^3}{c}, \ \bar{F}_e = \frac{F_e R^3}{c}, \ \bar{F}_n = \frac{F_n R^3}{c}, \ \bar{F}_t = \frac{F_t R^3}{c},
\end{aligned} \tag{2.3}$$

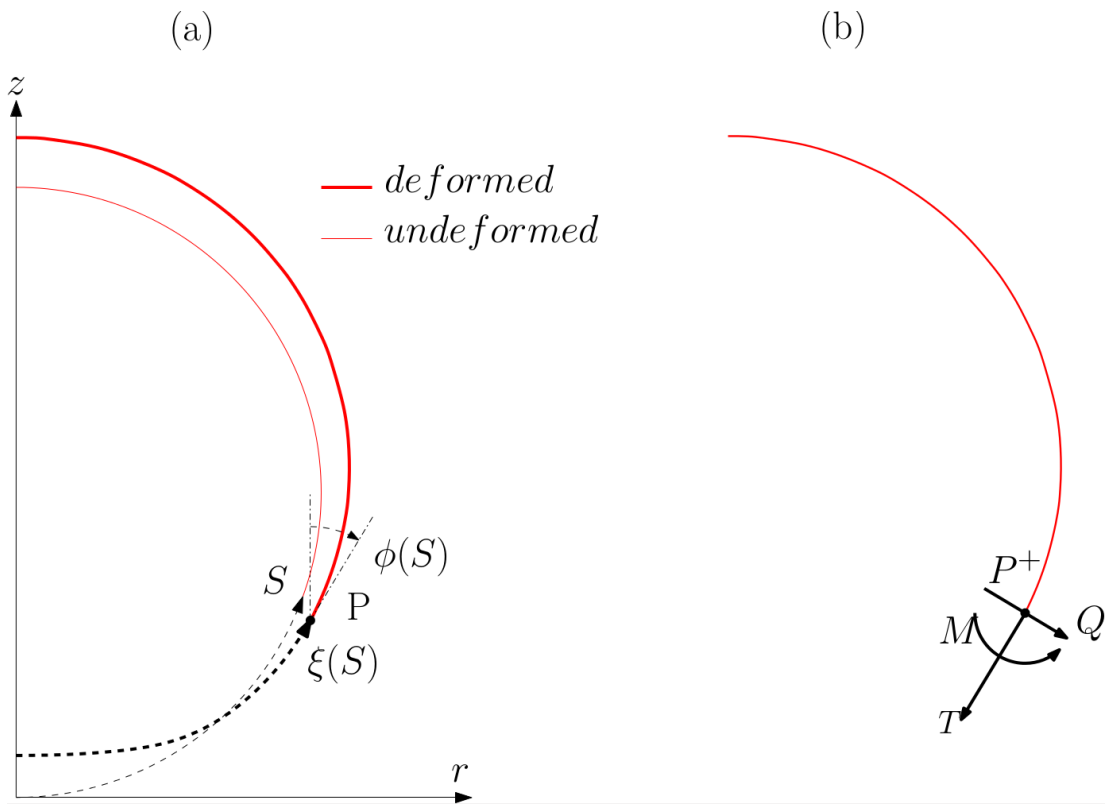

Fig 2.2: (a) Arc length and tangent angle over the membrane, (b) Forces and moment along a cut in the membrane.

In all simulations, we set the tangential component of snare force F_t on the vesicle to zero. In the Appendix A2, we derived in detail the six ordinary differential equations governing the deformation of the vesicle membrane (the final forms of these equations are given in eqs. A2.85 & A2.87):

$$\dot{\bar{Q}} = -\frac{\bar{Q}}{\bar{r}}\dot{\bar{\xi}}\sin\phi - 2\bar{H}\dot{\bar{\xi}}\left[\bar{d} + \bar{H}^2 + \left(2\bar{H} + \frac{\cos\phi}{\bar{r}}\right)\frac{\cos\phi}{\bar{r}}\right] + \dot{\bar{\xi}}\,\bar{p},$$

$$\dot{\phi} = \dot{\bar{\xi}}\left(2\bar{H} + \frac{\cos\phi}{\bar{r}}\right),$$

$$\dot{\bar{H}} = \dot{\bar{\xi}}\bar{Q},$$

$$\dot{\bar{r}} = \dot{\bar{\xi}}\sin\phi,$$

$$\dot{\bar{z}} = \dot{\bar{\xi}}\cos\phi,$$

$$\dot{\bar{d}} = \left(\bar{F}_e\cos\phi + \bar{F}_t\right)\dot{\bar{\xi}},$$

2.4a-f

where the dot denotes differentiation with respect to the normalized undeformed arc length $\bar{S}$, and

$$\dot{\bar{\xi}} \equiv \frac{\sin\bar{S}}{\bar{r}},$$ 2.4g

Eq. 2.4a represents force balance in the normal direction (eq. A2.83). Eqs. 2.4b and 2.4c are rearranged form of the mean curvature (eq. A2.74) and shear force (eq. A2.77) definitions, respectively. Eqs. 2.4d and 2.4e represent the geometric relationship between the variables (eq. A2.65), whereas, eq. 2.4f is obtained from the force balance in tangential direction (eq. A2.84). The generalized pressure $\bar{p}$ in Eq. 2.4a is related to the normalized osmotic pressure $\bar{p}_0$, the electrostatic force per unit area, $\bar{F}_e$ and the normal component of the line load applied at $\bar{S} = \bar{S}_0$, $\bar{F}_n$ by

$$\bar{p} = \bar{p}_0 + \bar{F}_e\sin\phi + \bar{F}_n\delta\left(\bar{S} - \bar{S}_0\right),$$ 2.4h

where $\delta(\bar{S} - \bar{S}_0)$ is the Dirac delta function.

These differential equations are supplemented with the boundary conditions:

$$\begin{aligned}
&\phi(\bar{S}=0)=\frac{\pi}{2},\\
&\bar{Q}(\bar{S}=0)=0,\\
&\bar{r}(\bar{S}=0)=0,\\
&\phi(\bar{S}=\pi)=-\frac{\pi}{2},\\
&\bar{Q}(\bar{S}=\pi)=0,\\
&\bar{r}(\bar{S}=\pi)=0.
\end{aligned} \qquad \text{2.5a-f}$$

The boundary conditions defined above describe the symmetry in the vesicle geometry. About the symmetry (z) axis, the curve has zero slope and the out of plane shear $\bar{Q}$ is zero, at both $\bar{S}=0$ and π. Also, for the continuity of the geometry, we impose $\bar{r}=0$ at both $\bar{S}=0$ and π.

The notation for positive shear force and tension is described in Fig 2.b. Finally, the expression for the normalized in-plane tension T in both the vesicle and plasma membranes is given by

$$\bar{T}=\frac{TR^2}{c}=\frac{R^2}{c}\left(-d-cH^2-cH\frac{cos\phi}{r}\right). \qquad \text{2.6}$$

2.3.2 Governing equations for plasma membrane

The governing equations for the deformation of the plasma membrane are the same as eqs. 2.4a-2.4f, (see SI for details) except that eq. 2.4g must be replaced by

$$\dot{\bar{\xi}}=\frac{\bar{S}}{\bar{r}} \qquad \text{2.7}$$

This change is due to the difference between the reference configurations (one is a sphere and the other a flat surface). The boundary conditions are:

$$\phi(\bar{S}=0)=\frac{\pi}{2},$$
$$\bar{Q}(\bar{S}=0)=0,$$
$$\bar{r}(\bar{S}=0)=0,$$
$$\phi\left(\bar{S}=\frac{L}{R}\right)=\frac{\pi}{2},$$
$$\bar{z}\left(\bar{S}=\frac{L}{R}\right)=0,$$
$$\bar{T}\left(\bar{S}=\frac{L}{R}\right)=\left[-\bar{d}-\bar{H}^2-\bar{H}\frac{cos\phi}{\bar{r}}\right]_{\bar{S}=\frac{L}{R}}=\bar{T}_0\equiv\frac{T_0R^2}{c} \qquad \text{2.8a-f}$$

The first three boundary conditions eqs. 2.8a-2.8c are due to axisymmetry. Eq. 2.8f states that the tension in the plasma membrane approaches the pretension at the boundary. This boundary condition along with eqs. 8d and 8f allow the plasma membrane to deflect only in horizontal direction. Had we replaced this boundary condition with a clamped condition, the deflection everywhere would be zero because of area incompressibility.

The coupled differential equations given by eqs. 2.4a-2.4g and eq. 2.7 with the boundary conditions given by eqs. 2.5a-2.5f and eqs. 2.8a-2.8f are solved using the MATLAB® bvp4c solver. The input parameters for the solver are the osmotic pressure p_0 across the vesicle membrane, which remains fixed throughout the deformation, SNARE-machinery force parameters (S_0 and F), electrostatic force (F_e), and pretension (T_0) in the plasma membrane.

2.4 Results

We first study the dependence of the deformed shape on magnitude of the line force F, for the case where force is equal and opposite on the vesicle and plasma membrane. The location of force application is fixed at $\bar{S}_0=\pi/6$ on both the vesicle

and plasma membrane, as shown in Fig 2.3. We vary the strength of the line force in the range of $5-20$ in dimensionless terms, which is equivalent to a total force between $66-266\ pN$. In our axisymmetric model, this force represents the total force exerted by all the SNARE complexes attached to the vesicle. For example, Gao et al. [17] found that the unzipping force for a single SNARE complex ranges from 2 to 20 pN. This force range should be treated as the lower estimate of the forces exerted in vivo, since in the study the SNARE complex unzippering occur at the range of seconds, while the process of neuronal fusion occurs at the scale of microseconds. If we assume that the force of 20pN or somewhat higher unzips a single SNARE complex in vivo, the force range explored in our study would be sufficient to separate 3-6 SNARE complexes. Fig 2.3 shows the deformed shapes of the membranes for four different values of $\bar{F}$. Note that the minimum separation between the membranes does not occur at the bottom of the vesicle, as is usually assumed, but near the point of load application where the SNARE complex is located. For practical purposes, the point of load application can be used as an estimate for the minimum separation. This separation is representative of the separation between the C-termini transmembrane domain of Syb and Syx. Fig 2.4 shows this estimate of minimum separation versus the applied force. The separation decreases rapidly with increasing applied force, with the rate of decrease of separation becoming slower at higher loads. Note that the minimum separation in the simulations is greater than twice the Debye length of our system, which is consistent with the DH approximation.

As shown in Fig 2.5a, the entire vesicle membrane is under tension and the maximum tension occurs at the bottom of the deformed vesicle. However, due to the direction of

the applied force, part of the plasma membrane can be under compression despite the pretension. Our results show that the maximum compression occurs at the center of the plasma membrane as shown in Fig 2.5b. Because the applied force in the plasma membrane has a tangential component, the tension is discontinuous across the line of load application as shown in Fig 2.5b. Fig 2.6 shows that these maxima are quite insensitive to the surface charge densities, that is, *increasing the surface charge density on the plasma membrane by a factor* ~ 3 *does not affect the maximum tension and compression for a given applied force*. The rupture strength of a lipid bilayer is approximately $10\ \mathrm{mN/m}$ [38,39], which on our non-dimensional scale turns out to be ~ 44 units. Therefore, the range of SNARE forces used in our analysis is not sufficient to cause rupture.

The results in Figs 2.3-2.6 are for membranes that are subjected to equal and opposite forces. We also carried out calculations for the case where the applied forces are always normal to the deformed surfaces. Our numerical result shows that except for the fact that the plasma membrane has much less compression, there are no qualitative differences between these two loading configurations; therefore, plots similar to Figs 2.3-2.6 for this other loading conditions are given in the Appendix A2. For the rest of this paper, we will focus on the case in which the applied forces are equal and opposite.

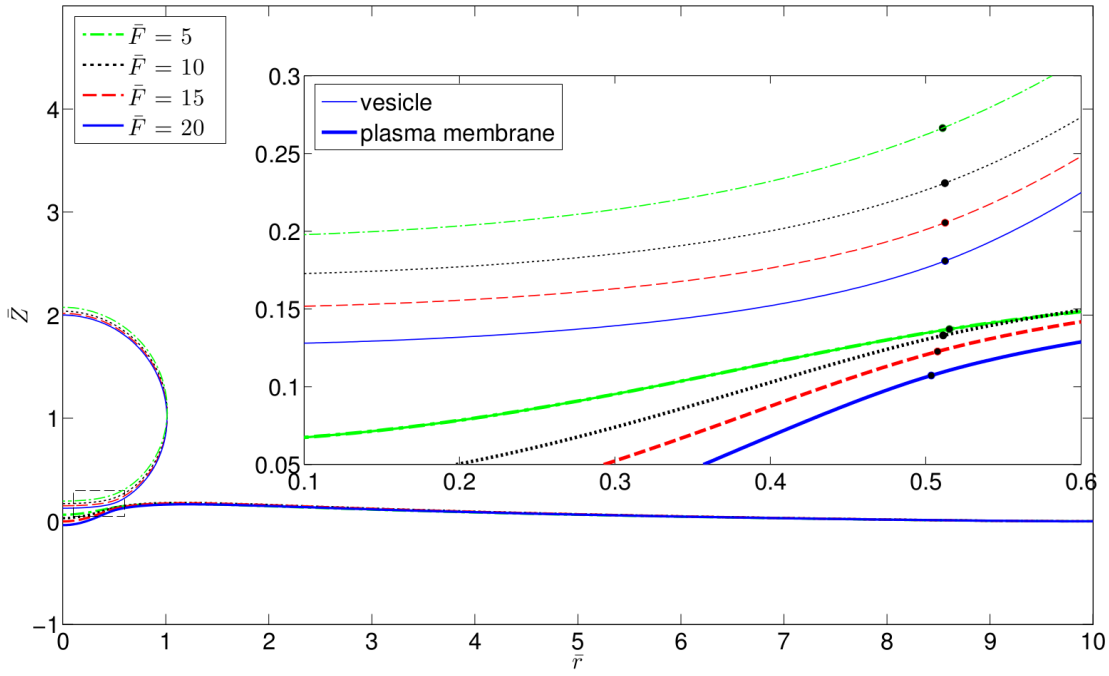

Fig 2.3: Deformed geometry for different force magnitudes. The thick lines represent the plasma membrane and the thin lines represent the vesicle. The inset shows the zoomed-in section near the load application point (shown as •). The parameters of the analysis are: load application point, $\bar{S}_0 = \pi / 6$**, pretension in plasma membrane,** $\bar{T}_0 = 1$ **and vesicle pressure.** $\bar{p}_0 = 1$ **.**

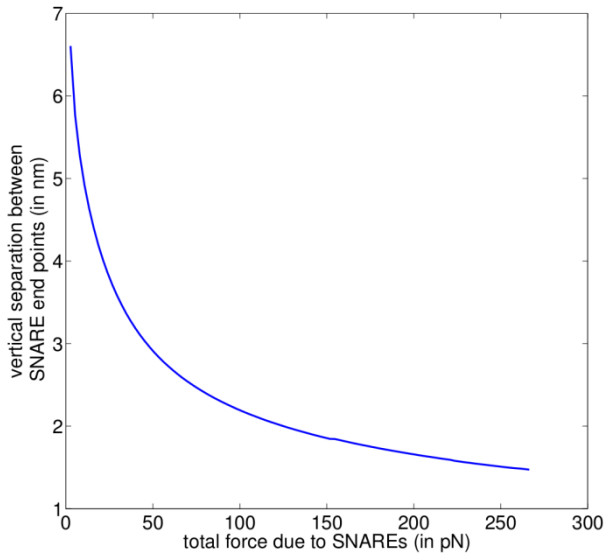

Fig 2.4: Separation between the two C-termini (of Syx and Syb) of SNARE-machinery with the strength of the line force

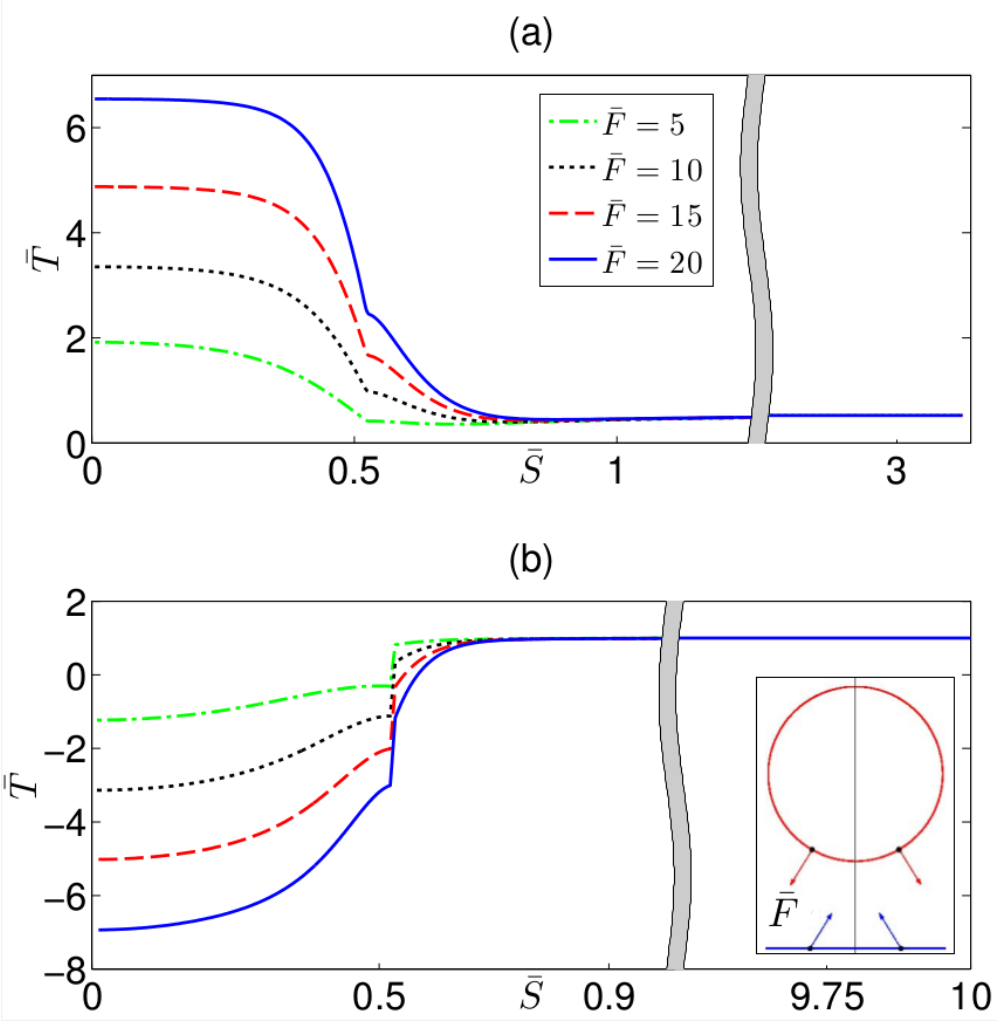

Fig 2.5: Tension along the arc length for the vesicle (a) and the plasma membrane (b). The inset in (b) shows the location of force on the vesicle and the plasma membrane in the undeformed configuration.

Next, we vary the location of the SNARE-machinery on both vesicle and plasma membrane ($\bar{S}_0$), and keep $\bar{F}$ fixed. It is interesting to note that, because the magnitude of the line force is fixed, increasing $\bar{S}_0$ to $\bar{S}_0'$ is equivalent to increasing the number of SNAREs by a factor of $sin\bar{S}_0' / sin\bar{S}_0$ in our simulation. Fig 2.7 shows that increasing $\bar{S}_0$ increases the deformation of the membranes, bringing them closer. The

tension (compression) in the membranes also increases with $\bar{S}_0$, as shown in Fig 2.8 and Fig 2.9. Note that as $\bar{S}_0$ increases, there is a smaller jump in tension in the plasma membrane. This result is due to the fact that, as $\bar{S}_0$ increases, the deformed plasma membrane surface reorients so that the direction of the SNARE force is closer to the surface normal. Fig 2.10 shows that, as the SNARE-machinery moves away from the center (increasing $\bar{S}_0$), the maximum tension increases rapidly. Recall in Fig 2.6 the maximum tension and compression vary approximately linearly with the magnitude of the applied force. Therefore, the slope of the lines in Fig 2.10 increases with $\bar{S}_0$.

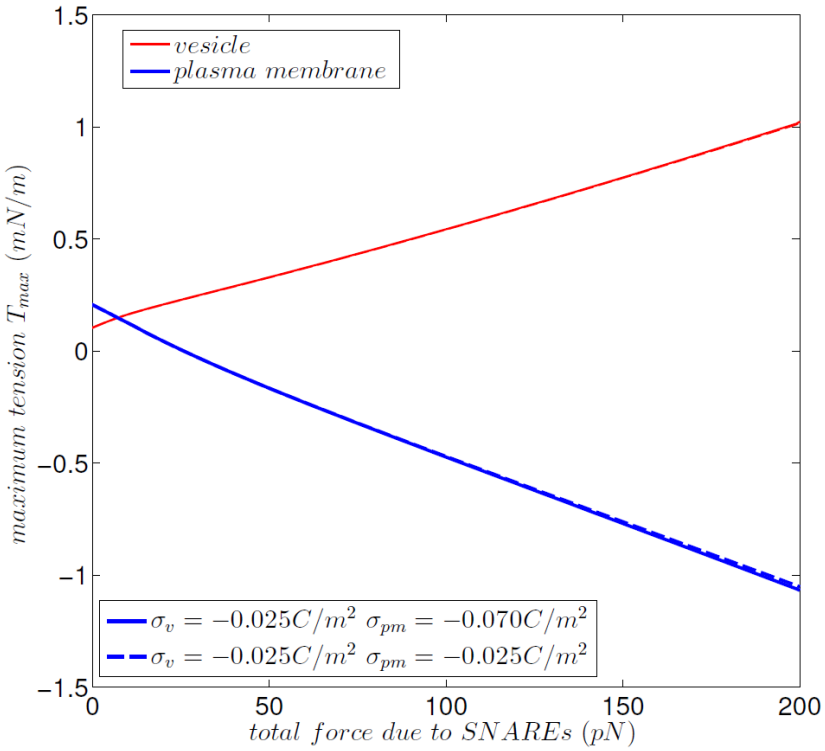

Fig 2.6: Maximum tension in vesicle and compression in plasma membrane as the load is increased for different surface charge densities.

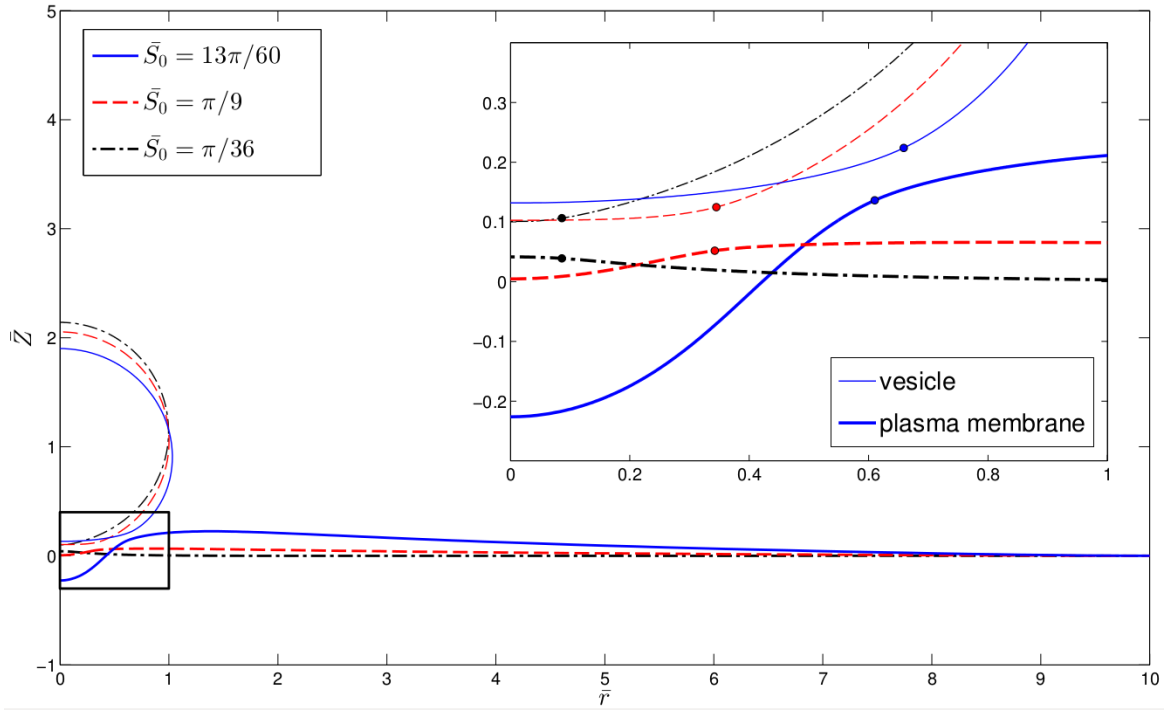

Fig 2.7: Deformed geometry of the membranes under varying force location, while keeping its magnitude the same. The inset shows the location of the force application point (●) on the deformed geometry for different cases. The parameters are: line force magnitude, $\bar{F} = 20$, pretension in plasma membrane, $\bar{T}_0 = 1$ and vesicle pressure. $\bar{p}_0 = 1$.

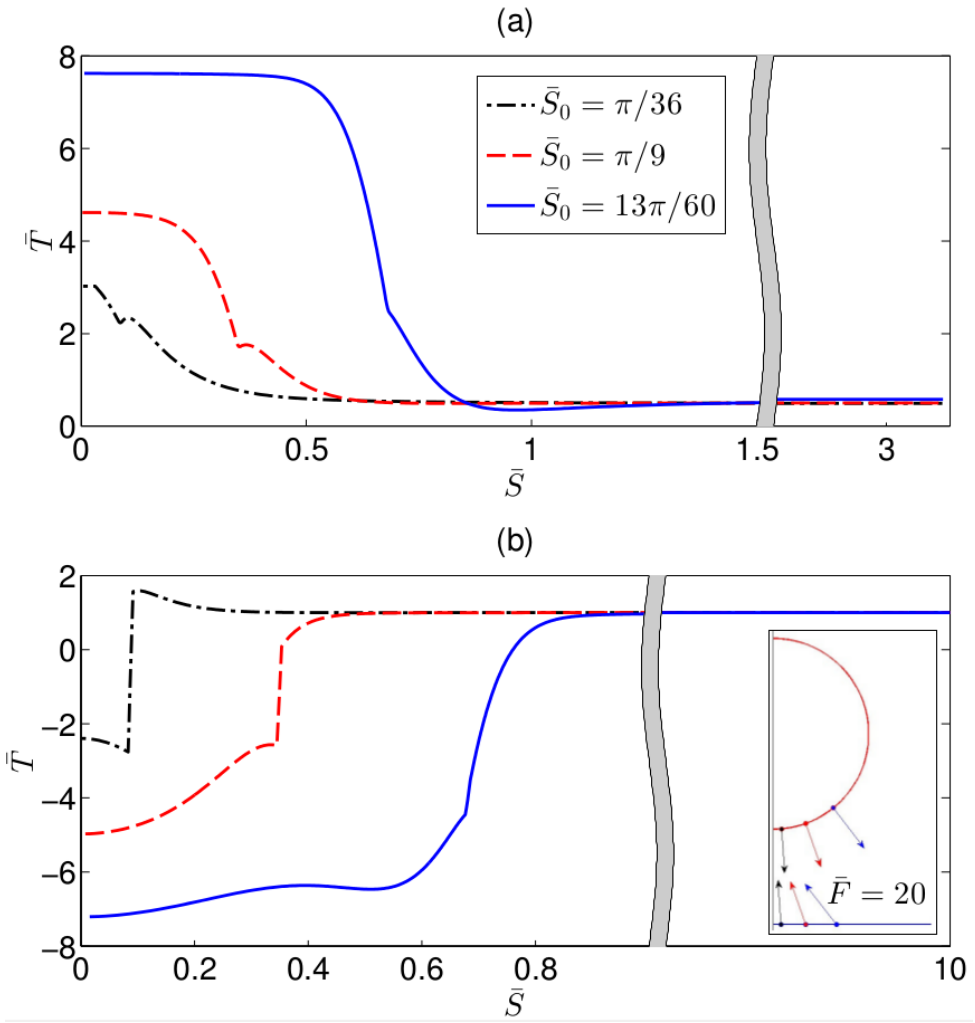

Fig 2.8: Tension along the arc length of the vesicle (a) and the plasma membrane (b), when the location of the SNARE-machinery force is varied. Inset in (b) shows the different locations of the SNARE-mechanism.

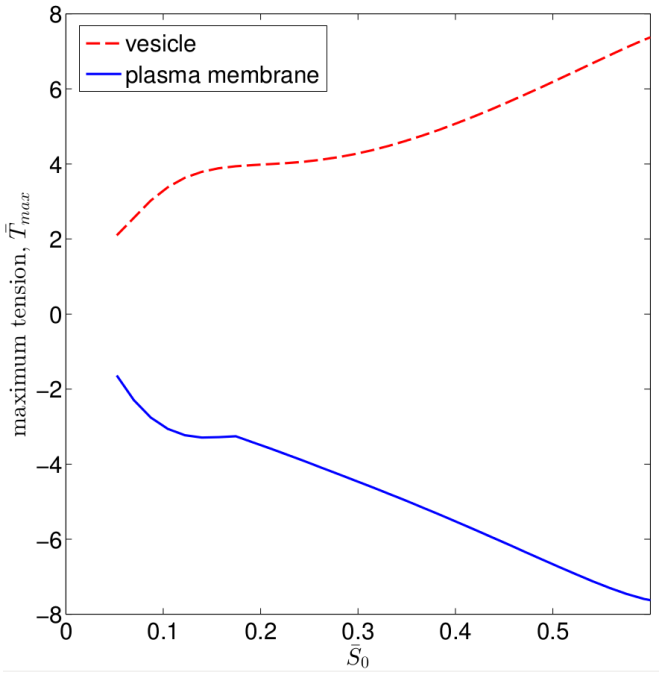

Fig 2.9: Maximum tension in the vesicle and the plasma as the location of the force is varied

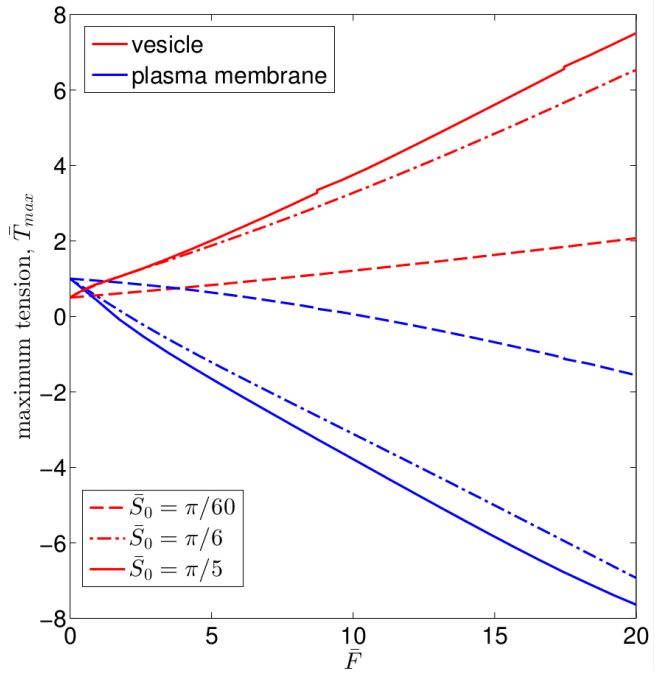

Fig 2.10: Maximum tension in the vesicle and plasma as the magnitude of force supplied by the SNARE-machinery is increased for different locations of the SNARE-machinery.

Our pretension boundary condition allows the plasma membrane to deflect. In the real system of synaptic vesicle fusion, pretension in the membranes is due to the osmotic pressure inside the neuron cell relative to its surroundings. In particular, the case of infinite pretension is equivalent to a rigid substrate which was studied earlier by Blount et al. [29] (see introduction).

To determine the influence of pretension in the plasma membrane, we keep the SNARE-machinery force at a fixed magnitude and location, while varying the pretension imposed at the far end of the plasma membrane. Fig 2.11 shows the deformed shapes for two different values of pretension $\bar{T}_0$, the deformation in the plasma membrane as well as that of the vesicle, decreases as the pretension increases. The distributions of tension in the membranes are shown in Fig 2.12 for two different pretensions. For the larger pretension, the entire plasma membrane is under tension. The critical dimensionless pretension where this occurs is 7, as shown in Fig 2.13, where we plot the maximum tension (compression) of the plasma membrane versus pretension. Interestingly, the maximum tension in the vesicle decreases with pretension. Fig 2.13 shows why this is the case: the minimum separation between the plasma membrane and the vesicle increases as the pretension becomes higher. The increase in separation results in a decrease in the electrostatic repulsion. Because the electrostatic force has a tangential component along the vesicle surface, lowering this force lowers the membrane tension.

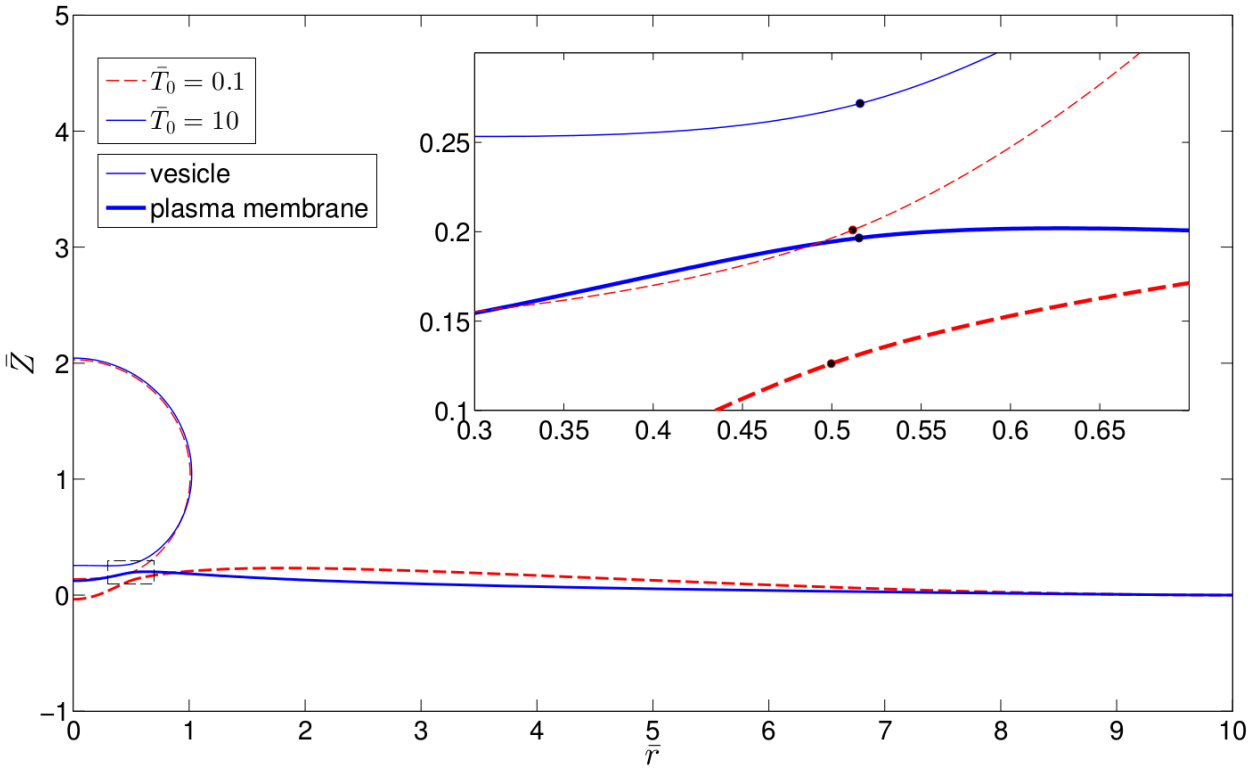

Fig 2.11: Deformed geometry of the membranes as the pretension in the plasma membrane is varied. Inset shows the location (●) of the force on the deformed geometry. The parameters are: load application point, $\bar{S}_0 = \pi / 6$, line force magnitude $\bar{F} = 20$, and vesicle pressure, $\bar{p}_0 = 1$.

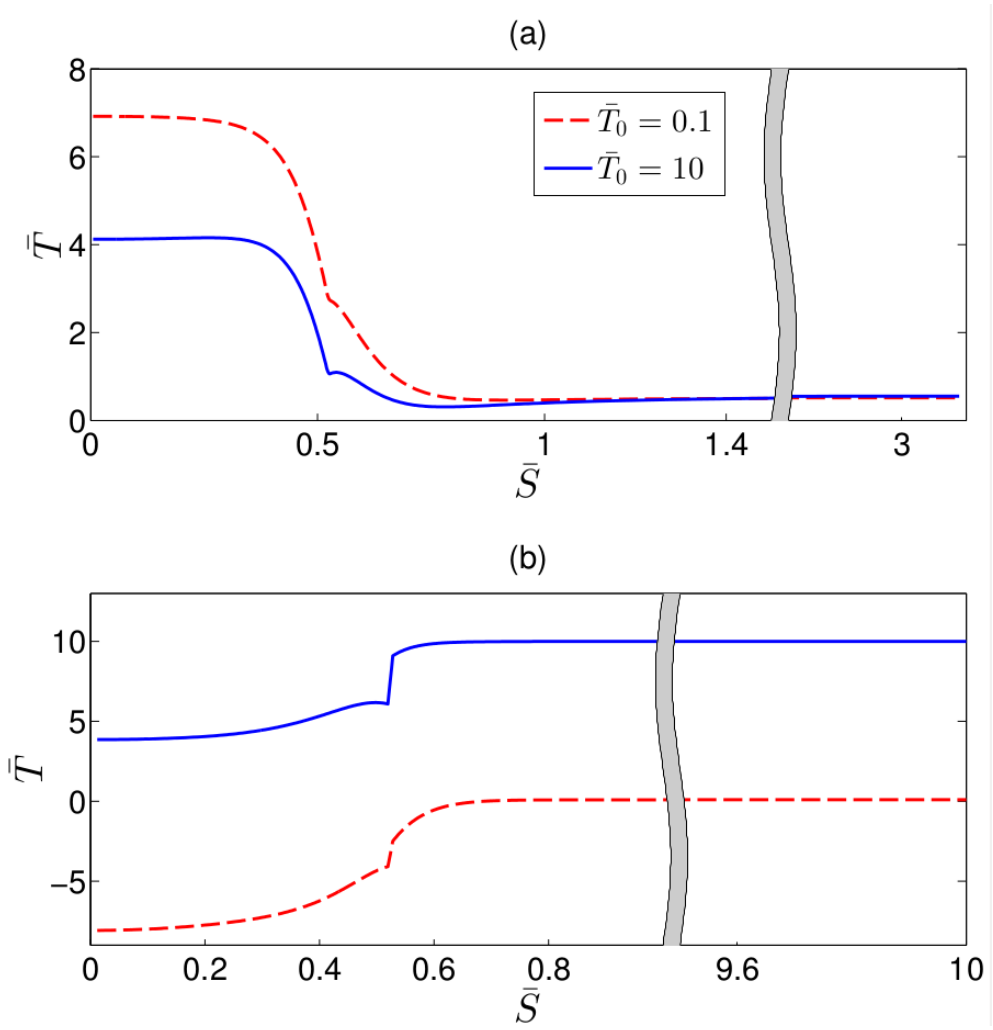

Fig 2.12: Tension in the vesicle and compression in the plasma membrane along the arc length for two different values of pretension.

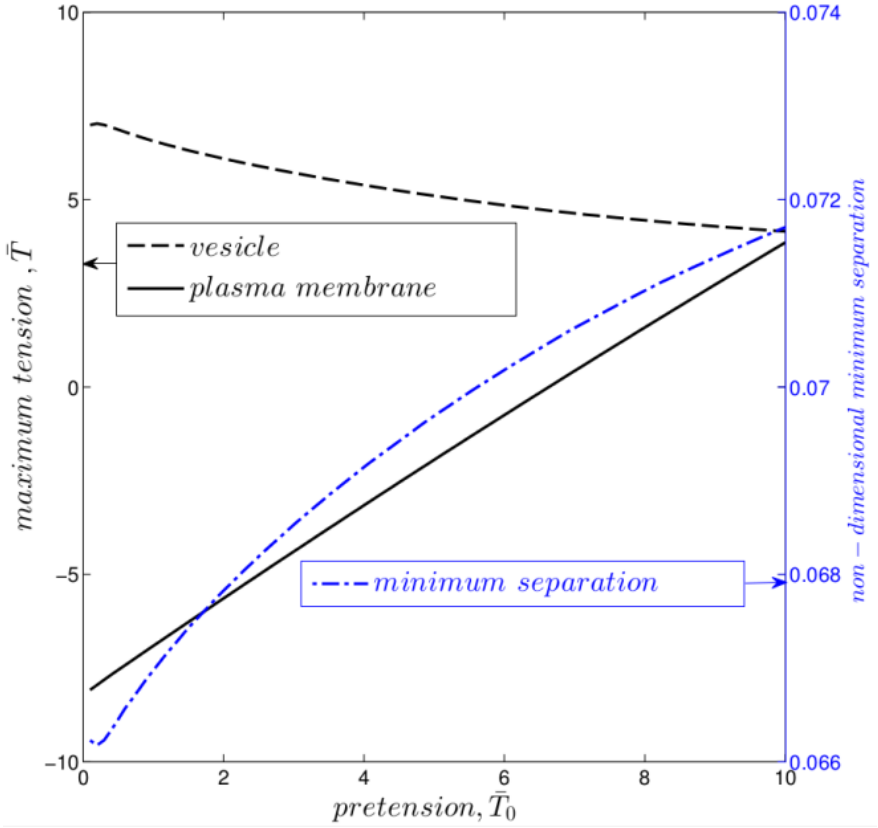

Fig 2.13: Maximum tension in the vesicle and maximum compression in the plasma membrane (on the left axis) and minimum separation between the vesicle and the plasma membrane (on the right axis) as pretension is varied

To determine the influence of osmotic pressure across the vesicle membrane, we keep the SNARE-machinery force at a fixed magnitude and location, while varying the osmotic pressure across the vesicle membrane. In the synaptic vesicles the osmolarity is $\sim 0.3\,\mathrm{Osm}$, which on non-dimensional scale induces a pressure of about ~ 70 inside the vesicle [40,41]. As stated in [41], the actual osmolarity could be lower than $0.3\,\mathrm{Osm}$, as some of the neurotransmitters can bind with the matrix inside the synaptic vesicle, resulting in a lower osmotic pressure. Fig 2.14 shows the deformed shapes for

three different values of osmotic pressure difference, it is evident that the deformation in the plasma membrane increases as the osmotic pressure increases. However, the minimum separation between the vesicle and the plasma membrane is nearly insensitive to the osmotic pressure. The distributions of tension in the membranes are shown in Fig 2.15 for three different pressure values. As expected, the profile of tension in the vesicle translates upward with a constant value proportional to the osmotic pressure. As a result, the maximum tension increases more rapidly in the vesicle, as compared to the plasma membrane, as shown in Fig 2.16. If the osmotic pressure of the vesicle is kept at a sufficiently high value, so that the peak tension at the vesicle bottom exceeds the failure tension value (~ 44 units on the dimensionless scale), then it could expose a site for fusion of the membranes.

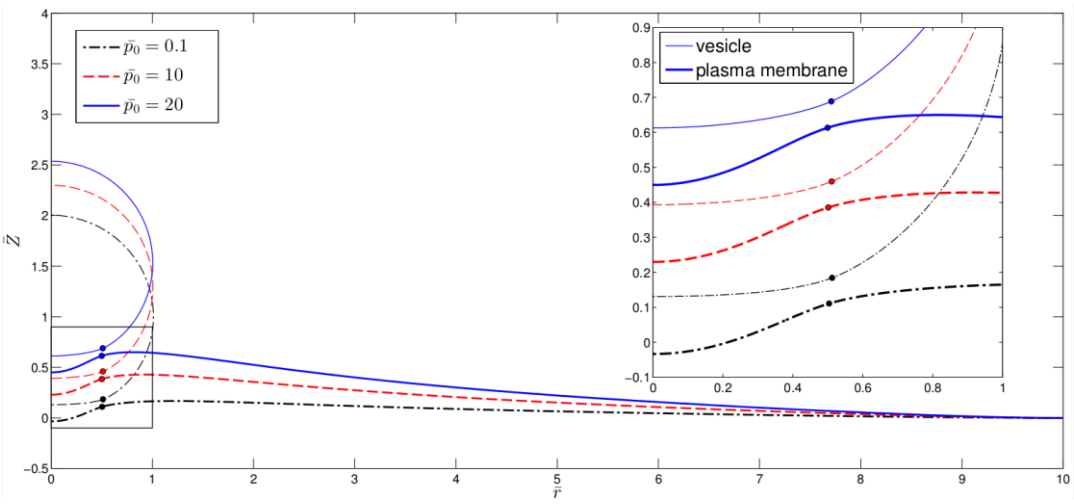

Fig 2.14: Deformed geometry of the membranes as the osmotic pressure in the plasma membrane is varied. Inset shows the location (•) of the force on the deformed geometry. The parameters are: load application point, $\bar{S}_0 = \pi / 6$, pretension in plasma membrane, $\bar{T}_0 = 1$ and line force magnitude $\bar{F} = 20$.

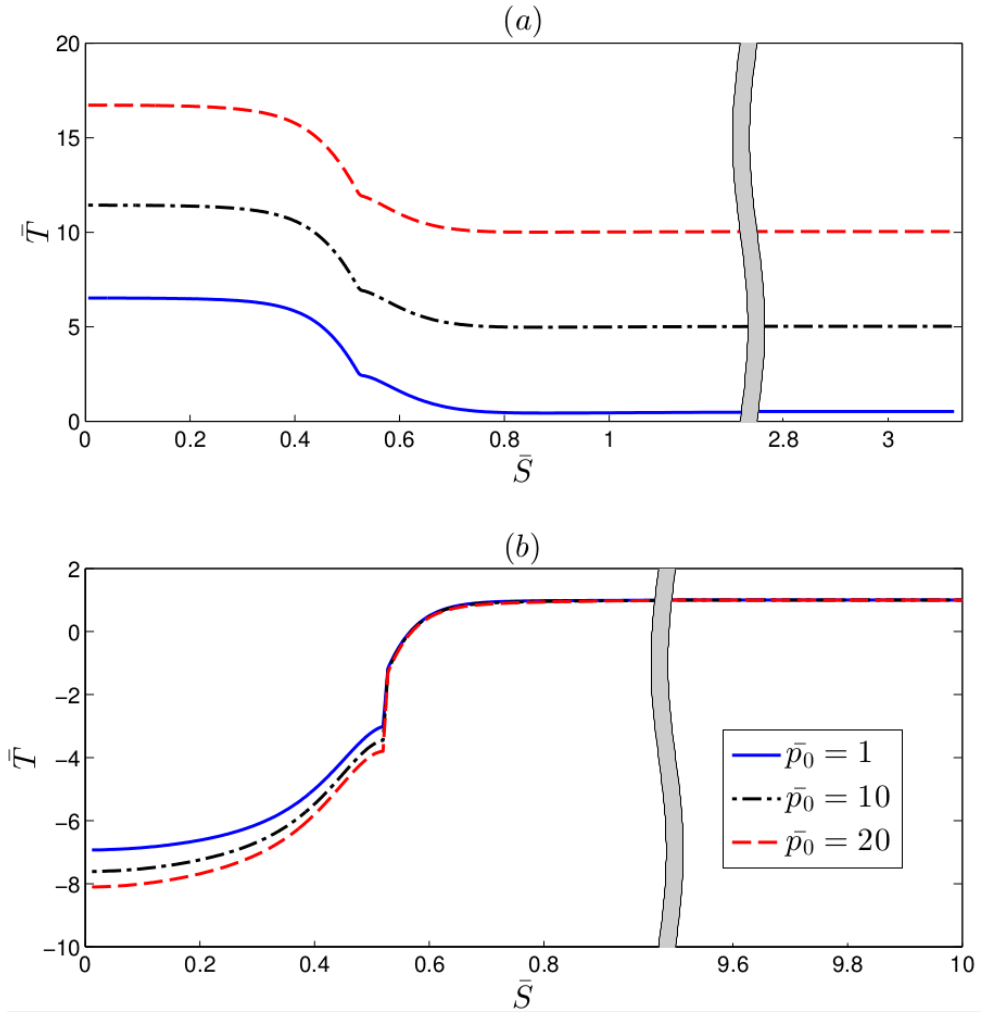

Fig 2.15: Tension in the vesicle and compression in the plasma membrane along the arc length for three different values of osmotic pressure.

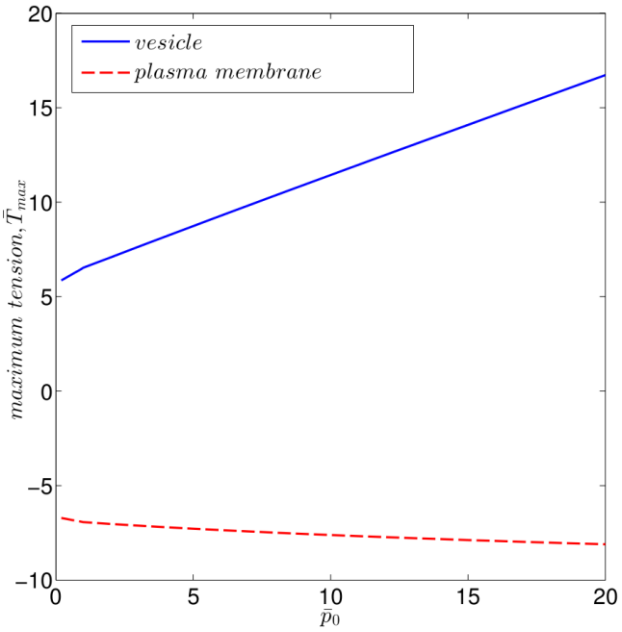

Fig 2.16: Maximum tension in the vesicle and plasma membrane as the magnitude of pressure across the vesicle is increased

2.5 Effect of Hemi-fusion

Numerous theoretical and experimental [2,42–45] studies suggested an intermediate step in the fusion process that involves the formation of a stalk and hemi-fusion diaphragm, followed by membrane rupture. The formation of stalk implies that instability developed at some location between the two bilayers, which induces a localized lipid rearrangement. Eventually, this rearrangement of lipids leads to the formation of a single bilayer, which is commonly known as hemi-fusion diaphragm. As mentioned above, our numerical results indicate that the shortest gap between the two membranes lies near the SNARE location. This supports the experimental observation that the trans-membrane segment of SNARE induces distortion in the lipid packing around it [46]. It is possible that this distortion will eventually lead to the lipid rearrangement in the membranes resulting into the formation of hemi-fusion

diaphragm. In the following, we propose that at this point of proximity hemi-fusion is initiated and propagates from there towards the bottom of the vesicle.

The exact mechanisms behind this complex sequence of events are still an active area of research. It is difficult to understand hemifusion using continuum membrane theory, because hemifusion is controlled by events on the nanometer scale. In this section, we consider a simpler question: assuming that there is a hemi-fused state, what is the tension in the hemi-fused region?

Because hemi-fusion involves very close contact between the lipid bilayers, it is reasonable to assume that the two membrane surfaces are completely dehydrated. Consistent with this assumption, hemi-fusion is modeled in our continuum approach by turning off the repulsive force inside a specified region on the membranes, which we define as the hemi-fused region. Thus, in the hemi-fused region, the outer surface of the vesicle is free of electrostatic repulsion and hence can be modeled as traction free. A limitation of our model is that it does not account for the fact that the hemi-fused region has only one bilayer instead of two. Because the real system consists of only one layer and we have neglected concentrated moments and shear at the edge of the hemi-fused region, the tension predicted by our model is expected to be lower than in the actual situation.

Details of these simulations are presented in the Appendix A2. Here we summarize the main results. Our key result is that the membrane tension increases with the length of the hemifused region. The deformation and tension are more severe than the case of without hemifusion. Our results suggest that hemifusion propagation increases the

chances of membrane rupture. Eventually a fusion pore formation is possible in the hemifused region, where tension is highest.

2.6 Summary and Conclusion

In this article we use a coarse–grained continuum model based on membrane theory to study the deformation and tension in the vesicle and base membranes during docking. The zipping action of the SNARE complex is represented by two sets of equal and opposite line forces acting on the membranes. The repulsive interaction between the membranes is represented using Debye-Huckel theory. The magnitude and location of these line forces are varied in our simulations to study their effects on tension and membrane deformation. We also study hemi-fusion by turning off the repulsive force in a region where the membranes are closest to each other. Our results can be summarized as follows:

- The closest approach between the vesicle and plasma membrane does not occur at the bottom of the vesicle, but near the location where the components of the SNARE complex are inserted into the membranes.
- The maximum in plane tension occurs at the bottom of the vesicle membrane.
- The maximum in plane tension increases linearly with the applied force.
- The maximum in plane tension is insensitive to the charge density of the surfaces. This can be explained by the fact that, the change in repulsive forces alters the separation between the membranes, while keeping the local deformation nearly the same as before.

- For small pretensions, the plasma membrane can be under compression, and the maximum compression occurs at the center, directly below the bottom of the vesicle. For normalized pretension greater than 7, the entire plasma membrane is under tension.
- As the location of force is moved away from the bottom of vesicle (which is equivalent to increasing the number of SNAREs in our simulation), the tension in the vesicle membrane increases.
- Hemi-fusion causes an increase in the in-plane tension of both the vesicle and the plasma membrane. We expect that this increase in the magnitude of the tension will eventually lead to rupture of the membranes, leading to fusion pore formation.

Bibliography

1. Brunger, A. T. 2001 Structure of proteins involved in synaptic vesicle fusion in neurons. *Annu Rev Biophys Biomol Struct* **30**, 157–171. (doi:10.1146/annurev.biophys.30.1.157)

2. Chen, Y. A. & Scheller, R. H. 2001 SNARE-mediated membrane fusion. *Nat Rev Mol Cell Biol* **2**, 98–106. (doi:10.1038/35052017)

3. Hay, J. C. 2001 SNARE complex structure and function. *Exp Cell Res* **271**, 10–21. (doi:10.1006/excr.2001.5368)

4. Jahn, R., Lang, T. & Südhof, T. C. 2003 Membrane Fusion. *Cell* **112**, 519–533. (doi:10.1016/s0092-8674(03)00112-0)

5. Rizo, J. & Rosenmund, C. 2008 Synaptic vesicle fusion. *Nat. Struct. & Mol. Biol.* **15**, 665–674. (doi:10.1038/nsmb.1450)

6. Deák, F., Shin, O.-H., Kavalali, E. T. & Südhof, T. C. 2006 Structural determinants of synaptobrevin 2 function in synaptic vesicle fusion. *J. Neurosci.* **26**, 6668–76. (doi:10.1523/JNEUROSCI.5272-05.2006)

7. Liang, B., Kiessling, V. & Tamm, L. K. 2013 Prefusion structure of syntaxin-1A suggests pathway for folding into neuronal trans-SNARE complex fusion

intermediate. *Proc. Natl. Acad. Sci. U. S. A.* **110**, 19384–9. (doi:10.1073/pnas.1314699110)

8. Gonzalo, S., Greentree, W. K. & Linder, M. E. 1999 SNAP-25 Is Targeted to the Plasma Membrane through a Novel Membrane-binding Domain. *J. Biol. Chem.* **274**, 21313–21318. (doi:10.1074/jbc.274.30.21313)

9. Söllner, T., Bennett, M. K., Whiteheart, S. W., Scheller, R. H. & Rothman, J. E. 1993 A protein assembly-disassembly pathway in vitro that may correspond to sequential steps of synaptic vesicle docking, activation, and fusion. *Cell* **75**, 409–418. (doi:10.1016/0092-8674(93)90376-2)

10. Rothman, J. E. 1994 Mechanisms of intracellular protein transport. *Nature* **372**, 55–63. (doi:10.1038/372055a0)

11. Gao, Y., Zorman, S., Gundersen, G., Xi, Z., Ma, L., Sirinakis, G., Rothman, J. E. & Zhang, Y. 2012 Single reconstituted neuronal SNARE complexes zipper in three distinct stages. *Science (80-.).* **337**, 1340–1343. (doi:10.1126/science.1224492)

12. Bykhovskaia, M., Jagota, A., Gonzalez, A., Vasin, A. & Littleton, J. T. 2013 Interaction of the complexin accessory helix with the C-terminus of the SNARE complex: molecular-dynamics model of the fusion clamp. *Biophys J* **105**, 679–690. (doi:10.1016/j.bpj.2013.06.018)

13. Canham, P. B. & Parkinson, D. R. 1970 The area and volume of single human erythrocytes during gradual osmotic swelling to hemolysis. *Can. J. Physiol. Pharmacol.* **48**, 369–376. (doi:10.1139/y70-059)

14. Evans, E. A., Waugh, R. & Melnik, L. 1976 Elastic area compressibility modulus of red cell membrane. *Biophys. J.* **16**, 585–595. (doi:10.1016/s0006-3495(76)85713-x)

15. Fasshauer, D., Otto, H., Eliason, W. K., Jahn, R. & Brunger, A. T. 1997 Structural changes are associated with soluble N-ethylmaleimide-sensitive fusion protein attachment protein receptor complex formation. *J Biol Chem* **272**, 28036–28041.

16. Helfrich, W. 1973 Elastic properties of lipid bilayers: theory and possible experiments. *Z. Naturforsch. C.* **28**, 693–703.

17. Jenkins, J. T. 1977 Static equilibrium configurations of a model red blood cell. *J Math Biol* **4**, 149–169.

18. Steigmann, D. J. 1999 Fluid Films with Curvature Elasticity. *Arch. Ration. Mech. Anal.* **150**, 127–152.

19. Mutz, M. & Helfrich, W. 1990 Bending rigidities of some biological model membranes as obtained from the Fourier analysis of contour sections. *J. Phys.* **51**, 991–1001.

20. Chizmadzhev, Y. A., Cohen, F. S., Shcherbakov, A. & Zimmerberg, J. 1995 Membrane mechanics can account for fusion pore dilation in stages. *Biophys. J.* **69**, 2489–2500. (doi:10.1016/S0006-3495(95)80119-0)

21. Rawicz, W., Olbrich, K. C., McIntosh, T., Needham, D. & Evans, E. 2000 Effect of chain length and unsaturation on elasticity of lipid bilayers. *Biophys. J.* **79**, 328–339. (doi:10.1016/S0006-3495(00)76295-3)

22. Boal, D. 2002 *Mechanics of the cell*. UK: Cambridge University Press.

23. Seifert, U. & Lipowsky, R. 1990 Adhesion of vesicles. *Phys. Rev. A* **42**, 4768–4771.

24. Lipowsky, R. & Seifert, U. 1991 Adhesion of Vesicles and Membranes. *Mol. Cryst. Liq. Cryst.* **202**, 17–25.

25. Steigmann, D., Baesu, E., Rudd, R., Belak, J. & McElfresh, M. 2003 On the variational theory of cell-membrane equilibria. *Interfaces Free Boundaries* **5**, 357–366.

26. Agrawal, A. & Steigmann, D. J. 2009 Modeling protein-mediated morphology in biomembranes. *Biomech. Model. Mechanobiol.* **8**, 371–379. (doi:10.1007/s10237-008-0143-0)

27. Agrawal, A. & Steigmann, D. J. 2011 A model for surface diffusion of trans-membrane proteins on lipid bilayers. *Z. Angew. Math. Phys.* **62**, 549–563. (doi:10.1007/s00033-011-0132-5)

28. Agrawal, A. & Steigmann, D. J. 2009 Boundary-value problems in the theory of lipid membranes. *Contin. Mech. Thermodyn.* **21**, 57–82.

29. Blount, M. J., Miksis, M. J. & Davis, S. H. 2013 The equilibria of vesicles adhered to substrates by short-ranged potentials. *Proc Math Phys Eng Sci* **469**, 20120729. (doi:10.1098/rspa.2012.0729)

30. Peitzsch, R. M., Eisenberg, M., Sharp, K. A. & McLaughlin, S. 1995 Calculations of the electrostatic potential adjacent to model phospholipid bilayers. *Biophys. J.* **68**, 729–38. (doi:10.1016/S0006-3495(95)80253-5)

31. Winiski, A. P., McLaughlin, A. C., McDaniel, R. V., Eisenberg, M. & McLaughlin, S. 1986 An experimental test of the discreteness-of-charge effect in positive and negative lipid bilayers. *Biochemistry* **25**, 8206–8214. (doi:10.1021/bi00373a013)

32. McIntosh, T. J., Magid, A. D. & Simon, S. A. 1990 Interactions between charged, uncharged, and zwitterionic bilayers containing phosphatidylglycerol. *Biophys. J.* **57**, 1187–1197. (doi:10.1016/S0006-3495(90)82638-2)

33. Argento, C., Jagota, A. & Carter, W. C. 1997 Surface formulation for molecular interactions of macroscopic bodies. *J. Mech. Phys. Solids* **45**, 1161–1183. (doi:10.1016/S0022-5096(96)00121-4)

34. Pekker, M. & Shneider, M. N. 2014 The surface charge of a cell lipid membrane.

35. Deserno, M. In press. Fluid lipid membranes – a primer.

36. Jenkins, J. T. 1977 Equations of Mechanical Equilibrium of a Model Membrane. *Siam J. Appl. Math.* **32**, 755–764. (doi:Doi 10.1137/0132063)

37. Long, R., Hui, C. Y., Jagota, A. & Bykhovskaia, M. 2012 Adhesion energy can regulate vesicle fusion and stabilize partially fused states. *J. R. Soc. Interface* **9**, 1555–1567. (doi:DOI 10.1098/rsif.2011.0827)

38. Olbrich, K., Rawicz, W., Needham, D. & Evans, E. 2000 Water permeability and mechanical strength of polyunsaturated lipid bilayers. *Biophys J* **79**, 321–327. (doi:10.1016/S0006-3495(00)76294-1)

39. Rawicz, W., Smith, B. A., McIntosh, T. J., Simon, S. A. & Evans, E. 2008 Elasticity, strength, and water permeability of bilayers that contain raft microdomain-forming lipids. *Biophys J* **94**, 4725–4736. (doi:DOI 10.1529/biophysj.107.121731)

40. Qu, L., Akbergenova, Y., Hu, Y. & Schikorski, T. 2009 Synapse-to-synapse variation in mean synaptic vesicle size and its relationship with synaptic morphology and function. *J. Comp. Neurol.* **514**, 343–52.

41. Blaustein M.P., Kao J.P.Y., M. D. R. 2012 *Cellular Physiology and Neurophysiology*. 2nd edn. Elsevier.

42. Jahn, R. & Scheller, R. H. 2006 SNAREs--engines for membrane fusion. *Nat Rev Mol Cell Biol* **7**, 631–643. (doi:10.1038/nrm2002)

43. Xu, Y., Zhang, F., Su, Z., McNew, J. A. & Shin, Y. K. 2005 Hemifusion in SNARE-mediated membrane fusion. *Nat Struct Mol Biol* **12**, 417–422. (doi:10.1038/nsmb921)

44. Giraudo, C. G., Hu, C., You, D., Slovic, A. M., Mosharov, E. V, Sulzer, D., Melia, T. J. & Rothman, J. E. 2005 SNAREs can promote complete fusion and hemifusion as alternative outcomes. *J Cell Biol* **170**, 249–260. (doi:10.1083/jcb.200501093)

45. Lu, X., Zhang, F., McNew, J. A. & Shin, Y. K. 2005 Membrane fusion induced by neuronal SNAREs transits through hemifusion. *J Biol Chem* **280**, 30538–30541. (doi:10.1074/jbc.M506862200)

46. Risselada, H. J., Kutzner, C. & Grubmuller, H. 2011 Caught in the act: visualization of SNARE-mediated fusion events in molecular detail. *Chembiochem* **12**, 1049–1055. (doi:10.1002/cbic.201100020)

Appendix A2

A2.1 Differential Geometry Primer

Like a plane in Cartesian coordinates, a surface can be defined using two independent variables, u^{α} (where $\alpha = 1, 2$).

Therefore, a point on space can be written as,

$$\underset{\sim}{r} = \underset{\sim}{r}(u^{\alpha}) . \qquad \text{A2.1}$$

A **local basis** can be defined in the tangent plane at a particular position as,

$$\underset{\sim}{a}_{\alpha} = \frac{\partial \underset{\sim}{r}}{\partial u^{\alpha}} = \underset{\sim}{r}_{,\alpha} , \qquad \text{A2.2}$$

where, comma denotes the partial derivative with respect to u^{α}. Thus, $\underset{\sim}{a}_1$ and $\underset{\sim}{a}_2$ are tangent vectors to curves with constant u^1 and u^2 at that particular position.

Reciprocal basis $\underset{\sim}{a}^{\beta}$ can be defined as,

$$\underset{\sim}{a}_{\alpha} \bullet \underset{\sim}{a}^{\beta} = \delta_{\alpha}^{\beta} . \qquad \text{A2.3}$$

Normal to the surface can be defined as,

$$\underset{\sim}{n} = \frac{\underset{\sim}{a}_1 \times \underset{\sim}{a}_2}{\left| \underset{\sim}{a}_1 \times \underset{\sim}{a}_2 \right|} , \qquad \text{A2.4}$$

as it can be seen that the normal is a unit vector by definition.

First fundamental form of surface $a_{\alpha\beta}$, is given by the following relation,

$$a_{\alpha\beta} = \underset{\sim}{a}_{\alpha} \bullet \underset{\sim}{a}_{\beta}, \qquad \text{A2.5}$$

where, $a_{\alpha\beta}$ is the symmetric metric tensor and its inverse matrix is $a^{\alpha\beta}$.

Using the fact that, normal is perpendicular to the tangent plane at a given position, one can get the **Second fundamental form of surface**, $b_{\alpha\beta}$ as,

$$\underset{\sim}{n} \bullet \underset{\sim}{a}_{\beta} = 0$$

$$\underset{\sim}{n}_{,\alpha} \bullet \underset{\sim}{a}_{\beta} + \underset{\sim}{n} \bullet \underset{\sim}{a}_{\beta,\alpha} = 0$$

$$b_{\alpha\beta} = -\underset{\sim}{n}_{,\alpha} \bullet \underset{\sim}{a}_{\beta} = \underset{\sim}{n} \bullet \underset{\sim}{a}_{\beta,\alpha}. \qquad \text{A2.6}$$

Again, we can see that $b_{\alpha\beta}$ is a symmetric tensor.

Mean curvature can be related to the surface parameters as,

$$H = \frac{1}{2} b_{\alpha}^{\alpha} = \frac{1}{2} a^{\alpha\beta} b_{\alpha\beta} = -\frac{1}{2} a^{\alpha\beta} \left(\underset{\sim}{n}_{,\alpha} \bullet \underset{\sim}{a}_{\beta} \right) = -\frac{1}{2} \underset{\sim}{n}_{,\alpha} \bullet \underset{\sim}{a}^{\alpha} \quad \text{A2.7}$$

Elemental area, can be written as,

$$dA = \left| \underset{\sim}{a}_1 du^1 \times \underset{\sim}{a}_2 du^2 \right| = \left| \underset{\sim}{a}_1 \times \underset{\sim}{a}_2 \right| du^1 du^2 = \sqrt{a}\, du^1 du^2. \qquad \text{A2.8}$$

Here, we used the result that $\left| \underset{\sim}{a}_1 \times \underset{\sim}{a}_2 \right| = \sqrt{a}$, which can be shown as follows,

$$a = \det \begin{vmatrix} a_{11} & a_{12} \\ a_{21} & a_{22} \end{vmatrix} = \det \begin{vmatrix} \underset{\sim}{a}_1 \bullet \underset{\sim}{a}_1 & \underset{\sim}{a}_1 \bullet \underset{\sim}{a}_2 \\ \underset{\sim}{a}_2 \bullet \underset{\sim}{a}_1 & \underset{\sim}{a}_2 \bullet \underset{\sim}{a}_2 \end{vmatrix} = \det \begin{vmatrix} \left| \underset{\sim}{a}_1 \right| \left| \underset{\sim}{a}_1 \right| & \left| \underset{\sim}{a}_1 \right| \left| \underset{\sim}{a}_2 \right| \cos\theta \\ \left| \underset{\sim}{a}_1 \right| \left| \underset{\sim}{a}_2 \right| \cos\theta & \left| \underset{\sim}{a}_2 \right| \left| \underset{\sim}{a}_2 \right| \end{vmatrix} = \left| \underset{\sim}{a}_1 \right|^2 \left| \underset{\sim}{a}_2 \right|^2 \sin^2\theta$$

$$a = \left| \underset{\sim}{a}_1 \times \underset{\sim}{a}_2 \right|^2 \Rightarrow \left| \underset{\sim}{a}_1 \times \underset{\sim}{a}_2 \right| = \sqrt{a} \qquad \text{A2.9}$$

<u>Note</u> : Using $a_{\alpha\beta}$ and $a^{\alpha\beta}$ for lowering and raising indices

A vector $\underset{\sim}{V}$ can be expressed in terms of its covariant and contravariant components as,

$$\underset{\sim}{V} = V^{\alpha}\underset{\sim}{a}_{\alpha} = V_{\beta}\underset{\sim}{a}^{\beta}$$

By performing dot products one can find a relationship between the covariant and contravariant components as,

$V^{\alpha} = V_{\beta}a^{\alpha\beta}$ and $V_{\alpha} = V^{\beta}a_{\alpha\beta}$.

When $\underset{\sim}{V} = \underset{\sim}{a}_{\alpha}$, it can be easily shown that,

$$\underset{\sim}{a}_{\alpha} = a_{\alpha\beta}\underset{\sim}{a}^{\beta}.$$

Similarly, when $\underset{\sim}{V} = \underset{\sim}{a}^{\alpha}$,

$$\underset{\sim}{a}^{\alpha} = a^{\alpha\beta}\underset{\sim}{a}_{\beta}.$$

Taking dot product of above two relations,

$$\delta_{\beta}^{\alpha} = a^{\alpha\gamma}a_{\beta\gamma}.$$

Thus it can be clearly seen that $a_{\alpha\beta}$ and $a^{\alpha\beta}$ can be used to raise and lower indices.

A2.1Covariant Differentiation

First we describe the general covariant differentiation for 3-D curvilinear coordinates. So, if one moves from one position to other by keeping a vector exactly same, both the components and basis vectors will change. Therefore, when defining the derivative of a vector,

$$\underset{\sim}{V} = V^{i}\underset{\sim}{a}_{i} = V_{j}\underset{\sim}{a}^{j}$$

Where, i, j and k can take values $1, 2$ and 3, differentiating with respect to u^k gives,

$$\underset{\sim}{V}_{,k} = V^i_{,k}\underset{\sim}{a}_i + V^i\underset{\sim}{a}_{i,k}$$

$$\underset{\sim}{V}_{,k} = V_{j,k}\underset{\sim}{a}^j + V_j\underset{\sim}{a}^j_{,k}$$

Now, let's define, $\underset{\sim}{a}_{i,k} = \Gamma^l_{i,k}\underset{\sim}{a}_l$

We can get a definition for $\underset{\sim}{a}^j_{,k}$ using the following identity.

$$\underset{\sim}{a}_i \bullet \underset{\sim}{a}^j = \delta^j_i$$

$$\Rightarrow \underset{\sim}{a}_{i,k} \bullet \underset{\sim}{a}^j + \underset{\sim}{a}_i \bullet \underset{\sim}{a}^j_{,k} = 0 \Rightarrow \underset{\sim}{a}_i \bullet \underset{\sim}{a}^j_{,k} = -\Gamma^l_{ik}\underset{\sim}{a}_l \bullet \underset{\sim}{a}^j$$

$$\Rightarrow \underset{\sim}{a}_i \bullet \underset{\sim}{a}^j_{,k} = -\Gamma^j_{ik} \Rightarrow \underset{\sim}{a}^j_{,k} = -\Gamma^j_{ik}\underset{\sim}{a}^i.$$

Therefore, the expression of covariant derivative can be simplified as,

$$\underset{\sim}{V}_{,k} = \left(V^i_{,k} + V^j\Gamma^i_{jk}\right)\underset{\sim}{a}_i = \left(V_{j,k} - V_l\Gamma^l_{jk}\right)\underset{\sim}{a}^j$$

$$\underset{\sim}{V}_{,k} = V^i_{|k}\underset{\sim}{a}_i = V_{j|k}\underset{\sim}{a}^j$$

where,

$$V^i_{|k} = V^i_{,k} + V^j\Gamma^i_{jk} \qquad \text{A2.10}$$

$$V_{j|k} = V_{j,k} - V_l\Gamma^l_{jk} \qquad \text{A2.11}$$

Considering the fact that, for the present case at given position the set of basis is $(\underset{\sim}{a}_\alpha, \underset{\sim}{n})$. So the relation of covariant differentiation for a vector $\underset{\sim}{V}\left(\underset{\sim}{V} = V^\alpha\underset{\sim}{a}_\alpha + V^n\underset{\sim}{n} = V_\beta\underset{\sim}{a}^\beta + V_n\underset{\sim}{n}\right)$ can now be written as,

$$\underset{\sim}{V}_{,\gamma} = V^\alpha_{,\gamma}\underset{\sim}{a}_\alpha + V^\alpha\underset{\sim}{a}_{\alpha,\gamma} + V^n_{,\gamma}\underset{\sim}{n} + V^n\underset{\sim}{n}_{,\gamma}$$

$$\underset{\sim}{V}_{,\gamma} = V^\alpha_{,\gamma}\underset{\sim}{a}_\alpha + V^\alpha\left[\Gamma^\beta_{\alpha\gamma}\underset{\sim}{a}_\beta + \Gamma^n_{\alpha\gamma}\underset{\sim}{n}\right] + V^n_{,\gamma}\underset{\sim}{n} + V^n\left[\Gamma^\beta_{n\gamma}\underset{\sim}{a}_\beta + \Gamma^n_{\gamma n}\underset{\sim}{n}\right]$$

$$\underset{\sim}{V}_{,\gamma} = \left[V^{\alpha}_{,\gamma} + V^{\beta}\Gamma^{\alpha}_{\beta\gamma} + V^{n}\Gamma^{\alpha}_{n\gamma} \right]\underset{\sim}{a}_{\alpha} + \left[V^{n}_{,\gamma} + V^{\beta}\Gamma^{n}_{\beta\gamma} + V^{n}\Gamma^{n}_{n\gamma} \right]\underset{\sim}{n}$$

$$\underset{\sim}{V}_{,\gamma} = V^{\alpha}_{|\gamma}\underset{\sim}{a}_{\alpha} + V^{n}_{|\gamma}\underset{\sim}{n} \qquad \text{A2.12}$$

where,

$$V^{\alpha}_{|\gamma} = V^{\alpha}_{,\gamma} + V^{\tau}\Gamma^{\alpha}_{\tau\gamma} + V^{n}\Gamma^{\alpha}_{n\gamma} \quad \& \quad V^{n}_{|\gamma} = V^{n}_{,\gamma} + V^{\tau}\Gamma^{n}_{\tau\gamma} + V^{n}\Gamma^{n}_{n\gamma}$$

Similarly,

$$\underset{\sim}{V}_{,\gamma} = V_{\beta,\gamma}\underset{\sim}{a}^{\beta} + V_{\beta}\underset{\sim}{a}^{\beta}_{,\gamma} + V_{n,\gamma}\underset{\sim}{n} + V_{n}\underset{\sim}{n}_{,\gamma}$$

$$\underset{\sim}{V}_{,\gamma} = V_{\beta,\gamma}\underset{\sim}{a}^{\beta} - V_{\beta}\left[\Gamma^{\beta}_{\alpha\gamma}\underset{\sim}{a}^{\alpha} + \Gamma^{\beta}_{n\gamma}\underset{\sim}{n} \right] + V_{n,\gamma}\underset{\sim}{n} - V_{n}\left[\Gamma^{n}_{\beta\gamma}\underset{\sim}{a}^{\beta} + \Gamma^{n}_{\gamma n}\underset{\sim}{n} \right]$$

$$\underset{\sim}{V}_{,\gamma} = \left[V_{\beta,\gamma} - V_{\alpha}\Gamma^{\alpha}_{\beta\gamma} - V_{n}\Gamma^{n}_{\beta\gamma} \right]\underset{\sim}{a}^{\beta} + \left[V_{n,\gamma} - V_{\beta}\Gamma^{\beta}_{n\gamma} - V_{n}\Gamma^{n}_{n\gamma} \right]\underset{\sim}{n}$$

$$\underset{\sim}{V}_{,\gamma} = V_{\beta|\gamma}\underset{\sim}{a}^{\beta} + V_{n|\gamma}\underset{\sim}{n} \qquad \text{A2.13}$$

where,

$$V_{\beta|\gamma} = V_{\beta,\gamma} - V_{\tau}\Gamma^{\tau}_{\beta\gamma} - V_{n}\Gamma^{n}_{\beta\gamma} \quad \& \quad V_{n|\gamma} = V_{n,\gamma} - V_{\tau}\Gamma^{\tau}_{n\gamma} - V_{n}\Gamma^{n}_{n\gamma}$$

The expressions for covariant differentiation in eq. A2.12 and eq. A2.13 can be simplified by using the following results,

$$\Gamma^{n}_{\beta\gamma} = \underset{\sim}{a}_{\beta,\gamma} \bullet \underset{\sim}{n} = b_{\gamma\beta} \qquad \text{A2.14}$$

$$\Gamma^{\alpha}_{n\gamma} = \underset{\sim}{n}_{,\gamma} \bullet \underset{\sim}{a}^{\alpha} = -b^{\alpha}_{\gamma} \qquad \text{A2.15}$$

$$\Gamma^{n}_{n\gamma} = \underset{\sim}{n}_{,\gamma} \bullet \underset{\sim}{n} = -b^{\alpha}_{\gamma}\underset{\sim}{a}_{\gamma} \bullet \underset{\sim}{n} = 0 \qquad \text{A2.16}$$

(for the eq. A2.14, we have used Weingarten's equation of surface from eq.A2.**Error! Reference source not found.**)

to get,

$$V^{\alpha}_{|\gamma} = V^{\alpha}_{,\gamma} + V^{\tau}\Gamma^{\alpha}_{\tau\gamma} - V^{n}b^{\alpha}_{\gamma} \quad \& \quad V^{n}_{|\gamma} = V^{n}_{,\gamma} + V^{\tau}b_{\gamma\tau}$$

$$V_{\beta|\gamma} = V_{\beta,\gamma} - V_{\tau}\Gamma^{\tau}_{\beta\gamma} - V_{n}b_{\gamma\beta} \quad \& \quad V_{n|\gamma} = V_{n,\gamma} + V_{\tau}b^{\tau}_{\gamma} \qquad \text{A2.17}$$

Thus finally giving us the expressions for **covariant differentiation** as,

$$\underset{\sim}{V}_{,\gamma} = \left(V^{\alpha}_{,\gamma} + V^{\tau}\Gamma^{\alpha}_{\tau\gamma} - V^{n}b^{\alpha}_{\gamma}\right)\underset{\sim}{a}_{\alpha} + \left(V^{n}_{,\gamma} + V^{\tau}b_{\gamma\tau}\right)\underset{\sim}{n} \qquad \text{A2.18}$$

and also,

$$\underset{\sim}{V}_{,\gamma} = \left(V_{\beta,\gamma} - V_{\tau}\Gamma^{\tau}_{\beta\gamma} - V_{n}b_{\gamma\beta}\right)\underset{\sim}{a}^{\beta} + \left(V_{n,\gamma} + V_{\tau}b^{\tau}_{\gamma}\right)\underset{\sim}{n} \qquad \text{A2.19}$$

A2.1.2 Divergence of vector

$$div\,\underset{\sim}{V} = \nabla \bullet \underset{\sim}{V} = V^{\alpha}_{|\alpha} \qquad \text{A2.20}$$

From the definition of covariant differentiation, one can get,

$$V^{\alpha}_{|\alpha} = V^{\alpha}_{,\alpha} + V^{\beta}\Gamma^{\alpha}_{\alpha\beta} \qquad \text{A2.21}$$

We can write the derivative $\underset{\sim}{a}_{\alpha,\beta}$ in terms of Christoffel's symbol of second kind and first kind as follows,

$$\underset{\sim}{a}_{\alpha,\beta} = \Gamma^{\gamma}_{\alpha\beta}\underset{\sim}{a}_{\gamma} = \Gamma_{\alpha\beta\gamma}\underset{\sim}{a}^{\gamma} \qquad \text{A2.22}$$

Taking dot product of both sides in eq. A2.**Error! Reference source not found.** with $\underset{\sim}{a}^{\tau}$ gives,

$$\Gamma^{\tau}_{\alpha\beta} = \Gamma_{\alpha\beta\gamma}a^{\gamma\tau} \qquad \text{A2.23}$$

We can get an expression for $\Gamma_{\alpha\beta\gamma}$ as follows.

Begin with the relation,

$$a_{\alpha\beta} = \underset{\sim}{a}_{\alpha} \bullet \underset{\sim}{a}_{\beta}$$

Differentiating both sided w.r.t. u^{γ},

$$\Rightarrow a_{\alpha\beta,\gamma} = \underset{\sim}{a}_{\alpha,\gamma} \bullet \underset{\sim}{a}_{\beta} + \underset{\sim}{a}_{\alpha} \bullet \underset{\sim}{a}_{\beta,\gamma}$$

$$\Rightarrow a_{\alpha\beta,\gamma} = \Gamma_{\alpha\gamma\beta} + \Gamma_{\beta\gamma\alpha}$$

On permuting these indices three times, following set of equations is obtained,

$$\Gamma_{\gamma\alpha\beta} + \Gamma_{\beta\gamma\alpha} \qquad = a_{\alpha\beta,\gamma}$$

$$\Gamma_{\gamma\alpha\beta} \qquad + \Gamma_{\alpha\beta\gamma} = a_{\beta\gamma,\alpha}$$

$$\Gamma_{\beta\gamma\alpha} + \Gamma_{\alpha\beta\gamma} = a_{\gamma\alpha,\beta}$$

which eventually gives us,

$$\Gamma_{\alpha\beta\gamma} = \frac{1}{2}\left[a_{\beta\gamma,\alpha} + a_{\gamma\alpha,\beta} - a_{\alpha\beta,\gamma} \right] \qquad \text{A2.24}$$

Therefore, in eq. A2.**Error! Reference source not found.**

$$\Gamma^{\alpha}_{\alpha\beta} = \frac{1}{2}\left[a_{\beta\gamma,\alpha} + a_{\gamma\alpha,\beta} - a_{\alpha\beta,\gamma} \right] a^{\alpha\gamma}$$

$$\Rightarrow \Gamma^{\alpha}_{\alpha\beta} = \frac{1}{2} a^{\alpha\gamma} a_{\alpha\gamma,\beta}$$

This can be shown with the help of calculations below.

$$a^{\alpha\gamma}\left(a_{\beta\gamma,\alpha} - a_{\alpha\beta,\gamma} \right) = a^{\alpha\gamma}\left(\underset{\sim}{a}_{\beta,\alpha} \bullet \underset{\sim}{a}_{\gamma} + \underset{\sim}{a}_{\gamma,\alpha} \bullet \underset{\sim}{a}_{\beta} - \underset{\sim}{a}_{\alpha,\gamma} \bullet \underset{\sim}{a}_{\beta} - \underset{\sim}{a}_{\beta,\gamma} \bullet \underset{\sim}{a}_{\alpha} \right)$$

$$= \underset{\sim}{a}_{\beta,\alpha} \bullet \underset{\sim}{a}^{\alpha} + a^{\alpha\gamma}\left(\underset{\sim}{a}_{\gamma,\alpha} \bullet \underset{\sim}{a}_{\beta} - \underset{\sim}{a}_{\alpha,\gamma} \bullet \underset{\sim}{a}_{\beta} \right) - \underset{\sim}{a}_{\beta,\gamma} \bullet \underset{\sim}{a}^{\gamma}$$

$$= \underset{\sim}{a}_{\beta,\alpha} \bullet \underset{\sim}{a}^{\alpha} + a^{\alpha\gamma}\left(\frac{\partial^2 \underset{\sim}{r}}{\partial u^{\gamma} \partial u^{\alpha}} \bullet \underset{\sim}{a}_{\beta} - \frac{\partial^2 \underset{\sim}{r}}{\partial u^{\alpha} \partial u^{\gamma}} \bullet \underset{\sim}{a}_{\beta} \right) - \underset{\sim}{a}_{\beta,\gamma} \bullet \underset{\sim}{a}^{\gamma}$$

$$= \underset{\sim}{a}_{\beta,\alpha} \bullet \underset{\sim}{a}^{\alpha} - \underset{\sim}{a}_{\beta,\gamma} \bullet \underset{\sim}{a}^{\gamma}$$

$$= \Gamma^{\tau}_{\alpha\beta} \underset{\sim}{a}_{\tau} \bullet \underset{\sim}{a}^{\alpha} - \Gamma^{\sigma}_{\beta\gamma} \underset{\sim}{a}_{\sigma} \bullet \underset{\sim}{a}^{\gamma}$$

$$= \Gamma^{\tau}_{\alpha\beta} \delta^{\alpha}_{\tau} - \Gamma^{\sigma}_{\beta\gamma} \delta^{\gamma}_{\sigma}$$

$$= \Gamma^{\alpha}_{\alpha\beta} - \Gamma^{\gamma}_{\beta\gamma}$$

$$= \Gamma^{\alpha}_{\alpha\beta} - \Gamma^{\gamma}_{\gamma\beta}$$

$$= 0$$

Therefore, the expression for divergence in eq.

A2.**Error! Reference source not found.** can be written as,

$$\nabla \bullet \underset{\sim}{V} = V^{\alpha}_{,\alpha} + V^{\beta} \Gamma^{\alpha}_{\alpha\beta} = V^{\alpha}_{,\alpha} + \frac{1}{2} V^{\beta} a_{\gamma\alpha,\beta} a^{\alpha\gamma} \qquad \text{A2.25}$$

From, the definition of derivative of determinant,

$$\frac{\partial a}{\partial u^{\gamma}} = \frac{\partial a}{\partial a_{\alpha\gamma}} \frac{\partial a_{\alpha\gamma}}{\partial u^{\beta}} = a a^{\alpha\gamma} \frac{\partial a_{\alpha\gamma}}{\partial u^{\beta}}$$

$$\Rightarrow a^{\alpha\gamma} a_{\alpha\gamma,\beta} = \frac{1}{a} \frac{\partial a}{\partial u^{\beta}} \qquad \text{A2.26}$$

Further simplification of eq. A2.**Error! Reference source not found.** gives,

$$\nabla \bullet \underset{\sim}{V} = V^{\alpha}_{,\alpha} + V^{\beta} \frac{1}{2a} \frac{\partial a}{\partial u^{\beta}} = V^{\alpha}_{,\alpha} + V^{\beta} \frac{1}{\sqrt{a}} \frac{\partial \sqrt{a}}{\partial u^{\beta}} = \frac{1}{\sqrt{a}} \frac{\partial \left(V^{\alpha} \sqrt{a} \right)}{\partial u^{\alpha}}$$

Therefore the **divergence of a vector** is given as,

$$\Rightarrow \nabla \bullet \underset{\sim}{V} = \frac{1}{\sqrt{a}} \frac{\partial \left(V^{\alpha} \sqrt{a} \right)}{\partial u^{\alpha}} \qquad \text{A2.27}$$

A2.1.3 Relation between curvatures and elements of b^{α}_{β}

Characteristic equation of matrix b^{α}_{β} is given as,

$$\lambda^2 - tr\left[b^{\alpha}_{\beta}\right]\lambda + \det\left[b^{\alpha}_{\beta}\right] = 0$$

$$\Rightarrow \lambda^2 - 2H\lambda + K = 0 \qquad \text{A2.28}$$

Using Cayley-Hamilton theorem,

$$b^{\alpha}_{\gamma} b^{\gamma}_{\beta} - 2Hb^{\alpha}_{\beta} + K\delta^{\alpha}_{\beta} = 0$$

$$\Rightarrow b^{\alpha\tau} a_{\gamma\tau} b_{\sigma\beta} a^{\sigma\gamma} - 2Hb^{\alpha}_{\beta} + K\delta^{\alpha}_{\beta} = 0$$
$$\Rightarrow b^{\alpha\tau} b_{\sigma\beta}\delta^{\sigma}_{\tau} - 2Hb^{\alpha}_{\beta} + K\delta^{\alpha}_{\beta} = 0$$
$$\Rightarrow b^{\alpha\tau} b_{\tau\beta} - 2Hb^{\alpha}_{\beta} + K\delta^{\alpha}_{\beta} = 0 \qquad \text{A2.29}$$

Using the above relation one can get,

$$b^{\alpha\beta} b_{\alpha\beta} - 2Hb^{\alpha}_{\alpha} + K\delta^{\alpha}_{\alpha} = 0$$

$$\Rightarrow b^{\alpha\beta} b_{\alpha\beta} = 4H^2 - 2K \qquad \text{A2.30}$$

A2.1.4 Weingarten Equation of surface

From the second fundamental form of the surface we know that

$$b_{\alpha\beta} = -\underset{\sim}{n}_{,\alpha} \bullet \underset{\sim}{a}_{\beta}$$

and also,

$$\underset{\sim}{n} \bullet \underset{\sim}{n} = 1 \Rightarrow \underset{\sim}{n}_{\alpha} \bullet \underset{\sim}{n} = 0$$

Using above two relations, it can be easily concluded that, $\underset{\sim}{n}_{,\alpha}$ has no component along $\underset{\sim}{n}$, and

$$\underset{\sim}{n}_{,\alpha} = -b_{\alpha\beta}\underset{\sim}{a}^{\beta} = -b_{\alpha\beta}a^{\gamma\beta}a_{\beta\gamma}\underset{\sim}{a}^{\beta} = -b_{\alpha}^{\gamma}\underset{\sim}{a}_{\gamma}$$

Thus Weingarten equation of surface is given as

$$\underset{\sim}{n}_{,\alpha} = -b_{\alpha}^{\gamma}\underset{\sim}{a}_{\gamma} \qquad \text{A2.31}$$

A2.1.5 Gauss equations of surface

Starting with the fact that, $\underset{\sim}{a}_{\alpha} \bullet \underset{\sim}{n} = 0$ and taking covariant derivative w.r.t. u^{β},

$$\underset{\sim}{a}_{\alpha|\beta} \bullet \underset{\sim}{n} + \underset{\sim}{a}_{\alpha} \bullet \underset{\sim}{n}_{|\beta} = 0 \Rightarrow \underset{\sim}{a}_{\alpha|\beta} \bullet \underset{\sim}{n} + \underset{\sim}{a}_{\alpha} \bullet \underset{\sim}{n}_{,\beta} = 0 \Rightarrow \underset{\sim}{a}_{\alpha|\beta} \bullet \underset{\sim}{n} = b_{\alpha\beta}$$

Also, substituting $\underset{\sim}{a}_{\alpha}$ in the definition of covariant derivative in eq. A2.**Error! Reference source not found.**, to get,

$$\underset{\sim}{a}_{\alpha|\beta} = \underset{\sim}{a}_{\alpha,\beta} - \underset{\sim}{a}_{\tau}\Gamma_{\alpha\beta}^{\tau} - \underset{\sim}{n}b_{\alpha\beta},$$

and taking dot product of both sides with $\underset{\sim}{a}^{\sigma}$,

$$\underset{\sim}{a}_{\alpha|\beta} \bullet \underset{\sim}{a}^{\sigma} = \underset{\sim}{a}_{\alpha,\beta} \bullet \underset{\sim}{a}^{\sigma} - \Gamma_{\alpha\beta}^{\tau}\underset{\sim}{a}_{\tau} \bullet \underset{\sim}{a}^{\sigma} - \underset{\sim}{n} \bullet \underset{\sim}{a}^{\sigma}b_{\alpha\beta} = 0$$

Thus the Gauss equation of surface is, $\underset{\sim}{a}_{\alpha|\beta} = b_{\alpha\beta}\underset{\sim}{n}$. A2.32

A2.2 Bilayer Membrane Calculations

Energy stored in a membrane due to bending can be given as,

$$W = cH^2, \qquad \text{A2.33}$$

where, W is the strain energy density, c is a material property known as lipid bilayer bending stiffness and H is mean curvature at a particular position.

Consider a patch of lipid bilayer membrane A, with curve C surrounding that area. Total strain energy U of the membrane patch can be written as,

$$U = \int_A cH^2 dA, \qquad \text{A2.34}$$

where, $dA = \sqrt{a}du^1du^2$ using result of eq. A2.**Error! Reference source not found.**. The local area incompressibility can be written as,

$$\delta(dA) = 0 \Rightarrow \delta\left(\sqrt{a}\right)du^1du^2 = 0 \Rightarrow \delta\left(\sqrt{a}\right) = 0 \qquad \text{A2.35}$$

Imposing the local area incompressibility, using the Lagrange multiplier $\gamma\left(u^\alpha\right)$, U can be modified as,

$$U = \int_A \left(cH^2 - \gamma\sqrt{a}\right)dA. \qquad \text{A2.36}$$

Next we introduce a variation to the surface, $\delta\underset{\sim}{r}$.

From the principle of virtual work one can say that,

$$\delta U = \delta P, \qquad \text{A2.37}$$

where, δP is the work done by external forces and moments acting on the membrane area A and on the curve C, surrounding the membrane.

Taking the variation of eq. A2.**Error! Reference source not found.**,

$$\delta U = \int_A \left[2cH\delta H - \gamma\delta\left(\sqrt{a}\right)\right] dA. \qquad \text{A2.38}$$

$\delta\sqrt{a}$ can be simplified as,

$$\delta\sqrt{a} = \frac{1}{2\sqrt{a}}\delta a = \frac{1}{2\sqrt{a}}\frac{\partial a}{\partial a_{\alpha\beta}}\delta a_{\alpha\beta},$$

using the relation from determinant theory,

$$\frac{\partial\left(\det A\right)}{\partial A_{ij}} = \left(\det A\right)A^{-1}_{ij},$$

to get,

$$\delta\sqrt{a} = \frac{1}{2\sqrt{a}}\delta a = \frac{1}{2\sqrt{a}}aa^{\alpha\beta}\delta a_{\alpha\beta} = \frac{\sqrt{a}}{2}a^{\alpha\beta}\delta\left(\underset{\sim}{a}_{\alpha}\bullet\underset{\sim}{a}_{\beta}\right) = \frac{\sqrt{a}}{2}a^{\alpha\beta}\left[\underset{\sim}{a}_{\alpha}\bullet\delta\left(\underset{\sim}{a}_{\beta}\right)+\underset{\sim}{a}_{\beta}\bullet\delta\left(\underset{\sim}{a}_{\alpha}\right)\right]$$

$$\Rightarrow \delta\sqrt{a} = \sqrt{a}\underset{\sim}{a}^{\alpha}\bullet\delta\left(\underset{\sim}{a}_{\alpha}\right). \qquad \text{A2.39}$$

Next we simplify δH.

Using the definition of H from eq. A2.**Error! Reference source not found.**,

$$\delta H = -\frac{1}{2}\delta\left(\underset{\sim}{a}^{\alpha}\right)\bullet\underset{\sim}{n}_{,\alpha} - \frac{1}{2}\underset{\sim}{a}^{\alpha}\bullet\delta\left(\underset{\sim}{n}_{,\alpha}\right). \qquad \text{A2.40}$$

Simplifying the first term in expression of δH gives,

$$-\delta\left(\underset{\sim}{a}^{\alpha}\right)\bullet\underset{\sim}{n}_{,\alpha} = a^{\alpha\beta}\delta\left(\underset{\sim}{a}_{\beta}\right)\bullet\underset{\sim}{n}_{,\alpha}.$$

Following are the steps for above.

$$\left[\delta\left(\underset{\sim}{a}^{\alpha}\right)+a^{\alpha\beta}\delta\left(\underset{\sim}{a}_{\beta}\right)\right]\bullet\underset{\sim}{n}_{,\alpha}=-\left[\delta\left(\underset{\sim}{a}^{\alpha}\right)+a^{\alpha\beta}\delta\left(\underset{\sim}{a}_{\beta}\right)\right]\bullet b_{\alpha}^{\tau}\underset{\sim}{a}_{\tau}$$

using the Weingarten equation $\underset{\sim}{n}_{,\alpha}=-b_{\alpha}^{\tau}\underset{\sim}{a}_{\tau}$

$$=-\left[\delta\left(\underset{\sim}{a}^{\alpha}\right)\bullet b_{\alpha}^{\tau}\underset{\sim}{a}_{\tau}+a^{\alpha\beta}\delta\left(\underset{\sim}{a}_{\beta}\right)\bullet b_{\alpha}^{\tau}\underset{\sim}{a}_{\tau}\right]$$

$$=-\left[b_{\alpha\tau}\delta\left(\underset{\sim}{a}^{\alpha}\right)\bullet\underset{\sim}{a}^{\tau}+a^{\alpha\beta}b_{\alpha}^{\tau}\delta\left(\underset{\sim}{a}_{\beta}\right)\bullet\underset{\sim}{a}_{\tau}\right]$$

using the symmetric nature of $b_{\alpha\tau}$,

$$=-\frac{1}{2}\left[b_{\alpha\tau}\delta\left(\underset{\sim}{a}^{\alpha}\bullet\underset{\sim}{a}^{\tau}\right)+b^{\beta\tau}\delta\left(\underset{\sim}{a}_{\beta}\bullet\underset{\sim}{a}_{\tau}\right)\right]$$

$$=-\frac{1}{2}\left[b_{\alpha\tau}\delta\left(a^{\alpha\tau}\right)+b^{\beta\tau}\delta\left(a_{\beta\tau}\right)\right]$$
$$=-\frac{1}{2}\left[b_{\alpha}^{\beta}a_{\beta\tau}\delta\left(a^{\alpha\tau}\right)+b_{\alpha}^{\beta}a^{\alpha\tau}\delta\left(a_{\beta\tau}\right)\right]$$
$$=-\frac{1}{2}b_{\alpha}^{\beta}\left[a_{\beta\tau}\delta\left(a^{\alpha\tau}\right)+a^{\alpha\tau}\delta\left(a_{\beta\tau}\right)\right]$$
$$=-\frac{1}{2}b_{\alpha}^{\beta}\delta\left(a^{\alpha\tau}a_{\beta\tau}\right)$$
$$=-\frac{1}{2}b_{\alpha}^{\beta}\delta\left(\delta_{\beta}^{\alpha}\right)=0$$

Thus, back in eq. A2.**Error! Reference source not found.**, the expression of δH can be written as,

$$\delta H=\frac{1}{2}a^{\alpha\beta}\delta\left(\underset{\sim}{a}_{\beta}\right)\bullet\underset{\sim}{n}_{,\alpha}-\frac{1}{2}\underset{\sim}{a}^{\alpha}\bullet\delta\left(\underset{\sim}{n}_{,\alpha}\right)\qquad\text{A2.41}$$

Plugging in the results from eqs.A2.**Error! Reference source not found.** and A2.**Error! Reference source not found.** into eq. A2.**Error! Reference source not found.** to get,

$$\delta U = \int_A \left[cHa^{\alpha\beta}\delta\left(\underset{\sim}{a}_\beta\right) \bullet \underset{\sim}{n}_{,\alpha} - cH\underset{\sim}{a}^\alpha \bullet \delta\left(\underset{\sim}{n}_{,\alpha}\right) - \gamma\sqrt{a}\underset{\sim}{a}^\alpha \bullet \delta\left(\underset{\sim}{a}_\alpha\right)\right] dA$$

We now expand the middle term in the integrand by using the chain rule of differentiation as follows,

$$-cH\underset{\sim}{a}^\alpha \bullet \delta(\underset{\sim}{n}_{,\alpha}) = -cH\underset{\sim}{a}^\alpha \bullet \delta(\underset{\sim}{n})_{,\alpha} = -(cH\underset{\sim}{a}^\alpha \bullet \delta\underset{\sim}{n})_{,\alpha} + (cH\underset{\sim}{a}^\alpha)_{,\alpha} \bullet \delta n \quad \text{A2.42}$$

Using definition of covariant differentiation of indexed quantities [1].

Consider a vector, $\underset{\sim}{T} = T^\alpha \underset{\sim}{a}_\alpha$

For the component T^α, covariant differentiation can be defined as

$$T^\alpha{}_{|\beta} = T^\alpha{}_{,\beta} + \Gamma^\alpha_{\beta\omega}T^\omega \Rightarrow T^\alpha{}_{,\beta} = T^\alpha{}_{|\beta} - \Gamma^\alpha_{\beta\omega}T^\omega$$

Now, consider $(cH\underset{\sim}{a}^\alpha \bullet \delta\underset{\sim}{n})_{,\alpha}$, which can be written as

$$(cH\underset{\sim}{a}^\alpha \bullet \delta\underset{\sim}{n})_{,\alpha} = (cH\delta\underset{\sim}{n} \bullet \underset{\sim}{a}^\alpha)_{,\alpha}$$

Comparing with the above definition we have $T^\alpha = cH\delta\underset{\sim}{n} \bullet \underset{\sim}{a}^\alpha$

$$\Rightarrow (cH\delta\underset{\sim}{n} \bullet \underset{\sim}{a}^\alpha)_{,\alpha} = (cH\delta\underset{\sim}{n} \bullet \underset{\sim}{a}^\alpha)_{|\alpha} - \Gamma^\alpha_{\alpha\omega}(cH\delta\underset{\sim}{n} \bullet \underset{\sim}{a}^\omega) \quad \text{A2.43}$$

So, eq. A2.**Error! Reference source not found.** further expands the first term in eq. A2.42.

Next, If we replace the component T^α with some vector $p\underset{\sim}{a}^\alpha$, where p is function of position

$$(p\underset{\sim}{a}^\alpha)_{|\beta} = (p\underset{\sim}{a}^\alpha)_{,\beta} + \Gamma^\alpha_{\beta\omega}(p\underset{\sim}{a}^\omega) \Rightarrow (p\underset{\sim}{a}^\alpha)_{,\beta} = (p\underset{\sim}{a}^\alpha)_{|\beta} - \Gamma^\alpha_{\beta\omega}(p\underset{\sim}{a}^\omega)$$

Now, consider $(cH\underset{\sim}{a}^\alpha)_{,\alpha}$

Comparing with the above definition we have $p\underset{\sim}{a}^\alpha = cH\underset{\sim}{a}^\alpha$

$$(cH\underset{\sim}{a}^{\alpha})_{,\alpha} = (cH\underset{\sim}{a}^{\alpha})_{|\alpha} - \Gamma^{\alpha}_{\alpha\omega} cH\underset{\sim}{a}^{\omega} \qquad \text{A2.44}$$

Substituting back the results from eqs. A2.**Error! Reference source not found.** and A2.**Error! Reference source not found.**, back into eq. A2.42, to get,

$$-cH\underset{\sim}{a}^{\alpha} \bullet \delta(\underset{\sim}{n}_{,\alpha}) = -(cH\delta\underset{\sim}{n} \bullet \underset{\sim}{a}^{\alpha})_{|\alpha} + \Gamma^{\alpha}_{\alpha\omega}(cH\delta\underset{\sim}{n} \bullet \underset{\sim}{a}^{\alpha}) + \left((cH\underset{\sim}{a}^{\alpha})_{|\alpha} - \Gamma^{\alpha}_{\alpha\omega} cH\underset{\sim}{a}^{\omega}\right) \bullet \delta(\underset{\sim}{n})$$

$$\Rightarrow -cH\underset{\sim}{a}^{\alpha} \bullet \delta(\underset{\sim}{n}_{,\alpha}) = -(cH\delta\underset{\sim}{n} \bullet \underset{\sim}{a}^{\alpha})_{|\alpha} + (cH\underset{\sim}{a}^{\alpha})_{|\alpha} \bullet \delta(\underset{\sim}{n}) \qquad \text{A2.45}$$

Surface divergence theorem states that,

$$\int_A F^{\alpha}_{|\alpha} dA = \int_C F^{\alpha} m_{\alpha} dA \qquad \text{A2.46}$$

Where, $\underset{\sim}{m}$ is normal to curve C as well as perpendicular to normal to the surface at that position.

Using surface divergence theorem in our calculations we can get,

$$-\int_A cH\underset{\sim}{a}^{\alpha} \bullet \delta(\underset{\sim}{n}_{,\alpha}) dA = -\int_A (cH\delta\underset{\sim}{n} \bullet \underset{\sim}{a}^{\alpha})_{|\alpha} dA + \int_A (cH\underset{\sim}{a}^{\alpha})_{|\alpha} \bullet \delta(\underset{\sim}{n}) dA$$

$$\Rightarrow -\int_A cH\underset{\sim}{a}^{\alpha} \bullet \delta(\underset{\sim}{n}_{,\alpha}) dA = -\int_C (cH\delta\underset{\sim}{n} \bullet \underset{\sim}{a}^{\alpha}) m_{\alpha} dl + \int_A (cH\underset{\sim}{a}^{\alpha})_{|\alpha} \bullet \delta(\underset{\sim}{n}) dA \qquad \text{A2.47}$$

Now, we use the following identities to simplify the above RHS in eq. A2.**Error! Reference source not found.**

$\underset{\sim}{n} \bullet \underset{\sim}{n} = 1 \Rightarrow \delta(\underset{\sim}{n}) \bullet \underset{\sim}{n} = 0$

$\underset{\sim}{a}_{\alpha} \bullet \underset{\sim}{n} = 0 \Rightarrow \delta(\underset{\sim}{n}) \bullet \underset{\sim}{a}_{\alpha} = -\delta(\underset{\sim}{a}_{\alpha}) \bullet \underset{\sim}{n}$

As it can be seen above equations, $\delta(\underset{\sim}{n})$ is a surface vector and can be written as,

$$\delta(\underset{\sim}{n}) = -\left[\underset{\sim}{n} \bullet \delta(\underset{\sim}{a}_{\alpha})\right] \underset{\sim}{a}^{\alpha} \qquad \text{A2.48}$$

Now consider the area integral term in eq. A2.**Error! Reference source not found.**

$$(cH\underset{\sim}{a}^{\alpha})_{|\alpha} \bullet \delta(\underset{\sim}{n}) = (cH_{,\alpha}\underset{\sim}{a}^{\alpha} + ch\underset{\sim}{a}^{\alpha}_{|\alpha}) \bullet \left[-\underset{\sim}{n} \bullet \delta(\underset{\sim}{a}_{\beta})\right]\underset{\sim}{a}^{\beta}$$

using the Gauss equation of surface, $\underset{\sim}{a}^{\alpha}_{|\alpha} = -b^{\alpha}_{\alpha}\underset{\sim}{n} \Rightarrow \underset{\sim}{a}^{\alpha}_{|\alpha} \bullet \underset{\sim}{a}^{\beta} = 0$

$$\Rightarrow (cH\underset{\sim}{a}^{\alpha})_{|\alpha} \bullet \delta(\underset{\sim}{n}) = (cH_{,\alpha}\underset{\sim}{a}^{\alpha} \bullet \underset{\sim}{a}^{\beta} + ch\underset{\sim}{a}^{\alpha}_{|\alpha} \bullet \underset{\sim}{a}^{\beta})\left[-\underset{\sim}{n} \bullet \delta(\underset{\sim}{a}_{\beta})\right]$$

$$\Rightarrow (cH\underset{\sim}{a}^{\alpha})_{|\alpha} \bullet \delta(\underset{\sim}{n}) = -cH_{,\alpha}a^{\alpha\beta}\underset{\sim}{n} \bullet \delta(\underset{\sim}{a}_{\beta}) \qquad \text{A2.49}$$

we also acknowledge the fact that covariant differentiation is equivalent to simple differentiation for un-indexed quantities [1], which gives $H_{|\alpha} = H_{,\alpha}$.

Thus integral in eq. A2.**Error! Reference source not found.** can be rewritten as,

$$-\int_{A} cH\underset{\sim}{a}^{\alpha} \bullet \delta(\underset{\sim}{n}_{,\alpha})dA = -\int_{C} (cH\delta\underset{\sim}{n} \bullet \underset{\sim}{a}^{\alpha})m_{\alpha}dl - \int_{A} cH_{,\alpha}a^{\alpha\beta}\underset{\sim}{n} \bullet \delta(\underset{\sim}{a}_{\beta})dA$$

Substituting back in our original integral expression we get,

$$\delta U = \int_{A}\left[cHa^{\alpha\beta}\underset{\sim}{n}_{,\alpha} - cH_{,\alpha}a^{\alpha\beta}\underset{\sim}{n} - \gamma\sqrt{a}\underset{\sim}{a}^{\beta}\right] \bullet \delta(\underset{\sim}{a}_{\beta})dA - \int_{C}(cH\underset{\sim}{a}^{\alpha} \bullet \delta\underset{\sim}{n})m_{\alpha}dl \qquad \text{A2.50}$$

Now we simplify the integrand of the area integral

$$\left[cHa^{\alpha\beta}\underset{\sim}{n}_{,\alpha} - cH_{,\alpha}a^{\alpha\beta}\underset{\sim}{n} - \gamma\sqrt{a}\underset{\sim}{a}^{\beta}\right] \bullet \delta\underset{\sim}{a}_{\beta} = \left[cHa^{\alpha\beta}\underset{\sim}{n}_{,\alpha} - cH_{,\alpha}a^{\alpha\beta}\underset{\sim}{n} - \gamma\sqrt{a}\underset{\sim}{a}^{\beta}\right] \bullet \delta(\underset{\sim}{r})_{,\beta}$$

A2.51

Considering each term individually to expand the above expression.

1) $\boldsymbol{-cH_{,\alpha}a^{\alpha\beta}\underset{\sim}{n} \bullet (\delta\underset{\sim}{r})_{,\beta}}$

$$-cH_{,\alpha}a^{\alpha\beta}\underset{\sim}{n} \bullet (\delta\underset{\sim}{r})_{,\beta} = -(cH_{,\alpha}a^{\alpha\beta}\delta\underset{\sim}{r} \bullet \underset{\sim}{n})_{,\beta} + (cH_{,\alpha}a^{\alpha\beta}\underset{\sim}{n})_{,\beta} \bullet \delta\underset{\sim}{r}$$

We consider the covariant differentiation as defined earlier for a component and vector respectively as,

$$-(cH_{,\alpha}a^{\alpha\beta}\delta\underset{\sim}{r}\bullet\underset{\sim}{n})_{,\beta}=-(cH_{,\alpha}a^{\alpha\beta}\delta\underset{\sim}{r}\bullet\underset{\sim}{n})_{|\beta}+\Gamma^{\beta}_{\beta\omega}(cH_{,\alpha}a^{\alpha\omega}\delta\underset{\sim}{r}\bullet\underset{\sim}{n})$$

and

$$(cH_{,\alpha}a^{\alpha\beta}\underset{\sim}{n})_{,\beta}=(cH_{,\alpha}a^{\alpha\beta}\underset{\sim}{n})_{|\beta}-\Gamma^{\beta}_{\beta\omega}cH_{,\alpha}a^{\alpha\omega}\underset{\sim}{n}$$

Here we have something of the form

$$(T^{\beta}\underset{\sim}{n})_{|\beta}$$

which can be simplified using the definition of covariant differentiation as,

$$\begin{aligned}(T^{\beta}\underset{\sim}{n})_{|\beta}&=(T^{\beta}\underset{\sim}{n})_{,\beta}+\Gamma^{\beta}_{\beta\omega}T^{\omega}\underset{\sim}{n}\\&=T^{\beta}_{,\beta}\underset{\sim}{n}+T^{\beta}\underset{\sim}{n}_{,\beta}+\Gamma^{\beta}_{\beta\omega}T^{\omega}\underset{\sim}{n}\\&=T^{\beta}\underset{\sim}{n}_{,\beta}+\left[T^{\beta}_{,\beta}+\Gamma^{\beta}_{\beta\omega}T^{\omega}\right]\underset{\sim}{n}\\&=T^{\beta}\underset{\sim}{n}_{,\beta}+T^{\beta}_{|\beta}\underset{\sim}{n}\end{aligned}$$

Here, we used the fact that,

$$T^{\beta}_{|\beta}=T^{\beta}_{,\beta}+\Gamma^{\beta}_{\beta\omega}T^{\omega}$$

and that the covariant differentiation of non-indexed quantities is equal to the partial derivative

$$\underset{\sim}{n}_{|\beta}=\underset{\sim}{n}_{,\beta}$$

Therefore, we can write the final expression as

$$\begin{aligned}-cH_{,\alpha}a^{\alpha\beta}\underset{\sim}{n}\bullet(\delta\underset{\sim}{r})_{,\beta}&=-(cH_{,\alpha}a^{\alpha\beta}\delta\underset{\sim}{r}\bullet\underset{\sim}{n})_{|\beta}+\Gamma^{\beta}_{\beta\omega}(cH_{,\alpha}a^{\alpha\omega}\delta\underset{\sim}{r}\bullet\underset{\sim}{n})\\&\quad+\left[cH_{,\alpha}a^{\alpha\beta}\underset{\sim}{n}_{,\beta}+(cH_{,\alpha}a^{\alpha\beta})_{|\beta}\underset{\sim}{n}-\Gamma^{\beta}_{\beta\omega}cH_{,\alpha}a^{\alpha\omega}\underset{\sim}{n}\right]\bullet\delta\underset{\sim}{r}\end{aligned}$$

$$-cH_{,\alpha}a^{\alpha\beta}\underset{\sim}{n}\bullet(\delta\underset{\sim}{r})_{,\beta}=-(cH_{,\alpha}a^{\alpha\beta}\delta\underset{\sim}{r}\bullet\underset{\sim}{n})_{|\beta}+\left[cH_{,\alpha}a^{\alpha\beta}\underset{\sim}{n}_{,\beta}+(cH_{,\alpha}a^{\alpha\beta})_{|\beta}\underset{\sim}{n}\right]\bullet\delta\underset{\sim}{r}$$

A2.52

2) $-\boldsymbol{\gamma\sqrt{a}\underset{\sim}{a}^{\beta}\bullet(\delta\underset{\sim}{r})_{,\beta}}$

$$-\gamma\sqrt{a}\underset{\sim}{a}^{\beta}\bullet(\delta\underset{\sim}{r})_{,\beta}=-(\gamma\sqrt{a}\delta\underset{\sim}{r}\bullet\underset{\sim}{a}^{\beta})_{,\beta}+(\gamma\sqrt{a}\underset{\sim}{a}^{\beta})_{,\beta}\bullet(\delta\underset{\sim}{r})$$

We consider the covariant differentiation as defined earlier for a component and vector respectively as,

$$-(\gamma\sqrt{a}\delta\underset{\sim}{r}\bullet\underset{\sim}{a}^{\beta})_{,\beta}=-(\gamma\sqrt{a}\delta\underset{\sim}{r}\bullet\underset{\sim}{a}^{\beta})_{|\beta}+\Gamma^{\beta}_{\beta\omega}(\gamma\sqrt{a}\delta\underset{\sim}{r}\bullet\underset{\sim}{a}^{\omega})$$

&

$$(\gamma\sqrt{a}\underset{\sim}{a}^{\beta})_{,\beta}=(\gamma\sqrt{a}\underset{\sim}{a}^{\beta})_{|\beta}-\Gamma^{\beta}_{\beta\omega}\gamma\sqrt{a}\underset{\sim}{a}^{\omega}$$

Substituting back into the parent equation, we get

$$-\gamma\sqrt{a}\underset{\sim}{a}^{\beta}\bullet(\delta\underset{\sim}{r})_{,\beta}=-(\gamma\sqrt{a}\delta\underset{\sim}{r}\bullet\underset{\sim}{a}^{\beta})_{|\beta}+\Gamma^{\beta}_{\beta\omega}\gamma\sqrt{a}\delta\underset{\sim}{r}\bullet\underset{\sim}{a}^{\omega}+\delta\underset{\sim}{r}\bullet\left[(\gamma\sqrt{a}\underset{\sim}{a}^{\beta})_{|\beta}-\Gamma^{\beta}_{\beta\omega}\gamma\sqrt{a}\underset{\sim}{a}^{\omega}\right]$$

$$-\gamma\sqrt{a}\underset{\sim}{a}^{\beta}\bullet(\delta\underset{\sim}{r})_{,\beta}=-(\gamma\sqrt{a}\delta\underset{\sim}{r}\bullet\underset{\sim}{a}^{\beta})_{|\beta}+\delta\underset{\sim}{r}\bullet(\gamma\sqrt{a}\underset{\sim}{a}^{\beta})_{|\beta}$$

A2.53

3) $\boldsymbol{cHa^{\alpha\beta}\underset{\sim}{n}_{,\alpha}\bullet(\delta\underset{\sim}{r})_{,\beta}}$

$$cHa^{\alpha\beta}\underset{\sim}{n}_{,\alpha}\bullet(\delta\underset{\sim}{r})_{,\beta}=(cHa^{\alpha\beta}\underset{\sim}{n}_{,\alpha}\bullet\delta\underset{\sim}{r})_{,\beta}-(cHa^{\alpha\beta}\underset{\sim}{n}_{,\alpha})_{,\beta}\bullet(\delta\underset{\sim}{r})$$

Here we can note that,

$$T^{\beta}=cHa^{\alpha\beta}\underset{\sim}{n}_{,\alpha}\bullet\delta\underset{\sim}{r}=cHa^{\alpha\beta}b^{\omega}_{\alpha}\underset{\sim}{a}_{\omega}\bullet\delta\underset{\sim}{r}=cHa^{\alpha\beta}b^{\omega}_{\alpha}\delta\underset{\sim}{r}\bullet\underset{\sim}{a}_{\omega}$$

is a component of vector(i.e. the vector T transforms). So we can use the covariant differentiation definition defined for components as,

$$(cHa^{\alpha\beta}\underset{\sim}{n}_{,\alpha}\bullet\delta\underset{\sim}{r})_{,\beta}=(cHa^{\alpha\beta}\underset{\sim}{n}_{,\alpha}\bullet\delta\underset{\sim}{r})_{|\beta}-\Gamma^{\beta}_{\beta\omega}(cHa^{\alpha\beta}\underset{\sim}{n}_{,\alpha}\bullet\delta\underset{\sim}{r})$$

& the corresponding definition for indexed vectors as,

$$(cHa^{\alpha\beta}\underset{\sim}{n}_{,\alpha})_{,\beta}=(cHa^{\alpha\beta}\underset{\sim}{n}_{,\alpha})_{|\beta}-\Gamma^{\beta}_{\beta\omega}cHa^{\alpha\omega}\underset{\sim}{n}_{,\alpha}$$

Substituting back into the parent equation, we get

$$cHa^{\alpha\beta}\underset{\sim}{n}_{,\alpha}\bullet(\delta\underset{\sim}{r})_{,\beta}=(cHa^{\alpha\beta}\underset{\sim}{n}_{,\alpha}\bullet\delta\underset{\sim}{r})_{|\beta}-\Gamma^{\beta}_{\beta\omega}(cHa^{\alpha\beta}\underset{\sim}{n}_{,\alpha}\bullet\delta\underset{\sim}{r})-\delta\underset{\sim}{r}\bullet\left[(cHa^{\alpha\beta}\underset{\sim}{n}_{,\alpha})_{|\beta}-\Gamma^{\beta}_{\beta\omega}cHa^{\alpha\omega}\underset{\sim}{n}_{,\alpha}\right]$$

$$cHa^{\alpha\beta}\underset{\sim}{n}_{,\alpha}\bullet(\delta\underset{\sim}{r})_{,\beta}=(cHa^{\alpha\beta}\underset{\sim}{n}_{,\alpha}\bullet\delta\underset{\sim}{r})_{|\beta}-\delta\underset{\sim}{r}\bullet(cHa^{\alpha\beta}\underset{\sim}{n}_{,\alpha})_{|\beta}\qquad\text{A2.54}$$

Eventually eq. A2.**Error! Reference source not found.**can be written as,

$$\left[cHa^{\alpha\beta}\underset{\sim}{n}_{,\alpha}-cH_{,\alpha}a^{\alpha\beta}\underset{\sim}{n}-\gamma\sqrt{a}\underset{\sim}{a}^{\beta}\right]\bullet\delta(\underset{\sim}{r})_{,\beta}=\left[cHa^{\alpha\beta}\underset{\sim}{n}_{,\alpha}\bullet\delta\underset{\sim}{r}-cH_{,\alpha}a^{\alpha\beta}\underset{\sim}{n}\bullet\delta\underset{\sim}{r}-\gamma\sqrt{a}\underset{\sim}{a}^{\beta}\bullet\delta\underset{\sim}{r}\right]_{|\beta}$$

$$-\left[cHa^{\alpha\beta}\underset{\sim}{n}_{,\alpha}-cH_{,\alpha}a^{\alpha\beta}\underset{\sim}{n}-\gamma\sqrt{a}\underset{\sim}{a}^{\beta}\right]_{|\beta}\bullet\delta\underset{\sim}{r}$$

A2.55

Substituting the result in eq. A2.**Error! Reference source not found.** back into the integral in eq. A2.**Error! Reference source not found.**, we get

$$\delta U=\int_A\left[\left[cHa^{\alpha\beta}\underset{\sim}{n}_{,\alpha}\bullet\delta\underset{\sim}{r}-cH_{,\alpha}a^{\alpha\beta}\underset{\sim}{n}\bullet\delta\underset{\sim}{r}-\gamma\sqrt{a}\underset{\sim}{a}^{\beta}\bullet\delta\underset{\sim}{r}\right]_{|\beta}+\left[-cHa^{\alpha\beta}\underset{\sim}{n}_{,\alpha}+cH_{,\alpha}a^{\alpha\beta}\underset{\sim}{n}+\gamma\sqrt{a}\underset{\sim}{a}^{\beta}\right]_{|\beta}\bullet\delta\underset{\sim}{r}\right]dA$$

$$-\int_C(cH\underset{\sim}{a}^{\alpha}\bullet\delta\underset{\sim}{n})m_{\alpha}dl$$

Using divergence theorem on first term of area integral,

$$\delta U=\int_A\left[-cHa^{\alpha\beta}\underset{\sim}{n}_{,\alpha}+cH_{,\alpha}a^{\alpha\beta}\underset{\sim}{n}+\gamma\sqrt{a}\underset{\sim}{a}^{\beta}\right]_{|\beta}\bullet\delta\underset{\sim}{r}dA$$

$$+\int_C\left[\left(cHa^{\alpha\beta}\underset{\sim}{n}_{,\beta}-cH_{,\beta}a^{\alpha\beta}\underset{\sim}{n}-\gamma\sqrt{a}\underset{\sim}{a}^{\alpha}\right)\bullet\delta\underset{\sim}{r}-(cH\underset{\sim}{a}^{\alpha}\bullet\delta\underset{\sim}{n})\right]m_{\alpha}dl\qquad\text{A2.56}$$

Next, we use Weingarten equation in the eq.

A2.**Error! Reference source not found.**

$$\underset{\sim}{n}_{,\alpha}=-b_{\gamma\alpha}\underset{\sim}{a}^{\gamma}$$

which gives,

$$\delta U = \int_A \left[cHb^{\alpha\beta} \underset{\sim}{a}_\alpha + cH_{,\alpha} a^{\alpha\beta} \underset{\sim}{n} + \gamma \sqrt{a} \underset{\sim}{a}^\beta \right]_{|\beta} \bullet \delta \underset{\sim}{r} dA$$
$$+ \int_C \left[\left(-cHb^{\alpha\beta} \underset{\sim}{a}_\beta - cH_{,\beta} a^{\alpha\beta} \underset{\sim}{n} - \gamma \sqrt{a} \underset{\sim}{a}^\alpha \right) \bullet \delta \underset{\sim}{r} - (cH \underset{\sim}{a}^\alpha \bullet \delta \underset{\sim}{n}) \right] m_\alpha dl$$

On the other hand the virtual work done by the forces and moment on the boundary **C** can be written as,

$$\delta P = \int_C (\underset{\sim}{F} \bullet \delta \underset{\sim}{r} + (\underset{\sim}{M} \times \underset{\sim}{n}) \bullet \delta \underset{\sim}{n}) dl + \int_A \left(t^\alpha \underset{\sim}{a}_\alpha + p \underset{\sim}{n} \right) \bullet \delta \underset{\sim}{r} \, dA$$

From the principal of virtual work $\delta U = \delta P$, stated in eq.

A2.**Error! Reference source not found.** to get,

$$\left[cHb^{\alpha\beta} \underset{\sim}{a}_\alpha + cH_{,\alpha} a^{\alpha\beta} \underset{\sim}{n} + \gamma \sqrt{a} \underset{\sim}{a}^\beta \right]_{|\beta} = p \underset{\sim}{n} + t^\alpha \underset{\sim}{a}_\alpha \qquad (a)$$
$$\underset{\sim}{F} = \left(-cHb^{\alpha\beta} \underset{\sim}{a}_\beta - cH_{,\beta} a^{\alpha\beta} \underset{\sim}{n} - \gamma \sqrt{a} \underset{\sim}{a}^\alpha \right) m_\alpha \qquad (b) \qquad \text{A2.57}$$
$$\underset{\sim}{M} \times \underset{\sim}{n} = -cH \underset{\sim}{a}^\alpha m_\alpha \qquad (c)$$

This set of equations is valid for any general patch of membrane, which has some pressure, p acting on the area A and force $\underset{\sim}{F}$ and moment $\underset{\sim}{M}$ acting on the curve C surrounding the membrane.

Eq. A2.**Error! Reference source not found.**-a is the local equilibrium equation relating normal pressure p and shear load $\underset{\sim}{t}$, on the membrane to the geometrical parameters of the membrane.

Expression for moment in eq. A2.**Error! Reference source not found.**-c can be further by simplified as follows,

$$\begin{aligned}
&\left(\underset{\sim}{M}\times\underset{\sim}{n}=-cHm_{\alpha}\underset{\sim}{a}^{\alpha}\right)\times\underset{\sim}{a}^{\beta}\\
&\Rightarrow\left(\underset{\sim}{a}^{\beta}\bullet\underset{\sim}{n}\right)\underset{\sim}{M}-\left(\underset{\sim}{M}\bullet\underset{\sim}{a}^{\beta}\right)\underset{\sim}{n}=cHm_{\alpha}\left(\underset{\sim}{a}^{\alpha}\times\underset{\sim}{a}^{\beta}\right)\\
&\Rightarrow-\left(\underset{\sim}{M}\bullet\underset{\sim}{a}^{\beta}\right)\underset{\sim}{n}=cHm_{\alpha}\varepsilon^{\alpha\beta}\underset{\sim}{n}\\
&\Rightarrow\underset{\sim}{M}\bullet\underset{\sim}{a}^{\beta}=-cHm_{\alpha}\varepsilon^{\alpha\beta}\\
&\Rightarrow\underset{\sim}{M}=-cHm_{\alpha}\varepsilon^{\alpha\beta}\underset{\sim}{a}_{\beta}
\end{aligned}$$

Equilibrium eq. A2.**Error! Reference source not found.**-a can further modified as,

$$\begin{aligned}
&\left[cHb^{\alpha\beta}\underset{\sim}{a}_{\alpha}+cH_{,\alpha}a^{\alpha\beta}\underset{\sim}{n}+\gamma\sqrt{a}\underset{\sim}{a}^{\beta}\right]_{|\beta}\\
&\qquad=\left[\left(cHb^{\alpha\beta}+\gamma\sqrt{a}a^{\alpha\beta}\right)\underset{\sim}{a}_{\alpha}+cH_{,\alpha}a^{\alpha\beta}\underset{\sim}{n}\right]_{|\beta}
\end{aligned}$$

using chain rule of covariant

ifferentiation,

$$=(cHb^{\alpha\beta}+\gamma\sqrt{a}a^{\alpha\beta})_{|\beta}\underset{\sim}{a}_{\alpha}+(cHb^{\alpha\beta}+\gamma\sqrt{a}a^{\alpha\beta})\underset{\sim}{a}_{\alpha|\beta}+(cH_{,\alpha}a^{\alpha\beta})_{|\beta}\underset{\sim}{n}+cH_{,\alpha}a^{\alpha\beta}\underset{\sim}{n}_{|\beta}$$

using the fact that covariant differentiation of un-indexed quantities is equivalent to the normal derivative ($\underset{\sim}{n}_{|\alpha}=n_{,\alpha}$) along with the Gauss ($\underset{\sim}{a}_{\alpha|\beta}=b_{\alpha\beta}\underset{\sim}{n}$) and

Weingarten ($n_{,\alpha}=-b_{\alpha}^{\beta}\underset{\sim}{a}_{\beta}$) equations of surface,

$$\begin{aligned}
&=(cHb^{\alpha\beta}+\gamma\sqrt{a}a^{\alpha\beta})_{|\beta}\underset{\sim}{a}_{\alpha}+(cHb^{\alpha\beta}+\gamma\sqrt{a}a^{\alpha\beta})b_{\alpha\beta}\underset{\sim}{n}+(cH_{,\alpha}a^{\alpha\beta})_{|\beta}\underset{\sim}{n}-cH_{,\tau}a^{\tau\beta}b_{\beta}^{\alpha}\underset{\sim}{a}_{\alpha}\\
&=\left[(cHb^{\alpha\beta}+\gamma\sqrt{a}a^{\alpha\beta})_{|\beta}-cH_{,\tau}b^{\tau\alpha}\right]\underset{\sim}{a}_{\alpha}+\left[(cHb^{\alpha\beta}b_{\alpha\beta}+\gamma\sqrt{a}b_{\alpha}^{\alpha})+(cH_{,\alpha}a^{\alpha\beta})_{|\beta}\right]\underset{\sim}{n}
\end{aligned}$$

Comparing the above simplification of eq.

A2.**Error! Reference source not found.**-a with its R.H.S. to get,

$$(cHb^{\alpha\beta} + \gamma\sqrt{a}a^{\alpha\beta})_{|\beta} - cH_{,\tau}b^{\tau\alpha} = t^{\alpha} \qquad (a)$$
$$cHb^{\alpha\beta}b_{\alpha\beta} + \gamma\sqrt{a}b^{\alpha}_{\alpha} + (cH_{,\alpha}a^{\alpha\beta})_{|\beta} = -p \qquad (b) \qquad \text{A2.58}$$

Eq.A2.**Error! Reference source not found.**-a is the tangential equilibrium equation of the membrane patch and eq. A2.**Error! Reference source not found.**-b is the normal equilibrium equation.

Eq. A2.**Error! Reference source not found.**-a can be further simplified by multiplying both sides with $a_{\alpha\omega}$,

$$\begin{aligned}
&(cHb^{\alpha\beta} + \gamma\sqrt{a}a^{\alpha\beta})_{|\beta}a_{\alpha\omega} - cH_{,\tau}b^{\tau\alpha}a_{\alpha\omega} = t^{\alpha}a_{\alpha\omega} \\
\Rightarrow\ &(cHb^{\beta}_{\omega} + \gamma\sqrt{a}\delta^{\beta}_{\omega})_{|\beta} - cH_{,\tau}b^{\tau}_{\omega} = t^{\alpha}a_{\alpha\omega} \\
\Rightarrow\ &cH_{,\beta}b^{\beta}_{\omega} + 2cHH_{,\omega} + \left(\gamma\sqrt{a}\right)_{,\omega} - cH_{,\tau}b^{\tau}_{\omega} = t^{\alpha}a_{\alpha\omega} \\
\Rightarrow\ &2cHH_{,\omega} + \left(\gamma\sqrt{a}\right)_{,\omega} = t^{\alpha}a_{\alpha\omega} \\
\Rightarrow\ &\left(cH^{2} + \gamma\sqrt{a}\right)_{,\alpha} = t^{\alpha}a_{\alpha\omega}
\end{aligned}$$

Here we have used the identity, $a_{\alpha\beta|\gamma} = 0$, proof of which is appended below.

$$a_{\alpha\beta} = \underset{\sim}{a}_{\alpha} \bullet \underset{\sim}{a}_{\beta}$$
$$a_{\alpha\beta|\gamma} = \underset{\sim}{a}_{\alpha|\gamma} \bullet \underset{\sim}{a}_{\beta} + \underset{\sim}{a}_{\alpha} \bullet \underset{\sim}{a}_{\beta|\gamma}$$

using the Gauss equation of surface $\underset{\sim}{a}_{\alpha|\gamma} = b_{\alpha\gamma}\underset{\sim}{n}$

$$\Rightarrow a_{\alpha\beta|\gamma} = b_{\alpha\beta}\underset{\sim}{n} \bullet \underset{\sim}{a}_{\beta} + \underset{\sim}{a}_{\alpha} \bullet b_{\beta\gamma}\underset{\sim}{n} = 0$$

and also the relation

$$b^{\beta}_{\alpha|\beta} = b^{\beta}_{\beta|\alpha} = 2H_{,\alpha}$$

which can be easily proved using Mainardi-Codazzi equation, $b_{\alpha\beta|\gamma} = b_{\alpha\gamma|\beta}$ and

$a_{\alpha\beta|\gamma} = 0$

Thus, the highly simplified form of the tangential equilibrium is given as,

$$\left(cH^2 + \gamma\sqrt{a}\right)_{,\alpha} = t^{\alpha} a_{\alpha\omega} \qquad \text{A2.59}$$

Using the expression of divergence from eq.

A2.**Error! Reference source not found.** and result in eq.

A2.**Error! Reference source not found.**, the normal equilibrium equation in eq.

A2.**Error! Reference source not found.**-b can be written as,

$$cH\left(4H^2 - 2K\right) + 2\gamma\sqrt{a}H + \frac{1}{\sqrt{a}}\left(c\sqrt{a}H_{,\alpha}a^{\alpha\beta}\right)_{,\beta} = p \quad \text{A2.60}$$

Thus, finally we can write the equilibrium equation for the case where a membrane has loading distribution in normal as well as tangential direction,

$$cH\left(4H^2 - 2K\right) + 2\gamma\sqrt{a}H + \frac{1}{\sqrt{a}}\left(c\sqrt{a}H_{,\alpha}a^{\alpha\beta}\right)_{,\beta} = p$$

$$\left(cH^2 + \gamma\sqrt{a}\right)_{,\alpha} = t^{\omega} a_{\alpha\omega}$$

and at any point in the membrane, Force and moment are given by the relation,

$$\underset{\sim}{F} = \left(-cHb^{\alpha\beta}\underset{\sim}{a}_{\beta} - cH_{,\beta}a^{\alpha\beta}\underset{\sim}{n} - \gamma\sqrt{a}\underset{\sim}{a}^{\alpha}\right)m_{\alpha}$$

$$\underset{\sim}{M} = -cHm_{\alpha}\varepsilon^{\alpha\beta}\underset{\sim}{a}_{\beta}$$

A2.3 Calculations for axisymmetric geometry

For the an axis-symmetric membrane we can define the geometry of the problem, by two surface coordinates, $u^1 = \theta, u^2 = S$, where θ is the angle of revolution about z axis and S is the arc length in the reference undeformed configuration as shown in Fig. A2.1.

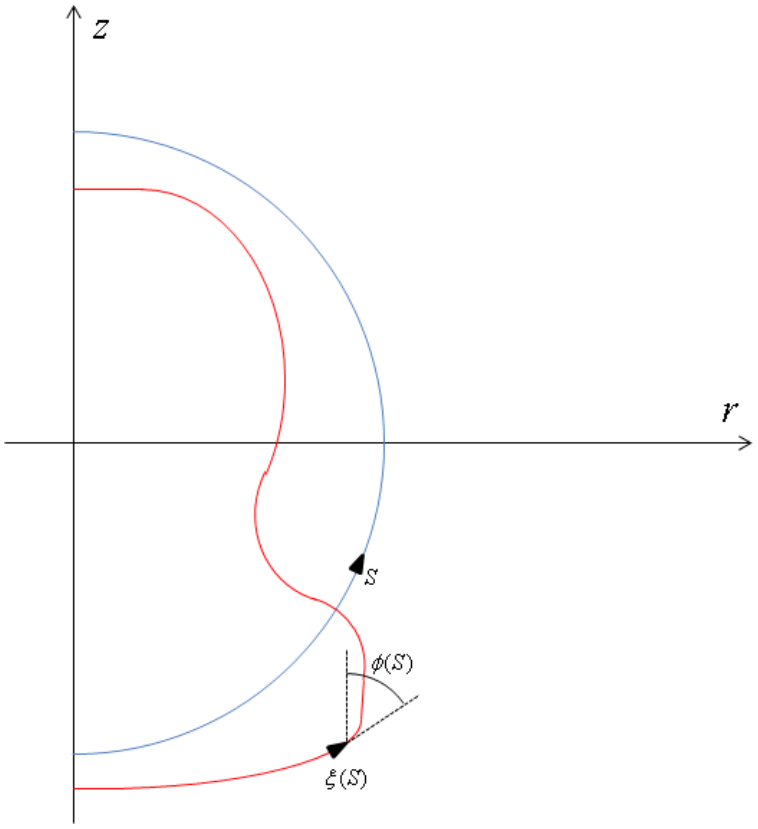

Fig. A2.1: undeformed and deformed configuration

As shown in the figure, **position of a point** can be written as,

$$\underset{\sim}{r} = r\cos\theta\,\hat{i} + r\sin\theta\,\hat{j} + z\,\hat{k}, \qquad \text{A2.61}$$

where, $\hat{i}, \hat{j}, \hat{k}$ are the Cartesian basis vectors. Fig. A2.1 shows the cross sectional plane for $\theta = \text{constant}$, with r & z are coordinates on that plane. Because of the axis-symmetry, r & z depend only on S .

Next, we introduce two new variables, ξ & ϕ, which are arc length and angle made by tangent with vertical respectively in deformed configuration. Again, by the virtue of axis-symmetry, ξ & ϕ only depend on undeformed arc length S.

As observed in Fig. A2.1,

$$\frac{\partial r}{\partial \xi} = \sin\phi, \ \frac{\partial z}{\partial \xi} = \cos\phi. \qquad \text{A2.62}$$

Now, we can define the **surface basis vectors**

as,

$$\underset{\sim}{a}_S = \frac{\partial \underset{\sim}{r}}{\partial S} = \frac{\partial r}{\partial \xi}\frac{\partial \xi}{\partial S}\cos\theta\hat{i} + \frac{\partial r}{\partial \xi}\frac{\partial \xi}{\partial S}\sin\theta\hat{j} + \frac{\partial z}{\partial \xi}\frac{\partial \xi}{\partial S}\hat{k} = \dot{\xi}\sin\phi\cos\theta\hat{i} + \dot{\xi}\sin\phi\sin\theta\hat{j} + \dot{\xi}\cos\phi\hat{k}$$

,

A2.63

$$\underset{\sim}{a}_\theta = \frac{\partial \underset{\sim}{r}}{\partial \theta} = -r\sin\theta\hat{i} + r\cos\theta\hat{j}, \qquad \text{A2.64}$$

where, $\dot{\xi} = \frac{\partial \xi}{\partial S}$. It can be clearly seen that both these basis vectors are orthogonal to each other as ,

$$\underset{\sim}{a}_S \bullet \underset{\sim}{a}_\theta = 0.$$

Normal can be defined as,

$$n = \frac{\underset{\sim}{a}_\theta \times \underset{\sim}{a}_S}{\left|\underset{\sim}{a}_\theta \times \underset{\sim}{a}_S\right|} = \cos\phi\cos\theta\hat{i} + \cos\phi\sin\theta\hat{j} - \sin\phi\hat{k}. \quad \text{A2.65}$$

Next, we define **first fundamental form of surface and its inverse** as,

$$\left[a_{\alpha\beta}\right] = \begin{matrix} \theta & S \\ \end{matrix} \begin{bmatrix} r^2 & 0 \\ 0 & \dot{\xi}^2 \end{bmatrix} \begin{matrix} \theta \\ S \end{matrix}, \quad \text{A2.66}$$

$$\left[a^{\alpha\beta}\right] = \left[a_{\alpha\beta}\right]^{-1} = \begin{matrix} \theta & S \\ \end{matrix} \begin{bmatrix} \frac{1}{r^2} & 0 \\ 0 & \frac{1}{\dot{\xi}^2} \end{bmatrix} \begin{matrix} \theta \\ S \end{matrix}. \quad \text{A2.67}$$

It can be easily shown that,

$$\underset{\sim}{a}_{\theta,\theta} = -r\cos\theta\hat{i} - r\sin\theta\hat{j},$$
$$\underset{\sim}{a}_{\theta,S} = \underset{\sim}{a}_{S,\theta} = -\dot{\xi}\sin\phi\sin\theta\hat{i} + \dot{\xi}\sin\phi\cos\theta\hat{j},$$
$$\underset{\sim}{a}_{S,S} = \left(\ddot{\xi}\sin\phi + \dot{\xi}\dot{\phi}\cos\phi\right)\left(\cos\theta\hat{i} + \sin\theta\hat{j}\right) + \left(\ddot{\xi}\cos\phi - \dot{\xi}\dot{\phi}\sin\phi\right)\hat{k}.$$

Thus, **second fundamental form of surface** is,

$$\left[b_{\alpha\beta}\right] = \left[\underset{\sim}{n} \bullet \underset{\sim}{a}_{\alpha,\beta}\right] = \begin{matrix} \theta & S \\ \end{matrix} \begin{bmatrix} -r\cos\phi & 0 \\ 0 & \dot{\phi}\dot{\xi} \end{bmatrix} \begin{matrix} \theta \\ S \end{matrix}, \quad \text{A2.68}$$

$$\left[b^{\alpha}_{\beta}\right] = \left[a^{\alpha\tau}\right]\left[b_{\tau\beta}\right] = \begin{bmatrix} \frac{1}{r^2} & 0 \\ 0 & \frac{1}{\dot{\xi}^2} \end{bmatrix} \begin{bmatrix} -r\cos\phi & 0 \\ 0 & \dot{\phi}\dot{\xi} \end{bmatrix} = \begin{matrix} \theta & S \\ \end{matrix} \begin{bmatrix} -\frac{\cos\phi}{r} & 0 \\ 0 & \frac{\dot{\phi}}{\dot{\xi}} \end{bmatrix} \begin{matrix} \theta \\ S \end{matrix}. \quad \text{A2.69}$$

Imposing local area incompressibility ($\sqrt{a} = \text{constant}$), we can get,

$$\sqrt{a} = r\dot{\xi} = R \Rightarrow \dot{\xi} = \frac{R}{r}, \qquad \text{A2.70}$$

where, R is the radial distance of a point in undeformed configuration.

Therefore, we can define **curvatures** as,

$$H = \frac{1}{2} b_{\alpha}^{\alpha} = \frac{1}{2}\left(\frac{\dot{\phi}}{\dot{\xi}} - \frac{\cos\phi}{r} \right) = \frac{1}{2}\left(\dot{\phi}\frac{r}{R} - \frac{\cos\phi}{r} \right), \quad \text{A2.71}$$

$$K = \det\left[b_{\alpha}^{\alpha} \right] = -\frac{\dot{\phi}}{\dot{\xi}}\frac{\cos\phi}{r} = -\left(2H + \frac{\cos\phi}{r} \right)\frac{\cos\phi}{r}. \quad \text{A2.72}$$

Using the expression of force from eq. A2.**Error! Reference source not found.**-b, one can get the **in plane and transverse shear forces**. As shown earlier, $\underset{\sim}{m}$ is normal to curve C, such that it is perpendicular to the normal to surface at that point. So if we cut our axis-symmetric geometry at a given z, we will have $\underset{\sim}{m}$ perpendicular to $\underset{\sim}{a}_{\theta}$ & $\underset{\sim}{n}$. Since $\underset{\sim}{a}_{\theta}$ & $\underset{\sim}{a}_{S}$ are also perpendicular, then it is easy to conclude that $\underset{\sim}{m}$ is parallel to $\underset{\sim}{a}_{S}$.

$$\underset{\sim}{m} = m_{\theta}\underset{\sim}{a}^{\theta} + m_{S}\underset{\sim}{a}^{S}$$

$$\underset{\sim}{a}^{S} \bullet \underset{\sim}{a}_{S} = 1 \Rightarrow \left| \underset{\sim}{a}^{S} \right| = \frac{1}{\dot{\xi}}$$

$$\because \left| \underset{\sim}{m} \right| = 1 \;\&\; m_{\theta} = 0 \Rightarrow m_{S} = \dot{\xi}$$

Therefore, we get $m_\theta = 0$ & $m_S = \dot{\xi}$. Also, due to axis-symmetry we can say that there is no component of force acting along $\underset{\sim}{a}_\theta$. Combining all these facts, we can write the expression of force as,

$$\underset{\sim}{F} = \left(-cHa^{22}b_2^2 - \gamma\sqrt{a}a^{22}\right)m_2\underset{\sim}{a}_2 - cH_{,S}a^{SS}m_S\underset{\sim}{n} = \left(-cH\frac{\dot{\phi}}{\dot{\xi}} - \gamma\sqrt{a}\right)\frac{\underset{\sim}{a}_S}{|\underset{\sim}{a}_S|} - \frac{cH_{,S}}{\dot{\xi}}\underset{\sim}{n}.$$

A2.73

Comparing this with the following expression of force,

$$F = T\frac{\underset{\sim}{a}_S}{|\underset{\sim}{a}_S|} - Q\underset{\sim}{n},$$

we get,

$$T = \left(-cH\frac{\dot{\phi}}{\dot{\xi}} - \gamma\sqrt{a}\right) \quad \& \quad Q = \frac{c\dot{H}}{\dot{\xi}}, \qquad \text{A2.74}$$

where, $\dot{H} = \dfrac{\partial H}{\partial S}$.

Now, we can use the above information for the deformed configuration to come up with its equilibrium equations, using eqs. A2.**Error! Reference source not found.** & A2.**Error! Reference source not found.**. For the axis-symmetric case we only have one variable i.e. S.

Thus equilibrium equations can be modified as,

$$\left(cH^2+\gamma\sqrt{a}\right)_{,S}=t^S a_{SS} \qquad \text{A2.75}$$

$$cH\left(4H^2-2K\right)+2\gamma\sqrt{a}H+\frac{1}{\sqrt{a}}\left(c\sqrt{a}H_{,S}a^{SS}\right)_{,S}=p \quad \text{A2.76}$$

Assuming a new variable d, such that,

$$d=cH^2+\gamma\sqrt{a} \qquad \text{A2.77}$$

And, we also get,

$$d_{,S}=t^S a_{SS} \qquad \text{A2.78}$$

Now using eq. A2.**Error! Reference source not found.**, γ could be eliminated from eq. A2.**Error! Reference source not found.** to get,

$$2H\left(d+c\left(H^2-K\right)\right)+\frac{1}{\sqrt{a}}\left(c\sqrt{a}H_{,S}a^{SS}\right)_{,S}=p \quad \text{A2.79}$$

Now using the definition of Q from eq. A2.**Error! Reference source not found.**, and the facts that $\sqrt{a}=r\dot{\xi}=R$ and $a^{SS}=\frac{1}{\dot{\xi}^2}$, to get

$$2H\left(d+c\left(H^2-K\right)\right)+\frac{1}{R}\left(rQ\right)_{,S}=p$$
$$\Rightarrow\frac{r}{R}Q_{,S}+\frac{Q}{R}r_{,S}+2H\left(d+c\left(H^2-K\right)\right)=p$$
$$\Rightarrow\frac{r}{R}Q_{,S}+\frac{Q}{R}r_{,S}+2H\left(d+c\left(H^2-K\right)\right)=p$$

Writing $Q_{,S}=\dot{Q}$ and $r_{,S}=\dot{r}$

$$\Rightarrow \frac{r}{R}\dot{Q} = p - 2H\left(d + c\left(H^2 - K\right)\right) - \frac{Q}{R}\dot{r}$$
$$\Rightarrow \dot{Q} = \frac{R}{r}p - 2H\frac{R}{r}\left(d + c\left(H^2 - K\right)\right) - \frac{Q}{r}\dot{r}$$

Again using the definition of K from eq. A2.**Error! Reference source not found.**, to get,

$$\Rightarrow \dot{Q} = -\frac{Q}{r}\dot{r} - 2H\frac{R}{r}\left[d + cH^2 + c\left(2H + \frac{\cos\phi}{r}\right)\frac{\cos\phi}{r}\right] + \frac{R}{r}p \quad \text{A2.80}$$

Next we simplify eq. A2.**Error! Reference source not found.**, starting with the idea that we have an electrostatic interaction happening between the two membranes facing each other and the force due to the interaction is only in vertical direction. Let the electrostatic force per unit area be denoted by, F_e. The main idea is to get t^S in eq. A2.**Error! Reference source not found.**.

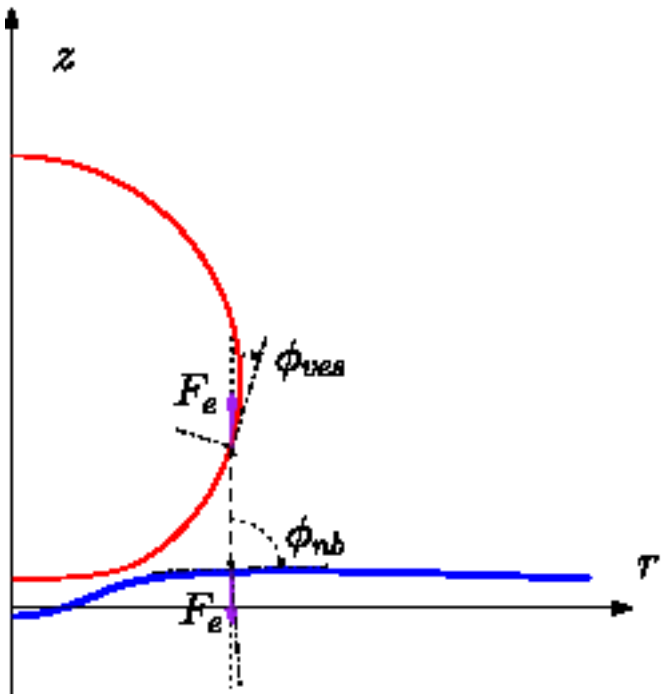

Fig. A2.2: electrostatics force on vesicle

Referring to the above figure, it can be seen that this vertical force could be resolved into 2 components, one normal to the membrane and one along the tangent to the arc at that particular point. Also, considering the tangential component of the concentrated load, F_t acting at some specific location, $S = S_0$. Thus, the net tangential force acting at a particular point on membrane can be written as,

$$t^S \underset{\sim}{a}_S = \left(F_e \cos\phi + F_t\right)\frac{\underset{\sim}{a}_S}{\left|\underset{\sim}{a}_S\right|} \quad \Rightarrow \quad t^S = \frac{F_e \cos\phi + F_t}{\left|\underset{\sim}{a}_S\right|} = \frac{F_e \cos\phi + F_t}{\dot{\xi}}$$

Thus, we can write eq. A2.**Error! Reference source not found.** as,

$$\dot{d} = t^S a_{SS} \Rightarrow \dot{d} = \frac{F_e \cos\phi + F_t}{\dot{\xi}}\dot{\xi}^2$$

$$\Rightarrow \dot{d} = \left(F_e \cos\phi + F_t\right)\frac{R}{r} \qquad \text{A2.81}$$

Also, we need to modify the expression of pressure used in eq. A2.**Error! Reference source not found.**, to include the effect of the normal component of the electrostatic interaction and the concentrated load at $S = S_0$, as follows

$$p = p_0 + F_e \sin\phi + F_n \delta\left(S - S_0\right)$$

Thus, we can finally write the complete set of coupled ODE's as follows:

$$\dot{Q} = -\frac{Q}{r^2} R\sin\phi - 2H\frac{R}{r}\left[d + cH^2 + c\left(2H + \frac{\cos\phi}{r}\right)\frac{\cos\phi}{r}\right] + \frac{R}{r}p,$$

$$\dot{\phi} = \frac{R}{r}\left(2H + \frac{\cos\phi}{r}\right),$$

$$\dot{H} = \frac{R}{r}\frac{Q}{c},$$

$$\dot{r} = \frac{R}{r}sin\phi,$$

$$\dot{z} = \frac{R}{r}cos\phi,$$

$$\dot{d} = \left(F_e \cos\phi + F_t\right)\frac{R}{r},$$

where,

$$p = p_0 + F_e \sin\phi + F_n \delta\left(S - S_0\right)$$

A2.4 Normalization for spherical vesicle

For the spherical vesicle with a undeformed radius ρ, radial position of a point is given by, $R = \rho \sin\left(\frac{S}{\rho}\right)$.

We use this in our set of ODE's to get the modified system of equations, as follows,

$$\dot{Q} = -\frac{Q}{r^2}\rho \sin\left(\frac{S}{\rho}\right)\sin\phi - 2H\rho\frac{\sin\left(\frac{S}{\rho}\right)}{r}\left[d + cH^2 + c\left(2H + \frac{\cos\phi}{r}\right)\frac{\cos\phi}{r}\right] + \rho\frac{\sin\left(\frac{S}{\rho}\right)}{r}p,$$

$$\dot{\phi} = \rho\frac{\sin\left(\frac{S}{\rho}\right)}{r}\left(2H + \frac{\cos\phi}{r}\right),$$

$$\dot{H} = \rho\frac{\sin\left(\frac{S}{\rho}\right)}{r}\frac{Q}{c},$$

$$\dot{r} = \rho\frac{\sin\left(\frac{S}{\rho}\right)}{r}sin\phi,$$

$$\dot{z} = \rho\frac{\sin\left(\frac{S}{\rho}\right)}{r}cos\phi,$$

$$\dot{d} = \left(F_e\cos\phi + F_t\right)\rho\frac{\sin\left(\frac{S}{\rho}\right)}{r},$$

where,

$$p = p_0 + F_e\sin\phi + F_n\delta\left(S - S_0\right)$$

Now, we normalize the quantities with ρ and c, such that

$$\bar{S}=\frac{S}{\rho},\quad \bar{r}=\frac{r}{\rho},\quad \bar{z}=\frac{\bar{z}}{\rho},\quad \bar{H}=\rho H,\quad \bar{Q}=\frac{Q\rho^2}{c},\quad \bar{d}=\frac{d\rho^2}{c},$$

$$\bar{p}=\frac{p\rho^3}{c},\quad \bar{F}_e=\frac{F_e\rho^3}{c},\quad \bar{F}_n=\frac{F_n\rho^3}{c},\quad \bar{F}_t=\frac{F_t\rho^3}{c}$$

This eventually gives us the following set of non-dimensional equations,

$$\dot{\bar{Q}}=-\frac{\bar{Q}}{\bar{r}^2}\sin\bar{S}\sin\phi-2\bar{H}\frac{\sin\bar{S}}{\bar{r}}\left[\bar{d}+\bar{H}^2+\left(2\bar{H}+\frac{\cos\phi}{\bar{r}}\right)\frac{\cos\phi}{\bar{r}}\right]+\frac{\sin S}{\bar{r}}\bar{p},$$

$$\dot{\phi}=\frac{\sin\bar{S}}{\bar{r}}\left(2\bar{H}+\frac{\cos\phi}{\bar{r}}\right),$$

$$\dot{\bar{H}}=\frac{\sin\bar{S}}{\bar{r}}\bar{Q},$$

$$\dot{\bar{r}}=\frac{\sin\bar{S}}{\bar{r}}sin\phi,$$ A2.82(a-f)

$$\dot{\bar{z}}=\frac{\sin\bar{S}}{\bar{r}}cos\phi,$$

$$\dot{\bar{d}}=\left(\bar{F}_e\cos\phi+\bar{F}_t\right)\frac{\sin\bar{S}}{\bar{r}},$$

where,

$$\bar{p}=\bar{p}_0+\bar{F}_e\sin\phi+\bar{F}_n\delta\left(\bar{S}-\bar{S}_0\right)$$

Also, we have the following set of boundary conditions to go along with the deformation of a pressurized vesicle (pressure acting normally outward) under the influence of electrostatic interaction with a substrate and a concentrated load,

$$\phi(\bar{S}=0)=\frac{\pi}{2},$$
$$\bar{Q}(\bar{S}=0)=0,$$
$$\bar{r}(\bar{S}=0)=0,$$
$$\phi(\bar{S}=\pi)=-\frac{\pi}{2},$$
$$\bar{Q}(\bar{S}=\pi)=0,$$
$$\bar{r}(\bar{S}=\pi)=0,$$

A2.83(a-f)

A2.5 Normalization for flat membrane

For the flat circular membrane with an undeformed in-plane radius L, radial distance of a point in reference configuration is given as $R=S$. We use this in our set of ODE's to get the modified system of equations, as follows,

$$\dot{Q}=-\frac{Q}{r^2}S\sin\phi-2H\frac{S}{r}\left[d+cH^2+c\left(2H+\frac{\cos\phi}{r}\right)\frac{\cos\phi}{r}\right]+\frac{S}{r}p,$$
$$\dot{\phi}=\frac{S}{r}\left(2H+\frac{\cos\phi}{r}\right),$$
$$\dot{H}=\frac{S}{r}\frac{Q}{c},$$
$$\dot{r}=\frac{S}{r}sin\phi,$$
$$\dot{z}=\frac{S}{r}cos\phi,$$
$$\dot{d}=\left(F_e\cos\phi+F_t\right)\frac{S}{r},$$

where,

$$p=p_0+F_e\sin\phi+F_n\delta\left(S-S_0\right)$$

Now, we normalize the quantities with ρ and c, such that

$$\bar{S} = \frac{S}{\rho}, \quad \bar{r} = \frac{r}{\rho}, \quad \bar{z} = \frac{\bar{z}}{\rho}, \quad \bar{H} = \rho H, \quad \bar{Q} = \frac{Q\rho^2}{c}, \quad \bar{d} = \frac{d\rho^2}{c},$$

$$\bar{p} = \frac{p\rho^3}{c}, \quad \bar{F}_e = \frac{F_e\rho^3}{c}, \quad \bar{F}_n = \frac{F_n\rho^3}{c}, \quad \bar{F}_t = \frac{F_t\rho^3}{c}$$

This eventually gives us the following set of non-dimensional equations,

$$\dot{\bar{Q}} = -\frac{\bar{Q}}{\bar{r}^2}\bar{S}\sin\phi - 2\bar{H}\frac{\bar{S}}{\bar{r}}\left[\bar{d} + \bar{H}^2 + \left(2\bar{H} + \frac{\cos\phi}{\bar{r}}\right)\frac{\cos\phi}{\bar{r}}\right] + \frac{S}{\bar{r}}\bar{p},$$

$$\dot{\phi} = \frac{\bar{S}}{\bar{r}}\left(2\bar{H} + \frac{\cos\phi}{\bar{r}}\right),$$

$$\dot{\bar{H}} = \frac{\bar{S}}{\bar{r}}\bar{Q},$$

$$\dot{\bar{r}} = \frac{\bar{S}}{\bar{r}}\sin\phi, \qquad \text{A2.84(a-f)}$$

$$\dot{\bar{z}} = \frac{\bar{S}}{\bar{r}}\cos\phi,$$

$$\dot{\bar{d}} = \left(\bar{F}_e\cos\phi + \bar{F}_t\right)\frac{\bar{S}}{\bar{r}},$$

where,

$$\bar{p} = \bar{p}_0 + \bar{F}_e\sin\phi + \bar{F}_n\delta\left(\bar{S} - \bar{S}_0\right)$$

Also, we have the following set of boundary conditions to go along with the deformation of a pressurized flat membrane (pressure acting normally outward) under the influence of electrostatic interaction with a substrate and a concentrated load,

$$\phi(\bar{S}=0)=\frac{\pi}{2},$$
$$\bar{Q}(\bar{S}=0)=0,$$
$$\bar{r}(\bar{S}=0)=0,$$
$$\phi\left(\bar{S}=\frac{L}{\rho}\right)=\frac{\pi}{2},$$
$$\bar{z}\left(\bar{S}=\frac{L}{\rho}\right)=0,$$
$$\bar{T}\left(\bar{S}=\frac{L}{\rho}\right)=\left[-\bar{d}-\bar{H}^2-\bar{H}\,\frac{cos\phi}{\bar{r}}\right]_{\bar{S}=\frac{L}{\rho}}=\bar{T}_0\left(=\frac{T_0\rho^2}{c},\right)$$

A2.85(a-f)

A2.6 Electrostatics force calculation

In this section we show the derivation for the electrostatics force per unit area.

Chemical Equilibrium

Consider the chemical concentration of an ionic species inside the neuron, with a z-z electrolyte. It is known that the far field potential inside the cell is φ_0 and the ionic concentration is c_0 as shown in Fig A2.3. Based on this information, we write a chemical equilibrium balance in terms of chemical potential equality as,

$$\mu(\mathrm{x})=\mu_0$$
$$\Rightarrow k_B T\log\left[\frac{c(x)}{c^*}\right]+ez\varphi=\underbrace{k_B T\log\left[\frac{c_0}{c^*}\right]+ez\varphi_0}_{far\ field}$$
$$\Rightarrow \log\left[\frac{c(x)}{c_0}\right]=\frac{ez}{k_B T}\left[\varphi_0-\varphi(x)\right]$$
$$\Rightarrow \log\left[\frac{c(x)}{c_0}\right]=\frac{ez}{k_B T}\left[\varphi_0-\varphi(x)\right]$$
$$\Rightarrow \log\left[\frac{c(x)}{c_0}\right]=-\frac{ez}{k_B T}\left[\varphi(x)-\varphi_0\right]$$

$$\Rightarrow c(x) = c_0 \exp\left(-\frac{ez}{k_B T}[\varphi(x) - \varphi_0] \right) \qquad \text{A2.86}$$

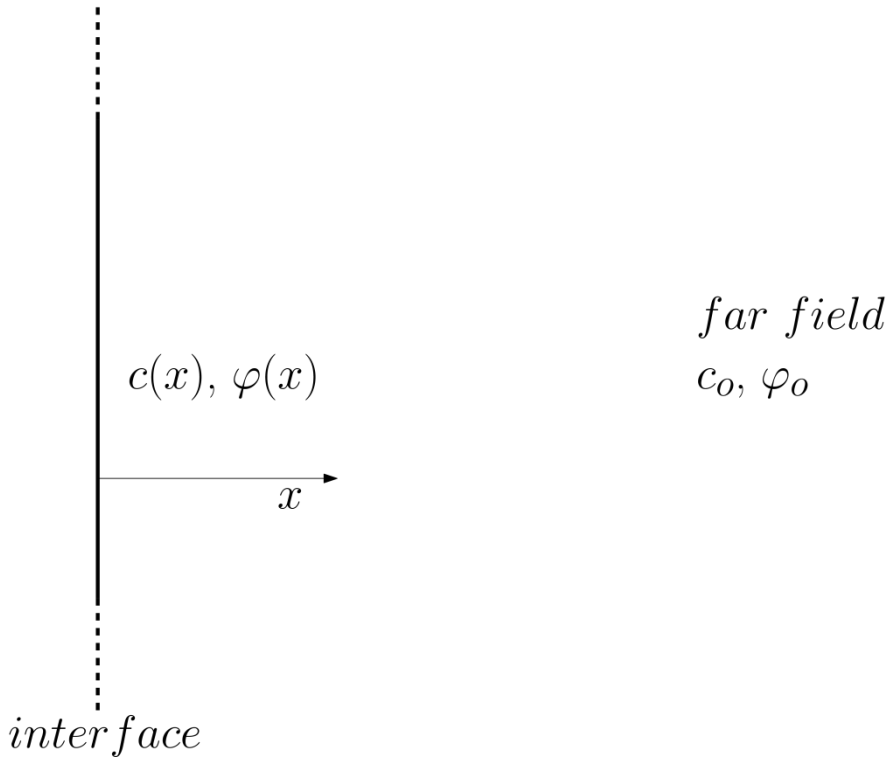

Fig A2.3 : near field and far field quantities inside the neuron

Poisson's equation

The Poisson's equation, governing potential inside the electrolyte solution is given as,

$$\nabla^2 \varphi = -\frac{\rho}{\varepsilon \varepsilon_0} \qquad \text{A2.87}$$

where,

ρ is the charge density inside the electrolyte,

ε is the dielectric constant of electrolyte,

ε_0 is the permeability of the vacuum.

Charge density of a electrolyte solution, with both cations and anions, can be defined using eq. A2.89 as,

$$\rho = ez\left[c_+(\mathrm{x}) + c_-(\mathrm{x})\right] = \underbrace{ezc_0 \exp\left(-\frac{ez}{k_B T}\left[\varphi(x) - \varphi_0\right]\right)}_{cations} - \underbrace{ezc_0 \exp\left(\frac{ez}{k_B T}\left[\varphi(x) - \varphi_0\right]\right)}_{anions}$$

A2.88

Substituting expression of charge density from eq. A2.91 into eq. A2.90, we get,

$$\nabla^2\varphi = -\frac{ezc_0}{\varepsilon\varepsilon_0}\exp\left(-\frac{ez}{k_B T}\left[\varphi(x) - \varphi_0\right]\right) + \frac{ezc_0}{\varepsilon\varepsilon_0}\exp\left(\frac{ez}{k_B T}\left[\varphi(x) - \varphi_0\right]\right)$$

$$\Rightarrow \nabla^2\varphi = \left(\frac{e^2 z^2 c_0}{\varepsilon\varepsilon_0 k_B T}\right)\left(\frac{k_B T}{ez}\right)\left[\exp\left(\frac{ez}{k_B T}\left[\varphi(x) - \varphi_0\right]\right) - \exp\left(-\frac{ez}{k_B T}\left[\varphi(x) - \varphi_0\right]\right)\right],$$

A2.89

let's assume,

$$l_D^2 = \left(\frac{\varepsilon\varepsilon_0 k_B T}{2e^2 z^2 c_0}\right) \text{ and } b = \frac{ez}{k_B T},$$

to rewrite the eq. A2.92 as,

$$\Rightarrow \nabla^2\varphi = \frac{1}{l_D^2}\frac{\sinh\left[b\left(\varphi(\mathrm{x}) - \varphi_0\right)\right]}{b}. \qquad \text{A2.90}$$

The equation above can be linearized to get, Debye-Huckel equation as,

$$\Rightarrow \nabla^2\varphi = \frac{\varphi(\mathrm{x}) - \varphi_0}{l_D^2}, \qquad \text{A2.91}$$

which can be written in 1-D case as,

$$\varphi_{,ii} = \frac{\varphi(\mathrm{x}) - \varphi_0}{l_D^2}\,. \qquad \text{A2.92}$$

Modified J-integral

The J-integral used to evaluate force in [2],

$$J = \int_s \left(\frac{D_i E_i}{2} n_1 - D_i n_i E_1 + \varepsilon\varepsilon_0 \frac{\varphi^2}{2l_D^2} n_1 \right) ds\,, \qquad \text{A2.93}$$

is only applicable to the corresponding Poisson Boltzmann equation,

$$\nabla^2 \varphi = \frac{\varphi}{l_D^2} \Rightarrow \varphi_{,ii} = \frac{\varphi}{l_D^2}\,. \qquad \text{A2.94}$$

For the governing equation A2.7, obtained in the analysis before, the modified J-integral is given as,

$$J = \int_s \left(\frac{D_i E_i}{2} n_1 - D_i n_i E_1 + \varepsilon\varepsilon_0 \frac{\left(\varphi - \varphi_0\right)^2}{2l_D^2} n_1 \right) ds\,. \qquad \text{A2.95}$$

The above J-integral should go to zero exactly when evaluated along a surface which doesn't include a singularity.

$$J = \int_s \left(\frac{D_i E_i}{2} n_1 - D_i n_i E_1 + \varepsilon\varepsilon_0 \frac{\left(\varphi - \varphi_0\right)^2}{2l_D^2} n_1 \right) ds$$

using $D_i = \varepsilon\varepsilon_0 E_i$,

$$\Rightarrow J = \int_s \left(\frac{\varepsilon\varepsilon_0 E_i^2}{2} n_1 - \varepsilon\varepsilon_0 n_i E_i E_1 + \varepsilon\varepsilon_0 \frac{\left(\varphi - \varphi_0\right)^2}{2l_D^2} n_1 \right) ds$$

using $E_i = \varphi_{,i}$,

$$\Rightarrow J = \int_s \left(\frac{\varepsilon\varepsilon_0 \varphi_{,i}^2}{2} n_1 - \varepsilon\varepsilon_0 n_i \varphi_{,i} \varphi_{,1} + \varepsilon\varepsilon_0 \frac{\left(\varphi - \varphi_0\right)^2}{2l_D^2} n_1 \right) ds$$

Using the Divergence theorem,

$$\Rightarrow J = \varepsilon\varepsilon_0 \int_V \left[\frac{\left(\varphi_{,i}^2\right)_1}{2} - \left(\varphi_{,i}\varphi_{,1}\right)_i + \frac{\left\{\left(\varphi - \varphi_0\right)^2\right\}_1}{2l_D^2} \right] dV$$

$$\Rightarrow J = \varepsilon\varepsilon_0 \int_V \left[\cancel{\varphi_{,i1}\varphi_{,i}} - \left(\varphi_{,ii}\varphi_{,1} + \cancel{\varphi_{,i}\varphi_{,1i}} \right) + \frac{\left(\varphi - \varphi_0\right)\varphi_{,1}}{l_D^2} \right] dV$$

now, using eq. A2.97, to get,

$$\Rightarrow J = \varepsilon\varepsilon_0 \int_V \left[\cancel{-\left(\frac{\varphi - \varphi_0}{l_D^2} \right) \varphi_{,1}} + \cancel{\frac{\left(\varphi - \varphi_0\right)\varphi_{,1}}{l_D^2}} \right] dV = 0$$

Clearly, this J-integral is the apt for eq. A2.97.

Based on this J-integral, we can write the expression of the force as follows,

$$J = \int_s \left(\frac{D_i E_i}{2} n_1 - D_i n_i E_1 + \varepsilon\varepsilon_0 \frac{\left(\varphi - \varphi_0\right)^2}{2l_D^2} n_1 \right) ds\,.$$

For the plane strain case, as shown in fig. A2.4, the gradient in potential φ is only along the x-direction. Therefore, the above expression simplifies to,

$$\Rightarrow J = \int_s \left(\frac{D_1 E_1}{2} n_1 - D_1 n_1 E_1 + \varepsilon\varepsilon_0 \frac{\left(\varphi - \varphi_0\right)^2}{2l_D^2} n_1 \right) ds\,,$$

$$\Rightarrow J = \int_s \left(-\frac{D_1 E_1}{2} n_1 + \varepsilon\varepsilon_0 \frac{\left(\varphi - \varphi_0\right)^2}{2l_D^2} n_1 \right) ds\,.$$

Also, from the geometry, it can be seen that for a particular path parallel to the membrane surfaces, the integrand is independent of the area, allowing us to write,

$$\Rightarrow J = \left(-\frac{D_1 E_1}{2} n_1 + \varepsilon\varepsilon_0 \frac{\left(\varphi - \varphi_0\right)^2}{2l_D^2} n_1 \right) A,$$

Where, A is the area of the membrane under consideration. Also J has dimensions of force, so force per unit area of the membranes is given as,

$$\Rightarrow f = -\frac{\varepsilon\varepsilon_0}{2}\left(\frac{d\varphi}{dx}\right)^2 n_1 + \frac{\varepsilon\varepsilon_0}{2l_D^2}\left(\varphi - \varphi_0\right)^2 n_1 . \qquad \text{A2.96}$$

Electrostatics between the inner surface of plasma membrane and outer surface of the vesicle

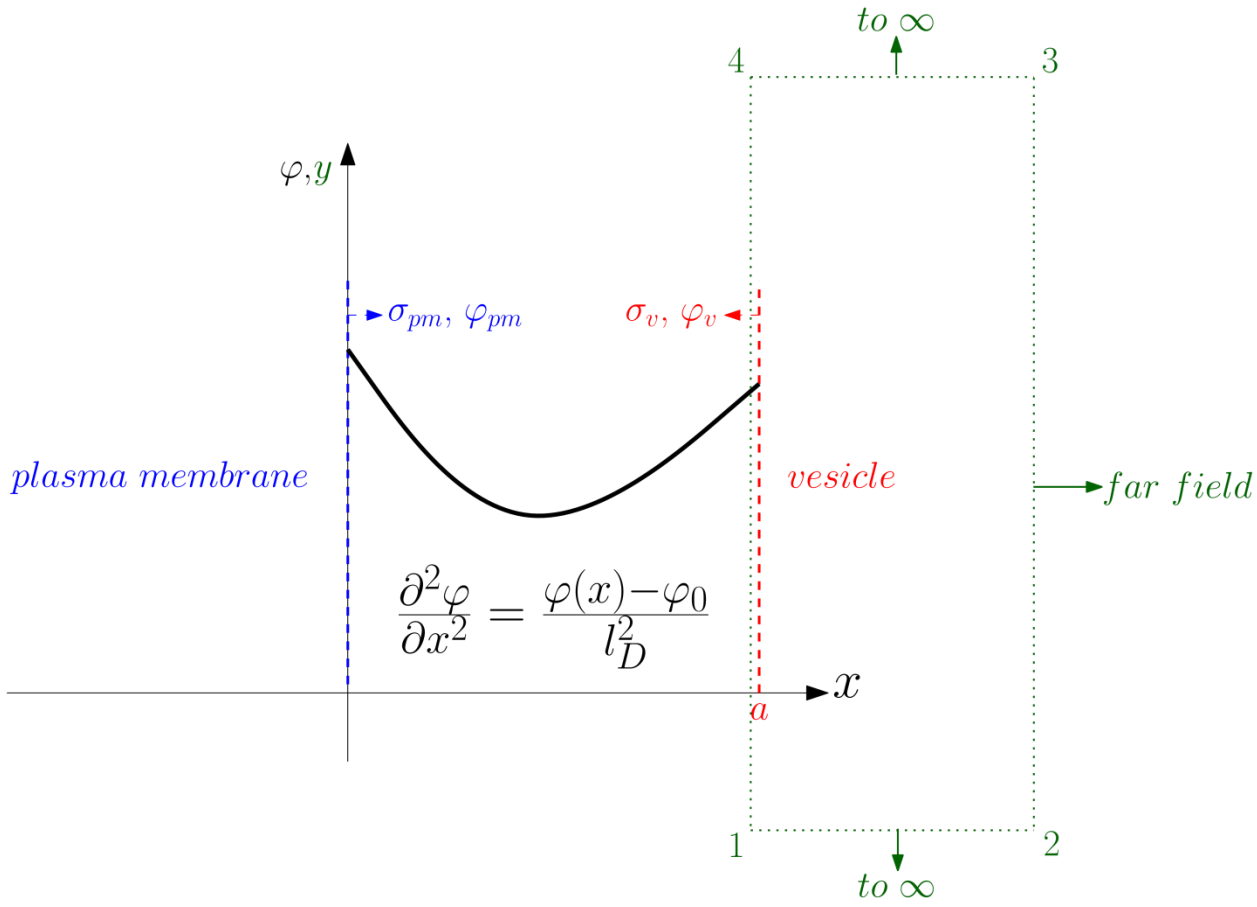

Fig A2.4: electrostatics between plasma membrane and vesicle

There are two possible scenarios when solving the DH equation. In the case of constant potential surfaces, the charge densities redistribute (for example K^+ ions) or degree of ionization (of lipid heads) varies, to maintain the potential value. The other case of constant surface charge density, involves fully ionized lipid heads with a fixed charge. These two cases are the representative of the possible extreme scenarios for a real lipid bilayer system. Constant potential represents, relatively softer electrostatic interactions compared to the constant charge density case. In the

present article we assume constant surface charge densities, to account for high forces from electrostatics.

Known parameters:

Debye length, $l_D = \sqrt{\frac{\varepsilon\varepsilon_0 k_B T}{2e^2 z^2 c_0}}$,

surface charge on vesicle, σ_v,

surface charge on inner surface of plasma membrane, σ_{pm}.

(We need to figure out an alternate parameter for σ_{pm}, as it is not known experimentally.)

Governing equation:

$$\frac{\partial^2 \varphi}{\partial x^2} = \frac{\varphi(\mathrm{x}) - \varphi_0}{l_D^2} \qquad \text{A2.97}$$

Non-dimensionalisation:

Length in non-dimensionalized by l_D

$$\bar{x} = \frac{x}{l_D}$$

and is done for potential by, $\frac{\sigma_v l_D}{\varepsilon\varepsilon_0}$,

$$\bar{\varphi} = \varphi\left(\frac{\varepsilon\varepsilon_0}{\sigma_v l_D}\right).$$

The non-dimensional equation is,

$$\frac{\partial^2 \bar{\varphi}}{\partial \bar{x}^2} = \bar{\varphi}(\bar{x}) - \bar{\varphi}_0. \qquad \text{A2.98}$$

The solution to equation is given by,

$$\bar{\varphi}(\bar{x}) = p\sinh(\bar{x}) + q\cosh(\bar{x}) + \bar{\varphi}_0 \qquad \text{A2.99}$$

Boundary conditions:

We have two charge boundary conditions at $x = 0$ and a, as

$$-\epsilon\epsilon_0 \left.\frac{\partial\varphi}{\partial x}\right|_{x=0} = \sigma_{pm} \text{ and } \epsilon\epsilon_0 \left.\frac{\partial\varphi}{\partial x}\right|_{x=a} = \sigma_v, \qquad \text{A2.100}$$

this, in non-dimensional forma can be written as,

$$-\left.\frac{\partial\bar{\varphi}}{\partial\bar{x}}\right|_{\bar{x}=0} = \frac{\sigma_{pm}}{\sigma_v} \text{ and } \left.\frac{\partial\bar{\varphi}}{\partial\bar{x}}\right|_{\bar{x}=\bar{a}} = 1. \qquad \text{A2.101}$$

Solution:

After applying the boundary conditions in eq. 13,

$$\bar{\varphi}(\bar{x}) = -\frac{\sigma_{pm}}{\sigma_v}\sinh(\bar{x}) + \frac{\cosh(\bar{x})}{\sinh(\bar{a})}\left[1 + \frac{\sigma_{pm}}{\sigma_v}\cosh(\bar{a})\right] + \bar{\varphi}_0. \qquad \text{A2.102}$$

Force between the membranes:

Based on the result of force per unit area expression, for two charged surfaces in an electrolyte [3], we have,

$$f = -\frac{\varepsilon\varepsilon_0}{2}\left(\frac{d\varphi}{dx}\right)^2 n_1 + \frac{\varepsilon\varepsilon_0}{2l_D^2}\left(\varphi - \varphi_0\right)^2 n_1. \qquad \text{A2.104}$$

In the non-dimensional form it can be written as,

$$\frac{\varepsilon\varepsilon_0}{\sigma_v^2} f = -\frac{1}{2}\left(\frac{\partial\bar{\varphi}}{\partial\bar{x}}\right)^2 n_1 + \frac{\left(\bar{\varphi}-\bar{\varphi}_0\right)^2}{2} n_1,$$

$$\Rightarrow \bar{f} = -\frac{1}{2}\left(\frac{\partial\bar{\varphi}}{\partial\bar{x}}\right)^2 n_1 + \frac{\left(\bar{\varphi}-\bar{\varphi}_0\right)^2}{2} n_1, \qquad \text{A2.105}$$

where, $\bar{f} = \frac{\varepsilon\varepsilon_0}{\sigma_v^2} f$.

The net force calculation is done around a loop which surrounds the vesicle membrane, as shown in Fig. A2.4. The force coming from the sides 12 and 34 is zero, as $n_1 = 0$ along the branches 12 and 34.

$\bar{f}_{12} = \bar{f}_{34} = 0.$

Along the far field branch 23, $n_1 = 1$, but $\bar{\varphi} = \bar{\varphi}_0$.

$$\Rightarrow \bar{f}_{23} = 0 + \frac{\left(\bar{\varphi}_0-\bar{\varphi}_0\right)^2}{2} = 0.$$

Along the side 41, we know the expression of the potential. Thus, net force on the vesicle membrane piece is along x direction, and is given by,

$\bar{f} = \bar{f}_{14}.$

For the sake of simplicity, we just say that,

$$\bar{\varphi}\left(\bar{x}\right) = p\sinh(\bar{x}) + q\cosh(\bar{x}) + \bar{\varphi}_0,$$

where, $p = -\frac{\sigma_{pm}}{\sigma_v}$ and $q = \frac{1}{\sinh(\bar{a})}\left[1 + \frac{\sigma_{pm}}{\sigma_v}\cosh(\bar{a})\right]$. Also $n_1 = -1.$

Next, we evaluate,

$$\bar{f}_{14} = \frac{1}{2}\left[p^2 \cosh^2 \bar{x} + q^2 \sinh^2 \bar{x} + 2pq \cosh \bar{x} \sinh \bar{x} \right]$$
$$-\frac{1}{2}\left[p^2 \cosh^2 \bar{x} + q^2 \sinh^2 \bar{x} + 2pq \cosh \bar{x} \sinh \bar{x} \right]$$
$$\Rightarrow \bar{f}_{14} = \frac{1}{2}\left[p^2 - q^2 \right] = -\frac{1}{2\sinh^2 \bar{a}}\left[1 + \frac{\sigma_{pm}^2}{\sigma_v^2} + 2\frac{\sigma_{pm}}{\sigma_v} \cosh \bar{a} \right].$$

Thus, we have the net force on the vesicle membrane as,

$$\bar{f} = -\frac{1}{2\sinh^2 \bar{a}}\left[1 + \frac{\sigma_{pm}^2}{\sigma_v^2} + 2\frac{\sigma_{pm}}{\sigma_v} \cosh \bar{a} \right], \qquad \text{A2.106}$$

this, in dimensional form can be written as,

$$f = -\frac{1}{2\varepsilon\varepsilon_0 \sinh^2 \left(a / l_D \right)}\left[\sigma_v^2 + \sigma_{pm}^2 + 2\sigma_v \sigma_{pm} \cosh \left(a / l_D \right) \right]. \qquad \text{A2.107}$$

Effect of surface charge on membrane deformation

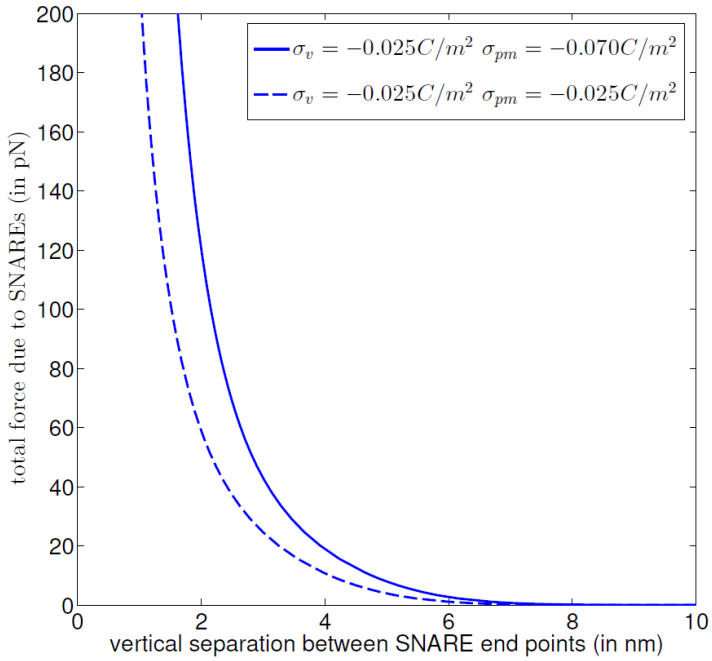

Fig A2.5: force versus SNARE end displacements for different charge densities

With SNARE-machinery force always normal to deformed vesicle and neuron base

Here we present our numerical results obtained under the assumption that the SNARE-machinery force is always normal to the deformed vesicle and the neuron base. Overall, the conclusion is that there is not much difference between the two loading conditions, which is because of the small tangential component of the SNARE-machinery force under the equal and opposite loading case. We have not considered the effect of the concentrated moment at point of load application. The reason to

ignore the moment is to avoid the discontinuity in the curvature of the shape, which is difficult to handle numerically.

Varying force magnitude

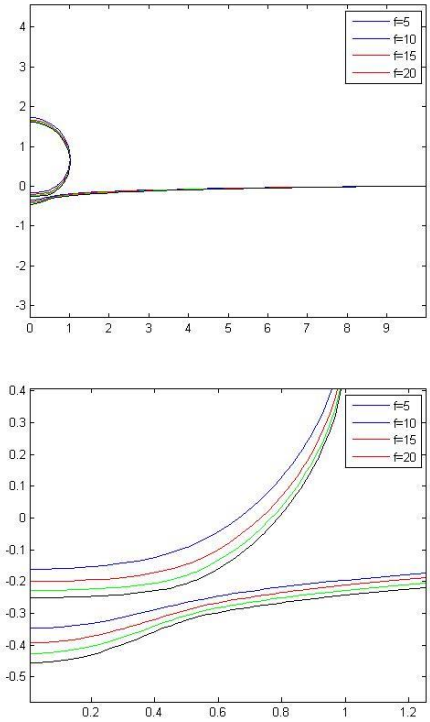

Fig. A2.6: Deformed shape of vesicle with different value of magnitude of force applied by protein, position of protein S=pi/6, deformable substrate.

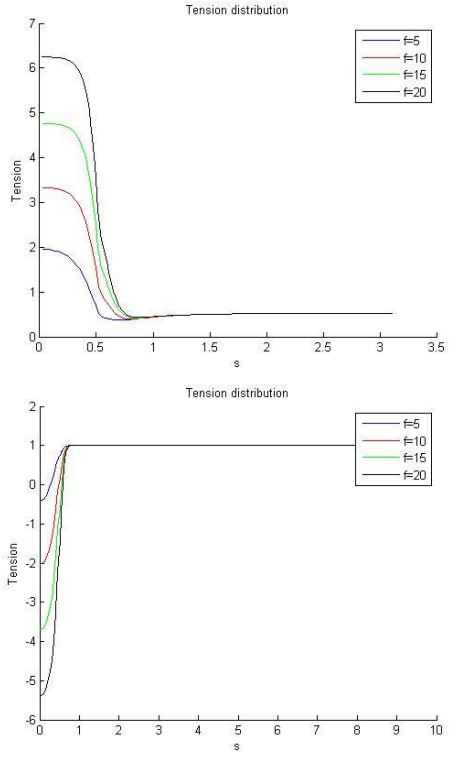

Vesicle Substrate

Fig. A2.7: In-plane tension distribution in vesicle and substrate with different value of magnitude of force applied by protein, position of protein S=pi/6, deformable substrate.

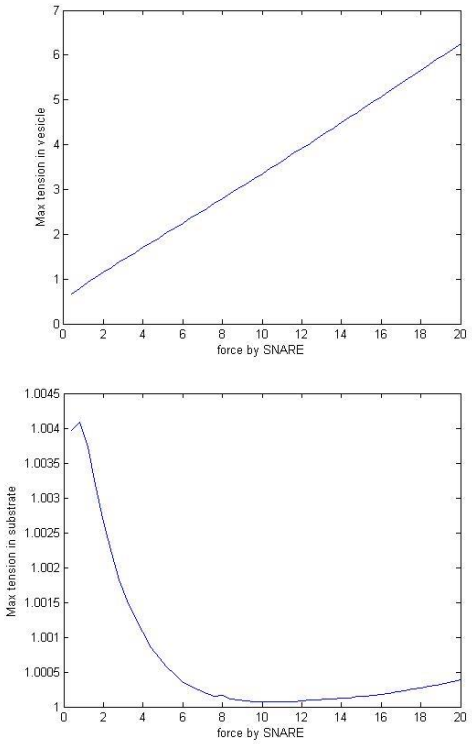

Vesicle Substrate

Fig. A2.8: Variation of peak of tension in vesicle and substrate with respect to value of magnitude of force applied by protein, position of protein S=pi/6, deformable substrate.

Varying force magnitude

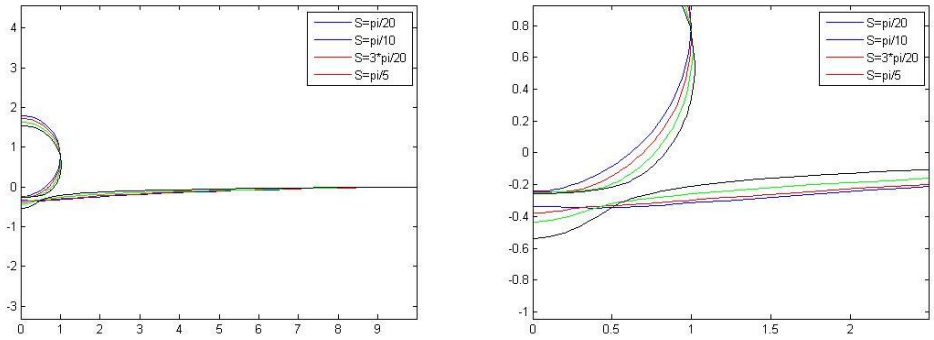

Fig. A2.9: Deformed shape of vesicle with different position of protein, f=20, deformable substrate.

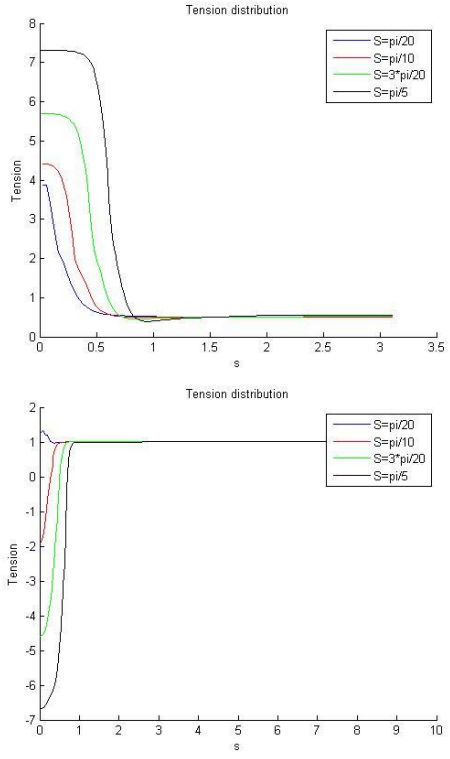

Vesicle Substrate

Fig. A2.10: In-plane tension distribution in vesicle and substrate with different position of protein, f=20, deformable substrate.

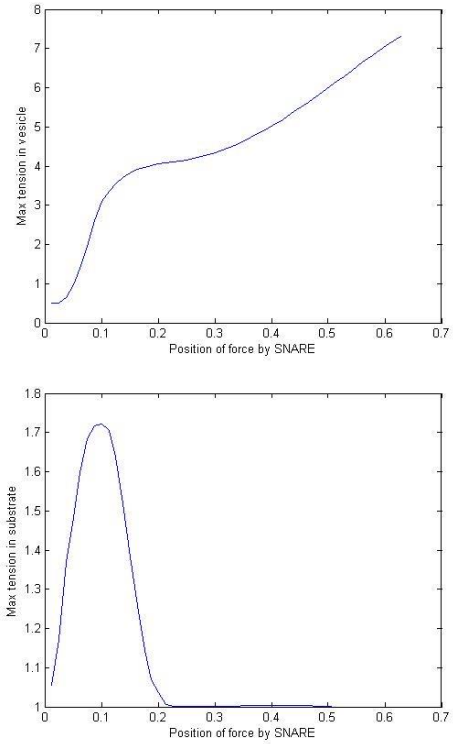

Vesicle Substrate

Fig. A2.11: Variation of peak of tension in vesicle and substrate with respect to position of protein, f=20, deformable substrate.

Varying force location

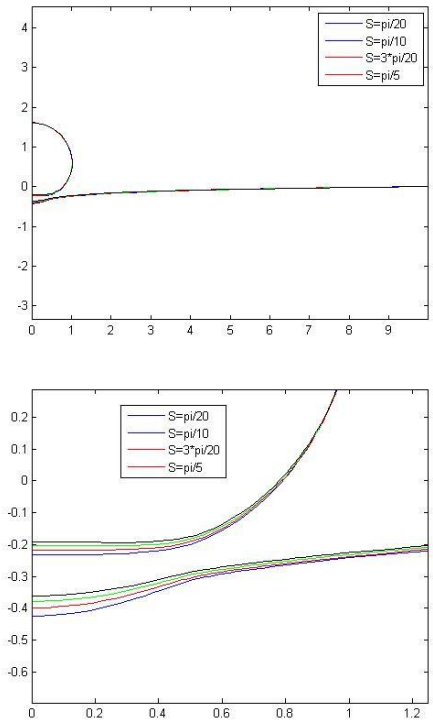

Fig. A2.12: Deformed shape of vesicle with different pretension of substrate, f=20, position of protein S=pi/6, deformable substrate.

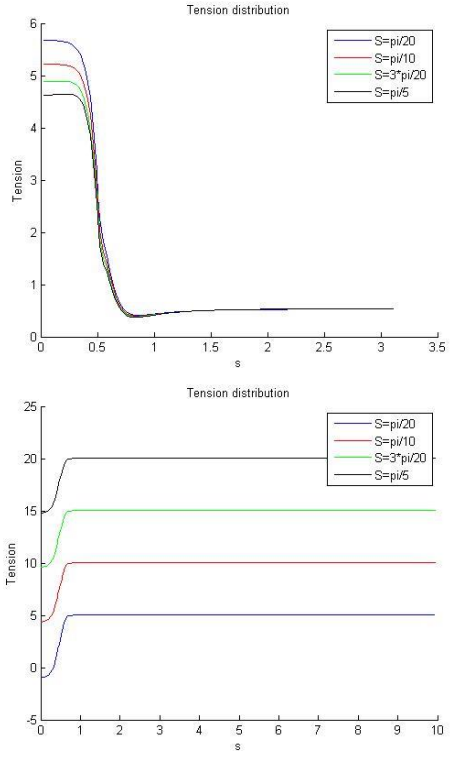

Vesicle Substrate

Fig. A2.3: In-plane tension distribution in vesicle and substrate with different pretension of substrate, f=20, position of protein S=pi/6, deformable substrate.

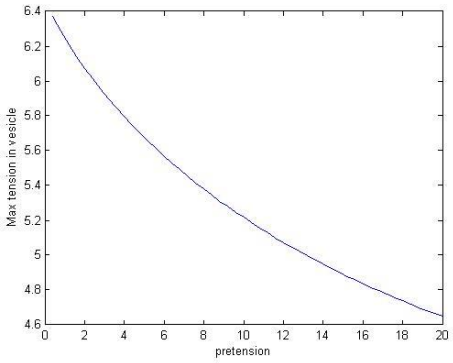

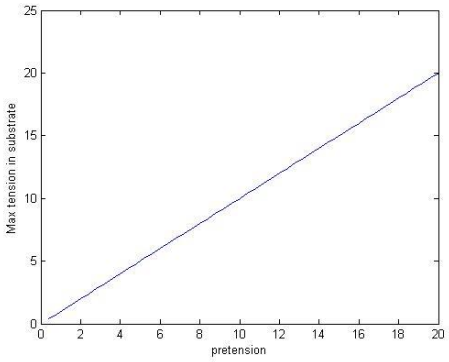

Vesicle Substrate

Fig. A2.4: Variation of peak of tension in vesicle and substrate with respect to pretension of substrate, f=20, position of protein S=pi/6, deformable substrate.

Effect of Hemi-fusion

Fig A2.14 shows the deformed shape of the two membranes after turning off the electrostatic repulsion in a small region $[\bar{S}_H, \bar{S}_L]$ at the point of closest approach $\bar{S}_L$, where $\bar{S}_H < \bar{S}_L$. We use $\bar{L}_H = \bar{S}_0 - \bar{S}_H$ as a length scale to specify the size of the hemi-fused region. The results in Fig A2.14 are obtained using 4 different $\bar{L}_H$. The largest $\bar{L}_H$ corresponds to $\bar{S}_H = 0$ where the repulsive force in the region between bottom of the vesicle and the point of closest approach is turned off. We also plot the deformation without hemi-fusion as a comparison. Our results show that turning off the repulsion brings the hemi-fused region into closer contact. For the case of $\bar{S}_H = 0$, the two membranes actually interpenetrate, and at this point our simulation breaks down.

The distributions of tension in the vesicle and plasma membrane are shown in Fig A2.15. Note that as the hemi-fusion region grows (increasing $\bar{L}_H$), the tension in the hemi-fused region increase significantly. This increase in tension may potentially result in the in-plane rupture of the membrane leading to the formation of a hole between vesicle and plasma membrane.

Next, we analyze the effect of variation of different parameters on the membrane deformations, before and after hemifusion. Evident from the results in Fig A2.16, as we increase the strength of line force, the maximum tension in the vesicle and maximum compression in the plasma membrane increases. Thus, full hemifusion intensifies the overall deformation of the system. In further studies of the effect of full

hemifusion, while varying pretension (Fig A2.17), force location (Fig A2.18) and vesicle pressure (Fig A2.19), the similar behavior is observed. In all the cases the deformation is more severe than the case of without hemifusion. From all these observations, we can propose that the hemifusion propagation increases the chances of membrane rupture if the conditions are sufficient to make it happen. Eventually a fusion pore formation is possible in the hemifused region, where tension is highest.

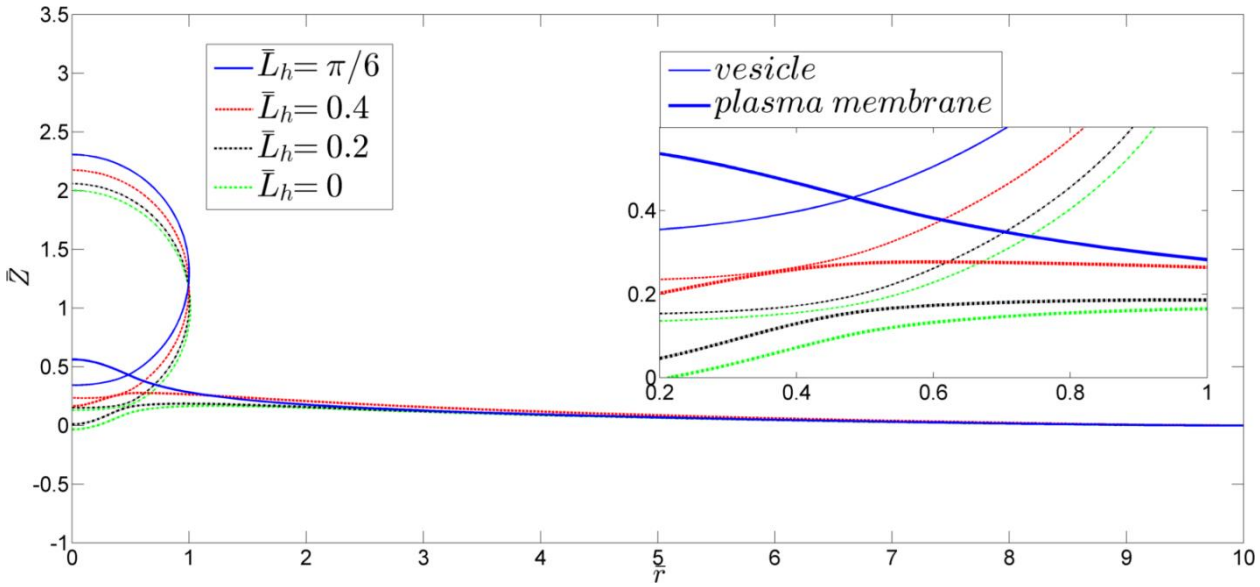

Fig A2.15 : Deformed shape of the vesicle with different hemi-fused region, assuming that the hemi-fused region is propagated inward. The parameters are: load application point, $\bar{S}_0 = \pi/6$**, pretension in plasma membrane,** $\bar{T}_0 = 1$**, line force magnitude** $\bar{F} = 20$ **and vesicle pressure,** $\bar{p}_0 = 1$**. Full hemi-fusion is defined as whole region from** $\bar{S} = \pi/6$ to 0

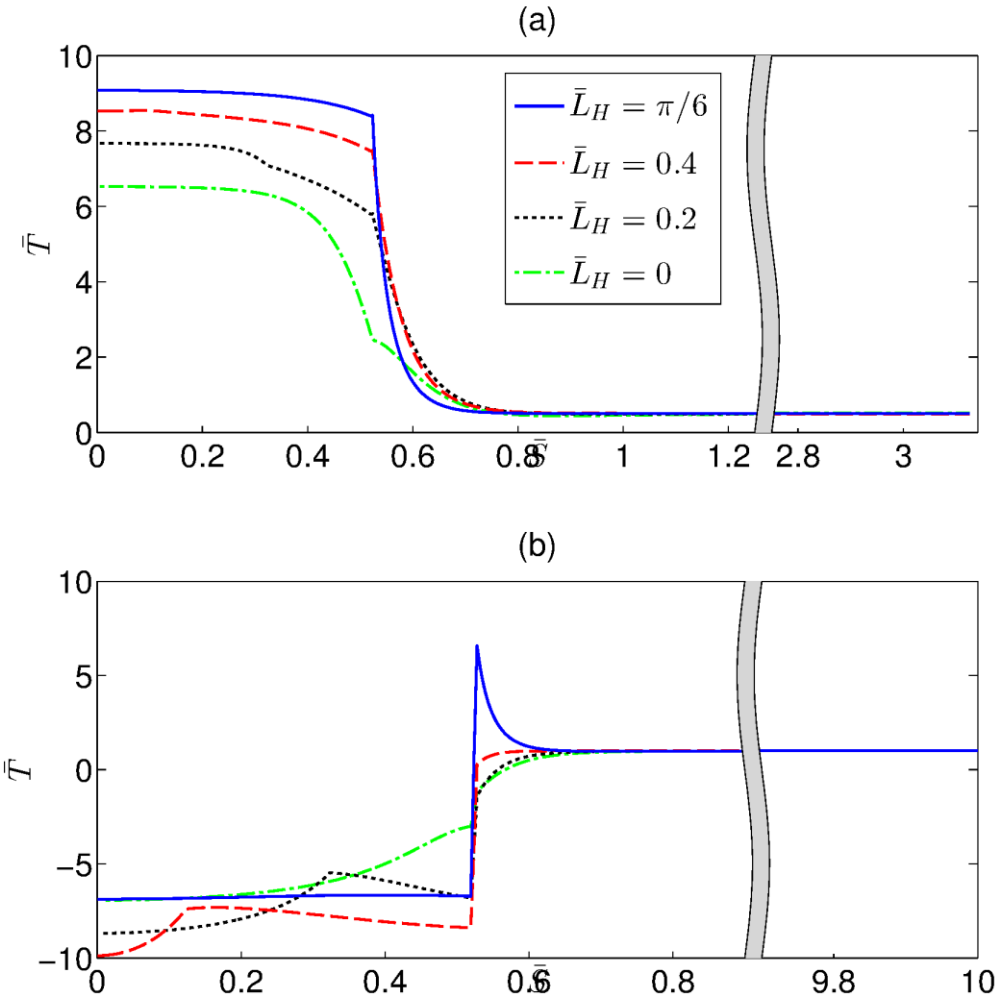

Fig A2.16: In-plane tension distribution in the vesicle and substrate with different hemi-fused regions, assuming that the hemi-fused region is propagated inward.

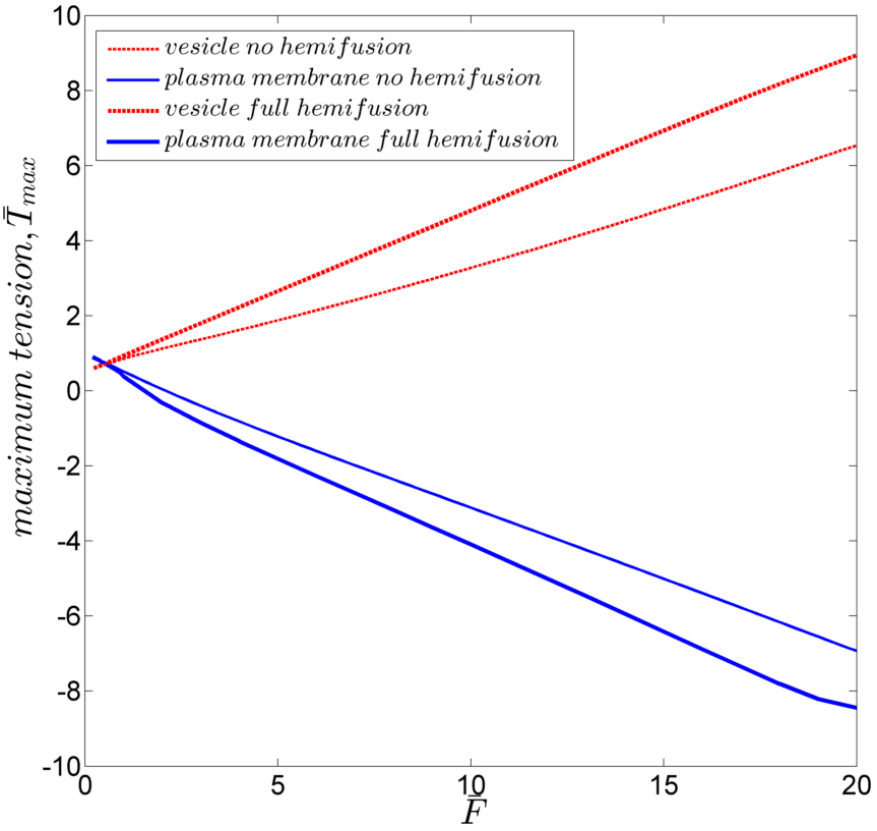

Fig A2.17: Variation of peak of tension in the vesicle and substrate with respect to the concentrated load magnitude. The parameters are: load application point, $\bar{S}_0 = \pi/6$**, pretension in plasma membrane,** $\bar{T}_0 = 1$ **and vesicle pressure,** $\bar{p}_0 = 1$**. Full hemi-fusion is defined as whole region from** $\bar{S} = \pi/6$ to 0

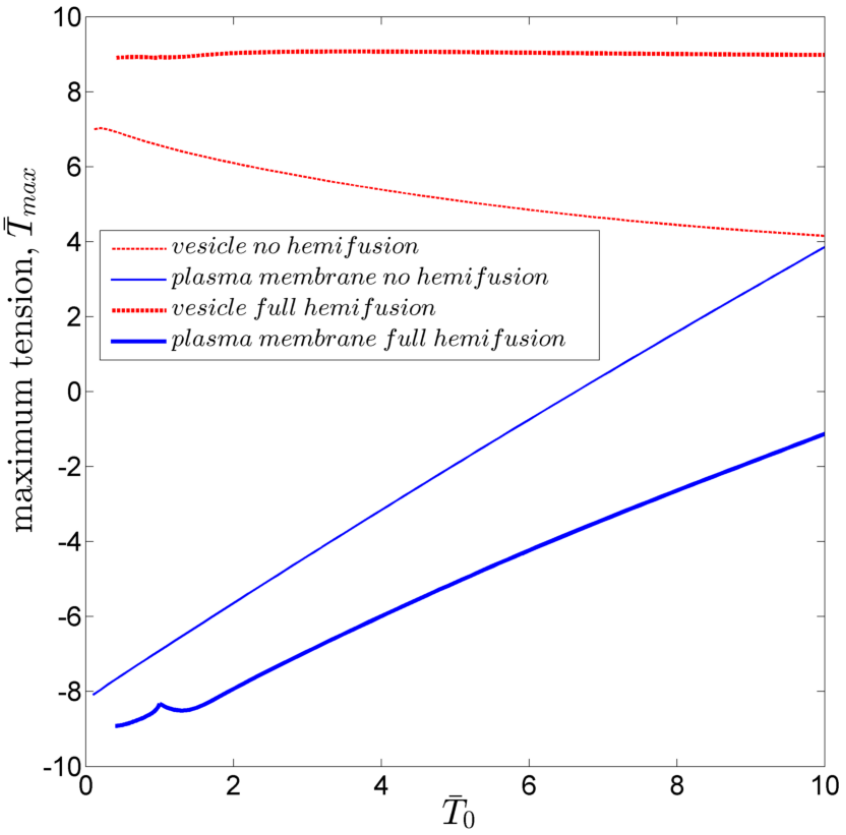

Fig A2.18: Variation of peak of tension in the vesicle and substrate with respect to the plasma membrane pretension. The parameters are: load application point, $\bar{S}_0 = \pi/6$**, line force magnitude,** $\bar{F} = 20$ **and vesicle pressure,** $\bar{p}_0 = 1$**. Full hemi-fusion is defined as whole region from** $\bar{S} = \pi/6$ to 0

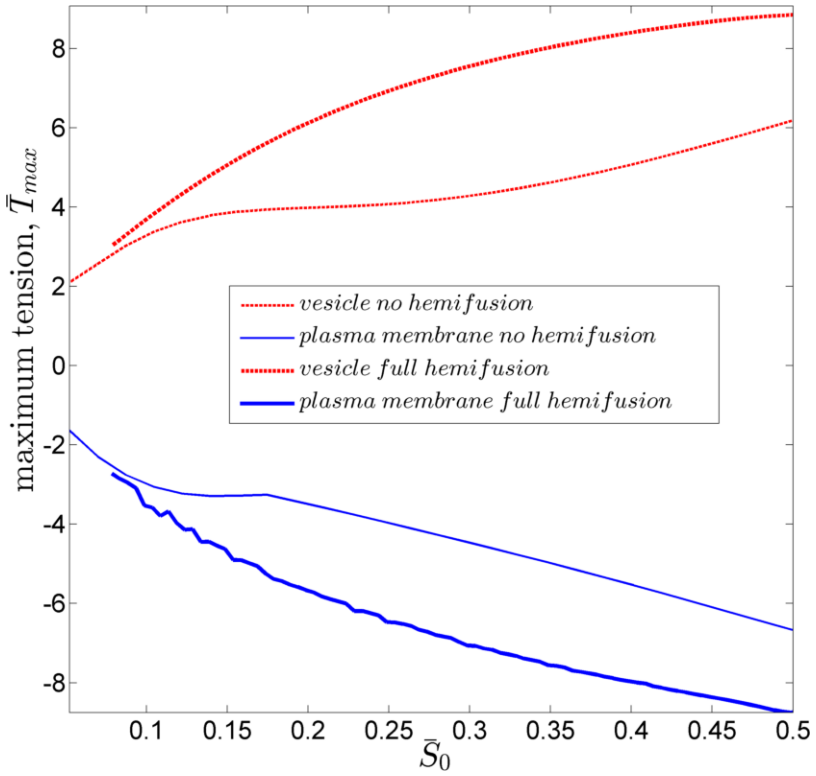

Fig A2.19: Variation of peak of tension in the vesicle and substrate with respect to the position. The parameters are: line force magnitude, $\bar{F} = 20$**, pretension in plasma membrane,** $\bar{T}_0 = 1$ **and vesicle pressure,** $\bar{p}_0 = 1$**. Full hemi-fusion is defined as whole region from** $\bar{S} = \bar{S}_0$ to $\bar{S} = 0$

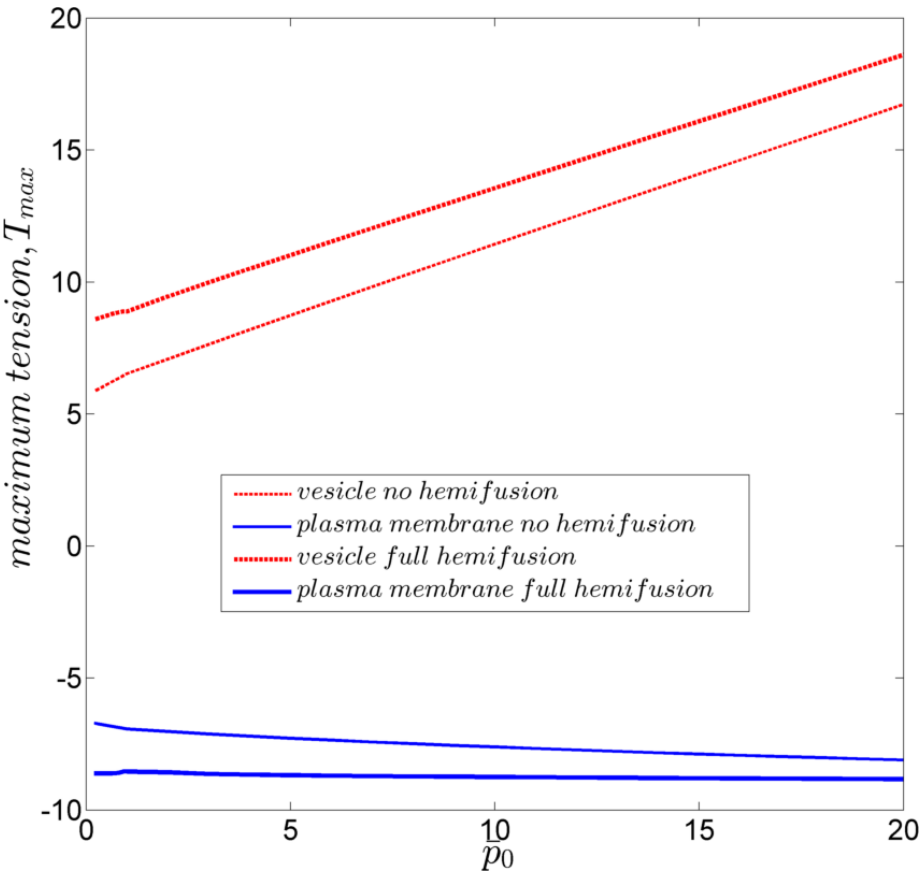

Fig A2.20: Variation of peak of tension in the vesicle and substrate with respect to the pressure inside the vesicle. The parameters are: load application point, $\bar{S}_0 = \pi/6$, line force magnitude, $\bar{F} = 20$ and pretension in plasma membrane, $\bar{T}_0 = 1$. Full hemi-fusion is defined as whole region from $\bar{S} = \pi/6$ to 0

Bibliography

[1] Pearson C., 1990, *Handbook of Applied Mathematics*, Springer.

[2]C. Khripin, A. Jagota, and C.-Y. Hui, "Electric fields in an electrolyte solution near a strip of fixed potential.," *J. Chem. Phys.*, vol. 123, no. 13, p. 134705, Oct. 2005.

[3]M. Bykhovskaia, A. Jagota, A. Gonzalez, A. Vasin, and J. T. Littleton, "Interaction of the complexin accessory helix with the C-terminus of the SNARE complex: molecular-dynamics model of the fusion clamp.," *Biophys. J.*, vol. 105, no. 3, pp. 679–90, Aug. 2013.

Chapter 3

Proteins of SNARE family play an inevitable role in the process of neurotransmission. Starting with the docking of the synaptic vesicle to the fusion pore formation leading to the release of neurotransmitter into the synaptic cleft, the complete pathway is majorly governed by SNARE proteins. Four helices from these proteins zip together to form SNARE complex. The force generated in the process of zippering counters the repulsive interactions between the membranes. These repulsive interactions arise mainly due to the electrostatic interactions between the lipid membranes and hydration pressure. The electrostatic interactions are a result of the charged/polar lipid molecule which constitutes the lipid membranes. For membrane fusion it is required that the water between the two lipid membranes is squeezed out and the lipid molecules from the two lipid bilayer membranes can see each other. The hydration pressure is the resistance against squeezing the water out of the gap between the synaptic vesicle and neuron plasma membranes. The water molecules are hydrogen bonded to charged/polar lipid heads in the membranes making it difficult to expose the lipid molecules from one lipid membrane to another. The balance between the SNARE complex force and repulsive interactions determines the final state of the docked synaptic vesicle. The deformation and state of stress in the membrane is the crucial for the membrane fusion and pore formation leading to the release of neurotransmitter into the synaptic cleft.

In the present chapter we present a study which combines a Coarse Grained Molecular Dynamics (CGMD) simulation of SNARE proteins with a continuum mechanics based model of lipid membranes. The CGMD simulation of SNARE complex is developed

by Prof. Anand Jagota and Nicole Fortoul at Lehigh University. The CGMD SNARE model has been calibrated against the experimental studies done on single SNARE unzippering. From this calibration the peak SNARE protein structural parameters are tuned so that the peak force matches with the experimental values. The continuum model of the lipid membrane used in the present work is a slightly improved version from the model presented in Chapter 2. The current continuum model takes into account both the hydration pressure and electrostatics into account to model the repulsive interactions.

In the following sections we describe the modeling of the SNARE complex and lipid membranes. That description is followed by combining the force displacement curves obtained from two systems to obtain an equilibrium configuration of the docked vesicle. This equilibrium configuration determines the minimum gap between the two membrane structures. This location of the minimum gap is expected to be the site where fusion is expected to initiate. We analyze how the minimum gap between the two membranes changes by varying the number of SNARE complex in the synaptic vesicle docking. We conclude that there is optimality in terms of number of SNARE complexes that can be employed to lead a docked vesicle towards membrane fusion and subsequently towards a fusion pore formation.

3.1 ABSTRACT

Synaptic transmission requires that vesicles filled with neurotransmitter molecules be docked to the plasma membrane by the SNARE protein complex. The SNARE complex applies attractive forces to overcome the long-range repulsion between the

vesicle and membrane. To understand how the balance between the attractive and repulsive forces defines the equilibrium docked state we have developed a model that combines the mechanics of vesicle/membrane deformation with a new coarse-grained model of the SNARE complex. The coarse-grained model of the SNARE complex is calibrated by comparison with all-atom molecular dynamics simulations as well as by force measurements in laser tweezer experiments. The model for vesicle/membrane interactions includes the forces produced by membrane deformation and hydration or electrostatic repulsion. Combining these two parts, the coarse-grained model of the SNARE complex with membrane mechanics and electrostatics, we study how the equilibrium docked state varies with the number of SNARE complexes. We find that a single SNARE complex is able to bring a typical synaptic vesicle to within a distance of about 3 nm from the membrane. Further addition of SNARE complexes shortens this distance, but an over-docked state of more than 4-6 SNAREs actually increases the equilibrium distance.

3.2 INTRODUCTION

The SNARE (soluble NSF-attachment protein receptors) (1, 2) complexes are the core protein machinery involved in synaptic vesicle docking and fusion. SNARE proteins form a link between vesicles and the plasma membrane, providing a mechanism for zippering the two together. The transmembrane vesicle associated protein synaptobrevin (Syb or v-SNARE) forms a four-helical bundle with the proteins SNAP-25 and the transmembrane protein syntaxin (Syx), which are attached to the neuronal plasma membrane and termed the "t-SNARE". SNAP-25 contributes two

helices (SN1 and SN2) to the bundle, while both Syx and Syb contribute one helix each (3, 4). During exocytosis the vesicles are first tethered or targeted towards the plasma membrane (>25nm (5)), then they are docked at the plasma membrane with the help of the adhesive forces provided by SNAREs. After docking, priming occurs which finally leads up to vesicle to membrane fusion (1). The zippering of the SNARE bundle is thought to provide the necessary force to bring the vesicle in proximity to the plasma membrane by overcoming the hydration or electrostatic repulsion between the two.

The process of synaptic vesicle docking and fusion can be viewed as deformation of a mechanical system, in which a synaptic vesicle, a nearly spherical lipid bilayer shell, is brought in proximity to the plasma membrane, a nearly flat lipid bilayer, under the influence of the attractive forces exerted by the SNARE complex. Key structural characteristics of the SNARE bundle have been determined experimentally, including its x-ray crystal structure (6) and the location of the layers thought to be essential to SNARE's function (7), which has been confirmed through single molecule force experiments (8). All-atom simulations have been performed to analyze the structural aspects of the SNARE bundle including detailed interactions between the different helices (9) as well as to investigate the effects of oxidation and reduction of the SNAP25 linker domain on the formation of the SNARE bundle (10). Some all-atom simulation work has been done on the unzippering of the SNARE bundle (11), however, time constraints prevent simulations for large displacements and longer time scales. In an effort to overcome timescale limitations, some coarse-grained (CG)

simulations have been performed (12, 13). Force-fields for CG simulations have been developed (14). However, to suit a wide range of applications, these force fields still need to be refined (15). Relatively little has been done on coupling the SNARE unzipping process to the vesicle-plasma membrane behavior to address questions including that of how docking depends on the number of SNAREs. This problem is difficult because it must capture large length scale deformations and electrostatics in the vesicle-plasma membrane system as well as amino acid-level chemical specificity that are essential to the functioning of the SNARE bundle.

There is significant debate about how many SNARE complexes are required to make synaptic fusion happen. Earlier studies suggested that 5 to 8 SNARE complexes form the fusion pore (16). However, recent studies suggest a smaller number of SNARE complexes. Thus, it was suggested recently that a single SNARE complex can trigger fusion, (17), while stating the fact that the fusion rate increases with the number of SNARE's. In (18), it has been proposed that two Syb units are required for fusion, based on fluorescence response of tagged Syb. The work done in (19) suggests that three SNARE units are needed to carry out the fusion, on the basis of fusion rate. At the same time, studies performed on model systems *in vitro* suggest numbers ranging between 5-11 (20).

To investigate how the number of SNARE complexes affects vesicle docking, we developed a continuum model of the lipid bilayers and combined it with a CG model for the SNARE which includes chemical specificity. Specifically, the proteins in the

SNARE bundle are represented by an alpha-carbon based CG model that includes both structural and chemical specificity by employing an elastic network model (ENM) (21, 22) and Miyazawa and Jernigan (MJ) contact energies (23–25), respectively. The SNARE CG model is calibrated to match the peak unzipping force determined by Gao et al. (8), and is used to calculate a force displacement curve for the unzipping process, along with snapshots of corresponding structures that provide information about the unzipping pathway. The continuum model for bilayer deformation is based on lipid membrane theory developed in Jenkins et al. (26) and is an extension of work done in Long et al. (27). It computes the force required to counter the vesicle-membrane repulsion, bringing the vesicle to a given distance from the membrane while taking full account of the vesicle and membrane deformation. Balancing the SNARE-induced attraction against the vesicle-membrane hydration or electrostatic repulsion provides us with information about the equilibrium gap between the two membranes for a given number of SNAREs. Based on this information we study the effect of the number of SNAREs from the point of view of the mechanics of the process.

3.3 MATERIALS AND METHODS

3.3.1 All Atom (AA) Simulations

We conducted all-atom molecular simulations of SNARE helices in order to obtain some of the parameters for the SNARE CG model. AA simulations of the four individual helices as well as the full SNARE bundle were performed using the GROMACS molecular simulation package (28) and the CHARM22 forcefield (29).

The starting structures for the 4 individual helices and the full SNARE bundle were extracted from the final timestep of a 40 ns AA simulation with initial configuration given by the high resolution x-ray structure 1N7S (7, 11). (See Supporting Material for a discussion.) For each set of runs, the corresponding structure was solvated in a waterbox (70 Å x 150 Å x 70 Å), and potassium ions were added to neutralize the overall charge. Additional potassium and chloride ions were added so that there was a 150mM concentration of KCl to mimic physiological conditions (30). All bonds were constrained. Dynamics were run at 300 K first using an NVT ensemble for 100 ps followed by NPT for 100 ps using the Parrinello-Rahman barostat. Five sets of 40 ns-long runs were conducted with a timestep of 2 fs for Syb, Syx, SN1, SN2, and the SNARE bundle. Computations were performed at the Texas Advanced Computing Center (TACC) through XSEDE resources.

3.3.2 SNARE Coarse-Grained Model

A principal result of this work is the development of a CG model for the SNARE complex. Our goal has been to make it as simple as possible while still retaining the identity of individual residues. As shown in Fig. 3.1 *A*, in our SNARE model every residue is represented by a bead located at the alpha carbon of that residue.

The size and mass of each bead are equivalent to the Van der Waals radius (31) and mass (31) of the bead's corresponding residue. Two major types of interactions were accounted for in this CG model, those within individual helices and those between them. An elastic network model (ENM) (21, 22) is used to represent the intra-helical

bonds and interactions that maintain the individual helical structure as shown in Fig. 3.1 *A*. Pairs of beads within the cutoff distance, R_c, on the same helix are said to be "in contact" and are connected by a harmonic spring with the energy potential

$$u_{spring} = \frac{1}{2} k_s (r - r_0)^2 \qquad 3.1$$

where k_s is the spring constant, r is the distance between the two beads, and r_0 is the natural length of the spring. From the 40 ns long individual helix AA simulations, it was observed that the natural state of each individual helix was a relatively straight conformation compared to the helices in the SNARE x-ray crystal structure. (The mean curvature of the helices in the SNARE bundle (3.11×10^7 1/m) is three times as large as that of the individual helices (1.03×10^7 1/m), see Supporting Material)). Because these straightened-out conformations represent the 'natural' or relaxed state of the helices, they were used to construct the ENM. This is important because, as the helices unzip from the main bundle and break their helix-helix contacts, they revert back to their natural straight conformation, releasing elastic energy.

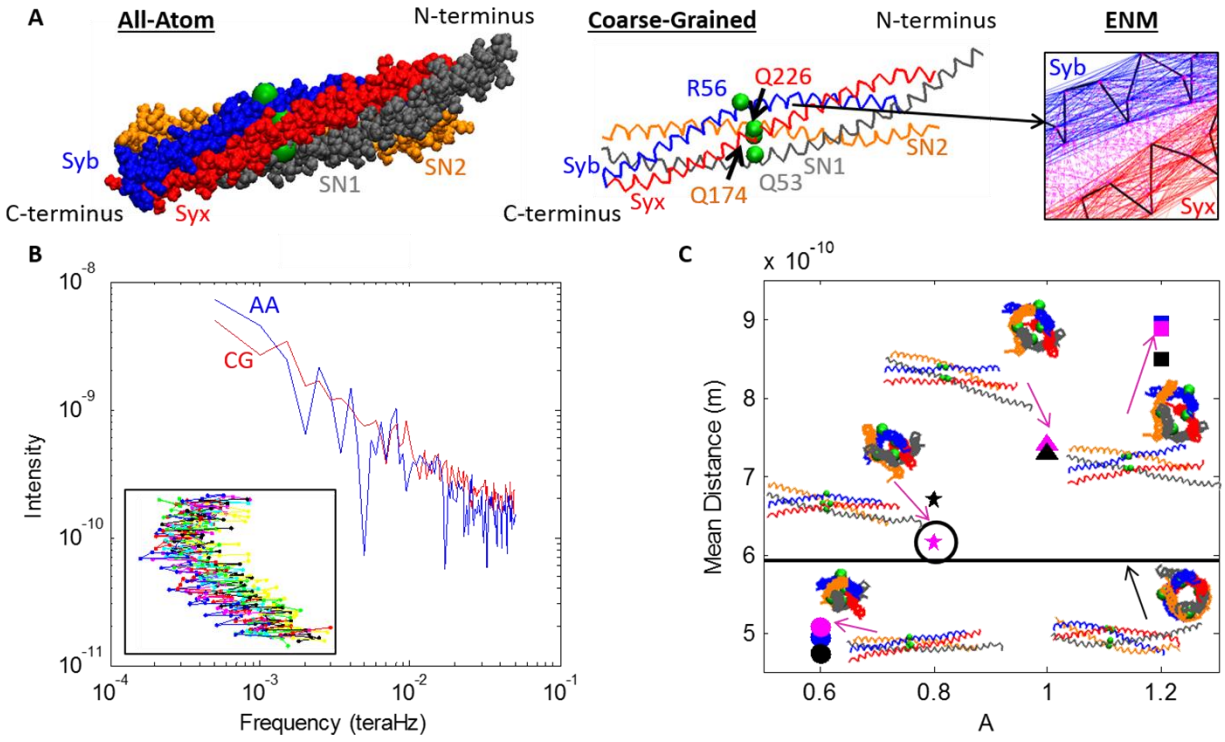

FIGURE 3.1 (*A*) The AA (*left*) and CG (*middle*) representations of the SNARE bundle are shown. Both models include helices Syb, Syx, SN1, and SN2 with each helix contributing one residue to the ionic layer (*beads*): R56, Q226, Q53, and Q174 respectively. The C-terminal ends of Syb and Syx play an integral role in the fusion process in that they attach to the vesicle (Syb) and plasma membrane (Syx). The ENM spring network (*right*) that maintains the individual helical structure is shown for Syb and Syx where the thick lines represents the Cα backbones and the thin lines represent ENM springs. The Miyazawa and Jernigan contacts between Syb and Syx are also represented (*dotted lines*). (*B*) The spectra used to compare the fluctuations of the AA and CG models are shown for Syb. Values for k_s of 0.0963 N/m and R_c of 20 Å were used for the CG model. The inset shows 10 snapshots of Syb during the corresponding AA

simulation. (*C*) Mean distance for different values of parameter *A* along with snapshots of the SNARE bundle. The original crystal is represented by the black line. The version chosen for simulation is marked by the black circle.

The values of k_s for the ENM were chosen by matching the spectrum of fluctuations of the AA simulations and the CG model for each helix independently. For the analysis of individual AA helix simulations, the positions of the alpha carbons were extracted every 10 ps. For each alpha carbon a time series of distance from its average location was calculated. The fast Fourier transform (FFT) was then computed for each bead's time series and averaged over all beads, yielding a single spectrum per helix. In order to make this comparison of the fluctuations, CG simulations were conducted for the 4 individual helices using Langevin dynamics at 300 K for a range of values of k_s. (Details on numerical implementation of the CG simulation are provided in Supporting Material.) The same FFT analysis was conducted for individual helix CG simulations as the AA simulations. The time length of simulations required was determined by conducting a normal modes analysis (NMA) on the CG model of the crystal structure, 1N7S, for all helices individually using different values of k_s. AA simulations were run for 2 ns, which is considerably longer than the characteristic time given as the inverse of the lowest natural frequency (See Table A3.1). In order to best match the fluctuations, the root mean squared deviation (RMSD) between the AA and CG spectra was found for each run. An example of the comparison of both spectra is shown in Fig. 3.1 *B* for Syb with k_s value of 0.0963 N/m. For all helices k_s was varied

between 0.00009 N/m and 0.4816 N/m and the resulting RMSD for all values of k_s are shown in Supporting Material. Based on these data, a value of 0.0963 N/m was chosen for k_s for all four helices.

The second main category of interactions in the CG model is helix-helix interactions that require chemical specificity. These interactions are implemented by utilizing Miyazawa and Jernigan (MJ) contact energies that provide a scalable reference for residue-residue interactions (23–25). Any beads on separate helices interact if they are within the MJ cutoff distance, R_{c_MJ}. To avoid checking the distance between every bead during every timestep, a neighborlist is built every 1000 steps. Any beads on different helices that are within 1.5* R_{c_MJ} of each other are added to the neighborlist. Contacts are determined from the pairs already chosen by the neighborlist.

Following Kim and Hummer (32), the interaction energy ε_{ij} between residues i and j of the SNARE structure is scaled from the Miyazawa and Jernigan contact energies e_{ij} (32).

$$\varepsilon_{ij} = \lambda(e_{ij} - e_0) \qquad 3.2$$

Note that there is no self-interaction, i.e., eq. 3.2 applies only for $i \neq j$. Also, these interactions operate only between residues on different helices, intra-helical interactions being already represented by the ENM. There are two tunable parameters, a scaling parameter, λ, and a shifting parameter, e_0. Throughout the tuning of parameters, e_0 was set to 0. Although it was available as an extra parameter, it was

not found necessary to match the SNARE structure and hence was not used in order to minimize the number of adjustable parameters.

Forces corresponding to the MJ contact energies are implemented using a slightly modified 6-12 LJ potential. The format of this potential varies depending on whether there is attraction or repulsion between these residues as well as if the distance between beads is greater than or less than that the distance at which the potential minimum occurs, r_{ij}^{0}. The sign of ε_{ij} determines whether the interaction between the residues is attractive (negative) or repulsive (positive). The modified Lennard Jones potentials (32) are

If $\varepsilon_{ij} < 0$:

$$u_{ij}(r) = 4\left|\varepsilon_{ij}\right|\left[\left(\frac{\sigma_{ij}}{r}\right)^{12} - \left(\frac{\sigma_{ij}}{r}\right)^{6}\right] \qquad 3.3$$

If $\varepsilon_{ij} > 0$ & $r < r_{ij}^{0}$

$$u_{ij}(r) = 4\left|\varepsilon_{ij}\right|\left[\left(\frac{\sigma_{ij}}{r}\right)^{12} - \left(\frac{\sigma_{ij}}{r}\right)^{6}\right] + 2\varepsilon_{ij} \qquad 3.4$$

If $\varepsilon_{ij} > 0$ & $r \geq r_{ij}^{0}$:

$$u_{ij}(r) = -4\left|\varepsilon_{ij}\right|\left[\left(\frac{\sigma_{ij}}{r}\right)^{12} - \left(\frac{\sigma_{ij}}{r}\right)^{6}\right] \qquad 3.5$$

where r is the distance between the two beads and σ_{ij} is the interaction radii. eq. 3.4 contains a shift in the potential that ensures that repulsive pairs of beads will always repel each other.

The interaction radii is defined as the average of the Van der Waals radii of residues i and j

$$\sigma_{ij} = A * \frac{\sigma_i + \sigma_j}{2} \qquad 3.6$$

where A is available as a tuning parameter and σ_i and σ_j are the Van der Waals radii of residues i and j. In order to match both CG and AA behavior and structure, A was adjusted to match the SNARE bundle width, defined as the diameter of the tube shaped space inside the bundle that can be seen if one looks along the center axis of SNARE. The reference bundle width was found by computing the mean distance of all of the nearest MJ contacts from the SNARE crystal structure determined from 1N7S. These 21 nearest contacts represent the distances between the inner residues of the bundle and therefore the bundle width. Fig. 3.1 *C* shows the mean distance for a few cases. The value of A is directly related to bundle width, and from Fig. 3.1 *C* we chose a value of A as 0.8 to produce a similar mean bundle width to the crystal structure. This value of A corresponds to interaction radii ranging from 3.6 Å for Gly-Gly and 5.44 Å for Trp-Trp (32).

The remaining parameter, λ, controls the strength of inter-helical interactions and was determined by calibrating the results of simulated force-extension behavior of the SNARE complex by the recent experimental study by Gao et al. (8), which provided characteristic forces for the unzipping of the 4 helix SNARE bundle pulled apart in an optical tweezer experiment. The value of λ was calibrated to match the measured

peak force of 14 to 19 pN (specifically, 17.2 pN). For our unzipping simulation the C-teriminal residues of Syx and Syb were each attached to a fixed bead by a spring with a spring constant k_{spb}. Displacement control was used on the bead attached to the C-terminal Syb bead as opposed to the actual Syb C-terminal bead in order to allow for rotation of the SNARE bundle. In order to see how much the orientation of the pulling force on the SNARE matters, the simulations were performed in two ways: by applying a displacement to pulling beads attached to Syb89 and Syx256 through a spring (as shown in the manuscript) and by directly applying displacements to Syb89 and Syx256. (The pulling beads allow for rotation of the SNARE bundle during the simulation and are hence less restrictive.) The results of these simulations were quite similar. To mimic the experimental setup in which the N-termini of Syx and Syb are connected, a FENE bond connecting the N-terminal residues of Syb and Syx was incorporated in the model to represent the additional residues and the N-terminal disulfide bridge that Gao et al.'s (8) experiment included. The potentials used to implement the FENE bond are

If $r(t) < r_{c\_FENE}$:

$$u_{FENE}(t) = -\frac{1}{2} k_F r_0^{\,2} \ln\left(1 - \left(\frac{r(\mathrm{t}) - \Delta}{r_0}\right)^2\right) \qquad 3.7$$

If $r(t) \geq r_{c\_FENE}$:

$$u_{FENE}(t) = -\frac{1}{2} k_F \left(r(\mathrm{t}) - \Delta\right)^2 \qquad 3.8$$

where r is the distance between two bonds at t, r_0 is the maximum bond length, Δ is the resting bond length or, in this case, the original distance between the two beads

(34), and r_{c_FENE} is 0.9* Δ. The value of r_0 was determined by the number of residues that the spring represents, 8 for Syb and 5 for Syx, times the maximum extension per residue, 3.65 Å (8). The FENE spring constant, k_F, used was the same at k_s for the ENM of 0.0963 N/m.

Before beginning the CG displacement control simulations, the SNARE structure was relaxed for 10^6 timesteps under quasi-static conditions, i.e., at 0 Kelvin. This relaxation was performed on the SNARE structure extracted from the final timestep of the 40 ns AA simulation in order to ensure that the initial structure was fully equilibrated. After this relaxation period, the C-termini beads were separated under displacement control using the two pulling beads that were discussed previously. The bead attached to the Syx C-terminus was held fixed, and all displacements were applied to the bead attached to the C-teriminal Syb bead. For each displacement, this bead was moved 1 Å along the vector between the two pulling beads. After each displacement was applied, the structure was relaxed for 10^5 timesteps in order to allow it to equilibrate. At the end of the relaxation period, the forces on both pulling beads were nearly identical, and these forces were recorded as a function of displacement (See Fig. A3.4).

Displacement control runs were conducted with eleven different values of λ between 0.16 and 0.72. This parameter directly adjusted the magnitude of the force, so it was used to match the peak unzipping force reported by Gao et al. (8) of between 14 pN and 19 pN. On this basis, a value of 0.3 was chosen to produce a peak force in the experimentally measured range of 17.2 pN.

3.3.3 Continuum Model of the Vesicle and Plasma Membrane

The vesicle and plasma membrane are subjected to forces from the SNARE complex drawing them together and distributed distance-dependent electrostatic and hydration repulsion. During this process, the vesicle and plasma membrane both deform considerably and the task of the continuum model is to obtain a consistent solution of the deformed shape subject to these forces. The continuum calculations are based on the formulation of Jenkins et al. (26) and its extension to SNARE-mediated fusion by Long et al. (27). The current axisymmetric continuum model extends these formulations to include concentrated forces due to the SNARE molecules and the electrostatic forces due to the charges on the membranes or hydration repulsion.

The axisymmetric geometry is shown schematically in Fig. 3.2. We use a cylindrical coordinate system (r,θ,z) where θ is the angle of revolution about the z axis. Owing to the axisymmetric assumption, the forces exerted by the zipping of the SNARE complexes are represented by a circle of line force of magnitude F on a spherical vesicle of radius R (see Fig. 3.2 *B*) as well as on the plasma membrane. This line force counters the repulsive forces between the vesicle and the plasma membrane. As shown in Fig. 3.2 *B*, the line force acts along a latitude of the undeformed vesicle and is constrained to remain normal to the deformed surface. The location of the latitude is specified by the arc length S_0 of a cross-section in the reference configuration, which is taken to be a spherical vesicle. Because the plasma membrane is very large compared to the vesicle radius, its reference configuration is taken to be a flat circular membrane of radius L under pretension, T_0. The SNARE forces act on a

circle of radius S_0 in the reference configuration, have the same magnitude F, and are always directed opposite to the force on the vesicle (Fig. 3.2 *B* and *C*).

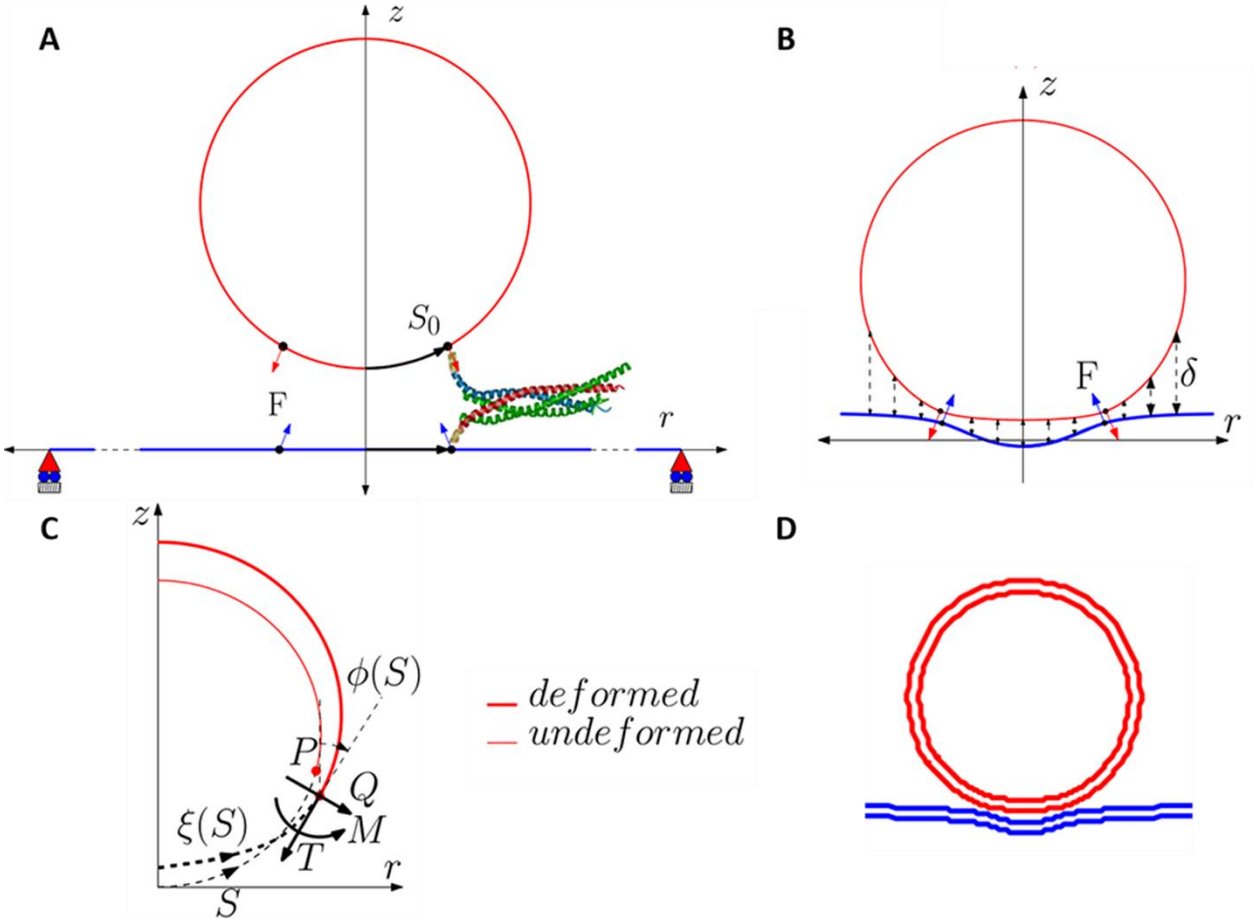

FIGURE 3.2 (*A*) A schematic of the axisymmetric model in the undeformed configuration, showing the location of SNARE and direction of force applied. (*B*) The repulsive forces (shown by the dotted lines) act on the deformed configuration of the vesicle as does the SNARE force, *F*. (*C*) The figure shows the convention for shear force (*Q*), in-plane tension (*T*), and moment (*M*) acting on the cross-section of the membrane a location ξ (*S*), where ϕ (S) is the tangent angle in the undeformed configuration measured from the vertical. (*D*) Example

of a deformed vesicle-plasma membrane complex for a 20-nm diameter vesicle docked by 15 SNAREs.

In our model, the repulsive force depends only on the local separation δ, as shown schematically in Fig. 3.2. Following Bykhovskaia et al. (11), electrostatic and hydration repulsion between the vesicle and plasma membrane are calculated using Derjaguin's approximation (35) in which interaction between curved surfaces is estimated assuming that the surfaces are locally flat. This approximation is valid if the length scale over which forces decay is much smaller than the radius of curvature of the vesicle. The applicable range of separations prior to vesicle to membrane fusion is 2-4 nm. In this range, the principal repulsive forces are due to electrostatics and hydration.

The functional form of both the electrostatic and hydration repulsion is approximately the same, an exponential decay. Electrostatics has the larger decay length (typically 1 nm under physiological conditions) and smaller prefactor (35). The decay length for hydration repulsion is in the 1-4 A range (35–38). Consequently, hydration dominates for small separation and electrostatics for larger separation. Much of the previous work suggests that the cross-over distance beyond which electrostatics dominates is about 1.5 nm (35, 37). However, recent work of Aeffner et al. (36) suggests that hydration repulsion exceeds electrostatic repulsion for distances upto about 3 nm. Based on the work of Aeffner et al. (36), we have performed calculations taking hydration repulsion to be the dominant repulsive interaction. However, given some

uncertainty regarding the relative importance of electrostatics and hydration, we have also computed results for the case where electrostatic repulsion is assumed to dominate. The hydration pressure takes on the form of an exponential decay:

$$P(d_w) = P_0 \exp(-d_w / \lambda_h) \qquad 3.9$$

where d_w is the lipid bilayer separation, P_0 is the hydration pressure amplitude, and λ_h is the decay length. According to Aeffner et al. (36), the prefactor, P_0, ranges from 0.24 – 4.13 GPa and λ_h ranges from 2.3 – 3.7 Å. We chose to use a value of 0.43 GPa for P_0 and a λ_h of 3.22 Å based on the parameters suggested for a synaptic vesicle corresponding to experiments performed in a physiologically relevant DOPC/Chol 70:30 mixture (36).

Local electrostatic interaction is determined by solving the Debye-Huckel equation for two infinite parallel planes separated by δ. We consider two limiting scenarios,

1) The membranes have fixed charge density throughout the process of docking. This corresponds to the case when the lipid molecules are completely ionized and have a fixed charge.
2) The membranes have fixed surface potential. This is achieved by adjusting the surface charge density of the ions in the Stern layer of the membrane or by varying the degree of ionization of the polarizable lipid molecules.

For the constant surface charge densities, the repulsive force along the z direction per unit area is given by

$$F_e = \frac{\sigma_1^2 + \sigma_2^2 + 2\sigma_1\sigma_2 \cosh(\delta / l_D)}{2\varepsilon\varepsilon_0 \sinh^2(\delta / l_D)} \qquad 3.10$$

where σ_1 and σ_2 are the surface charge densities of the vesicle and neuron base respectively, l_D is the Debye length, ε is the relative permittivity of water and ε_0 is the permittivity of vacuum. The choice of surface charge σ_1 is based on the electrophoretic measurement by Ohsawa et al. (39) and force-displacement measurement by Marra et al. (40). The reported value of surface charge is in the range 0.01 – 0.03 C/m^2. Also, assuming the same surface charge density on the outer leaflet of the plasma membrane and based on the observation by Pekker et al. (41) that a charge density difference of only ~0.0001C/m^2 between the inner and outer leaflet is necessary to maintain the resting potential difference of 70 mV for the neuron cell, we choose the value of $\sigma_1 = \sigma_2 = -0.025\text{C/m}^2$.

For the case of constant surface potential, the force per unit area is

$$F_e = \frac{l_D^2}{2\varepsilon\varepsilon_0} \frac{-\varphi_1^2 - \varphi_2^2 + 2\varphi_1\varphi_2 \cosh(\delta / l_D)}{\sinh^2(\delta / l_D)}. \qquad 3.11$$

When the two membrane structures are far away from each other, they have charge density given as $\sigma_1 = \sigma_2 = -0.025C/m^2$. The potential on an isolated surface and charge density are related by,

$$\varphi = \frac{l_D \sigma}{\varepsilon\varepsilon_0} \qquad 3.12$$

The value of surface potential for the bilayers $\varphi_1 = \varphi_2 = -25\text{mV}$, is evaluated using Eq. 3.12. As the vesicle approaches the membrane, the surface potential is held constant and Eq. 3.11 is used to obtain the force between the membranes. A similar approach was followed in (11). However, in that work the mechanics of SNARE opening was not coupled to the electrostatic repulsion, and the SNARE-end opening was picked at 1 nm, whereas here the minimum separation of SNARE-ends is taken to be 2 nm. Primarily for this reason, the repulsive electrostatic forces in the present work are in the range of tens of pN instead of the hundreds of pN quoted in (11). Relevant parameters for modeling electrostatic forces are listed in Table A3.3

3.3.3.1 Governing Equations for the Continuum Membrane Model and Their Solution

The vesicle-membrane system has been modeled under axisymmetry in an (r, θ, z) coordinate system. In the undeformed configuration, the vesicle is modeled as a sphere with radius R, whereas the undeformed plasma membrane is a circular disc of radius $L >> R$. As shown in Fig. 3.2, S refers to the undeformed arc length, whereas in the deformed configuration, the arc length is denoted by ξ. The tangent to the membrane makes an angle ϕ with the z axis and the mean curvature of the membrane surfaces is denoted by H.

The forces in the membranes are shear force, Q, and the in-plane tension, T, as shown in Fig. 3.2 *C*. The osmotic pressure inside the synaptic vesicle is represented by

p_0. As shown in Fig. 3.2 *B*, the repulsive electrostatic force per unit area, F_e in Eqs. 3.9 and 3.10, acts on both membranes, along the z direction. The force due to SNARE bundles is represented as line loads acting on the circles over the undeformed geometry of vesicle and plasma membrane (denoted by vectors F and $-F$, as shown in Fig. 3.2 *B*). On the vesicle, the radius of this circle, r_0, is determined by the geometrical compatibility condition which is based on the width of SNARE helix, d, and number of SNARE bundles, as,

$$r_0 = \frac{(\text{number of SNAREs}) \times d}{2\pi}. \qquad 3.13$$

The assumption here is that the packing of SNAREs is limited by steric hindrance between them and Eq. 3.13 represents the smallest radius that would accommodate the given number of bundles. The equivalent arc length value for load application is given by $S_0 = \sin^{-1}(\mathrm{r}_0/\mathrm{R})$. This arc length is same for both the vesicle and the membrane.

We assume that the strain energy density W of both membranes is given by,

$$W = c\,H^2, \qquad 3.14$$

and by variation of total energy, the governing equations for the vesicle-membrane system are obtained in Eqs. A3.11. These equations represent equilibrium in the normal (Eq. A3.11a) and tangential (Eq. A3.11f) directions at each point on the membranes. The geometrical constraints can be used to obtain Eqs. A3.11b-e. These governing equations form a non-linear system of ODE's. By specifying the input geometric parameters (R,L) and the force parameters (F, S_0, F_e and p_0), this system of ordinary differential equations (ODE's) can be solved numerically to obtain an

equilibrium configuration of the membrane system. We use the non-linear boundary value problem solver bvp4c in MATLAB© to solve the ODE's.

3.4 RESULTS

3.4.1 Force-Displacement Response of the Vesicle-Membrane Interaction

The equal and opposite forces on the Syx and Syb C-termini are transmitted to the plasma membrane and vesicle, respectively, as forces attracting the two together. Below separations separations of ~2.5 nm attractive forces are resisted primarily by hydration repulsion. A characteristic force-separation curve can be obtained for the vesicle-membrane system using the formulation described in section 3.2.3. By specifying the number of SNARE bundles attached to the vesicle-membrane system, the location of the line load can be determined using Eq. 3.13. The effect of zipping of SNARE bundle is simulated by varying the strength of the line load in small steps. For each increment in force, an equilibrium configuration of the membrane system is obtained, and hence we determine the separation between the two load points on vesicle and plasma membrane, respectively. This separation is the distance between residues Syb89 and Syx256. By varying the number of SNAREs, a series of force-separation curves can be obtained as shown in Fig. 3.3 *A*.

3.4.2 SNARE Force-Separation Curve

Fig. 3.3 *B* shows the results of a simulation in which the SNARE bundle has been pulled apart for a total end-to-end separation of 20 nm between the C-terminal Syb and Syx end beads.

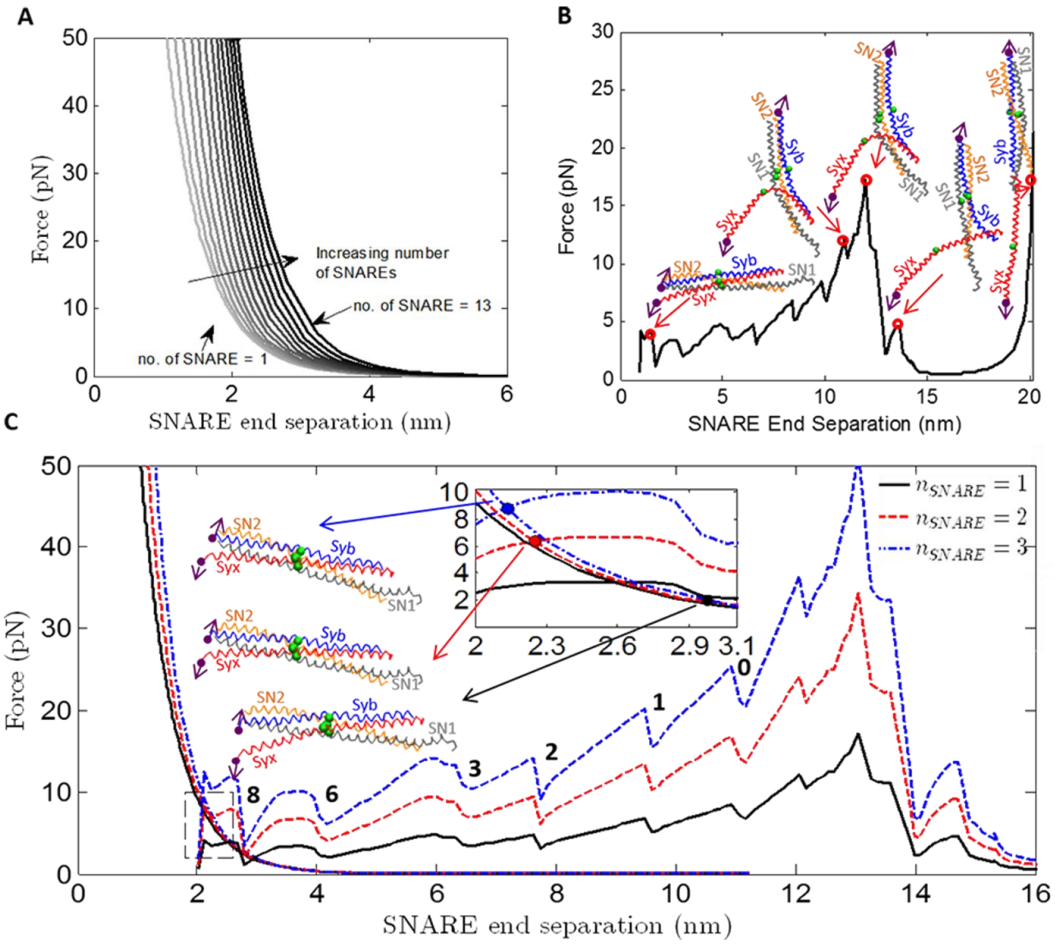

FIGURE 3.3 (*A*) Force versus SNARE end separation for the vesicle-membrane system for different numbers of SNAREs for the hydration repulsion case. (*B*) The force during separation of the ends of the SNARE bundle using λ of 0.30 for the CG model of SNARE along with snapshots of the SNARE bundle at the corresponding C-terminal end separation. The end separation is defined as the distance between the Syb and Syx C-terminal beads. Syb, Syx, the ionic layer

residues (*beads*), and the C-terminal residues (*beads with arrows*) that are attached to pulling beads are shown in each SNARE snapshot. The purple arrows correspond to the direction along which the C-terminal beads are being pulled. (*C*) The force as a function of Syb-Syx C-terminal distance is shown for the vesicle-membrane (the exponentially decreasing curves) and SNARE. One (*solid line*), two (*dash line*), and three (*dash-dot line*) SNAREs are shown in this plot. Intersections between the vesicle-membrane and SNARE force-displacement responses represent equilibrium states. There are a number of instabilities represented by load-drops. These correspond to separation of individual layers and have been so labeled.

Each drop in the force-displacement plot (Fig. 3.3 *B*) represents the system overcoming a barrier where there is a strong interaction between the SNARE bundles. Two examples are the snapshots at 10.9 nm and 11.9 nm in Fig. 3.3 *B*. With an increase of only 1.0 nm in displacement and little visible change in structure there is a significant (5.1 pN) increase in force to a peak value of 17.2 pN, after which the force immediately drops to about 2 pN. (Because a significant amount of the linker domain was not present in the crystal structure of SNARE that was used to build the CG model, the first force jump seen by Gao et al. (8) at 3 nm and 8-13 pN is not present in these results.) The CG model is able to capture the experimentally determined precipitous force-drop after which the remaining interactions holding the SNARE bundle together are relatively weak and are therefore not measurable in a force-controlled experiment. The subsequent increase in force is associated with stretching

of the linkage between the N termini of Syx and Syb, and presumably would not be present in a physiological setting. It is included here because this feature is also present in the experiments of Gao et al. (8). For simplicity, in the version of the elastic network model used here, we do not allow the helices to unravel, justified by the following facts. As the results of the next section show, the equilibrium separation for all the cases studied in this paper is about 3 nm or less. At these separations the force on each SNARE is < 5 pN. Based on the work of Gao et al. (2012) the first unwinding event occurs at ~10-12 pN. Thus our simplifying assumption (which will be relaxed in future work) that helices remain unfolded is justifiable for the range of openings and displacements representative of the equilibrium docked state. We have checked the sensitivity of our results to this assumption by allowing small portions of the unzippered region to unfold as shown in supporting material.

3.4.3 Combined SNARE and Vesicle-Membrane Results

In the previous two sections we have independently obtained force-separation results for the vesicle-membrane system (Fig. 3.3 *A*) and for the SNARE (Fig. 3.3 *B*). Before combining the two results, we first accounted for the fact that the distance between outer surfaces of the membranes is larger by about 2 nm than the distance between Syb89 and Syx256, the SNARE residues that we move apart (see Appendix A3). Specifically, we shifted the SNARE force displacement curve to the right by 2 nm in order to obtain this consistency. Clearly, in the combined SNARE-vesicle-membrane system there is a single force and corresponding displacement. Applying this

consistency condition between the two results determines equilibrium. Moreover, we can determine how equilibrium depends on the number of SNARES.

For systems with 1, 2, and 3 SNAREs, the information from Fig. 3.3 *A* and Fig. 3.3 *B* is combined to produce Fig. 3.3 *C*. Because it has been shown that SNAREs mediate vesicle to membrane fusion in a synchronous way, we assume that the force required to unzip two SNAREs would simply be twice the force required to unzip one SNARE, and so on (42, 43). In all three cases, the curves intersect at an equilibrium SNARE end separation of between 2 nm and 3 nm suggesting that even 1-3 SNAREs are sufficient to overcome hydration repulsion and allow the vesicle to dock at the plasma membrane. The corresponding structures for the intersection points for all three cases, shown in Fig. 3.3 *C*, also suggest there is no important conformational difference between the three structures other than a difference in the number of residues that have been unzippered.

It is instructive next to consider the energy landscape corresponding to the force-separation results shown in Fig. 3.3. For this purpose, the SNARE (positive) and vesicle-membrane (negative) force-separation results are integrated numerically. Fig. 3.4 *B* shows the results corresponding to the force-separation results shown in Fig. 3.3. Note that because the SNARE force-displacement response contains unstable jumps, the entire energy landscape is not represented in Figs. 3.4 *B*-*C*. Because of the nature of the displacement control simulations, there are several instabilities present in the original SNARE force separation curve. An example of one of these instabilities is the drop at 7.5 nm as shown in the SNARE curves in Fig. 3.3 *C*. Integrating across these instabilities makes the total energy of the system slightly more negative than it should

be (see Appendix A3). Figs. 3.4 *B*-*C* show contour plots of interaction energy as a function of the number of SNAREs and end-to-end separation. Fig. 3.4 *B* shows the results for a vesicle with radius of 20 nm, representing a synaptic vesicle. The gray circles represent the global energy minimum for each value of number of SNARES, corresponding to force equilibria in Fig. 3.3. An example of how these minima were determined is shown in Fig. 3.4 *A* that was used to determine the global energy minimum for 1 SNARE for the hydration repulsion case. It is striking that a single SNARE produces a distinct energy minimum at ~3 nm. As the number of SNAREs increases to 4 SNAREs the equilibrium SNARE end separation decreases. For 4-8 SNAREs there is little difference in the equilibrium separation. For 5 SNAREs the total energy per SNARE is ~ -17 kT which is quite consistent with the 13 – 27 kT range reported by Zorman et al. (44). With increase in the number of SNAREs over 8, the equilibrium SNARE separation slowly increases; the minimum separation (~ 2.1 nm) is achieved with 4 bundles. Thus, we may conclude that 4-8 SNAREs are sufficient to complete the zippering process and to bring the membrane and the vesicle at a distance of 2.1 nm. Importantly, a larger number of SNARE bundles do not bring the vesicle closer to the membrane, because steric hindrance pushes them out to a larger radius.

We next explored how electrostatics would affect the vesicle to plasma membrane repulsion. We recalculated the continuum model results using a fixed surface charge of -0.025 C/m^2 on the vesicle and the membrane with electrostatic repulsion as shown in Fig. A3.9 *B*. For this case for one SNARE the end separation is ~2.4nm which is smaller than the 3 nm seen for the hydration repulsion case. However, when more than

one SNARE is added to the system, the equilibrium SNARE end separation is constant at ~2 nm for 2-13 SNAREs. In this case, the equilibrium configuration of the SNARE bundle would be a nearly completely zipped conformation. For this case with 4 SNARES the total energy per SNARE is ~ -14 kT which again within the range of 13 – 27 kT reported by Zorman et al. (44).

We next explored how the vesicle size would affect the number of SNAREs required to dock a vesicle to the membrane. Figs. A3.10 *B* and *D* show the results for the case of a vesicle that is 100 nm in radius, corresponding to vesicles in neurosecretory cells. For the hydration repulsion case, there is a considerable difference between the 20nm and 100nm vesicles. For the 100nm case the minimum separation is also reached with 4 SNAREs, however that minimum separation is ~2.5nm as opposed to ~2.1nm for the 20nm vesicle. For the case of electrostatic repulsion with a constant surface charge, the only difference between the two cases is for 1 and 2 SNAREs. For the 100nm vesicle case the equilibrium separation is ~3.4nm as opposed to ~2.4nm for the 20nm vesicle. Additionally for 2 SNAREs there is also a larger separation for the 100nm vesicle of 3nm as opposed to 2nm for the 20nm vesicle. However for 3 of more SNAREs there is little difference between the two vesicle sizes because both SNARE configurations are nearly completely zippered.

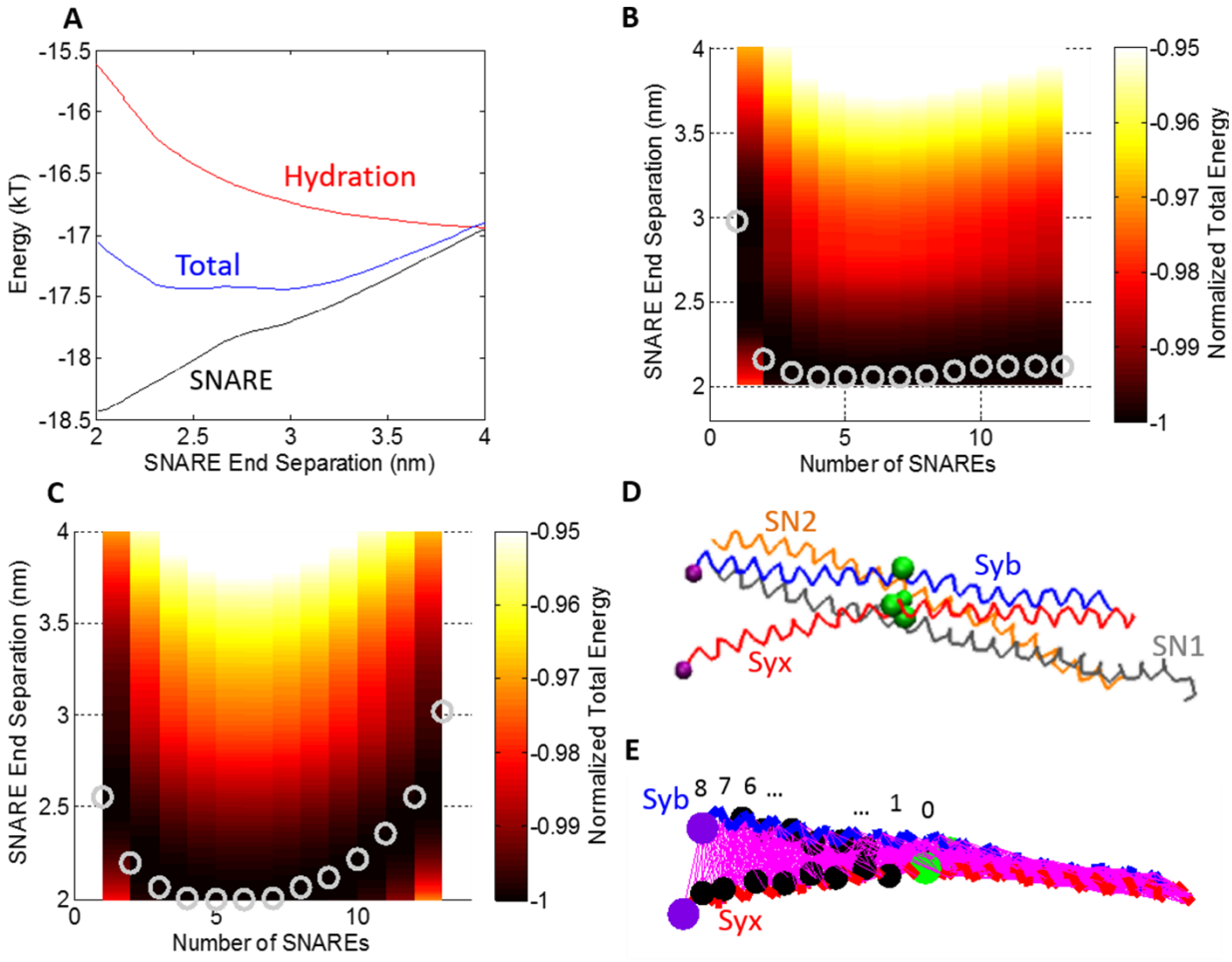

FIGURE 3.4 (*A*) Energy as a function of SNARE end separation when repulsion between the vesicle and plasma membrane is dominated by hydration repulsion. The energetic contributions from SNARE (attractive), hydration (repulsive), and the total (their sum) are shown. The hydration repulsion has been shifted vertically by -17 kT for clarity. (*B*) Contour plot of total energy as a function of SNARE end separation distance for different numbers of SNAREs under hydration repulsion. Circles correspond to global energy minima representing the equilibrium SNARE end separation for a given number of SNAREs. Vesicle

radius is 20 nm. (*C*) Contour plot of total energy as a function of SNARE end separation distance for different numbers of SNAREs under electrostatic repulsion for a fixed charge of -0.025 C/m^2 on the vesicle and the membrane in the limit of high tension in the vesicle and plasma membrane. For this case, minimum lateral separation between the SNARE bundles has been increased from 3 nm to 4nm. (*D*) The structure of SNARE corresponding to the case shown in Fig. 4 *B*, number of SNAREs=1. Syb, Syx, SN1, SN2 are shown with the ionic layer residues indicated as large beads. *(E*) The same structure as in Fig. 4 *D* but showing only Syb and Syx for clarity. All contacts for residues within 2σ of each other are indicated with thin lines.

Fig. 3.4 *B* and *C* represent results for an optimized set of parameters describing molecular details and electrostatic forces. To judge the robustness of the conclusions gleaned from these results, we explored several variations of parameters including (1) allowing a portion of Syb to melt with the surface charge held constant, (2) holding the surface potential constant instead of surface charge, (3) high osmotic pressure in the vesicle and low pretension in the plasma membrane, and (4) the limit of high tension in both the vesicle and plasma membranes. These variations in the modeling assumptions generally make little difference in the conclusions drawn from Fig. 3.4 (see Appendix A3). The main conclusion that 4-8 SNAREs bring the vesicle to the minimum distance away from the membrane still holds. Because the equilibria of interest for the problem addressed in this work occur at relatively small separation and forces, in our model we have not allowed the helices to unravel. In order to see the

potential effect of unraveling, the first two helical turns of Syb were melted and the force displacement curve for SNARE was calculated from Fig. 3.3 *B*. The resulting energy surface for this case for a 20 nm vesicle with hydration repulsion is shown in Fig. A3.11 *A*. 4-10 SNAREs brings the vesicle within a minimal distance of the plasma membrane. However, that minimal distance is ~2.4nm as opposed to the ~2.1nm for the case where Syb is not permitted to unravel.

In an effort to compare to the experimental prefusion structures of the vesicle and plasma membrane as shown by Malsam et al. (45) and Hernandez et al. (46), the continuum model was calculated using high osmotic pressure in the vesicle and low pretension in the plasma membrane. However, the resulting energy surface for this modification to the base cases shown in Fig. 3.4 has little effect on the results because the repulsive force is dominated by hydrostatic repulsion as shown in Fig. A3.14.

The limit of high tension in both the vesicle and plasma membrane was studied using an analytical model described in the Supporting Material. In order to test the sensitivity of the solution to the location of the SNAREs, calculated using Eq. 3.13, the diameter of the SNARE bundle was varied from 2 nm, Fig. A3.17 *A*, to 4nm, whereas the base case used 3nm. This variation seems to have the most significant effect on the solution. Decreasing the size of the SNARE bundle still yields a similar result in that for more than one SNARE the bundle is nearly completely zipped shut. On the other hand when the size of the SNARE bundle is increased, instead of having a nearly fully zippered bundle, there is a minimum separation that occurs at 4 SNAREs. With the addition of more than 5 SNAREs the equilibrium separation again begins to increase all the way up to ~3nm with 13 SNAREs.

Fig. 3.4 *D* and *E* show the equilibrium structures of SNARE at a 2.1 nm separation for the case shown in Fig. 3.4 *B*. SN1 and SN2 were removed from the structure for clarity in Fig. 3.4 *E*, and the residues of Syb and Syx that were "in contact" were determined. Because the Miyazawa and Jernigan forces greatly decrease after a separation of ~2*σ, that distance was used as the criteria for 2 residues being in contact. At the start of the displacement control simulation, Syb and Syx had 574 contacts between them. After a 2.1 nm separation, only 449 contacts remained. The removed contacts begin to create a crack-like defect separating the helices. After the 2.1 nm separation, residues 89 (Trp) of Syb and 256 (Lys) of Syx were still in contact. These residues are still far away from the ionic layer showing that the SNARE bundle had not yet unzipped to that point.

3.5 DISCUSSION AND CONCLUSION

The docking of vesicles onto the plasma membrane of a neuron involves interplay between the SNARE complexes that provide attractive forces, long-range repulsion between the vesicle and membrane, and deformation of all three components. Although each of these components has previously been investigated in detail, to understand the biophysics and mechanics of vesicle docking it is imperative to combine them. We report here the first model which couples chemical specificity of the SNARE complex with hydration, electrostatic, and mechanical forces imposed on the vesicle and plasma membrane. Such a model can serve as a tool to investigate how mutations in the SNARE complex could affect the docking and fusion process.

We have developed separate coarse-grained models for the deformation of the SNARE complex and of the vesicle-membrane assembly. The vesicle-membrane model is based on a continuum description of membrane deformation subjected to either hydration or electrostatic repulsion and forces from the SNARE complexes. The fusion of lipid bilayers have been extensively modeled (47) to capture the intermediate states of fusion, including stalk formation, and to understand their energetics. Our goal in this study was to understand the forces produced by membrane bending and hydration or electrostatic repulsion that need to be overcome by the SNARE complexes to dock a vesicle to the membrane. The continuum membrane model was coupled with a coarse grain model of the SNARE complex. The SNARE forces are represented in the continuum membrane model as an axisymmetric line force, an assumption that is increasingly accurate for increasing number of SNAREs. (A single SNARE at the axis of symmetry also presumably results in axisymmetric deformations of the vesicle/membrane.) For a given number of SNARES, the model holds fixed their anchor points in the vesicle and plasma membrane. This constraint potentially affects our results. However, we note that the position of the SNARE anchor points does vary as we change the number of SNAREs (Eq. 3.13). The number of SNAREs was varied from 1-13. Usually, for 2 or more SNAREs there is little difference in the equilibrium separation, suggesting that the model results probably will not vary much if we remove the constraint of holding the positions fixed.

The CG SNARE model is based on an elastic-network representation of each of the helices combined with Miyazawa-Jernigan potentials to capture inter-helical interactions. It is a minimalistic model that still represents residue-specificity. Its

few parameters are calibrated either by comparison with all-atom MD simulations of individual SNAREs, or by comparison to experimentally measured forces to separate a single SNARE complex, Gao et al.(8) Specifically, we match the experimentally observed peak force of 17.2 pN force. Each of the two models separately yields a force-separation relationship. Enforcing consistency between the two yields equilibrium configurations for the SNARE-vesicle-membrane complex, for a given number of SNAREs.

As the first application of our model, we explored here the effect of the number of SNARE complexes on the mechanics of vesicle docking and the prefusion state of the SNARE complex. It is still a matter of debate as to how many SNARE complexes need to assemble prior to the fusion process. High concentration of Syb on the vesicle (~70 copies (48)), as well t-SNARE clusters at docking sites (49) suggest that *in vivo* fusion may be mediated by multiple SNARE complexes. At the same time, experiments and model systems suggest that one (50), two (18), or three (19, 51, 52) could be sufficient. Other studies, however, suggest a larger number of SNARE complexes per fusion, ranging between 5 and 11 (16, 20, 53). Finally, recent studies suggest that the number of assembled SNARE complexes may determine the release efficiency (54) and that it may vary (55). Thus, how vesicle docking might depend on the number of SNARE complexes remains an open question, previously not addressed from the biophysical and biomechanical point of view.

We find that one SNARE complex is sufficient to dock the vesicle onto the membrane. As few as 2-3 SNAREs are sufficient to bring the distance between the membrane and vesicle to the minimum and thus to complete the docking process. Interestingly, there

is a point of diminishing returns such that a larger number of SNAREs (i.e., an over-docked state) does not further reduce the vesicle-membrane separation. The corresponding predicted SNARE end-to-end separation is in the range 2-3 nm (56, 57) but one can expect significant fluctuation about the equilibrium state because the energy profile is relatively shallow (Fig. 3.4 *A*). This picture of a partially zippered docked state is consistent with the conclusions of an in-vivo toxin cleavage assay in crayfish neuromuscular junctions. In this work, we only model docking, not fusion. That is, we calculate the equilibrium separation between the vesicle and plasma membrane during docking. The lower bound of ~2 nm separation between the vesicle and plasma membrane is based on the steric hindrance of having to fit the SNARE bundles between the two surfaces. This distance is probably a bit too large for fusion to occur, which suggests that some additional mechanism other than SNARE zippering must act for fusion.

Several variations in the model including calculations under fixed charge, fixed surface potential, high vesicle pressure and high membrane tension, and varying vesicle radius have all shown similar results.

Our results are consistent with the view that a prefusion state involves a partially assembled SNARE complex (58–60) which keeps the vesicle at a short distance from the plasma membrane in anticipation of Ca2+-induced fusion rather than the alternative view that SNARE zippering represents a final step of exocytosis and rapidly progresses once nucleated (61). Specifically, our model robustly predicts an equilibrium separation between the vesicle and the membrane to be on the order of 2.0-3.0 nm corresponding to opening of at most layer 8.

Bibliography

1. Südhof, T.C. 1995. The synaptic vesicle cycle: a cascade of protein-protein interactions. Nature. 375: 645–653.

2. Hanson, P.I., J.E. Heuser, and R. Jahn. 1997. Neurotransmitter release - four years of SNARE complexes. Curr. Opin. Neurobiol. 7: 310–315.

3. Söllner, T., M.K. Bennett, S.W. Whiteheart, R.H. Scheller, and J.E. Rothman. 1993. A protein assembly-disassembly pathway in vitro that may correspond to sequential steps of synaptic vesicle docking, activation, and fusion. Cell. 75: 409–418.

4. Rothman, J.E. 1994. Mechanisms of intracellular protein transport. Nature. 372: 55–63.

5. Gracheva, E.O., E.B. Maryon, M. Berthelot-Grosjean, and J.E. Richmond. 2010. Differential regulation of synaptic vesicle tethering and docking by UNC-18 and TOM-1. Front. Synaptic Neurosci. .

6. Sutton, R.B., D. Fasshauer, R. Jahn, and A.T. Brunger. 1998. Crystal structure of a SNARE complex involved in synaptic exocytosis at 2.4 A resolution. Nature. 395: 347–353.

7. Ernst, J.A., and A.T. Brunger. 2003. High resolution structure, stability, and synaptotagmin binding of a truncated neuronal SNARE complex. J. Biol. Chem. 278: 8630–8636.

8. Gao, Y., S. Zorman, G. Gundersen, Z. Xi, L. Ma, G. Sirinakis, J.E. Rothman, and Y. Zhang. 2012. Single reconstituted neuronal SNARE complexes zipper in three distinct stages. Science. 337: 1340–3.

9. Durrieu, M.-P., R. Lavery, and M. Baaden. 2008. Interactions between neuronal fusion proteins explored by molecular dynamics. Biophys. J. 94: 3436–3446.

10. Bock, L. V., B. Hutchings, H. Grubmüller, and D.J. Woodbury. 2010. Chemomechanical regulation of SNARE proteins studied with molecular dynamics simulations. Biophys. J. 99: 1221–1230.

11. Bykhovskaia, M., A. Jagota, A. Gonzalez, A. Vasin, and J.T. Littleton. 2013. Interaction of the complexin accessory helix with the C-terminus of the SNARE complex: molecular-dynamics model of the fusion clamp. Biophys J. 105: 679–690.

12. Durrieu, M.P., P.J. Bond, M.S.P. Sansom, R. Lavery, and M. Baaden. 2009. Coarse-grain simulations of the R-SNARE fusion protein in its membrane environment detect long-lived conformational sub-states. ChemPhysChem. 10: 1548–1552.

13. Lindau, M., B.A. Hall, A. Chetwynd, O. Beckstein, and M.S.P. Sansom. 2012. Coarse-grain simulations reveal movement of the synaptobrevin C-terminus in response to piconewton forces. Biophys. J. 103: 959–69.

14. Marrink, S.J., H.J. Risselada, S. Yefimov, D.P. Tieleman, and A.H. De Vries. 2007. The MARTINI force field: Coarse grained model for biomolecular simulations. J. Phys. Chem. B. 111: 7812–7824.

15. Lamberg, A., and T. Taniguchi. 2014. Coarse-grained computational studies of supported bilayers: current problems and their root causes. J. Phys. Chem. B. 118: 10643–52.

16. Han, X., C.-T. Wang, J. Bai, E.R. Chapman, and M.B. Jackson. 2004. Transmembrane segments of syntaxin line the fusion pore of Ca2+-triggered exocytosis. Science. 304: 289–292.

17. Van den Bogaart, G., and R. Jahn. 2011. Counting the SNAREs needed for membrane fusion. J Mol Cell Biol. 3: 204–205.

18. Sinha, R., S. Ahmed, R. Jahn, and J. Klingauf. 2011. Two synaptobrevin molecules are sufficient for vesicle fusion in central nervous system synapses. Proc Natl Acad Sci U S A. 108: 14318–14323.

19. Mohrmann, R., H. de Wit, M. Verhage, E. Neher, and J.B. Sorensen. 2010. Fast vesicle fusion in living cells requires at least three SNARE complexes. Science (80-.). 330: 502–505.

20. Karatekin, E., J. Di Giovanni, C. Iborra, J. Coleman, B. O'Shaughnessy, M. Seagar, and J.E. Rothman. 2010. A fast, single-vesicle fusion assay mimics physiological SNARE requirements. Proc Natl Acad Sci U S A. 107: 3517–3521.

21. Zhang, Z., J. Pfaendtner, A. Grafmuller, and G.A. Voth. 2009. Defining coarse-grained representations of large biomolecules and biomolecular complexes from elastic network models. Biophys J. 97: 2327–2337.

22. Chu, J.W., and G.A. Voth. 2006. Coarse-grained modeling of the actin filament derived from atomistic-scale simulations. Biophys J. 90: 1572–1582.

23. Miyazawa, S., and R.L. Jernigan. 1985. Estimation of effective interresidue contact energies from protein crystal structures: quasi-chemical approximation. Macromolecules. 18: 534–552.

24. Miyazawa, S., and R.L. Jernigan. 1996. Residue-residue potentials with a favorable contact pair term and an unfavorable high packing density term, for simulation and threading. J. Mol. Biol. 256: 623–644.

25. Miyazawa, S., and R.L. Jernigan. 1999. Self-consistent estimation of inter-residue protein contact energies based on an equilibrium mixture approximation of residues. Proteins Struct. Funct. Genet. 34: 49–68.

26. Jenkins, J.T. 1977. Static equilibrium configurations of a model red blood cell. J Math Biol. 4: 149–169.

27. Long, R., C.Y. Hui, A. Jagota, and M. Bykhovskaia. 2012. Adhesion energy can regulate vesicle fusion and stabilize partially fused states. J. R. Soc. Interface. 9: 1555–1567.

28. Hess, B., C. Kutzner, D. Van Der Spoel, and E. Lindahl. 2008. GROMACS 4: Algorithms for highly efficient, load-balanced, and scalable molecular simulation. J. Chem. Theory Comput. 4: 435–447.

29. Foloppe, N., and A.D. Mackerell. 2000. All-Atom Empirical Force Field for Nucleic Acids : I . Parameter Optimization Based on Small Molecule and Condensed Phase Macromolecular Target Data. J. Comput. Chem. 21: 86–104.

30. Walter, A.J.L.R.R. 2002. Molecular Biology of the Cell. .

31. Creighton, T.E. 1993. Proteins: structures and molecular properties. 2nd ed. New York: W. H. Freeman and Company.

32. Kim, Y.C., and G. Hummer. 2008. Coarse-grained Models for Simulations of Multiprotein Complexes: Application to Ubiquitin Binding. J. Mol. Biol. 375: 1416–1433.

33. Cooke, I.R., and M. Deserno. 2005. Solvent-free model for self-assembling fluid bilayer membranes: Stabilization of the fluid phase based on broad attractive tail potentials. J. Chem. Phys. 123.

34. Argento, C., A. Jagota, and W.C. Carter. 1997. Surface formulation for molecular interactions of macroscopic bodies. J. Mech. Phys. Solids. 45: 1161–1183.

35. McIntosh, T.J., A.D. Magid, and S.A. Simon. 1990. Interactions between charged, uncharged, and zwitterionic bilayers containing phosphatidylglycerol. Biophys. J. 57: 1187–1197.

36. Aeffner, S., T. Reusch, B. Weinhausen, and T. Salditt. 2012. Energetics of stalk intermediates in membrane fusion are controlled by lipid composition. Proc. Natl. Acad. Sci. 109: E1609–E1618.

37. McIntosh, T.J., and S.A. Simon. 1994. Hydration and steric pressures between phospholipid bilayers. Annu. Rev. Biophys. Biomol. Struct. 23: 27–51.

38. Marra, J. 1986. Direct measurement of the interaction between phosphatidylglycerol bilayers in aqueous electrolyte solutions. Biophys. J. 50: 815–825.

39. Ohsawa, K., M. Murata, and H. Ohshima. 2005. Zeta potential and surface charge density of polystyrene-latex; comparison with synaptic vesicle and brush border membrane vesicle. Colloid Polym. Sci. 264: 1005–1009.

40. Marra, J. 1986. Direct measurement of the interaction between phosphatidylglycerol bilayers in aqueous electrolyte solutions. Biophys. J. 50: 815–825.

41. Pekker, M., and M.N. Shneider. 2014. The surface charge of a cell lipid membrane. arXiv Prepr. arXiv. : 1401–1407.

42. Risselada, H.J., C. Kutzner, and H. Grubmüller. 2011. Caught in the act: visualization of SNARE-mediated fusion events in molecular detail. Chembiochem. 12: 1049–55.

43. Risselada, H.J., and H. Grubmüller. 2012. How SNARE molecules mediate membrane fusion: Recent insights from molecular simulations. Curr. Opin. Struct. Biol. 22: 187–196.

44. Zorman, S., A. Rebane, L. Ma, G. Yang, M.A. Molski, J. Coleman, F. Pincet, J.E. Rothman, and Y. Zhang. 2014. Common intermediates and kinetics, but different energetics, in the assembly of SNARE proteins. Elife. 3: e03348.

45. Malsam, J., D. Parisotto, T.A.M. Bharat, A. Scheutzow, J.M. Krause, J.A.G. Briggs, and T.H. Söllner. 2012. Complexin arrests a pool of docked vesicles for fast Ca2+-dependent release. EMBO J. 31: 3270–3281.

46. Hernandez, J.M., A. Stein, E. Behrmann, D. Riedel, A. Cypionka, Z. Farsi, P.J. Walla, S. Raunser, and R. Jahn. 2012. Membrane Fusion Intermediates via Directional and Full Assembly of the SNARE Complex. Science (80-.). 336: 1581–1584.

47. Chernomordik, L. V, and M.M. Kozlov. 2008. Mechanics of membrane fusion. Nat. Struct. Mol. Biol. 15: 675–683.

48. Takamori, S., M. Holt, K. Stenius, E.A. Lemke, M. Grønborg, D. Riedel, H. Urlaub, S. Schenck, B. Brügger, P. Ringler, S.A. Müller, B. Rammner, F. Gräter, J.S. Hub, B.L. De Groot, G. Mieskes, Y. Moriyama, J. Klingauf, H. Grubmüller, J. Heuser, F. Wieland, and R. Jahn. 2006. Molecular Anatomy of a Trafficking Organelle. Cell. 127: 831–846.

49. Knowles, M.K., S. Barg, L. Wan, M. Midorikawa, X. Chen, and W. Almers. 2010. Single secretory granules of live cells recruit syntaxin-1 and synaptosomal associated protein 25 (SNAP-25) in large copy numbers. Proc. Natl. Acad. Sci. U. S. A. 107: 20810–20815.

50. Van den Bogaart, G., M.G. Holt, G. Bunt, D. Riedel, F.S. Wouters, and R. Jahn. 2010. One SNARE complex is sufficient for membrane fusion. Nat. Struct. Mol. Biol. 17: 358–364.

51. Hua, Y., and R.H. Scheller. 2001. Three SNARE complexes cooperate to mediate membrane fusion. Proc. Natl. Acad. Sci. U. S. A. 98: 8065–8070.

52. Shi, L., Q.-T. Shen, A. Kiel, J. Wang, H.-W. Wang, T.J. Melia, J.E. Rothman, and F. Pincet. 2012. SNARE Proteins: One to Fuse and Three to Keep the Nascent Fusion Pore Open. Science (80-.). 335: 1355–1359.

53. Megighian, A., M. Zordan, S. Pantano, M. Scorzeto, M. Rigoni, D. Zanini, O. Rossetto, and C. Montecucco. 2013. Evidence for a radial SNARE super-

complex mediating neurotransmitter release at the Drosophila neuromuscular junction. J Cell Sci. 126: 3134–3140.

54. Acuna, C., Q. Guo, J. Burré, M. Sharma, J. Sun, and T.C. Südhof. 2014. Microsecond dissection of neurotransmitter release: SNARE-complex assembly dictates speed and Ca2+ sensitivity. Neuron. 82: 1088–1100.

55. Hernandez, J.M., A.J.B. Kreutzberger, V. Kiessling, L.K. Tamm, and R. Jahn. 2014. Variable cooperativity in SNARE-mediated membrane fusion. Proc. Natl. Acad. Sci. U. S. A. : 1–6.

56. Prashad, R.C., and M.P. Charlton. 2014. SNARE zippering and synaptic strength. PLoS One. 9.

57. Hua, S.Y., and M.P. Charlton. 1999. Activity-dependent changes in partial VAMP complexes during neurotransmitter release. Nat. Neurosci. 2: 1078–1083.

58. Sørensen, J.B., K. Wiederhold, E.M. Müller, I. Milosevic, G. Nagy, B.L. de Groot, H. Grubmüller, and D. Fasshauer. 2006. Sequential N- to C-terminal SNARE complex assembly drives priming and fusion of secretory vesicles. EMBO J. 25: 955–966.

59. Walter, A.M., K. Wiederhold, D. Bruns, D. Fasshauer, and J.B. Sørensen. 2010. Synaptobrevin N-terminally bound to syntaxin-SNAP-25 defines the primed vesicle state in regulated exocytosis. J. Cell Biol. 188: 401–413.

60. Li, F., D. Kümmel, J. Coleman, K.M. Reinisch, J.E. Rothman, and F. Pincet. 2014. A half-zippered SNARE complex represents a functional intermediate in membrane fusion. J. Am. Chem. Soc. 136: 2456–2464.

61. Jahn, R., and D. Fasshauer. 2012. Molecular machines governing exocytosis of synaptic vesicles. Nature. 490: 201–207.

62. Schlick, T. 2002. Molecular modeling and simulation: an interdisciplinary guide. New York: Springer.

63. Kubo, R. 2002. The fluctuation-dissipation theorem. Reports Prog. Phys. 29: 255–284.

64. Bruce Alberts Julian Lewis Keith Roberts, and Peter Walter, Alexander Johnson, M.R. 2002. Molecular Biology of the Cell. 4th ed. New York: Garland Science.

65. Ohsawa, K., H. Ohshima, and S. Ohki. 1981. Surface potential and surface charge density of the cerebral-cortex synaptic vesicle and stability of vesicle suspension. Biochim Biophys Acta. 648: 206–214.

66. Deserno, M. Fluid lipid membranes – a primer. 2007. http://www.cmu.edu/biolphys/deserno/pdf/membrane_theory.pdf

67. Kweon, D.H., C.S. Kim, and Y.K. Shin. 2002. The membrane-dipped neuronal SNARE complex: A site-directed spin labeling electron paramagnetic resonance study. Biochemistry. 41: 9264–9268.

68. Kweon, D.-H., C.S. Kim, and Y.-K. Shin. 2003. Regulation of neuronal SNARE assembly by the membrane. Nat. Struct. Biol. 10: 440–447.

69. Kim, C.S., D.H. Kweon, and Y.K. Shin. 2002. Membrane topologies of neuronal SNARE folding intermediates. Biochemistry. 41: 10928–10933.

70. Stein, A., G. Weber, M.C. Wahl, and R. Jahn. 2009. Helical extension of the neuronal SNARE complex into the membrane. Nature. 460: 525–528.

Appendix A3

A3.1 Coarse-Grained Simulations: Solution Procedure

CG simulations were conducted for the 4 individual helices using Langevin dynamics at 300 K for a range of values of k_s. The Langevin equation (1) includes an inertial term, a viscous term, a random force term, and a potential energy term, respectively, in the form

$$m\ddot{x}(t) = -\gamma\dot{x}(t) + R(t) - \nabla E \qquad \text{A3.1}$$

where m is the mass of each bead, $\ddot{x}(t)$ is the bead's acceleration at time t, γ is the damping constant, $\dot{x}(t)$ is the bead's velocity at t, $R(t)$ is a random force that represents the protein's interaction with the surrounding fluid, and E is the potential energy governing the solute that includes ENM forces. The fluctuation-dissipation theorem (2) connects the random force and viscous drag

$$\langle R(t) \cdot R(t') \rangle = 6\gamma k_B T \delta(t - t') \qquad \text{A3.2}$$

where k_B is Boltzman's constant, T is temperature, $R(t')$ is the random force applied at t', and $\delta(t - t')$ is the Dirac delta function. Written as a system of equations for all beads, the Langevin equation takes the form

$$[M]\{\ddot{u}(t)\} = -\gamma\{\dot{u}(t)\} + \{R(t)\} - [k]\{u(t)\} \quad \text{A3.3}$$

where [*M*] is a diagonal mass matrix, $\{\ddot{u}(t)\}, \{\dot{u}(t)\}, and\ \{u(t)\}$ are column vectors containing the accelerations, velocities, and positions in the x, y, and z directions for each bead, $\{R(t)\}$ is a column vector containing the random force in the x, y, and z directions for each bead, and $[k]$ is a stiffness matrix.

The standard deviation of the random force is derived from Eqs. A3.2 and A3.3 to be

$$SD = \sqrt{\frac{2m\gamma k_B T}{\Delta t}} \quad \text{A3.4}$$

where Δt is the timestep. The friction coefficient is dependent on the bead type as well

$$\gamma = \frac{6\pi\eta a}{m} \quad \text{A3.5}$$

where a is the Van der Waals radius of the bead and η is the viscosity of water. The timestep used for Langevin dynamics was based on the characteristic time, τ, that is defined as

$$\tau = \sqrt{\frac{m}{k_s}} \quad \text{A3.6}$$

where m is the maximum bead mass. The timestep was adjusted to match the diffusion of a bead attached to a spring. Using this technique, the timestep was determined to be 43.4 fs or τ/20.

In order to model the dynamics of the coarse-grained model, the Langevin dynamics equation was solved using a generalized Verlet algorithm (1)

$$\dot{x}^{n+1/2} = \dot{x}^{n} + m^{-1}\frac{\Delta t}{2}\left[-\nabla E(x^{n}) - \gamma M\dot{x}^{n} + R^{n}\right] \quad \text{A3.7}$$

$$x^{n+1} = x^{n} + \Delta t\dot{x}^{n+1/2} \quad \text{A3.8}$$

$$\dot{x}^{n+1} = \dot{x}^{n+1/2} + m^{-1}\frac{\Delta t}{2}\left[-\nabla E(x^{n+1}) - \gamma M\dot{x}^{n+1} + R^{n+1}\right] \quad \text{A3.9}$$

where n is the timestep. The position is calculated from the half velocity, and then the position and half velocity are both used to calculate the full velocity.

A3.2 ENM Reference State

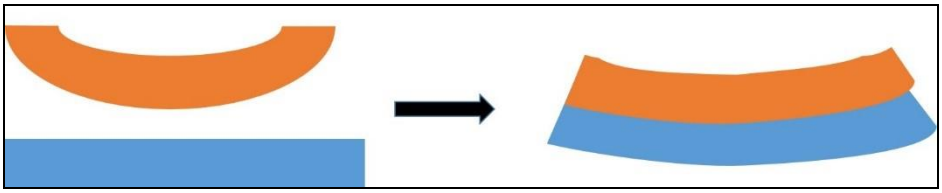

FIGURE A3.1 A model showing two beams. The reference or zero energy state for both beams is when they are separated from each other. When the beams

form a bundle, mutual interactions deform them into some shape with associated stored energy that will be released when the beams are separated.

For each of the helices there exists a relaxed, natural, or reference state, and we maintain that the relaxed state of the springs that comprise the elastic network model should be defined in this reference state. This idea is illustrated in the Fig A3.1. Say we have two helices (orange and blue) with two different reference states (bent and straight). When the two helices come into contact with each other, they will both deform to form an equilibrium structure. If we assume the energy of the system to be 0 on the left, some energy is required to bend both helices to form the combined structure on the right. In our model we use our references states, like those on the left, to help us calculate the energy stored in the bundle that can be released as the bundle is pulled apart.

The existence of such a reference state is not contingent upon its viability as a stable state for an actual isolated helix. Although Syb by itself is largely unstructured, we can still define the Syb helix by itself, i.e., removed from the other SNARE helices. It is a notional state used merely to obtain the frozen or stored elastic energy in the SNARE bundle. That is, all that is required is that the helical forms be stable as a bundle and that we have a systematic procedure by which to define springs on a relaxed state, again, regardless of whether the relaxed state actually exists.

We recognize that in many sources in the literature it is noted that Syb is largely unstructured when not in the presence of the SNARE bundle. We conducted 40 ns all-atom simulation of the individual SNARE helices, starting with a configuration

extracted from the crystal structure. We found that this timescale was more than sufficient to allow all of the helices to straighten into relatively straight rod-like conformations. It was also short enough that each rod retained its helical structure. Because of this separation of time scales – time to relax an individual helix << time required for it to lose it structure – we were able to define the natural or reference state of each helix on which to construct the elastic spring network.

A3.3 Determining the Cut-Off Distance and Spring Constant in the Elastic Network Model for SNARES

Coordinates from the straightened out helical structures were extracted from the individual AA simulations, and the connectivity and natural length of the ENM springs for each helix were determined based on these structures. If the cutoff distance is too small, the proteins will denature. If it is too large, simulation speed will be compromised with no significant improvement in representation. In order to find an optimal value, this distance was adjusted and a histogram was created for each helix to show the total number of springs that were connected to each bead. The minimum criterion for the number of springs was that each bead should be connected by a spring to all of its nearest neighbors. It was concluded that a cutoff distance of a minimum of 10 Å yielded at least 4 springs per bead, which satisfied this criteria. After further investigation, it was determined that R_c was required to be at least 20 Å in order to maintain the helical structure of each helix during AA simulations. The

histogram for the final value of R_c, 20 Å, for the helix Syb is shown in Fig. A3.2. The histograms for the other three helices are similar.

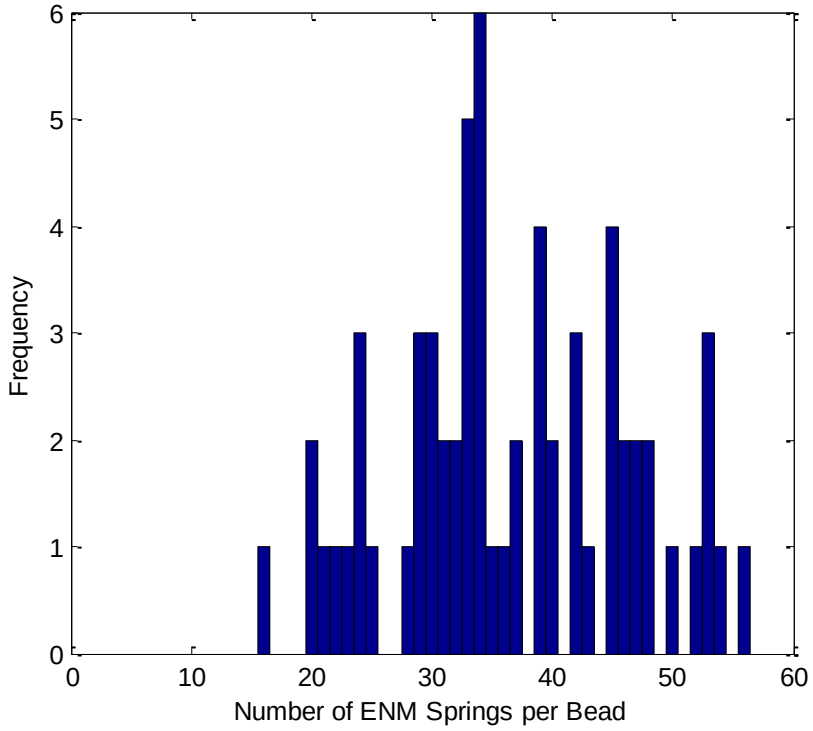

FIGURE A3.2 A histogram for the number of ENM springs per bead is shown for Syb with a value of 20 Å for R_c.

The values of k_s for the ENM were chosen by matching the spectrum of fluctuations of the AA simulations and the CG model. For the analysis of individual AA helix simulations, the positions of the alpha carbons were extracted every 10 ps. For each alpha carbon a time series of distance from average location was calculated. The fast Fourier transform (FFT) was then evaluated for each bead's time series. The average was taken over all beads yielding a single spectrum per helix. In order to make this

comparison of the fluctuations, CG simulations were conducted for the 4 individual helices using Langevin dynamics at 300 K for a range of values of k_s. The time length of simulations required was determined by conducting a normal modes analysis (NMA) on the CG model of the crystal structure, 1N7S, for all helices individually using different values of k_s. AA simulations were run for 2 ns, which is considerably longer than the characteristic time given as the inverse of the lowest natural frequency. The results for Syb are shown in Table A3.1.

TABLE A3.1 The lowest natural frequencies and characteristic times for Syb determined are shown below for different values of k_s

k_s (N/m)	**Lowest Natural Frequency Squared $(1/ns)^2$**	**Time (ns)**
0.0963	4.53	4.70E-01
0.1926	9.05	3.32E-01
0.2889	1.36	2.71E-01
0.3853	1.81	2.35E-01
0.4816	2.26	2.10E-01

For Syb, as was seen for all helices, the characteristic times are significantly less than 1 ns. As a result the AA simulations were analyzed for the first 2 ns of the trajectories, and the CG test simulations were conducted for 2 ns and analyzed with data collected every 2 ps. In order to best match the fluctuations, the root mean

squared deviation (RMSD) between the AA and CG spectra was found for each run. An example of the comparison of both spectra is shown in Fig. A3.3 for Syb with k_s value of 0.0963 N/m. The RMSD for all helices for all values of k_s are shown in Table A3.2 with the minimum RMSD values shaded in grey.

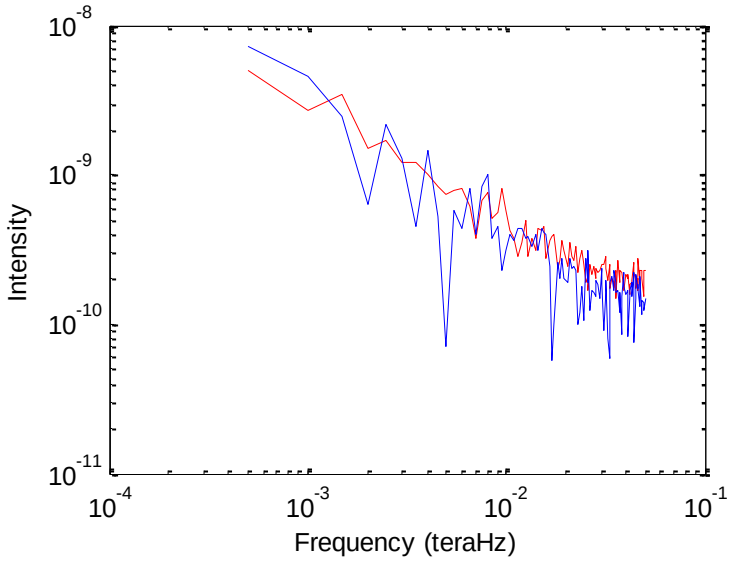

FIGURE A3.3 The spectra used to compare the fluctuations of the AA (*blue*) and CG (*red*) models are shown for Syb for 2 ns. Values of k_s as 0.0963 N/m and R_c of 20 Å were used for the CG model. An RMSD of 4.7E-10 was found.

TABLE A3.2 The RMSD values between the AA and CG fluctuation spectra are shown below for all helices for a range of values of k_s. The minimum RMSD values are shaded in grey.

k_s (N/m)	**Syb RMSD**	**Syx RMSD**	**SN1 RMSD**	**SN2 RMSD**
0.00009	9.6450e-09	1.0532e-08	1.2658e-08	9.5905e-09
0.0009	4.9432e-09	5.5075e-09	6.7327e-09	4.6640e-09

0.0096	1.4341e-09	1.1056e-09	1.5941e-09	1.7538e-09
0.0481	7.4334e-10	1.4651e-09	8.5729e-10	1.6778e-09
0.0963	4.7077e-10	4.3346e-10	1.3671e-09	2.3080e-09
0.1444	7.2271e-10	9.9229e-10	1.5680e-09	1.1604e-09
0.1926	1.4341e-09	1.1064e-09	1.5941e-09	1.7539e-09
0.2889	1.2019e-09	1.5654e-09	2.7382e-09	3.0644e-09
0.3853	1.7372e-09	2.0310e-09	3.2207e-09	3.3413e-09
0.4816	2.4969e-09	2.8429e-09	3.2951e-09	3.5652e-09

Based on the data in Table A3.2, a value of 0.0963 N/m was chosen for k_s for all four helices. For Syb and Syx, this corresponds to the value of k_s with the smallest RMSD. For SN1 and SN2 however, the minimum RMSD occurs either a little above or below k_s of 0.0963 N/m. Because the RMSD is still very small for these two helices with that value of k_s, it was chosen to use a consistent value of k_s for all helices.

A3.4 Calibration of λ and Displacement Orientation

As described in the SNARE CG model portion in the methods section, the value of λ was adjusted in order to match the peak force reported by Gao et al. (3) of 14 – 19 pN. We conducted a series of displacement control simulations at 0K for a set of λ values ranging from 0.30 to 0.72. Displacement was applied in steps and the system allowed to relax. Relaxation to equilibrium was monitored by tracking the forces acting on the C-terminal beads of Syb and Syx as shown in Fig. A3.4. Each force spike corresponds to a displacement being applied to the C-terminal bead of Syb. After 10^5 timesteps,

both forces relax to nearly the same value, which is taken as the equilibrium force for that displacement, and the next displacement step is then applied.

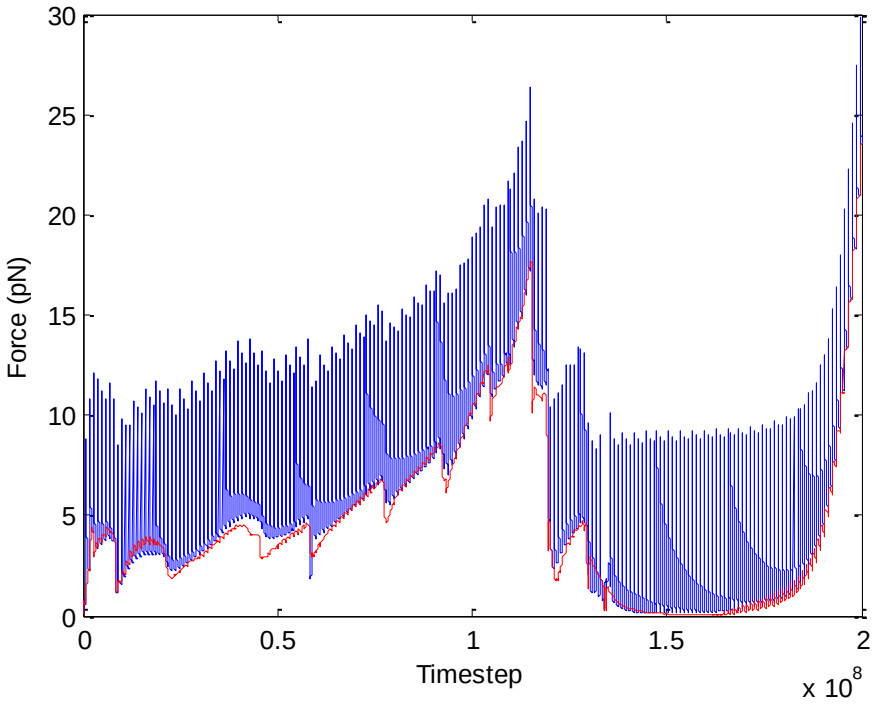

FIGURE A3.4 The force as a function of timestep is shown for a displacement control run with λ set to 0.30. The forces on the C-terminal beads of Syb (*blue*) and Syx (*red*) are shown. Each spike in the Syb force corresponds to application of a new displacement step. A total displacement of 20 nm is shown.

The resulting force displacement curves for a few of these runs for varying λ are shown in Fig. A3.5.

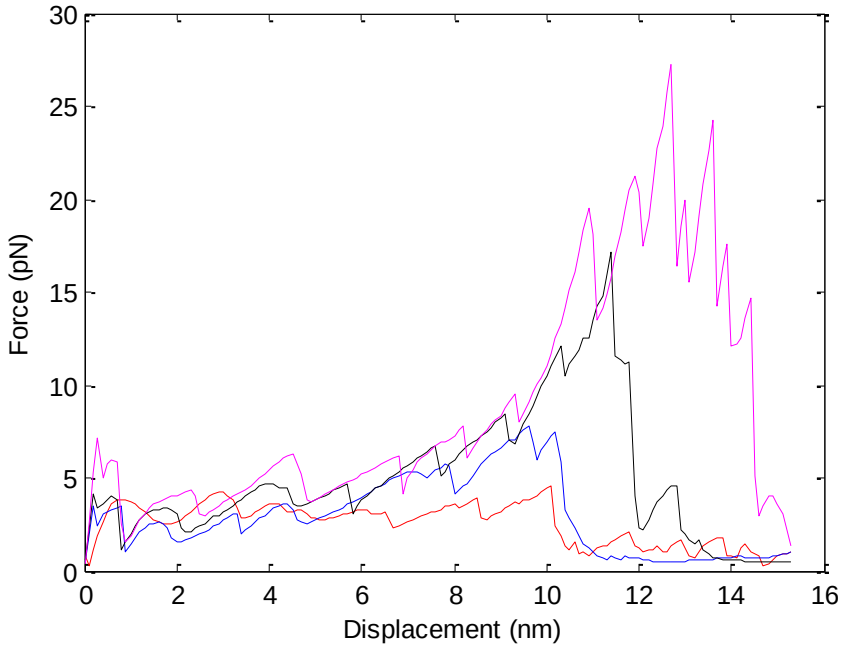

FIGURE A3.5 Force displacement curves are shown for displacement control simulations done using λ values of 0.16 (*red*), 0.24 (*blue*), 0.30 (*black*), and 0.40 (*magenta*).

It was clear that as λ was increased, the peak force increased as well. By choosing its value to be 0.3, we attained a peak force of 17.2 pN that lies in the experimentally measured range.

A3.5 SNARE Force Displacement Instabilities and Their Effect on Energy

There are several mechanical instabilities in the force-separation curve of the SNARE, for example at 7.5 nm in Fig. 3.3 *C*. These usually correspond to "breaking" of one of the layers. When the system jumps from one stable point to the next, it does not

follow the equilibrium force-separation relationship between these two points; instead, it lies above it. When we integrate the force-separation curve to obtain energies, we consequently compute a slightly larger magnitude (more negative) than it should be. This does not affect any of the predictions about stable equilibria.

A3.6 Continuum Governing Equations and Their Solution

The axisymmetric deformation of the vesicle-membrane system can be reduced to the solution of a set of ordinary differential equations. The undeformed configuration of the vesicle is a sphere of radius R with arc-length in a cross-section denoted by S whereas, the plasma membrane occupies the interior of a circle of radius $L \gg R$. We introduce the notation ϕ to denote the angle made by the tangent to a point on the cross-section of the deformed membrane in the (r,z) plane with the z axis (see Fig. A3.5 *A*). Briefly, the equations describing the deformation involve the shear force Q, the angle ϕ, the mean curvature H, the deformed arc length ξ, the deformed coordinates of a generic material point (r,z) which has an arc length coordinate S in the undeformed configuration. To expedite the analysis, we introduce the following normalized variables:

$$\bar{S} = \frac{S}{R}, \quad \bar{r} = \frac{r}{R}, \quad \bar{z} = \frac{z}{R}, \quad \bar{H} = RH, \quad \bar{\xi} = \frac{\xi}{R},$$
$$\bar{Q} = \frac{QR^2}{c}, \ \bar{d} = \frac{dR^2}{c}, \qquad \text{A3.10}$$
$$\bar{p}_0 = \frac{p_0 R^3}{c}, \ \bar{F}_e = \frac{F_e R^3}{c}, \ \bar{F}_n = \frac{F_n R^3}{c}, \ \bar{F}_t = \frac{F_t R^3}{c},$$

where,

p_0 is the osmotic pressure of the vesicle,

d is an integration constant resulting from integrating the tangential force equilibrium equation (see supplementary information for details),

F_e is the electrostatic force per unit area of the membrane and is always along z direction,

F_t is the tangential component of the concentrated load at the material point S_0 in the deformed membrane,

F_n is the normal component of the concentrated load at the material point S_0 deformed membrane.

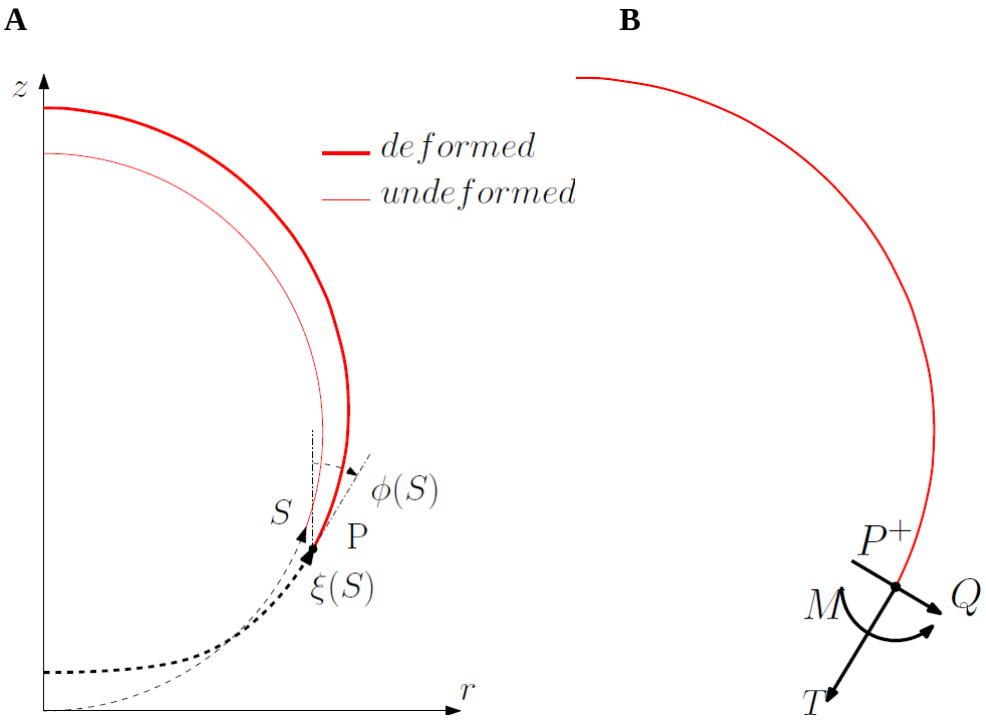

FIGURE A3.6 (*A*) Arc length and tangent angle over the membrane, (*B*) Forces and moment along the cut in the membrane.

As shown above non-dimensionalization of all the length scales is done by the radius of the undeformed vesicle, R. As c has units of energy, we use it to non-dimensionalize force per unit length quantities i.e. in-plane tension, T and out of plane shear, Q by c/R^2. Also force per unit area quantities, p_0, F_e, F_t and F_n are made dimensionless by c/R^3.

Also, in both the loading conditions it has been assumed that the F_t for vesicle is always zero. There are six ordinary differential equations governing the deformation of the vesicle membrane, they are:

$$\dot{\bar{Q}} = -\frac{\bar{Q}}{\bar{r}}\dot{\bar{\xi}}\sin\phi - 2\bar{H}\dot{\bar{\xi}}\left[\bar{d} + \bar{H}^2 + \left(2\bar{H} + \frac{\cos\phi}{\bar{r}}\right)\frac{\cos\phi}{\bar{r}}\right] + \dot{\bar{\xi}}\,\bar{p},$$

$$\dot{\phi} = \dot{\bar{\xi}}\left(2\bar{H} + \frac{\cos\phi}{\bar{r}}\right),$$

$$\dot{\bar{H}} = \dot{\bar{\xi}}\bar{Q},$$

$$\dot{\bar{r}} = \dot{\bar{\xi}}\sin\phi,$$

$$\dot{\bar{z}} = \dot{\bar{\xi}}\cos\phi,$$

$$\dot{\bar{d}} = \left(\bar{F}_e\cos\phi + \bar{F}_t\right)\dot{\bar{\xi}} \qquad \text{(A3.11a- A3.11f)}$$

where, the dot denotes differentiation with respect to the normalized undeformed arc length $\bar{S}$, and

$$\dot{\bar{\xi}} \equiv \frac{\sin\bar{S}}{\bar{r}} \quad . \qquad \text{(A3.11g)}$$

The normalized normal force acting on the deformed membrane surface, $\bar{p}$ in Eq. A3.11a is related to the osmotic pressure of the vesicle, $\bar{p}_0$, the electrostatic force per

unit area, $\bar{F}_e$ and the normal component of the concentrated load applied at $\bar{S} = \bar{S}_0$, $\bar{F}_n$ by,

$$\bar{p} = \bar{p}_0 + \bar{F}_e \sin\phi + \bar{F}_n \delta\left(\bar{S} - \bar{S}_0\right) \qquad \text{(A3.11h)}$$

where, $\delta(\bar{S} - \bar{S}_0)$ is the Dirac delta function.

These differential equations are supplemented with the boundary conditions:

$$\begin{aligned}
&\phi(\bar{S} = 0) = \frac{\pi}{2}, \\
&\bar{Q}(\bar{S} = 0) = 0, \\
&\bar{r}(\bar{S} = 0) = 0, \\
&\phi(\bar{S} = \pi) = -\frac{\pi}{2}, \\
&\bar{Q}(\bar{S} = \pi) = 0, \\
&\bar{r}(\bar{S} = \pi) = 0,
\end{aligned} \qquad \text{(A3.12a- A3.12f)}$$

The boundary conditions defined above essentially represent the symmetry in the vesicle geometry. About the symmetry axis, the curve has zero slope and out of plane shear $\bar{Q}$ is zero, at both $\bar{S} = 0$ and π. Also, for the continuity of the geometry, we impose $\bar{r} = 0$ at both $\bar{S} = 0$ and π.

The notation for positive shear force and tension is described in Fig. A3.6. Finally, the expression for the in-plane tension in both the vesicle and plasma membrane is given by,

$$\bar{T} = \frac{TR^2}{c} = \frac{R^2}{c}\left(-d - cH^2 - cH\,\frac{cos\phi}{r}\right). \qquad \text{(A3.13)}$$

The governing equations for the deformation of the plasma membrane is very similar, except that Eq. A3.11g must be replaced by,

$$\dot{\bar{\xi}} = \frac{\bar{S}}{\bar{r}} \tag{A3.14}$$

This change is due to the difference between the reference configurations. The boundary conditions are:

$$\begin{aligned}
&\phi(\bar{S}=0) = \frac{\pi}{2}, \\
&\bar{Q}(\bar{S}=0) = 0, \\
&\bar{r}(\bar{S}=0) = 0, \\
&\phi\left(\bar{S}=\frac{L}{R}\right) = \frac{\pi}{2}, \\
&\bar{z}\left(\bar{S}=\frac{L}{R}\right) = 0, \\
&\bar{T}\left(\bar{S}=\frac{L}{R}\right) = \left[-\bar{d} - \bar{H}^2 - \bar{H}\frac{cos\phi}{\bar{r}}\right]_{\bar{S}=\frac{L}{R}} = \bar{T}_0 \equiv \frac{T_0 R^2}{c}
\end{aligned} \tag{A3.15a- A3.15f}$$

The boundary conditions at $\bar{S}=0$ is due to axisymmetry. Eq. A3.15f states that the tension in the plasma membrane approaches the pretension at the boundary. This boundary condition allows the neuron membrane to deflect. Had we replaced this boundary condition with a clamped condition, the deflection everywhere would be zero because of area incompressibility.

The coupled ODE's in Eqs. A3.11 - A3.15 with the boundary conditions are solved using the MATLAB® bvp4c solver. The input parameters for the solver are the

osmotic pressure p_0 across the vesicle membrane which remains fixed throughout the deformation, SNARE-machinery force parameters (S_0 and magnitude F), electrostatic force and pretension (T_0) in the plasma membrane.

A3.7 Example Problem of Continuum Model

Here we show an example of the results of the calculation of vesicle-membrane interaction. In this example, the location of force application is fixed at $\bar{S}_0 = \frac{\pi}{6}$ on both the vesicle and neuron base, as shown in Fig. A3.7. This location of load application corresponds to the number of SNAREs of 21. Parameters used in the continuum model are shown in Table A3.3.

TABLE A3.3 Parameters used for the continuum model of the vesicle and plasma membrane

Parameter	**Value**	**Comment**
Permittivity of vaccum, ε_0	8.85 x 10^{-12} Fm^{-1}	
Dielectric constant of water, ε	80	dimensionless
Ion concentration inside neuron, c_0	200 mM (4)	(1-1) electrolyte
Debye length, l_D	0.67nm	$l_D = \sqrt{\frac{\varepsilon\varepsilon_o k_B T}{2q^2 z^2 c_o}}$
Synaptic vesicle radius, R	20nm (5)	
Surface charge of vesicle and inside	-0.025 Cm^{-2}, -0.025 Cm^{-2}	

of plasma membrane, σ_1 and σ_2	(5–7)	
Surface potential of vesicle and inside of plasma membrane, φ_1 and φ_2	-25 mV, -25 mV	
Bending rigidity of lipid bilayer, κ_c	~20 k_BT (8)	8.28 x 10^{-20} J

The strength of the line force is varied in the range of $5-20$ in dimensionless terms, which is equivalent to a net force between $66-266\ pN$. Fig. A3.7 shows the deformed shapes of the membranes for four different values of $\bar{F}$. The inset on the right shows the calculated relationship between applied force and separation between load application points. The force decreases rapidly with increasing separation, reflecting the steep decay of the electrostatic repulsion.

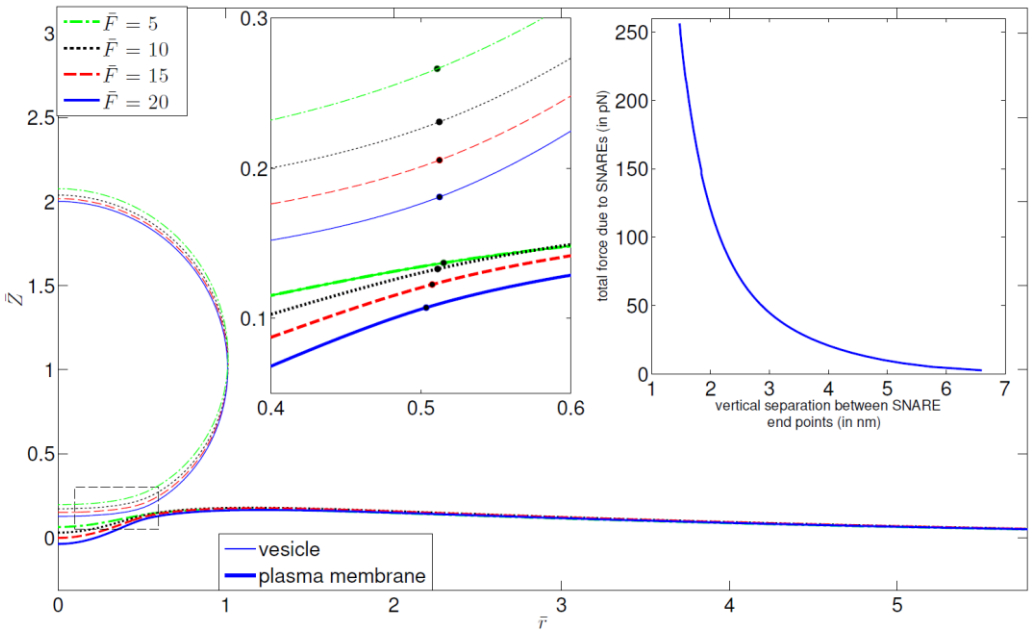

FIGURE A3.7 Deformed geometry for different force magnitudes. The thick lines represent the neuron base and the thin lines represent the vesicle. The inset on the left shows the zoomed in section of the load application point (*shown as* •) and the inset on the right shows the vertical separation between the two ends of SNARE-machinery versus the net SNARE force. The parameters are for the analysis are: load application point, $\bar{S}_0 = \pi / 6$**, pretension in plasma membrane,** $\bar{T}_0 = 1$ **and vesicle pressure.** $\bar{p}_0 = 1$ **.**

A3.8 SNARE Force Separation Curve Shift

To compare the attractive force imposed by the SNARE bundle to the repulsive force on the vesicle, we need a consistent definition of separation. The distance connecting the final residue beads (Syb89 and Syx256) is shorter than the distance between the outside membrane surfaces due to the presence of other parts of the SNARE. To address this issue, we created a static coarse grained structure of a 20 nm vesicle and plasma membrane with a partially opened SNARE at its equilibrium configuration as shown in the figure below. We found that distance between the outer surface of the membranes is actually about ~1nm further apart than the distance between Syb89 and Syx256. We have therefore added this distance when comparing the attractive force on the SNARE to the repulsive force on the vesicle. Adding the initial separation between Syb89 and Syx256, the minimum distance allowed between the membranes at the point of force application is about 2nm. Another related effect is that inter-SNARE-bundle repulsion can increase the minimum lateral separation. We have

considered two additional cases where we take lateral SNARE bundle width to be 2 and 4 nm (an additional Debye screening length increase in radius in the latter case). The larger lateral spacing makes the effect of number of SNAREs significantly stronger but the minimum separation and the number of SNAREs needed to achieve it does not change much.

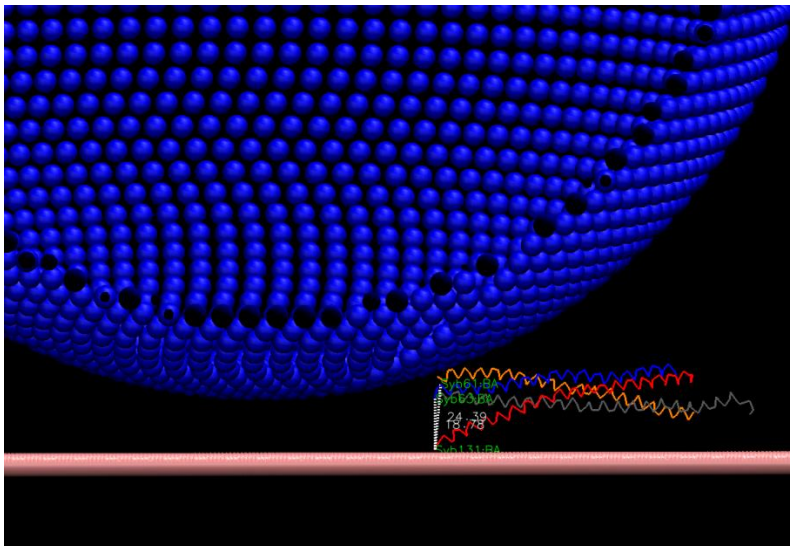

Figure A3.8. Drawing of a vesicle near a plane along with a model for the SNARE bundle.

A3.9 Choice of SNARE Model

The CG simulation model was built using the SNARE X-ray crystal structure 1N7S that includes Syb (27-89), Syx (189-256), SN1 (5-83), and SN2 (139-204). We recognize that this structure only includes part of the Syb linker domain (85-95) and none of the linker domain of Syx (256-266). However, we believe that our choice of placing the membrane outer surface at residues 89 and 256 is correct. Our choice is

based on the following papers (9, 10) that show Syb insertion in the membrane starts at Trp 89. Specifically, they show that 89-94 is unstructured but is inserted in the membrane. Similarly, the following paper shows that for Syx, residues after 261 are in the lipid bilayer. Specifically, 261-266 are unstructured but inside the lipid bilayer (11). The following study (12) also concludes that the linker domains (256-266) and (85-95) are buried in the top layer of the membrane. Because the reference distance from the hydration repulsion is the outer surface of the membrane, to be consistent we believe that it is quite appropriate to define SNARE displacement from 88 for Syb to 256 for Syx, within some uncertainty of a just a few residues.

Whether or not the linker domains have unraveled is debatable. It was shown in Gao et al's optical tweezer experiment that the Syb linker domain unravels at 10-13 pN. Because the equilibrium SNARE end-end distances of interest in this work are <~ 3nm), our maximum force only reaches (<5pN) and neglecting helix unraveling in our model is justifiable. Nevertheless, in order to check the robustness of our solution against unraveling, we did melt two helical turns of Syb (including up to residue 91). The principal effect is that the minimum equilibrium separation increases from 2 nm to 2.5 nm for both hydration and electrostatic repulsion with a constant charge.

A3.10 Robustness of Model Results

To judge the sensitivity of our main conclusions on the various assumptions we have made, we carried out a number of other simulations. Our main conclusion is that the

principal results of our model are quite robust with respect to uncertainty in the assumptions made.

A3.10.1 Electrostatics: We explored how electrostatics would affect the vesicle to plasma membrane repulsion. Fig. A3.9 shows results for the case where hydration repulsion is replaced by electrostatics using a fixed surface charge of -0.025 C/m^2 on the vesicle and the membrane. Evidently, with these parameters the electrostatic repulsion is weaker than the hydration repulsion. For one SNARE the end separation is ~2.4nm, which is smaller than the 3 nm seen for the hydration repulsion case (Fig. 3.4 *B*). However, when more than 1 SNARE is added to the system, the equilibrium SNARE end separation is constant at ~2 nm for 2-13 SNAREs, that is, it would be completely zippered shut.

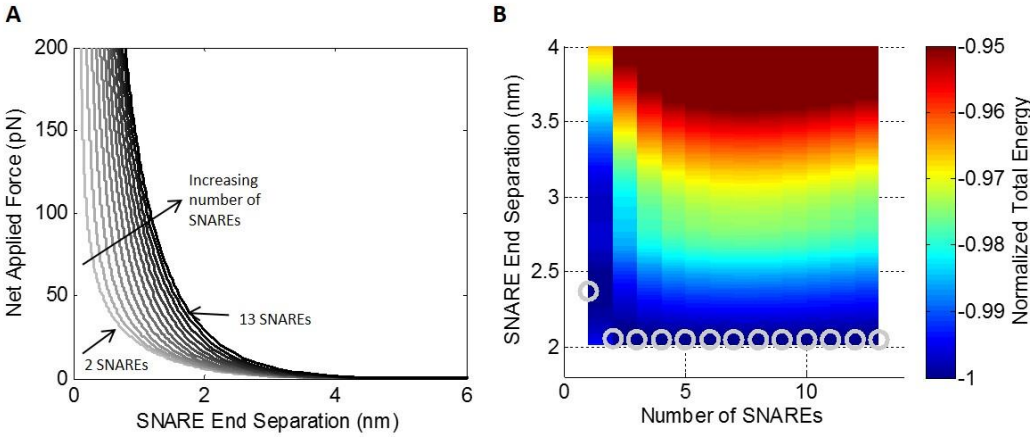

FIGURE A3.9 (*A*) The force in the membrane/vesicle system is shown as a function of SNARE end separation for a vesicle radius of 20nm with electrostatic repulsion with a fixed surface charge. (*B*) The corresponding contour plot of total

energy as a function of SNARE end separation distance and the number of SNAREs. Gray circles correspond to global energy minima representing the equilibrium SNARE end separation for a given number of SNAREs.

A3.10.2 Larger vesicles: Although our primary interest is in the smaller synaptic vesicles, the model can also be applied to study larger vesicles. Fig. A3.10 shows results for the case of a 100 nm vesicle.

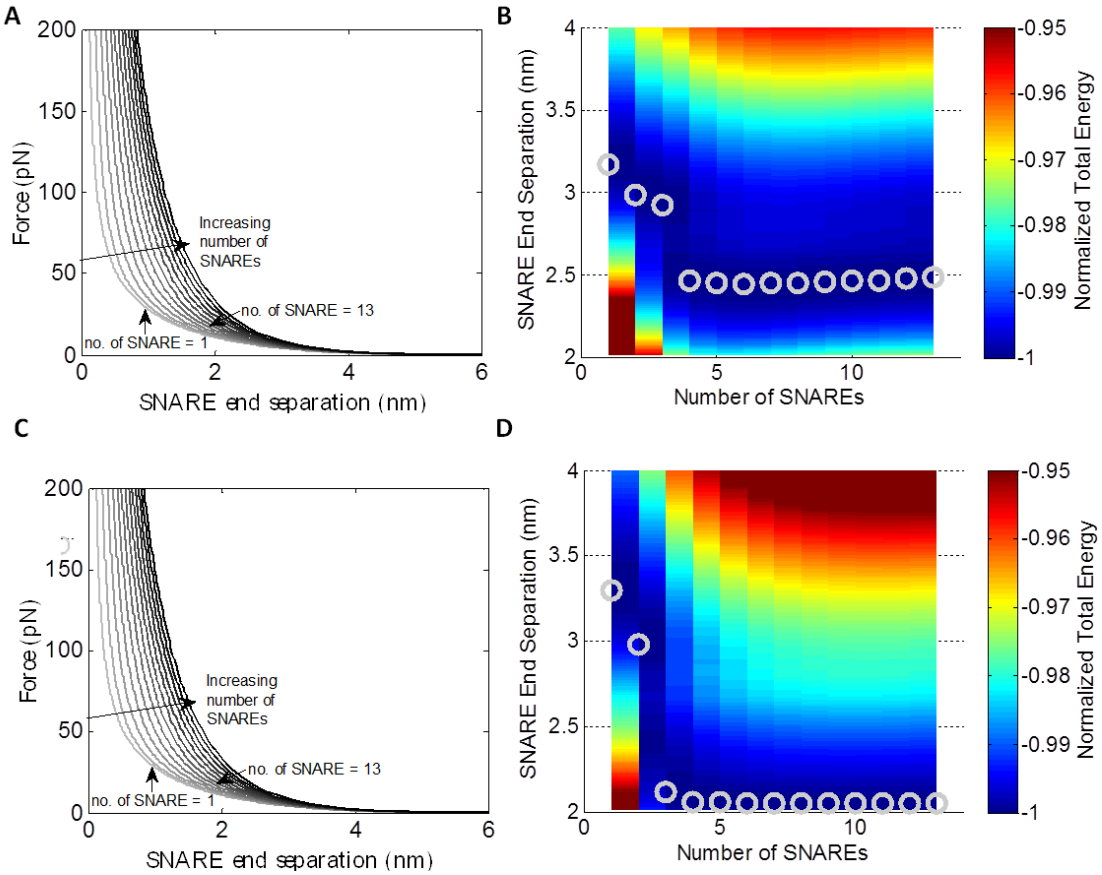

FIGURE A3.10 The force in the membrane/vesicle system is shown as a function of SNARE end separation for a vesicle radius of 100nm with (*A*) hydration repulsion and (*C*) electrostatic repulsion with a fixed surface charge. Contour plots of total energy as

a function of SNARE end separation distance and the number of SNAREs are shown for a vesicle radius of 100nm with (*B*) hydration repulsion and (*D*) electrostatic repulsion with a fixed surface charge. Gray circles correspond to global energy minima representing the equilibrium SNARE end separation for a given number of SNAREs.

For the hydration repulsion case the minima are significantly larger than those found for the 20nm case shown in Fig. 3.4 *B.* For four or more SNAREs the equilibrium separation is ~2.5nm which is different from the 20nm case where the separation is ~2nm and the SNARE bundle can be nearly fully zippered. For the case of electrostatic repulsion, for larger number of SNAREs the repulsion is still insufficient to open the SNARE except when there are three or fewer SNAREs.

A3.10.3Fixed Potential: We also carried out computations assuming a fixed potential of -25 mV on the vesicle and on the membrane as opposed to the fixed surface charge case that was assumed in the majority of the paper. The resulting force separation curves for the 20nm and 100nm vesicle cases are very similar to the case of fixed charge. This is not unexpected because the electrostatic force for fixed charge versus fixed potential cases becomes nearly the same for separations greater than the Debye screening length.

A3.10.4 Unraveling of Syb: Several other modifications were made to the cases shown in Fig. 3.4. There is some question about whether part of the syb helix unravels. We

have argued that the forces are small enough that the helical structure should be preserved. However, to test the effect on our prediction of potential unraveling, we allowed 2 helical turns to unravel and be represented by elasticity of a worm-like chain coil. Because the Syb helix touches the membrane at residue 91 and the CG model only contains up to residue 89, an extra 2 residues were added to the unraveled portion of Syb. The force displacement curve for the melted portions of Syb were modeled using a worm like chain model following Gao et al.(3) The force extension relationship was calculated using the Marko-Siggia formula

$$F = \frac{k_B T}{P_{melt}} \left[\frac{1}{4\left(1 - \frac{x_{melt}}{L_{melt}}\right)^2} + \frac{x_{melt}}{L_{melt}} - \frac{1}{4} \right] \tag{A3.16}$$

where P_{melt} is the persistence length of the melted segment (0.6 nm) and x_{melt} is the end to end distance of the melted segment. L_{melt}, the maximum end to end distance of the melted segment, was calculated assuming a 0.365 nm contour length per residue (3) which totaled to 1.3 nm due to ~2 helical turns being melted. The master force displacement curve was slightly adjusted by deleting the portions of the curve that corresponded to the 7 residues that are now accounted for using the WLC model. The SNARE end separation, x_{SNARE}, was defined by

$$x_{SNARE}(F) = x_{melt}(F) + x_{bundle}(F) + BW \tag{A3.17}$$

where x_{melt} is the end to end distance of the melted portion of Syb, x_{bundle} is described using the manipulated master force curve described in this section, and BW is the width of the SNARE bundle or the distance between the Syb and Syx C-termini when no external force is being applied. The corresponding results are shown is shown in Fig. A3.11 *A* for a 20nm vesicle with hydration repulsion and Fig. A3.12 *A* for a 20nm vesicle with electrostatic repulsion and a fixed surface charge.

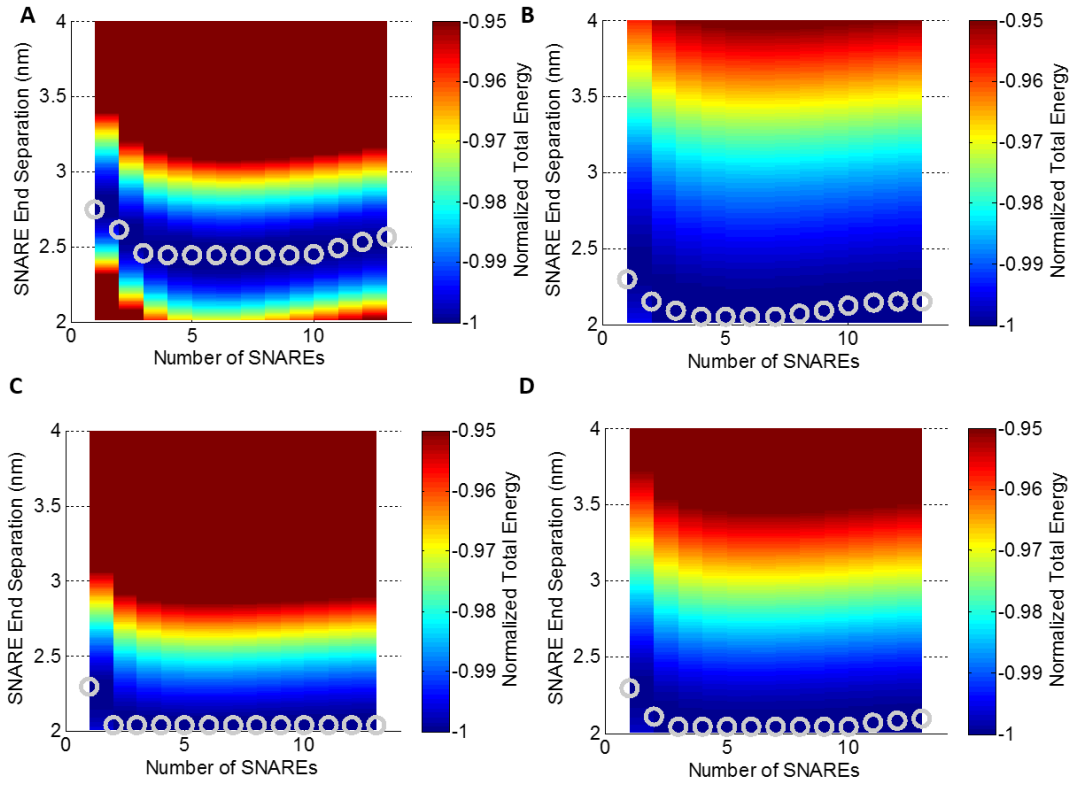

FIGURE A3.11 For a 20nm vesicle with hydration repulsion, contour plots of normalized total energy as a function of SNARE end separation distance and the number of SNAREs are shown. Gray circles correspond to energy minima representing the equilibrium SNARE end separation for a given number of

SNAREs. Several cases are shown: (*A*) 2 helical turns unraveled, (*B*) Syx frozen, (*C*) SNAP25 frozen, and (*D*) Syx and SNAP25 frozen.

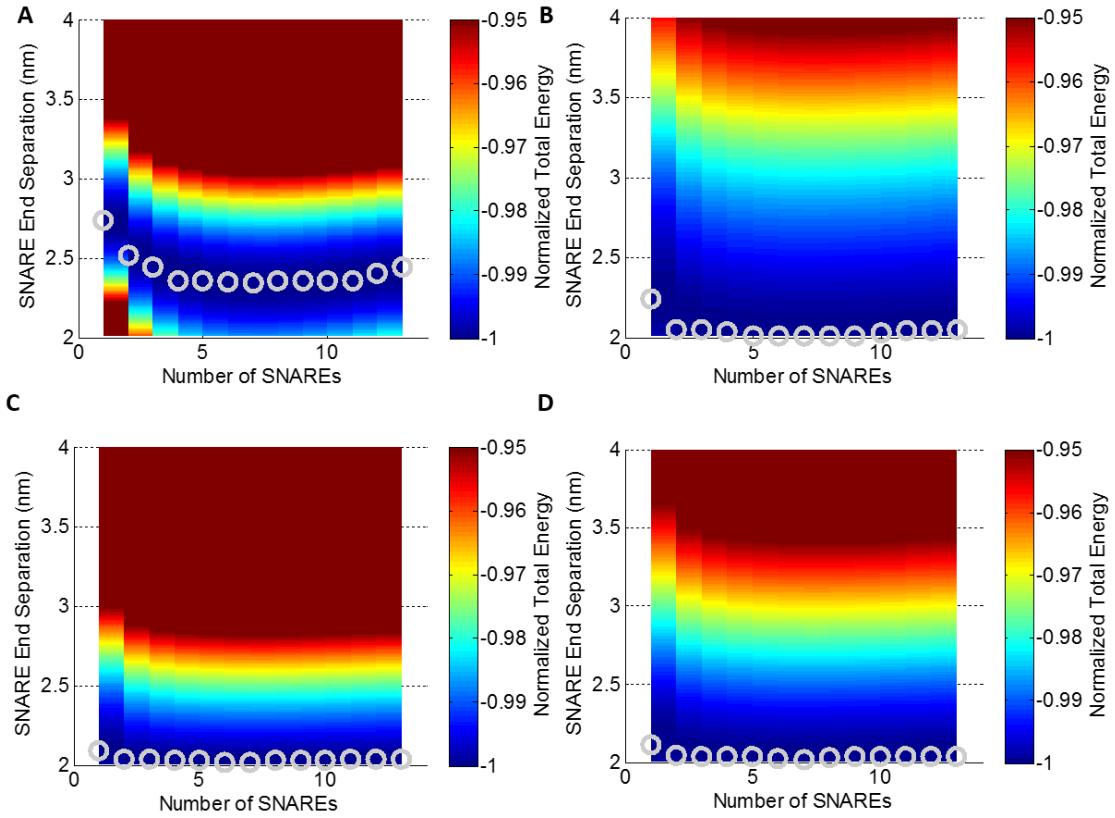

FIGURE A3.12 For a 20nm vesicle with electrostatic repulsion assuming a fixed surface charge, contour plots of normalized total energy as a function of SNARE end separation distance and the number of SNAREs are shown. Gray circles correspond to energy minima representing the equilibrium SNARE end separation for a given number of SNAREs. Several cases are shown: (*A*) 2 helical turns unraveled, (*B*) Syx frozen, (*C*) SNAP25 frozen, and (*D*) Syx and SNAP25 frozen.

In both cases, the results differ from those seen in Fig. 3.4 when unraveling was not permitted. For the case of hydration repulsion, the minimum separation is somewhat larger (~2.4 nm) than that shown in Fig. 3.4 *B* (~2.1 nm). There is a similar difference for the case of electrostatic repulsion.

A3.10.5 Freezing SNAP25 or Syx: In our simulations we allowed SNAP25 helices to be free to adjust their orientation. This mimics the optical tweezers experiment used to calibrate our model. However, the situation *in vivo* is likely different with SNAP25 and/or Syx constrained against motion. In order to see the effects of the positioning of SNAP25 in relation to the SNARE bundle we studied three variations: freezing Syx, freezing SNAP25, and freezing both Syx and SNAP25. When Syx was frozen, SNAP25 still remained associated with Syb. Anytime that SNAP25 was frozen at all, it remained associated with Syx. The energy calculations were repeated for the hydration repulsion case (Fig. A3.11) and the electrostatic repulsion case with fixed surface charge (Fig. A3.12). The freezing of helices in all of these cases has little effect on the minimum distance and number of SNAREs. The principal difference occurs for the one-SNARE case where the equilibrium distance reduces significantly.

A3.10.6 High Osmotic Pressure and Low Pretension Limit

Figs. 3.2 and A3.7 show cases of low osmotic pressure and plasma membrane tension where the plasma membrane bulges near the axis of symmetry because the attractive forces draw the two membranes to each other at their point of application but near the axis of symmetry only repulsion acts. Experiments suggest that prior to vesicle to

membrane fusion, the vesicle retains its spherical shape while the plasma membrane surface conforms when the two are in contact (13, 14). The continuum model was recalculated using high osmotic pressure in the vesicle and low pretension in the plasma membrane with constant potential. The resulting structures are shown for 10 and 15 SNAREs in Fig. A3.16.

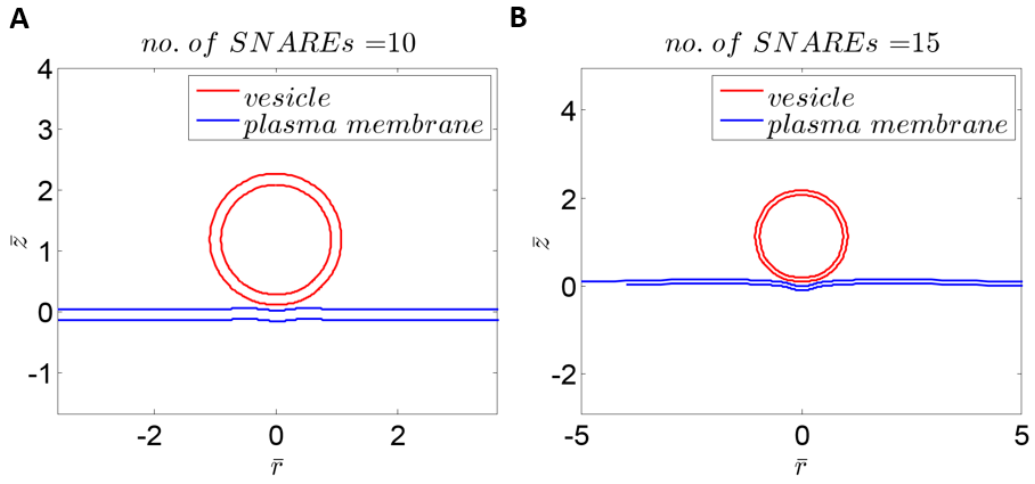

FIGURE A3.13 For a 20nm vesicle with high osmotic pressure and low pretension in the plasma membrane with constant potential the vesicle and plasma membrane structures are shown including their bilayer thickness for (*A*) 10 SNAREs and (*B*) 15 SNAREs.

Under the conditions of high osmotic pressure and low pretension when 10 SNAREs are present there is little bulging of the plasma membrane and the vesicle remains spherical when the vesicle and plasma membrane are brought together. The separation is relatively constant which is consistent with the Malsam et al.(13) and Hernandez et

al. (14). As the number of SNAREs is increased to 15, there is some bulging in the plasma membrane at the axis of symmetry. The vesicle has retained its spherical shape while the plasma membrane bends to conform to it.

The energy surface for this case is shown in Fig. A3.14. We note that there is little difference between these and those of Fig. 3.4 *B*. This suggests that our model is robust with respect to this uncertainty. (In particular, the value of vesicle osmotic pressure is difficult to estimate.)

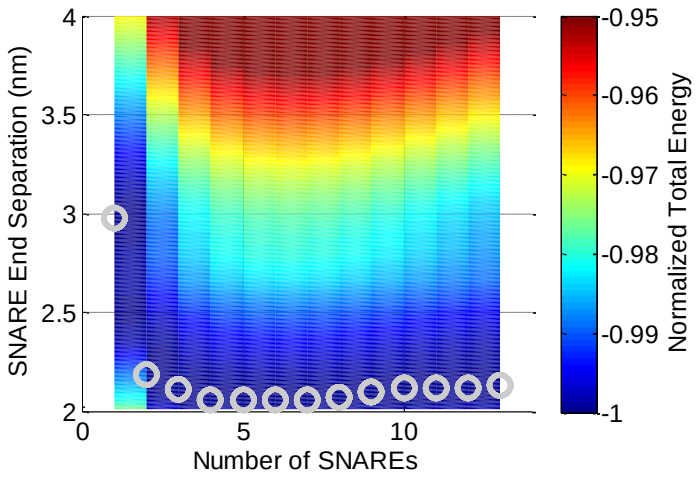

FIGURE A3.14 Contour of normalized total energy as a function of SNARE end separation and number of SNAREs for a 20nm vesicle with high osmotic pressure and low pretension in the plasma membrane, and with constant potential on the vesicle and plasma membrane. White circles correspond to energy minima representing the equilibrium SNARE end separation for a given number of SNAREs.

A3.10.7 High Vesicle Pressure, High Membrane Tension Vesicle-Membrane Model

In order to display the effects of the deformation considered in the continuum model, a more simplified analytical model of the Vesicle-Membrane system based on Bykhovskaia et al.(15) was calculated. The parameters used in the analytical model were consistent with those used in the continuum model as described in Section 3.3. Consider the case in which vesicle pressure P_o and the membrane tension T are sufficiently large such that neither the vesicle nor the membrane deform as they approach each other. In this case Bykhovskaia et al.(15) have shown that the force between the vesicle and membrane is given by

$$F = \frac{2\pi R\varepsilon\varepsilon_0}{l_D}\left(\frac{2\varphi_1\varphi_2}{\sinh\left(\frac{a}{l_D}\right)} - (\varphi_1^2+\varphi_2^2)\left(\coth\left(\frac{a}{l_D}\right)-1\right)\right) \qquad \text{(A3.18)}$$

for fixed surface potential and

$$F = \frac{\pi R l_D}{\varepsilon\varepsilon_0}\left(\frac{2\sigma_1\sigma_2}{\sinh\left(\frac{a}{l_D}\right)} + (\sigma_1^2+\sigma_2^2)\left(\coth\left(\frac{a}{l_D}\right)-1\right)\right) \qquad \text{(A3.19)}$$

for fixed charge. The force separation curves are shown for the vesicle-plasma membrane for several cases using this model in Figs. A3.15 and A3.16.

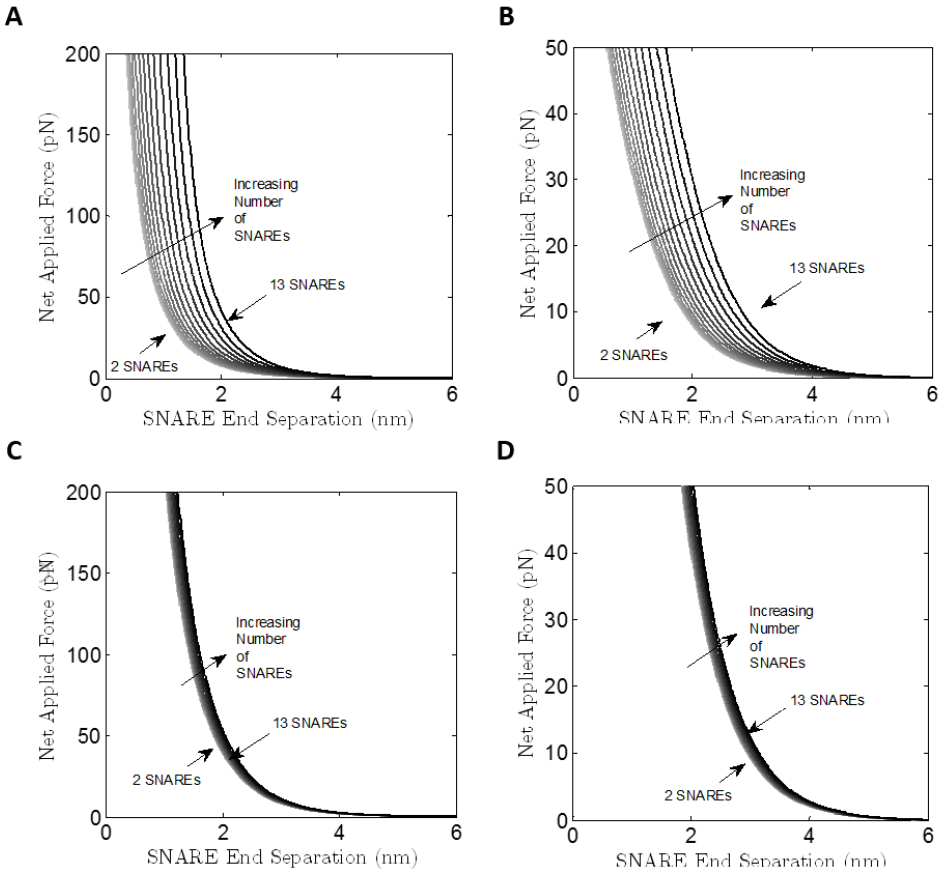

FIGURE A3.15 For the high vesicle pressure high membrane tension limiting case, the net applied force in the membrane/vesicle system is shown as a function of SNARE end separation for a vesicle with a (*A*) 20nm radius with fixed charge, (*B*) 20nm radius with fixed surface potential, (*C*) 100nm radius with fixed charge, and (*D*) 100nm radius with fixed surface potential.

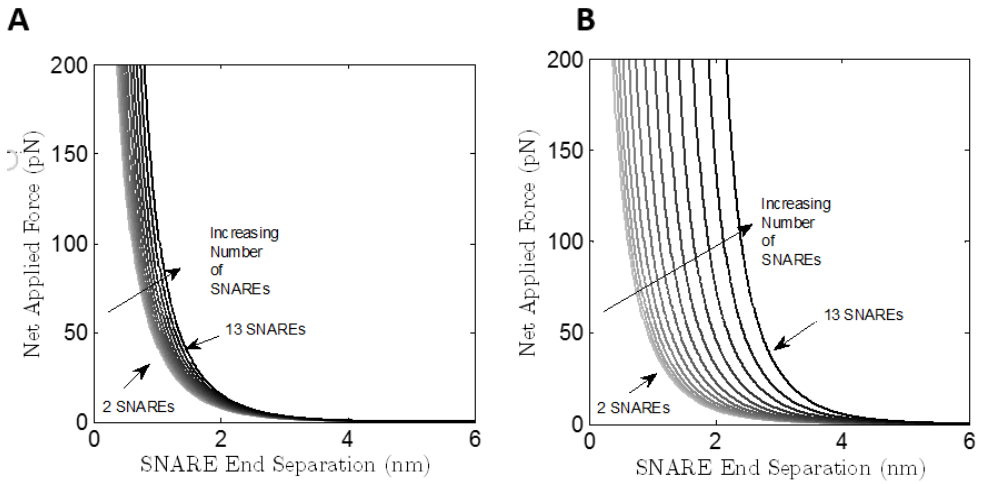

FIGURE A3.16 For the high vesicle pressure high membrane tension limiting case, the net applied force in the membrane/vesicle system is shown as a function of SNARE end separation for a radius for a vesicle with a 20nm radius with fixed charge when (*A*) the SNARE bundle diameter is 2nm and (*B*) the SNARE bundle diameter is 2nm.

A3.10.8 Effect of Lateral Bundle Width: Figure A3.17 shows results of a test of the sensitivity of the solution to the location of the SNAREs when the lateral size of the SNARE bundle was varied from 2nm in Fig. A3.17 *A* to 4nm in Fig. A3.17 *B* (the base case used is 3nm, Fig. 3.4 *B*). Increasing the lateral width of the SNARE bundle seems to have a significant effect on the solution. There is a minimum separation at 4 SNAREs. With the addition of more than 5 SNAREs the equilibrium separation again begins to increase all the way up to ~3nm with 13 SNAREs.

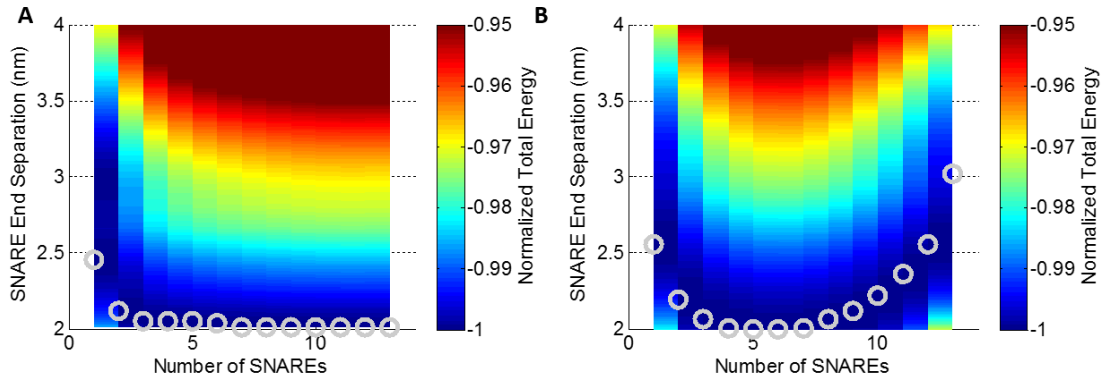

FIGURE A3.17 For the high pressure high tension limiting case, contour plots of normalized total energy as a function of SNARE end separation distance and the number of SNAREs are shown. Gray circles correspond to energy minima representing the equilibrium SNARE end separation for a given number of SNAREs. Several cases are shown for the vesicle with a radius of 20nm and fixed charge. The size of the SNARE bundle was varied to (*A*) 2nm and (*B*) 4nm.

1. SUPPORTING REFERENCES

1. Schlick, T. 2002. Molecular modeling and simulation: an interdisciplinary guide. New York: Springer.

2. Kubo, R. 2002. The fluctuation-dissipation theorem. Reports Prog. Phys. 29: 255–284.

3. Gao, Y., S. Zorman, G. Gundersen, Z. Xi, L. Ma, G. Sirinakis, J.E. Rothman, and Y. Zhang. 2012. Single reconstituted neuronal SNARE complexes zipper in three distinct stages. Science. 337: 1340–3.

4. Bruce Alberts Julian Lewis Keith Roberts, and Peter Walter, Alexander Johnson, M.R. 2002. Molecular Biology of the Cell. 4th ed. New York: Garland Science.

5. Ohsawa, K., H. Ohshima, and S. Ohki. 1981. Surface potential and surface charge density of the cerebral-cortex synaptic vesicle and stability of vesicle suspension. Biochim Biophys Acta. 648: 206–214.

6. Marra, J. 1986. Direct measurement of the interaction between phosphatidylglycerol bilayers in aqueous electrolyte solutions. Biophys. J. 50: 815–825.

7. Pekker, M., and M.N. Shneider. 2014. The surface charge of a cell lipid membrane. arXiv Prepr. arXiv. : 1401–1407.

8. Deserno, M. Fluid lipid membranes – a primer. 2007. http://www.cmu.edu/biolphys/deserno/pdf/membrane_theory.pdf

9. Kweon, D.H., C.S. Kim, and Y.K. Shin. 2002. The membrane-dipped neuronal SNARE complex: A site-directed spin labeling electron paramagnetic resonance study. Biochemistry. 41: 9264–9268.

10. Kweon, D.-H., C.S. Kim, and Y.-K. Shin. 2003. Regulation of neuronal SNARE assembly by the membrane. Nat. Struct. Biol. 10: 440–447.

11. Kim, C.S., D.H. Kweon, and Y.K. Shin. 2002. Membrane topologies of neuronal SNARE folding intermediates. Biochemistry. 41: 10928–10933.

12. Stein, A., G. Weber, M.C. Wahl, and R. Jahn. 2009. Helical extension of the neuronal SNARE complex into the membrane. Nature. 460: 525–528.

13. Malsam, J., D. Parisotto, T.A.M. Bharat, A. Scheutzow, J.M. Krause, J.A.G. Briggs, and T.H. Söllner. 2012. Complexin arrests a pool of docked vesicles for fast Ca2+-dependent release. EMBO J. 31: 3270–3281.

14. Hernandez, J.M., A. Stein, E. Behrmann, D. Riedel, A. Cypionka, Z. Farsi, P.J. Walla, S. Raunser, and R. Jahn. 2012. Membrane Fusion Intermediates via Directional and Full Assembly of the SNARE Complex. Science (80-.). 336: 1581–1584.

15. Bykhovskaia, M., A. Jagota, A. Gonzalez, A. Vasin, and J.T. Littleton. 2013. Interaction of the complexin accessory helix with the C-terminus of the SNARE complex: molecular-dynamics model of the fusion clamp. Biophys J. 105: 679–690.

Chapter 4

During the process of neurotransmission in a healthy neuron, a large number of synaptic vesicles are docked at the synapse. These docked vesicles wait for an electric impulse commonly known as an action potential. Upon the arrival of the action potential, these vesicles fire the packed neurotransmitter towards the neighboring neuron and hence transmitting the neural information. It is believed that a neuron fires approximately 100 synaptic vesicles over a course of 10 mins [1]. New neurotransmitter filled synaptic vesicles are supplied at the synapse to replenish the stock of active vesicles. This docking is mediated by the SNARE proteins, which brings the synaptic vesicle close to the neuron plasma membrane. During the process of docking, SNARE force is employed to encounter the hydrodynamic forces. The hydrodynamic forces originate from the flow of physiological fluid away from the spacing between the synaptic vesicle and neuron plasma membrane. The hydrodynamic force determines the time taken by SNARE complexes to dock a vesicle and make it fusion ready by positioning it close to the neuron plasma membrane. In this chapter we present a continuum mechanics based model to estimate the docking time. Experimentally, the docking time has been measured to be ~250 msecs [2]. We have used a lubrication theory based transient solution scheme along with a simplified continuum model of the system to calculate the value of docking time. We observed that during the docking, SNARE force needs to go through a rapid change of magnitude to produce the required docking time of the order of msecs. The nature of force needed for docking can provide insight into the structure of the SNARE proteins and their zippering. This model can also be used to predict the

docking time for a similar system based on the force variation during the course of process.

4. 1 Abstract

Synaptic vesicle fusion is a crucial step in the neurotransmission process. Neurotransmitter-filled vesicles are pre-docked at the synapse, by the mediation of ribbon structures and SNARE proteins at the ribbon synapses. An electric impulse triggers the fusion process of pre-docked vesicle, leading to the formation of fusion pore and subsequently resulting into the release of neurotransmitter into the synaptic cleft. In the present work, a continuum model of lipid membrane along with lubrication theory is used to determine the traverse time of the synaptic vesicle under the influence of hydrodynamic forces. We find that the traverse time is strongly dependent on how fast the driving force decays or grows with closure of the gap between vesicle and plasma membrane. If the right behavior is chosen, the traverse time obtained is of the order of few hundred milliseconds and lies within the experimentally obtained value of ~ 250 msecs [2]. We hypothesize two different force behaviors, which comply with the experimental findings of pre-fusion docking of synaptic vesicle at the ribbon synapses. The common theme in the proposed force models is that driving force has to very rapidly increase or decrease with the amount of clamping.

4.2 Introduction

For a continuous neurotransmission process, neurotransmitter-filled synaptic vesicles are resupplied and primed for fusion, at the ribbon synapse. These vesicles are docked at the synapse by ribbon structures [3], [4] and proteins of the SNARE (Soluble N-

ethylmaleimide-sensitive-factor Attachment protein REceptor) family [5]–[9]. Specifically, there are 3 SNARE family proteins involved in the docking process: Synaptobrevin 2 (syb), Syntaxin 1 (syx) and SNAP-25 [10]. Syb is attached to the synaptic vesicle at one end, and is referred as 'v-SNARE' [11]. Attached to the plasma membrane are the 't-SNAREs': Syx and SNAP-25 [12], [13]. During the pre-fusion docking process, the ribbon structure drives the vesicle to the synapse so that the v-SNARE and t-SNAREs are within striking distance of each other allowing clamping to initiate [2].

Using flouresence microscopy, Zenisek et al. [2] showed that the time to dock a vesicle is about 250 msecs. From this, they concluded that it takes about 250 msecs for the pre-fusion docking machinery to close the gap between the membranes from $\sim 20\,\text{nm}$ [2] to $\sim 2\,\text{nm}$ [14]. The separation of $\sim 2\,\text{nm}$, is often considered as the distance below which electrostatic and hydration pressure dominates [14]–[17]. At this stage, vesicle is referred to as fusion ready, and it waits for an electric impulse to initiate the fusion process [2], [18], [19]. Beyond this separation ($> 2\,\text{nm}$), the dominant impeding force for the docking comes from hydrodynamics. As the vesicle is pulled towards the plasma membrane, water has to be squeezed out. For this to occur, an outwards pressure gradient is required. This pressure deforms the membranes and affects the traverse time.

In this paper, we model this phase of vesicle docking where hydrodynamics forces are dominant. Our results show that the traverse time is very sensitive to the time history of the driving force. To agree with the time measured by Zenisek et al. [2], the driving

force should either decay or rise very rapidly with the gap closure. The length scale over which this rapid force change takes place is of the order of few nanometers.

4.3 Materials and Methods

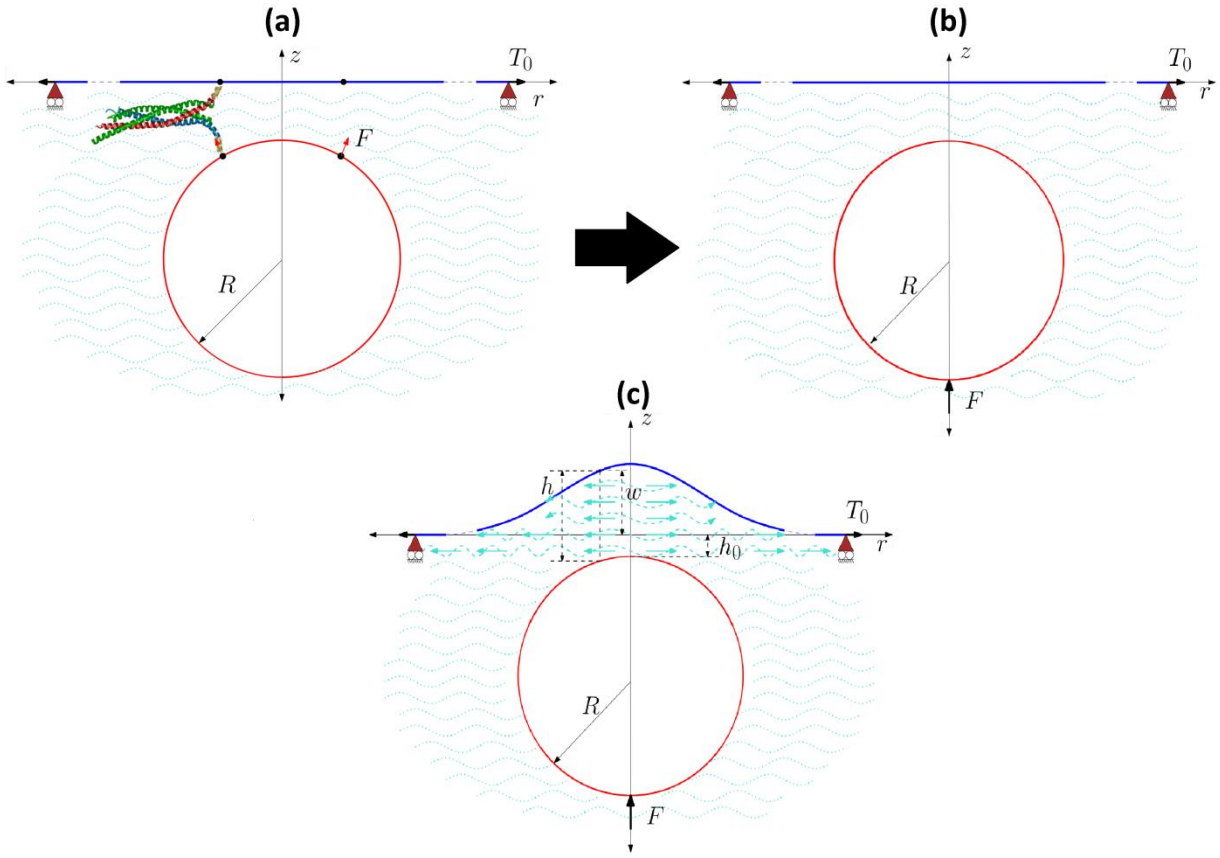

Fig 4.1: (a) Synaptic vesicle docking mediated by ribbon structure and SNARE proteins, (b) the driving force is represented by single force acting on the south pole of the vesicle (c) deformed plasma membrane under hydrodynamic and driving force, horizontal arrows indicate direction of fluid flow.

4.3.1 Model: Geometry, Fluid flow and Membrane mechanics

The synaptic vesicle is assumed to be a *rigid* sphere of radius R. The entire compliance of the system comes from the plasma membrane of the neuron. A justification is that cryo-electron micrsocopy images of synaptic vesicles docked near the plasma membrane shows very little deformation [20], [21] in the vesicles. This could be due to high osmotic pressure across the synaptic vesicle membrane [22], pretaining to the high concentration of neurotransmitter inside it. In addition, the vesicle is expected to be stiffer since it is much smaller than the plasma membrane. Therefore, our model lumps all the deformation to the much larger plasma membrane which before deformation, is modeled as a flat circular disk with radius l. It is held at the edge $(r = l)$ by a tension force, which is the pretension, T_0 of the neuron. Varying this pretension will allow us to change the compliance of the system. The plasma membrane is modeled as a lipid bilayer using a continuum theory developed by Jenkins et al. and Steigmann et al. [23]–[26]. The continuum theory has been used in literature for mechanistic modelling of the lipid membrane associated processes in red blood cell shape analysis [23], receptor-mediated endocytosis [27], micropipette aspiration of and curvature sorting of proteins [28]–[31], two component lipid membrane systems [32], [33], vesicle adhesion [34]–[37], and synaptic vesicle fusion [14], [38], [39].

The fluid layer between vesicle and plasma membrane is assumed to be sufficiently thin so we can use Reynold's equation in elasto-hydrodynamic lubrication theory to model the flow [40]–[45]. This theory is well suited for the present problem for the following reasons,

1) The flow between the synaptic vesicle and plasma membrane is in the low Reynold's number regime, hence it can assumed to be laminar,

2) The film thickness is relatively small compared to the size of the synaptic vesicle.

As in Zenisek et al. [1], we assume the driving force to overcome hydrodynamics is provided by the ribbon structure and SNARE complex. Because the vesicle is rigid, the driving force can represented by a point force F acting on the south pole of the vesicle as shown in Figs. 4.1a and 4.1b. The magnitude of this force depends on the number of SNARE complex, n acting on the vesicle which can vary from $n=1$ to 11 [46]–[50]. This membrane model is coupled with a hydrodynamic solver based on lubrication theory. This allows us to determine the flow as well as the traverse time of the vesicle given the time history of *F*.

4.3.2 Lubrication theory

The problem is axisymmetric. For axisymmetric flow, Reynold's equation is [51],

$$\nabla\left(h^3\nabla p\right)=12\eta\frac{\partial h}{\partial t}. \qquad 4.1$$

where r is the radial distance from the symmetry axis (z axis) of the vesicle (see Fig. 4.1c), ∇ is the gradient operator in cylindrical coordinates, $h(r,t)$ is the thickness of the fluid film, $p(r,t)$ is the fluid pressure and η is the dynamic viscosity of water. The film thickness $h(r,t)$ is related to the deflection of the membrane $w(r,t)$ and the shape of the sphere by,

$$h(r,t)=-h_0(t)+\frac{r^2}{2R}+w(r,t), \qquad 4.2$$

where $h_0(t)$ is the vertical separation between the lowermost point on the sphere and the plasma membrane at $r = l$, where the membrane deflection $w(r,t)$ is zero, as shown in Fig. 4.1c. We assume l to be much greater than the region where pressure is significant. The second term on the right hand side of eq. 4.2 approximates the local shape of the sphere by a paraboloid.

4.3.3 Elastic deformation of the plasma membrane : Calculation of w

The deformation of the membrane is coupled to the flow via the fluid pressure, $p(r,t)$ which acts normal to the surface. The governing equations of the lipid membrane in the full form can be used to obtain the deformation in the plasma membrane for a general pressure distribution. For the present work, the governing equations have been linearized under the small deflection assumption (see SI for details). The linearized equation is found to be,

$$\frac{\kappa}{2}\nabla^4 w(r,t) - T_0 \nabla^2 w(r,t) = -p(r,t), \qquad 4.4$$

where κ is the bending rigidity of the lipid membrane. Eq. 4.4 is solved analytically (see SI for details) and the deflection $w(r,t)$ is found to be,

$$w(r,t) = \frac{1}{T_0}\left[K_0\left(\sqrt{2T_0}r\right)\int_0^r I_0\left(\sqrt{2T_0}\xi\right) p(\xi,t)\xi d\xi + I_0\left(\sqrt{2T_0}r\right)\int_r^\infty K_0\left(\sqrt{2T_0}\xi\right) p(\xi,t)\xi d\xi \right], \qquad 4.5$$

where, $I_0(r)$ and $K_0(r)$ are the modified Bessel functions of the 1st and 2nd kind respectively.

4.3.4 Numerical solution

Details of the numerical methods are given in SI. Briefly, the rigid sphere (vesicle) is moved towards the plasma membrane at a prescribed rate, $\frac{\partial h_0}{\partial t}$. For a given h_0 and $\frac{\partial h_0}{\partial t}$, eq. 4.1 is solved iteratively, to determine the pressure distribution, $p(r,t)$ at a given time. The force F is calculated using the force balance equation,

$$F = 2\pi \int_0^l p(r,t) r dr . \qquad 4.6$$

4.4 Results

Much insight can be gained by considering the special case of an undeformable plasma membrane. This case provides a lower bound for the traverse time. Also, since the solution is exact, we can study analytically how the traverse time depends on the variation of clamping force with time. Details of solution are provided in the SI, here we state the key results.

4.4.1 Undeformable plasma membrane limit

$F(t) = nF_1(t)$, $t > 0$, denote the time history of force, where n is the number of SNARE complexes and $F_1(t)$ is the force exerted by one SNARE complex. Let us first assume that the force acting on the vesicle is a constant independent of time, that is,

$$F_1(t) = 17\,pN , \qquad \text{for all } t > 0 , \qquad 4.7$$

where 17pN is the *peak* force exerted by one SNARE complex [52]. The tranverse time t_f is found to be (see SI for details)

$$t_f = \frac{6\eta\pi R^2}{F}\ln\left(\frac{h_{0i}}{h_{0f}}\right), \qquad 4.8$$

where, $h_{0i} \approx 20nm$ and $h_{0f} \approx 2nm$ are the separations between the vesicle and plasma membrane at $t = 0$ and $t = t_f$ respectively. The presence of the logarithmic function indicates that the traverse time is insensitive to the initial separation. Fig. 3 shows the dependence of the traverse time versus to number of SNARE complexes. For $n = 4$, it is about 200 nanoseconds, which is *6 orders of magnitude smaller* than the experimental value of 250 milliseconds [2].

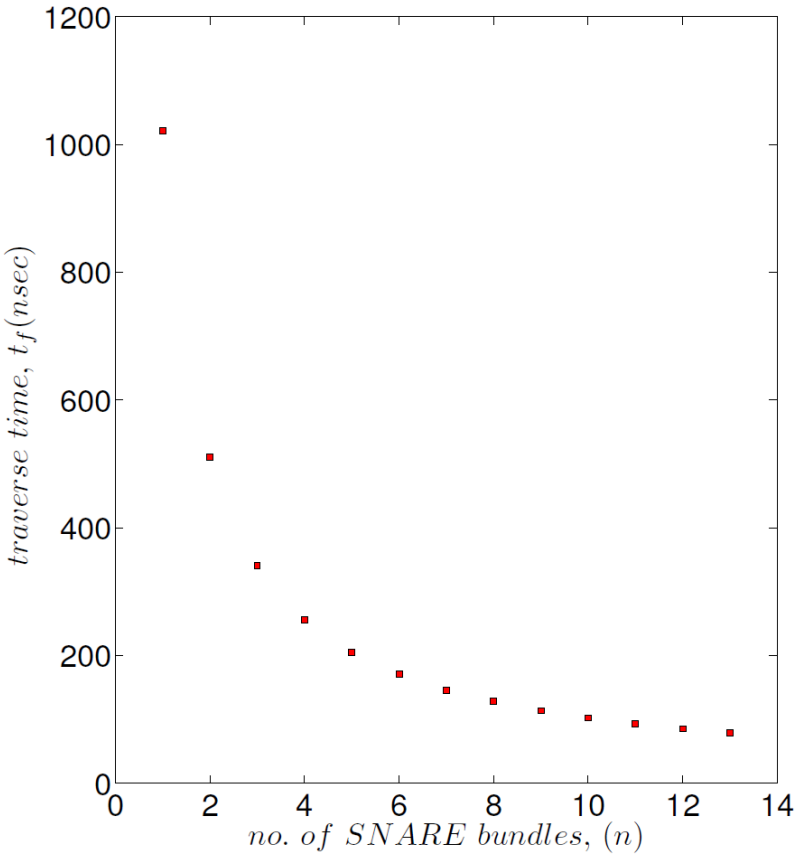

Fig 4.2: Traverse time of the vesicle for a constant force.

Experiments suggested that the SNARE clamping force is not a *constant*, but varies with distance between the clamps [52], [53]. This motivates us to use a clamping force that varies with distance between the sphere and the membrane, for the present case, this distance is $h_0(t)$. We assume that,

$$F(t) = nF_{1\max}\left[\frac{h_0(t)}{h^*}\right]^m, \qquad \text{for all } t > 0, \tag{4.9}$$

where, m governs the rate of decay of force (larger m implies faster decay) and $h^* \approx 20nm$, the separation between the synaptic vesicle pool and plasma membrane [2], is used as a scaling parameter for the separation and $F_{1,\,max} = 17\,pN$. Eq. 4.9 states that clamping force is maximum when the SNARE complex zipping starts and reduces to a very small value towards the end of docking. The traverse time for this particular force history is (see SI for details),

$$t_f = \frac{6\eta\pi R^2}{mnF_{1max}}\left[\left(\frac{h^*}{h_{0f}}\right)^m - \left(\frac{h^*}{h_{0i}}\right)^m\right]. \tag{4.10}$$

Fig. 4.3 plots t_f versus the number of SNARE complexes *n*. It shows that the traverse time is very sensitive to the rate of decay the SNARE's clamping force. To agree with the experimental result of Zenisek et al. [2], the force has to decay rapidly with separation, with *m* between 5.5 - 6.5.

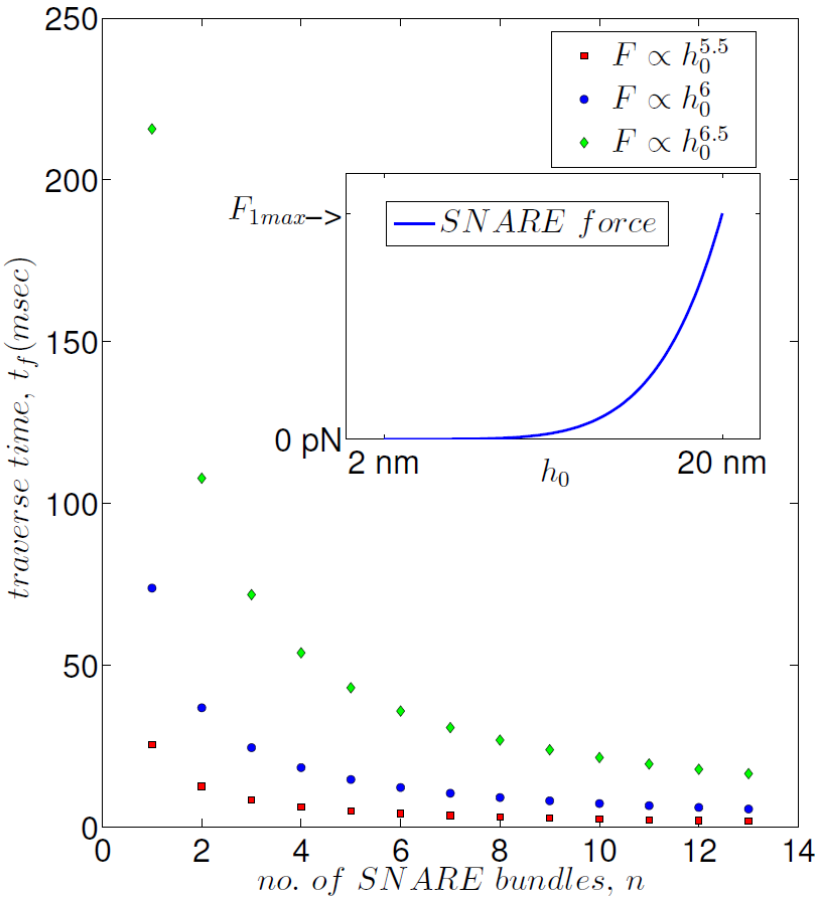

Fig 4.3: Traverse time of the vesicle versus number of SNAREs using eq. 4.10. *m* governs the rate of decay of SNARE force with distance.

4.4.2 Deformable membrane

The result in previous section shows that decay of clamping force is the dominant factor controlling the traverse time. For example, increasing the number of SNARE complexes or the clamping force will not change the traverse time by several orders of magnitude. However, one may still argue that membrane deformation can also increase the traverse time, here we study this possibility by solving eq. 1 in conjunction with the eq. 4.5. All calculations are performed with $\eta = 0.001$ Pa-sec

(kinematic viscosity of water) and $R = 20\,nm$. We fixed the bending stiffness of the membrane to be $\kappa \sim 20 k_B T$ [54]. This means that the compliance of system depends on the pretension T_0. We vary the decay constant, m, the number of SNARE complexes n and T_0, which controls the compliance of the system.

Fig. 4.4 plots the logarithm of the transverse time t_f versus the decay exponent m, for $n = 1$ and for three different plasma membrane tension T_0 . Consistent with the undeformable membrane case, the traverse time is extremely sensitive to the decay constant m. This result is in conjunction with result of our previous section, that is, the force to dock the vesicle must be derived from the posterior part of the SNARE complex. In particular, varying the complaince of the system by changing T_0, has negligible impact on the traverse time compared to that of m.

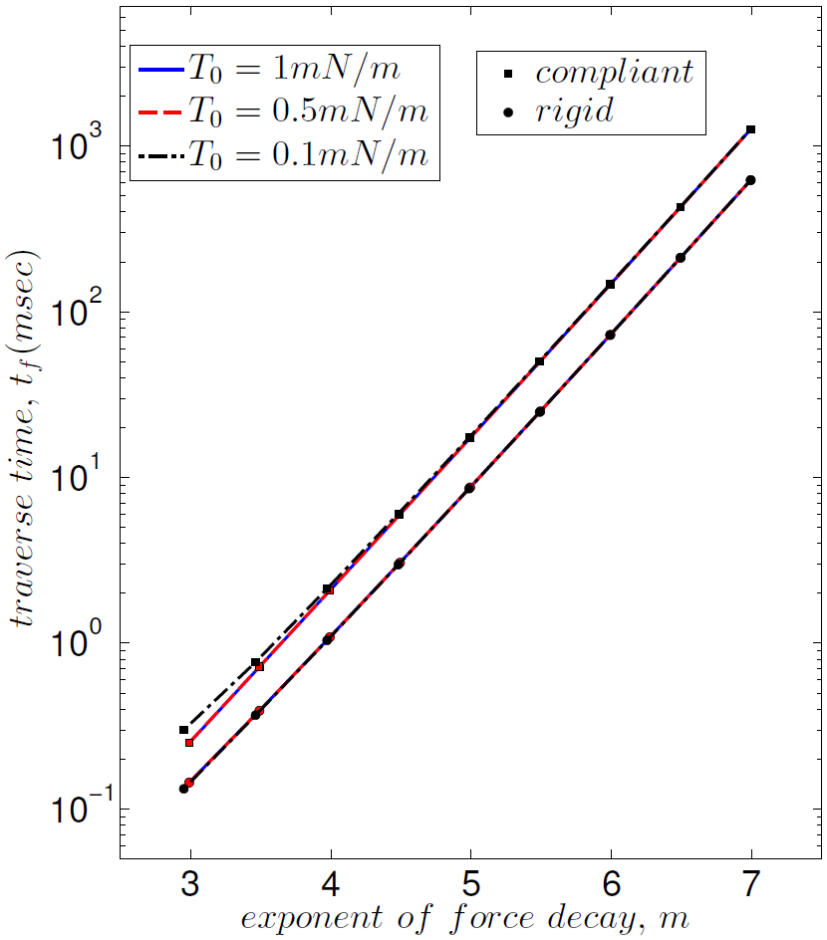

Fig 4.4: traverse time with varying decay exponent, for $n = 1$

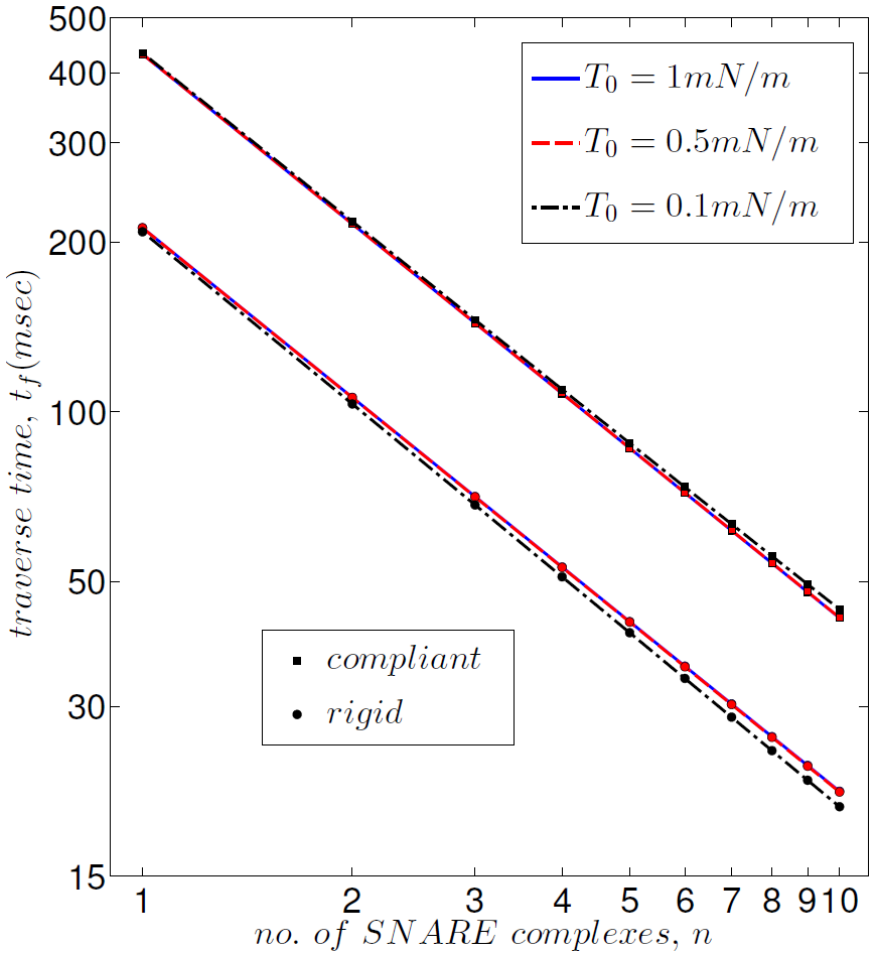

Fig 4.5: Traverse time with varying number of SNAREs

Fig. 4.5 shows the effect of varying the number of SNARE complexes, n on the traverse time, with $m = 6.5$ and three different values of T_0. The traverse time is a straight line in a log-log plot, indicating that the transverse time is inversely proportional to n, which is consistent with eq. 4.10 (un-deformable membrane). Again, variation in membrane pretension T_0 has little effect on traverse time, indicating that the compliance of the system plays a secondary role in controlling the traverse time. Clearly, the traverse time is much more sensitive to the decay constant than the number of SNARE complexes.

The effect of pretension T_0 is shown in Fig. 4.6. As one increases the pretension, the traverse time very slowly approaches the undeformable membrane limit given by eq. 4.10. Our numerical result shows that the traverse time is approximately constant for $T_0 \geq 10^{-2} mN/m$. This is about three orders of magnitude smaller than the rupture strength ($T_{rupture} = 10 mN/m$, [55], [56]) of lipid membranes. This result again supports the fact that compliance or pretension is not an important factor compared to decay behavior in determining the traverse time of the synaptic vesicle.

As expected the traverse time of the synaptic vesicle is always higher for deformable membranes. Our numerical result shows that when the synaptic vesicle is docked $\sim 2nm$ from the plasma membrane, the deformation in the plasma membrane was negligible. This result is in agreement with the cryo-electron microscopy images of the synapse, which shows negligible deformation in the plasma membrane, with synaptic vesicle docked and ready for fusion [20], [21].

(a) (b)

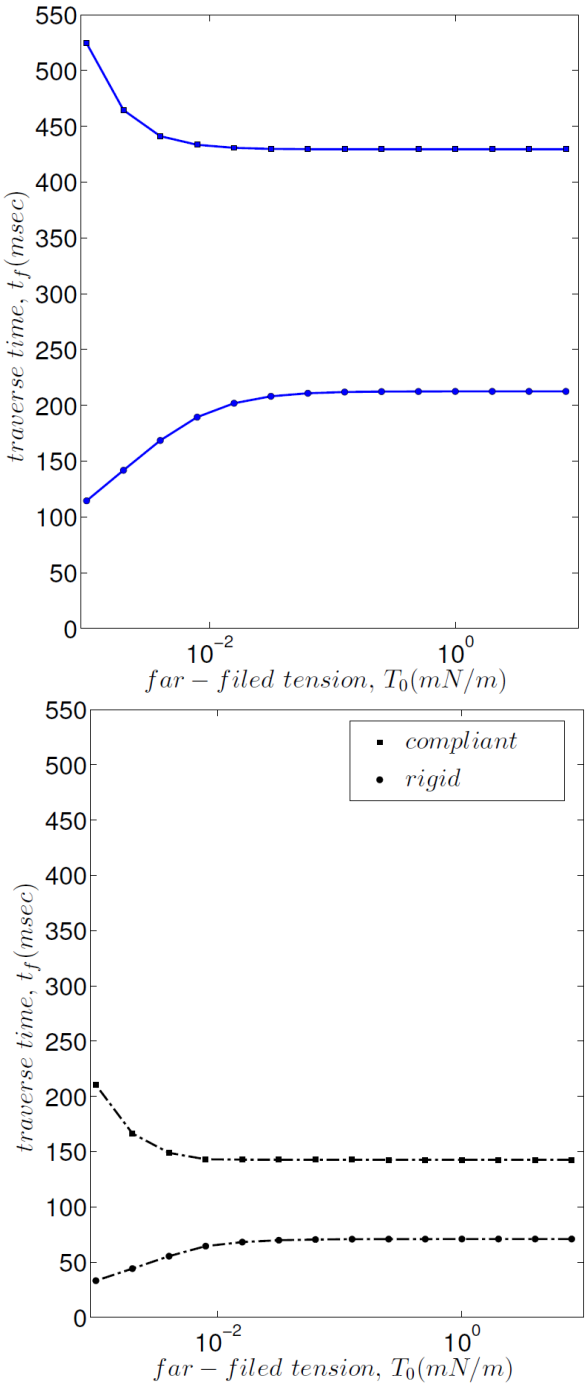
550
500
450
400
350
300
250
200
150
100
50
0
10^{-2}
10^{0}
$traverse\ time,\ t_f(msec)$
$far-filed\ tension,\ T_0(mN/m)$
$compliant$
$rigid$

(c)

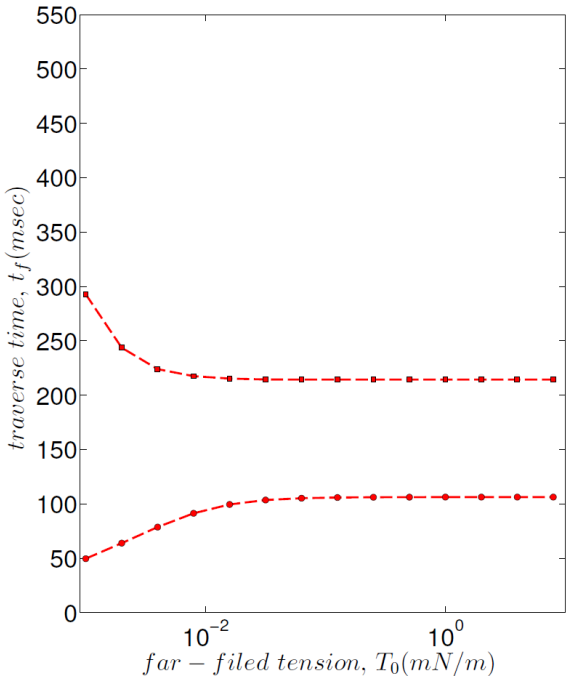

Fig 4.6: Traverse time with varying number of pretension, for number of SNAREs (a) $n=1$ **(b)** $n=2$ **and (c)** $n=3$

4.4.3 Different force model

From the comparison of rigid and compliant model of the plasma membrane, a very clear conclusion can be drawn that the traverse time is extremely sensitive to how the driving force varies with distance between clamps. The elasticity of the membrane and the magnitude of the force have relatively small effect on the traverse time. The force behavior described in the previous analysis is in agreement with the force behavior obtained from SNARE *un-zipping* experiment [52], [53]. However, it is possible that the SNARE complex zipping behavior can be very different and the ribbon structure might drive the vesicle for a part of its traversal. In the light of this, we propose to study another force model. Since we have demonstrated that the compliance of membrane has little effect on the transverse time, all results in this section are obtained

using the undeformable plasma membrane limit where an exact solution can be found. The force behavior is assumed to have the form:

$$F(t) = nF_{1\max}\left[\frac{h^*}{h_0(t)}\right]^m . \qquad \text{for all } h_0(t) \geq h^* \qquad 4.11$$

This force model is based on the idea that as the SNARE complex zips, the force increases. The clamping force reaches a maximum value $nF_{1\max}$ when the synaptic vesicle is within $h^* \sim 2\,nm$ proximity of the plasma membrane, after which strong repulsive forces (electrostatic and hydration forces) acts to resist docking (not modeled by eq. 4.11). The parameter m in eq. 4.11 controls the rate of increase of the clamping force.

Fig. 4.7a plots the traverse time versus the number of SNARE complexes for three different values of m. It should be noted that, a change in the value of m impacts the traverse time much severely than changing the value of SNARE complexes. In order to reach a traverse time of 250 msecs, we find $m \approx -6.5$. The variation of force versus h_0 is shown for $m \approx -6.5$ is given in the insert of Fig. 4.7a showing that, the SNARE force changes in a matter of few nanometers. For most of the traverse the vesicle is driven towards the plasma membrane by the ribbon structure and for the last stretch SNARE proteins take over the task.

Fig. 4.7b shows the effect of varying the peak force which can be applied by the SNARE complex on the traverse time. The peak force was varied in the range as reported in the literature [52], [53]. The impact is not yet as big as varying the exponent of force behavior.

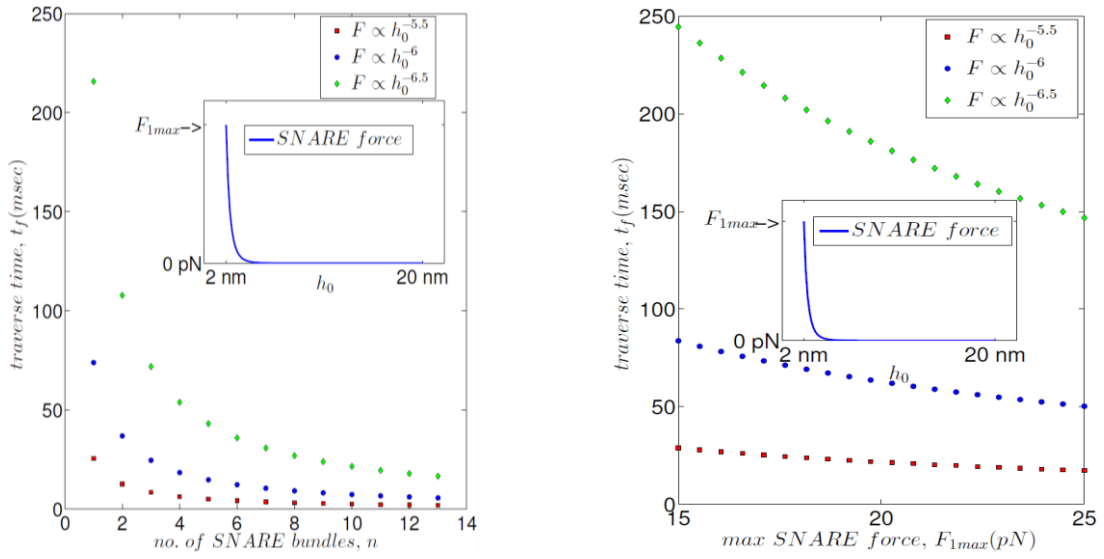

(a) (b)

Fig 4.7: Traverse time of synaptic vesicle vs. a) number of SNARE complex when $F_{1max} = 17\,pN$ b) F_{1max} when number of SNARE complexes, $n = 1$

4.5 Conclusions

Using elasto-hydrodynamic lubrication theory, we determine the docking time of a synaptic vesicle against the plasma membrane of a neuron. This docking is driven by the force exerted by the SNARE complexes and is resisted by hydrodynamics.

The main conclusions are:

1. The decay of the clamping force of SNARE complex is the most important factor in determining the traverse time of the synaptic vesicle.
2. The effect of membrane pre-tension and number of SNARE complex is negligible in comparison to the impact of the decay in clamping force.
3. The rapid clamping force decay indicates the possibility that the posterior segment of SNARE complex is the force generating machinery.

4. The clamping force decays down to very small values by the end of docking process, when the vesicle is fusion ready. Our result suggests the possibility of other force regulating machineries that are needed to bring the synaptic vesicle closer to the plasma membrane for exocytosis. This is still a subject of debate, but complexin (cpx) is believed to be a force regulatory agent which initiates the further clamping of the SNARE complex on the arrival of electric impulse [57]–[61].

Bibliography

[1] K. Ikeda and J. M. Bekkers, “Counting the number of releasable synaptic vesicles in a presynaptic terminal.,” *Proc. Natl. Acad. Sci. U. S. A.*, vol. 106, no. 8, pp. 2945–2950, 2009.

[2] D. Zenisek, J. A. Steyer, and W. Almers, “Transport, capture and exocytosis of single synaptic vesicles at active zones.,” *Nature*, vol. 406, no. 6798, pp. 849–54, Aug. 2000.

[3] R. Heidelberger, W. B. Thoreson, and P. Witkovsky, “Synaptic transmission at retinal ribbon synapses,” *Progress in Retinal and Eye Research*, vol. 24, no. 6. pp. 682–720, 2005.

[4] A. J. Mercer and W. B. Thoreson, *The dynamic architecture of photoreceptor ribbon synapses: cytoskeletal, extracellular matrix, and intramembrane proteins.*, vol. 28, no. 6. 2011.

[5] J. B. Bock and R. H. Scheller, “SNARE proteins mediate lipid bilayer fusion.,” *Proc. Natl. Acad. Sci. U. S. A.*, vol. 96, no. 22, pp. 12227–12229, 1999.

[6] Y. A. Chen and R. H. Scheller, “SNARE-mediated membrane fusion.,” *Nat. Rev. Mol. Cell Biol.*, vol. 2, no. 2, pp. 98–106, 2001.

[7] R. Jahn and R. H. Scheller, “SNAREs--engines for membrane fusion.,” *Nat. Rev. Mol. Cell Biol.*, vol. 7, no. 9, pp. 631–43, 2006.

[8] J. G. Duman and J. G. Forte, “What is the role of SNARE proteins in membrane fusion?,” *Am. J. Physiol. Cell Physiol.*, vol. 285, no. 71, pp. C237–C249, 2003.

[9] M. A. Poirier, W. Xiao, J. C. Macosko, C. Chan, Y. K. Shin, and M. K. Bennett, “The synaptic SNARE complex is a parallel four-stranded helical

bundle.," *Nat. Struct. Biol.*, vol. 5, no. 9, pp. 765–769, 1998.

[10] J. Rizo and C. Rosenmund, "Synaptic vesicle fusion.," *Nat. Struct. Mol. Biol.*, vol. 15, no. 7, pp. 665–74, 2008.

[11] F. Deák, O.-H. Shin, E. T. Kavalali, and T. C. Südhof, "Structural determinants of synaptobrevin 2 function in synaptic vesicle fusion.," *J. Neurosci.*, vol. 26, no. 25, pp. 6668–76, 2006.

[12] B. Liang, V. Kiessling, and L. K. Tamm, "Prefusion structure of syntaxin-1A suggests pathway for folding into neuronal trans-SNARE complex fusion intermediate.," *Proc. Natl. Acad. Sci. U. S. A.*, vol. 110, no. 48, pp. 19384–9, 2013.

[13] S. Gonzalo, W. K. Greentree, and M. E. Linder, "SNAP-25 is targeted to the plasma membrane through a novel membrane- binding domain," *J. Biol. Chem.*, vol. 274, no. 30, pp. 21313–21318, 1999.

[14] N. Fortoul, P. Singh, C.-Y. Hui, M. Bykhovskaia, and A. Jagota, "Coarse-Grained Model of SNARE-Mediated Docking.," *Biophys. J.*, vol. 108, no. 9, pp. 2258–69, 2015.

[15] S. Aeffner, T. Reusch, B. Weinhausen, and T. Salditt, "Energetics of stalk intermediates in membrane fusion are controlled by lipid composition.," *Proc. Natl. Acad. Sci. U. S. A.*, vol. 109, no. 25, pp. E1609–18, Jun. 2012.

[16] L. J. Lis, M. McAlister, N. Fuller, R. P. Rand, and V. a Parsegian, "Interactions between neutral phospholipid bilayer membranes.," *Biophys. J.*, vol. 37, no. March, pp. 657–665, 1982.

[17] R. P. Rand and V. A. Parsegian, "Hydration forces between phospholipid

bilayers," *BBA - Reviews on Biomembranes*, vol. 988, no. 3. pp. 351–376, 1989.

[18] F. Valtorta, M. Pennuto, D. Bonanomi, and F. Benfenati, "Synaptophysin: Leading actor or walk-on role in synaptic vesicle exocytosis?," *BioEssays*, vol. 26, no. 4. pp. 445–453, 2004.

[19] W. Almers, F. W. Tse, W. Almers, W. Almers, L. A. Breckenridge, A. E. Spruce, H. L. Atwood, F. W. Tse, G. I. Augustine, M. P. Charlton, S. J. Smith, W. E. Balch, B. S. Glick, J. E. Rothman, J. Bentz, N. Duzgunes, S. Nir, W. J. Bowen, H. I. Martin, W. A. Braell, L. J. Breckenridge, W. Almers, L. J. Breckenridge, W. Almers, B. Cecarelli, W. Hurlbut, J. E. Chad, R. Eckert, M. J. Clague, C. Schoch, L. Zech, R. Blumenthal, J. Del Castillo, B. Katz, R. Diaz, L. S. Mayorga, P. J. Weidman, J. E. Rothman, P. D. Stahl, F. A. Dodge, R. Rahamimoff, N. Duzgunes, J. Paiement, K. B. Freeman, N. Lopez, J. Wilschut, D. Papahadjopoulos, H. Ellens, D. P. Siegel, D. Alford, P. L. Yeagle, L. Boni, L. J. Lis, P. J. Quinn, J. Bentz, J. M. Fernandez, E. Neher, B. D. Gomperts, J. E. Heuser, T. S. Reese, B. Hille, B. Hochner, H. Parnas, I. Parnas, R. C. Jackson, J. H. Crabb, B. Katz, R. Miledi, D. E. Knight, P. F. Baker, R. Llinas, I. Z. Steinberg, K. Walton, A. Mallart, J. L. Brigant, E. M. McLachlan, M. D. Miyamoto, S. J. Morris, D. P. Sarkar, J. M. White, R. Blumenthal, S. Nir, K. Klappe, D. Hoekstra, P. Novick, S. Ferro, R. Schekman, H. B. Pollard, A. L. Burns, E. Rojas, R. P. Rand, V. A. Parsegian, S. Redman, S. M. Simon, R. R. Llinas, S. J. Smith, G. J. Augustine, A. E. Spruce, L. J. Breckenridge, A. K. Lee, W. Almers, T. Stegmann, R. W. Doms, A. Helenius, T. Stegmann, S. Nir, J. Wilschut, J. H. Steinbach, C. F. Stevens, T. C. Sudhof, M. Baumert, M. S.

Perin, R. Jahn, L. Thomas, K. Hartung, D. Langosch, H. Rehm, E. Bamberg, W. W. Franke, H. Betz, A. J. Verkleij, J. M. White, J. Wilschut, S. Nir, J. Scholma, D. Hoekstra, P. G. Woodman, G. Warren, R. S. Zucker, and A. L. Fogelson, "Transmitter release from synapses: Does a preassembled fusion pore initiate exocytosis?," *Neuron*, vol. 4, no. 6, pp. 813–818, Jun. 1990.

[20] F. Torri-Tarelli, "Temporal coincidence between synaptic vesicle fusion and quantal secretion of acetylcholine," *J. Cell Biol.*, vol. 101, no. 4, pp. 1386–1399, Oct. 1985.

[21] T. A. M. Bharat, J. Malsam, W. J. H. Hagen, A. Scheutzow, T. H. Söllner, and J. A. G. Briggs, "SNARE and regulatory proteins induce local membrane protrusions to prime docked vesicles for fast calcium-triggered fusion.," *EMBO Rep.*, vol. 15, no. 3, pp. 308–14, Mar. 2014.

[22] L. Qu, Y. Akbergenova, Y. Hu, and T. Schikorski, "Synapse-to-synapse variation in mean synaptic vesicle size and its relationship with synaptic morphology and function," *J. Comp. Neurol.*, vol. 514, no. 4, pp. 343–352, 2009.

[23] J. T. Jenkins, "Static equilibrium configurations of a model red blood cell," *J Math Biol*, vol. 4, no. 2, pp. 149–169, 1977.

[24] J. T. Jenkins, "The Equations of Mechanical Equilibrium of a Model Membrane," *SIAM J. Appl. Math.*, vol. 32, no. 4, pp. 755–764, Jun. 1977.

[25] D. J. Steigmann, "Fluid Films with Curvature Elasticity," *Arch. Ration. Mech. Anal.*, vol. 150, no. 2, pp. 127–152, Dec. 1999.

[26] D. Steigmann, E. Baesu, R. Rudd, J. Belak, and M. McElfresh, "On the

variational theory of cell-membrane equilibria," *Interfaces Free Boundaries*, vol. 5, no. 4, pp. 357–366, 2003.

[27] H. Gao, W. Shi, and L. B. Freund, "Mechanics of receptor-mediated endocytosis.," *Proc. Natl. Acad. Sci. U. S. A.*, vol. 102, no. 27, pp. 9469–9474, 2005.

[28] T. Baumgart, B. R. Capraro, C. Zhu, and S. L. Das, "Thermodynamics and mechanics of membrane curvature generation and sensing by proteins and lipids.," *Annu. Rev. Phys. Chem.*, vol. 62, pp. 483–506, 2011.

[29] T. Baumgart, S. T. Hess, and W. W. Webb, "Imaging coexisting fluid domains in biomembrane models coupling curvature and line tension.," *Nature*, vol. 425, no. 6960, pp. 821–824, 2003.

[30] P. Singh, P. Mahata, T. Baumgart, and S. L. Das, "Curvature sorting of proteins on a cylindrical lipid membrane tether connected to a reservoir," *Phys. Rev. E - Stat. Nonlinear, Soft Matter Phys.*, vol. 85, no. 5, 2012.

[31] S. Das, "Influence of the bending rigidity and the line tension on the mechanical stability of micropipette aspirated vesicles," *Phys. Rev. E - Stat. Nonlinear, Soft Matter Phys.*, vol. 82, no. 2, 2010.

[32] T. Baumgart, S. Das, W. W. Webb, and J. T. Jenkins, "Membrane elasticity in giant vesicles with fluid phase coexistence.," *Biophys. J.*, vol. 89, no. 2, pp. 1067–80, Aug. 2005.

[33] G. Cox, J. Lowengrub, M. O, B. A. and H. R, H. W, M. H. and G. J, A. S. C. Y. Z. J. and C. F. Kuzmin P, D. G. V. Y. P. B. and M. H. Lundmark R, Z. J. and K. M, S. O. and L. R. Dobereinerand H-G, C. I. and D. M, L. S. and A. D, A. J. M.

and A. M. B, J. F. and L. R, J. F. and L. R, S. U, B. K. and L. R. Seifert U, D. S. W. W. and J. J. Baumgart T, H. S. and W. W. Baumgart T, E. E. and Y. A, E. E, E. E, H. G. and G. R. E. Powers T R, C. P. B, J. J. and B. T. Das S, L. R, A. D. K. K. and T. T. Kawakatsu T, G. W. and G. G, G. G. and L. R. Kumar P, K. D. and G. G. Kohyama T, G. T. and L. R. Gutlederer E, S. U, O. D. S. A. and D.-V. A. Farge E, F. F, O. C, N. D. and E. E, K. J. N. D. S. I. and S. E. Döbereiner H G, B. J. S. and G. B. S, G. W, B. N. L. R. and D. R. Riske K, C. S. and S. P. Garca-Saez A, H. W. B. and Z. J, M. M. and D. C. P. Schmid S, S. A. and H. W. Hannah M, C. L. and Z. J, R. K. M.-A. V. L. J.-M. L. R. and D. R. Haluska C, A. S. B. N. N. V. R. K. A. and L. R. Dimova R, R. R. and von G. H, de F. P. and B. W, H. H. and M. H, S. Y. and H. H. Shibuya A, C. O. and T. P. Emsellem V, M. J. F. and L. A. Fygenson D K, and C. Y. G.-B. M.-A. A. T. and S. J. Tsafrir I, "The effect of spontaneous curvature on a two-phase vesicle," *Nonlinearity*, vol. 28, no. 3, pp. 773–793, Mar. 2015.

[34] S. Das, "Adhesion of vesicles to curved substrates," *Phys. Rev. E*, vol. 77, no. 1, p. 011907, Jan. 2008.

[35] X.-H. Zhou, J.-L. Liu, and S.-L. Zhang, "Adhesion of a vesicle on an elastic substrate: 2D analysis.," *Colloids Surf. B. Biointerfaces*, vol. 110, pp. 372–8, Oct. 2013.

[36] A. Ramachandran, T. H. Anderson, L. G. Leal, and J. N. Israelachvili, "Adhesive interactions between vesicles in the strong adhesion limit.," *Langmuir*, vol. 27, no. 1, pp. 59–73, Jan. 2011.

[37] M. Deserno and W. Gelbart, "Adhesion and Wrapping in Colloid− Vesicle

Complexes," *J. Phys. Chem. B*, pp. 5543–5552, 2002.

[38] R. Long, C.-Y. Hui, A. Jagota, and M. Bykhovskaia, "Adhesion energy can regulate vesicle fusion and stabilize partially fused states.," *J. R. Soc. Interface*, vol. 9, no. 72, pp. 1555–67, 2012.

[39] T. Liu, P. Singh, J. T. Jenkins, A. Jagota, M. Bykhovskaia, and C.-Y. Hui, "A continuum model of docking of synaptic vesicle to plasma membrane," *J. R. Soc. Interface*, vol. 12, no. 102, pp. 20141119–20141119, Dec. 2014.

[40] P. Yang and S. Wen, "Pure squeeze action in an isothermal elastohydrodynamically lubricated spherical conjunction part 2. Constant speed and constant load results," *Wear*, vol. 142, no. 1, pp. 17–30, Feb. 1991.

[41] P. Yang and S. Wen, "Pure squeeze action in an isothermal elastohydrodynamically lubricated spherical conjunction part 1. Theory and dynamic load results," *Wear*, vol. 142, no. 1, pp. 1–16, Feb. 1991.

[42] H. Christensen, "Elastohydrodynamic Theory of Spherical Bodies in Normal Approach," *J. Lubr. Technol.*, vol. 92, no. 1, p. 145, 1970.

[43] H. Christensen, "The Oil Film in a Closing Gap," *Proc. R. Soc. A Math. Phys. Eng. Sci.*, vol. 266, no. 1326, pp. 312–328, Mar. 1962.

[44] R. H. Davis, J.-M. Serayssol, and E. J. Hinch, "The elastohydrodynamic collision of two spheres," *J. Fluid Mech.*, vol. 163, no. -1, p. 479, Apr. 2006.

[45] M. Scaraggi and B. N. J. Persson, "Time-Dependent Fluid Squeeze-Out Between Soft Elastic Solids with Randomly Rough Surfaces," *Tribol. Lett.*, vol. 47, no. 3, pp. 409–416, Jun. 2012.

[46] E. Karatekin, J. Di Giovanni, C. Iborra, J. Coleman, B. O'Shaughnessy, M.

Seagar, and J. E. Rothman, “A fast, single-vesicle fusion assay mimics physiological SNARE requirements,” *Proc. Natl. Acad. Sci.*, vol. 107, no. 8, pp. 3517–3521, 2010.

[47] R. Mohrmann, H. de Wit, M. Verhage, E. Neher, and J. B. Sørensen, “Fast vesicle fusion in living cells requires at least three SNARE complexes.,” *Sci. (New York, NY)*, vol. 330, no. 6003, pp. 502–505, 2010.

[48] R. Sinha, S. Ahmed, R. Jahn, and J. Klingauf, “Two synaptobrevin molecules are sufficient for vesicle fusion in central nervous system synapses,” *Proc. Natl. Acad. Sci. U. S. A.*, vol. 108, no. 34, pp. 14318–14323, 2011.

[49] G. Van Den Bogaart and R. Jahn, “Counting the SNAREs needed for membrane fusion,” *J. Mol. Cell Biol.*, vol. 3, no. 4, pp. 204–205, 2011.

[50] X. Han, C.-T. Wang, J. Bai, E. R. Chapman, and M. B. Jackson, “Transmembrane segments of syntaxin line the fusion pore of Ca2+-triggered exocytosis.,” *Science*, vol. 304, no. 5668, pp. 289–292, 2004.

[51] O. Reynolds, “On the Theory of Lubrication and Its Application to Mr. Beauchamp Tower’s Experiments, Including an Experimental Determination of the Viscosity of Olive Oil,” *Philos. Trans. R. Soc. London*, vol. 177, no. January, pp. 157–234, 1886.

[52] Y. Gao, S. Zorman, G. Gundersen, Z. Xi, L. Ma, G. Sirinakis, J. E. Rothman, and Y. Zhang, “Single reconstituted neuronal SNARE complexes zipper in three distinct stages,” *Science (80-.).*, vol. 337, no. 6100, pp. 1340–1343, 2012.

[53] D. Min, K. Kim, C. Hyeon, Y. H. Cho, Y.-K. Shin, and T.-Y. Yoon, “Mechanical unzipping and rezipping of a single SNARE complex reveals

hysteresis as a force-generating mechanism.," *Nat. Commun.*, vol. 4, p. 1705, 2013.

[54] R. Dimova, "Recent developments in the field of bending rigidity measurements on membranes," *Advances in Colloid and Interface Science*, vol. 208. pp. 225–234, 2014.

[55] W. Rawicz, B. A. Smith, T. J. McIntosh, S. A. Simon, and E. Evans, "Elasticity, strength, and water permeability of bilayers that contain raft microdomain-forming lipids.," *Biophys. J.*, vol. 94, no. 12, pp. 4725–36, Jun. 2008.

[56] K. Ohsawa, M. Murata, and H. Ohshima, "Zeta potential and surface charge density of polystyrene-latex; comparison with synaptic vesicle and brush border membrane vesicle," *Colloid Polym. Sci.*, vol. 264, no. 12, pp. 1005–1009, Dec. 1986.

[57] Y. Lai, J. Diao, D. J. Cipriano, Y. Zhang, R. A. Pfuetzner, M. S. Padolina, and A. T. Brunger, "Complexin inhibits spontaneous release and synchronizes Ca2+-triggered synaptic vesicle fusion by distinct mechanisms," *Elife*, vol. 3, p. e03756, 2014.

[58] J. Malsam, D. Parisotto, T. A. M. Bharat, A. Scheutzow, J. M. Krause, J. A. G. Briggs, T. H. Söllner, and T. H. So, "Complexin arrests a pool of docked vesicles for fast Ca2+-dependent release.," *EMBO J.*, vol. 31, no. 15, pp. 3270–81, 2012.

[59] R. T. Wragg, D. Snead, Y. Dong, T. F. Ramlall, I. Menon, J. Bai, D. Eliezer, and J. S. Dittman, "Synaptic Vesicles Position Complexin to Block

Spontaneous Fusion," *Neuron*, vol. 77, no. 2, pp. 323–334, 2013.

[60] R. J. Hobson, Q. Liu, S. Watanabe, and E. M. Jorgensen, "Complexin maintains vesicles in the primed state in C. elegans," *Curr. Biol.*, vol. 21, no. 2, pp. 106–113, 2011.

[61] T. Trimbuch and C. Rosenmund, "Should I stop or should I go? The role of complexin in neurotransmitter release.," *Nat. Rev. Neurosci.*, vol. 17, no. 2, pp. 118–25, 2016.

Appendix A4

A4.1 Lubrication Theory

In this section we show the derivation of Reynolds equation, which governs the fluid flow between two surfaces. The schematic is shown in the Fig A4.1, where the red and blue areas represent the surfaces which are in motion, and the vertical height between two points on the surface is $h(x,z)$.

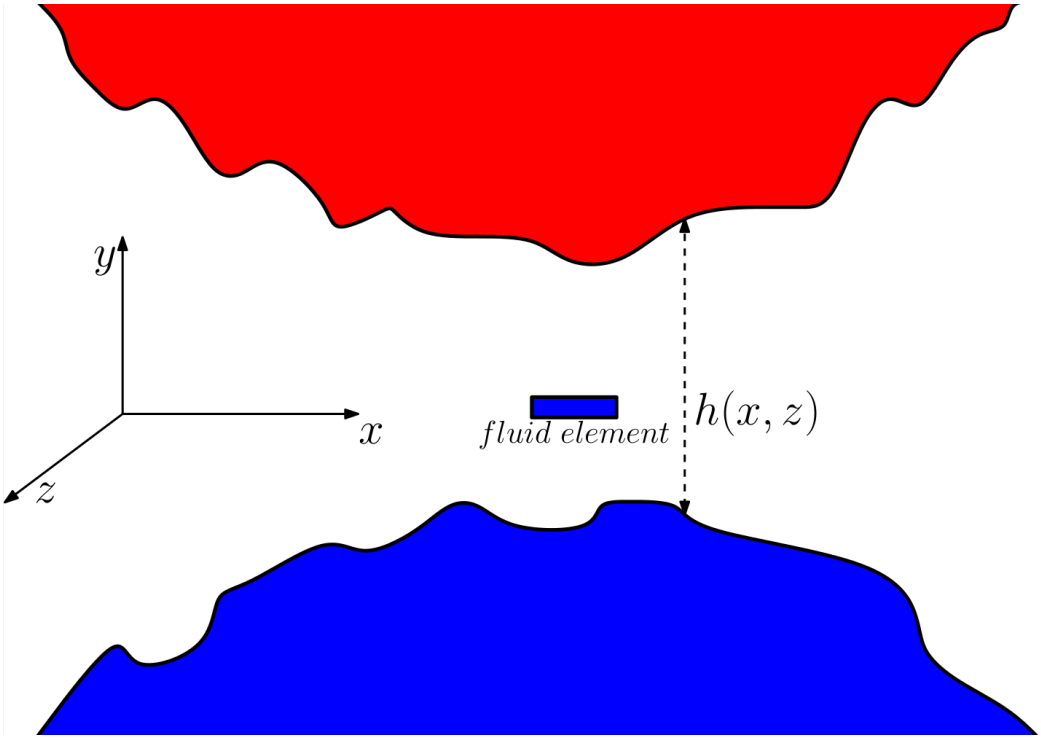

Fig A4.1 : Schematic

In the following derivation, we start with the Navier-Stokes equation, do a scaling analysis to keep the dominant components of the equation and finally getting to the Reynold's equation.

A4.1.1 Navier Stokes equations

The most general form of Navier-Stokes equation is given as,

$$\rho\frac{\partial u}{\partial t}=\rho X-\frac{\partial p}{\partial x}+\frac{2}{3}\frac{\partial}{\partial x}\left[\eta\left(\frac{\partial u}{\partial x}-\frac{\partial w}{\partial z}\right)\right]+\frac{2}{3}\frac{\partial}{\partial x}\left[\eta\left(\frac{\partial u}{\partial x}-\frac{\partial v}{\partial y}\right)\right]+\frac{\partial}{\partial y}\left[\eta\left(\frac{\partial u}{\partial y}+\frac{\partial v}{\partial x}\right)\right]+\frac{\partial}{\partial z}\left[\eta\left(\frac{\partial w}{\partial x}+\frac{\partial u}{\partial z}\right)\right],$$
$$\rho\frac{\partial v}{\partial t}=\rho Y-\frac{\partial p}{\partial y}+\frac{2}{3}\frac{\partial}{\partial y}\left[\eta\left(\frac{\partial v}{\partial y}-\frac{\partial w}{\partial z}\right)\right]+\frac{2}{3}\frac{\partial}{\partial y}\left[\eta\left(\frac{\partial v}{\partial y}-\frac{\partial u}{\partial x}\right)\right]+\frac{\partial}{\partial x}\left[\eta\left(\frac{\partial u}{\partial y}+\frac{\partial v}{\partial x}\right)\right]+\frac{\partial}{\partial z}\left[\eta\left(\frac{\partial w}{\partial y}+\frac{\partial v}{\partial z}\right)\right],$$
$$\rho\frac{\partial w}{\partial t}=\rho Z-\frac{\partial p}{\partial z}+\frac{2}{3}\frac{\partial}{\partial z}\left[\eta\left(\frac{\partial w}{\partial z}-\frac{\partial v}{\partial y}\right)\right]+\frac{2}{3}\frac{\partial}{\partial z}\left[\eta\left(\frac{\partial w}{\partial z}-\frac{\partial u}{\partial x}\right)\right]+\frac{\partial}{\partial x}\left[\eta\left(\frac{\partial u}{\partial z}+\frac{\partial w}{\partial x}\right)\right]+\frac{\partial}{\partial y}\left[\eta\left(\frac{\partial w}{\partial y}+\frac{\partial v}{\partial z}\right)\right],$$

A4.1

where,

ρ is the density of the fluid,

u,v and w are the velocity components of fluid in x,y and z directions, respectively,

X,Y and Z are the body force components on fluid in x,y and z directions,

respectively,

η is the fluid viscosity.

Assuming that, there is no body force on the fluid and also neglecting the inertial term, the Navier-Stokes equations can simplified to,

$$\frac{\partial p}{\partial x}=\frac{2}{3}\frac{\partial}{\partial x}\left[\eta\left(\frac{\partial u}{\partial x}-\frac{\partial w}{\partial z}\right)\right]+\frac{2}{3}\frac{\partial}{\partial x}\left[\eta\left(\frac{\partial u}{\partial x}-\frac{\partial v}{\partial y}\right)\right]+\frac{\partial}{\partial y}\left[\eta\left(\frac{\partial u}{\partial y}+\frac{\partial v}{\partial x}\right)\right]+\frac{\partial}{\partial z}\left[\eta\left(\frac{\partial w}{\partial x}+\frac{\partial u}{\partial z}\right)\right]$$
$$\frac{\partial p}{\partial y}=\frac{2}{3}\frac{\partial}{\partial y}\left[\eta\left(\frac{\partial v}{\partial y}-\frac{\partial w}{\partial z}\right)\right]+\frac{2}{3}\frac{\partial}{\partial y}\left[\eta\left(\frac{\partial v}{\partial y}-\frac{\partial u}{\partial x}\right)\right]+\frac{\partial}{\partial x}\left[\eta\left(\frac{\partial u}{\partial y}+\frac{\partial v}{\partial x}\right)\right]+\frac{\partial}{\partial z}\left[\eta\left(\frac{\partial w}{\partial y}+\frac{\partial v}{\partial z}\right)\right]\ ,$$
$$\frac{\partial p}{\partial z}=\frac{2}{3}\frac{\partial}{\partial z}\left[\eta\left(\frac{\partial w}{\partial z}-\frac{\partial v}{\partial y}\right)\right]+\frac{2}{3}\frac{\partial}{\partial z}\left[\eta\left(\frac{\partial w}{\partial z}-\frac{\partial u}{\partial x}\right)\right]+\frac{\partial}{\partial x}\left[\eta\left(\frac{\partial u}{\partial z}+\frac{\partial w}{\partial x}\right)\right]+\frac{\partial}{\partial y}\left[\eta\left(\frac{\partial w}{\partial y}+\frac{\partial v}{\partial z}\right)\right]$$

A4.2

We choose the following non-dimensionalizing scheme for the eqs. A4.2,

1) Time is non-dimensionalized by a characteristic time of the system, τ_0. Hence,

   $t = \tau_0 \bar{t}$.

2) Length dimensions associated in y-direction are normalized by local film thickness, h. Therefore,

   $y = h\bar{y}$ and $v = \frac{h}{\tau_0}\bar{v}$.

3) Length dimensions associated in x and z directions are normalized by characteristic length of the system, l, where, $\frac{h}{l} << 1$. Therefore,

   $x = h\bar{x},\ z = h\bar{z}, u = \frac{l}{\tau_0}\bar{u}$ and $w = \frac{l}{\tau_0}\bar{w}$.

4) Density is normalized by room temperature density, ρ_0, which results in,

   $\rho = \rho_0\bar{\rho}$.

5) Viscosity is normalized as, $\eta = \frac{\rho_0 l^2}{\tau_0}\bar{\eta}$.

6) Pressure is normalized as, $p = \frac{\rho_0 l^2}{\tau_0^2}\bar{p}$.

Applying this normalization scheme to the system of eqs. A4.2, to get,

$$\frac{\partial \bar{p}}{\partial \bar{x}} = \frac{2}{3}\frac{\partial}{\partial \bar{x}}\left[\bar{\eta}\left(\frac{\partial \bar{u}}{\partial \bar{x}} - \frac{\partial \bar{w}}{\partial \bar{z}}\right)\right] + \frac{2}{3}\frac{\partial}{\partial \bar{x}}\left[\bar{\eta}\left(\frac{\partial \bar{u}}{\partial \bar{x}} - \frac{\partial \bar{v}}{\partial \bar{y}}\right)\right] + \frac{\partial}{\partial \bar{y}}\left[\bar{\eta}\left(\frac{\partial \bar{u}}{\partial \bar{y}}\left(\frac{l}{h}\right)^2 + \frac{\partial \bar{v}}{\partial \bar{x}}\right)\right] + \frac{\partial}{\partial \bar{z}}\left[\bar{\eta}\left(\frac{\partial \bar{w}}{\partial \bar{x}} + \frac{\partial \bar{u}}{\partial \bar{z}}\right)\right]$$

$$\frac{\partial \bar{p}}{\partial \bar{z}} = \frac{2}{3}\frac{\partial}{\partial \bar{z}}\left[\bar{\eta}\left(\frac{\partial \bar{w}}{\partial \bar{z}} - \frac{\partial \bar{v}}{\partial \bar{y}}\right)\right] + \frac{2}{3}\frac{\partial}{\partial \bar{z}}\left[\bar{\eta}\left(\frac{\partial \bar{w}}{\partial \bar{z}} - \frac{\partial \bar{u}}{\partial \bar{x}}\right)\right] + \frac{\partial}{\partial \bar{x}}\left[\bar{\eta}\left(\frac{\partial \bar{u}}{\partial \bar{z}} + \frac{\partial \bar{w}}{\partial \bar{x}}\right)\right] + \frac{\partial}{\partial \bar{y}}\left[\bar{\eta}\left(\frac{\partial \bar{w}}{\partial \bar{y}}\left(\frac{l}{h}\right)^2 + \frac{\partial \bar{v}}{\partial \bar{z}}\right)\right]$$

,

A4.3

Eq. A4.2 b, the Navier-Stokes equation in y-direction is identically satisfied on both sides. The pressure gradient in y direction is negligible compared to the pressure gradients in x and z directions. On the right hand side, the quantities are also very small compared to the corresponding terms in eqs. A4.2 a & c.

Looking at the eq. A4.3, the terms which are scaled by, $\left(\frac{l}{h}\right)^2 [>>1]$ are dominant and rest of the terms can be neglected on the right hand side. This gives,

$$\frac{\partial \bar{p}}{\partial \bar{x}} = \frac{\partial}{\partial \bar{y}}\left[\bar{\eta}\left(\frac{\partial \bar{u}}{\partial \bar{y}}\left(\frac{l}{h}\right)^2\right)\right] \quad \text{and} \quad \frac{\partial \bar{p}}{\partial \bar{z}} = \frac{\partial}{\partial \bar{y}}\left[\bar{\eta}\left(\frac{\partial \bar{w}}{\partial \bar{y}}\left(\frac{l}{h}\right)^2\right)\right]. \qquad \text{A4.4}$$

On plugging back the dimensional term into eqs. A4.4, one gets back the dimensional form as,

$$\frac{\partial p}{\partial x} = \frac{\partial}{\partial y}\left[\eta\left(\frac{\partial u}{\partial y}\right)\right] \quad \text{and} \quad \frac{\partial p}{\partial z} = \frac{\partial}{\partial y}\left[\eta\left(\frac{\partial w}{\partial y}\right)\right]. \qquad \text{A4.5}$$

For an iso-viscous system, the equations can be modified as,

$$\frac{\partial p}{\partial x} = \eta\frac{\partial^2 u}{\partial y^2} \quad \text{and} \quad \frac{\partial p}{\partial z} = \eta\frac{\partial^2 w}{\partial y^2}. \qquad \text{A4.6}$$

This same set of equations can also be obtained by a force balance on a fluid element shown in Figs. A4.1 and A4.2.

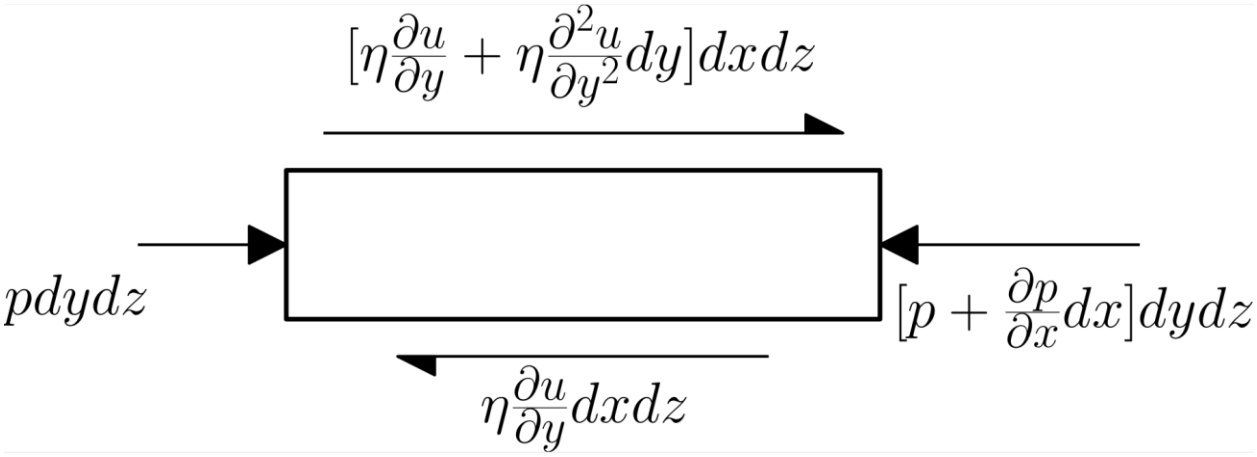

Fig A4.1 : Force balance on a fluid element

By doing a simple force balance in x-direction, on a fluid element between the two surfaces, as shown in Fig. A4.2, we can write the governing equations for fluid flow as,

$$\frac{\partial p}{\partial x} = \eta \frac{\partial^2 u}{\partial y^2}. \qquad \text{A4.7}$$

Similarly, a force balance in z direction will give us the equation,

$$\frac{\partial p}{\partial z} = \eta \frac{\partial^2 w}{\partial y^2}. \qquad \text{A4.8}$$

In the above expressions,

p is the pressure in the vertical fluid column and is assumed to be invariant along y axis,

η is the fluid viscosity.

Both eqs. A4.7 and A4.8 can be integrated twice each, to get the fluid velocities as,

$$u = \frac{1}{2\eta}\frac{\partial p}{\partial x}y^2 + \frac{A}{\eta}y + B \ , \qquad \text{A4.9}$$

$$w = \frac{1}{2\eta}\frac{\partial p}{\partial z}y^2 + \frac{C}{\eta}z + D\,. \qquad \text{A4.10}$$

Boundary conditions relevant to vesicle adhesion problem

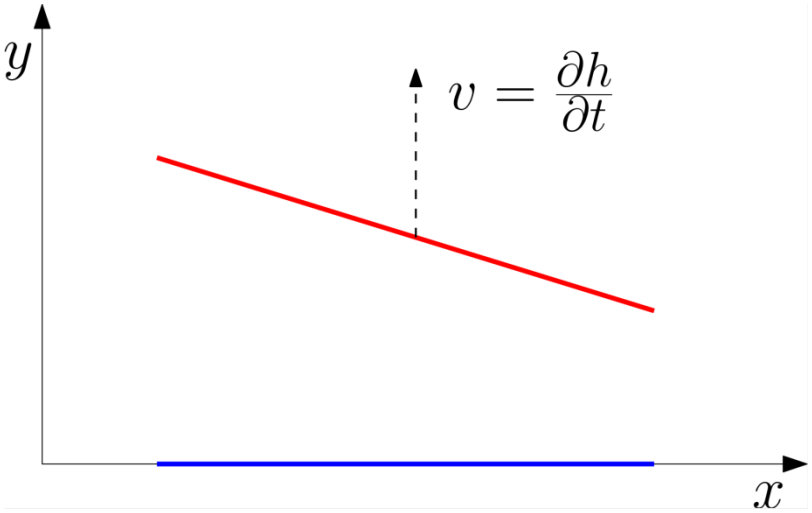

Fig A4.2 : Velocity boundary conditions

For the case of lipid membrane fusion and adhesion, the only velocity element is the one in vertical direction, $v = \frac{\partial h}{\partial t}$. Therefore, we have following boundary conditions for the velocity profiles obtained above in eqs. A4.9 and A4.10,

$$u = 0, v = 0 \text{ and } w = 0, \text{ at } y = 0\,, \qquad \text{A4.11}$$

$$u = 0, v = \frac{\partial h}{\partial t} \text{ and } w = 0, \text{ at } y = h\,. \qquad \text{A4.12}$$

Using these boundary conditions in eqs. A4.9 and A4.10, we get,

$$u = \frac{1}{2\eta}\frac{\partial p}{\partial x}\left(y^2 - hy\right)\,, \qquad \text{A4.13}$$

$$w = \frac{1}{2\eta}\frac{\partial p}{\partial z}\left(y^2 - hy\right). \qquad \text{A4.14}$$

Volume flow rates

The volume flow rate per unit length, in x and z direction can be defined as,

$$V_x = \int_0^h u dy = -\frac{h^3}{12\eta}\frac{\partial p}{\partial x}\ , \qquad \text{A4.15}$$

$$V_z = \int_0^h w dy = -\frac{h^3}{12\eta}\frac{\partial p}{\partial z}\ . \qquad \text{A4.16}$$

Continuity equation

The continuity equation for fluid is,

$$\frac{\partial \rho}{\partial t} + \frac{\partial(\rho u)}{\partial x} + \frac{\partial(\rho v)}{\partial y} + \frac{\partial(\rho w)}{\partial z} = 0. \qquad \text{A4.17}$$

For a constant density system, the equation can be simplified to,

$$\frac{\partial u}{\partial x} + \frac{\partial v}{\partial y} + \frac{\partial w}{\partial z} = 0. \qquad \text{A4.18}$$

On integrating this equation with respect to y, between the limits 0 and h, we get,

$$\int_0^h \frac{\partial u}{\partial x} dy + \int_0^h \frac{\partial v}{\partial y} dy + \int_0^h \frac{\partial w}{\partial z} dy = 0.$$

Using Leibnitz rule of integration,

$$\frac{\partial}{\partial x}\int_0^h u dy - \underbrace{u|_h}_{=0}\frac{\partial h}{\partial x} + v|_h - v|_0 + \frac{\partial}{\partial z}\int_0^h w dy - \underbrace{w|_h}_{=0}\frac{\partial h}{\partial z} = 0,$$

$$\Rightarrow \frac{\partial}{\partial x}\int_0^h u dy + \frac{\partial h}{\partial t} + \frac{\partial}{\partial z}\int_0^h w dy = 0,$$

$$\Rightarrow \frac{\partial V_x}{\partial x} + \frac{\partial V_z}{\partial z} + \frac{\partial h}{\partial t} = 0.$$

Plugging in the expressions of V_x and V_y into the expression above to get,

$$\Rightarrow \frac{\partial}{\partial x}\left(h^3 \frac{\partial p}{\partial x}\right)+\frac{\partial}{\partial z}\left(h^3 \frac{\partial p}{\partial z}\right)=12\eta \frac{\partial h}{\partial t}. \qquad \text{A4.19}$$

Eq. A4.19 above is referred to as Reynold's equation. In this case, it has been modified to account for the fluid squeezing between two surfaces, one held fixed and other approaching it along the vertical direction.

In more general form for any other geometry (spherical, cylindrical or Cartesian), it can written as,

$$\nabla\left(h^3 \nabla p\right)=12\eta \frac{\partial h}{\partial t}. \qquad \text{A4.20}$$

A4.2 Rigid sphere against a rigid substrate

Dimensional analysis

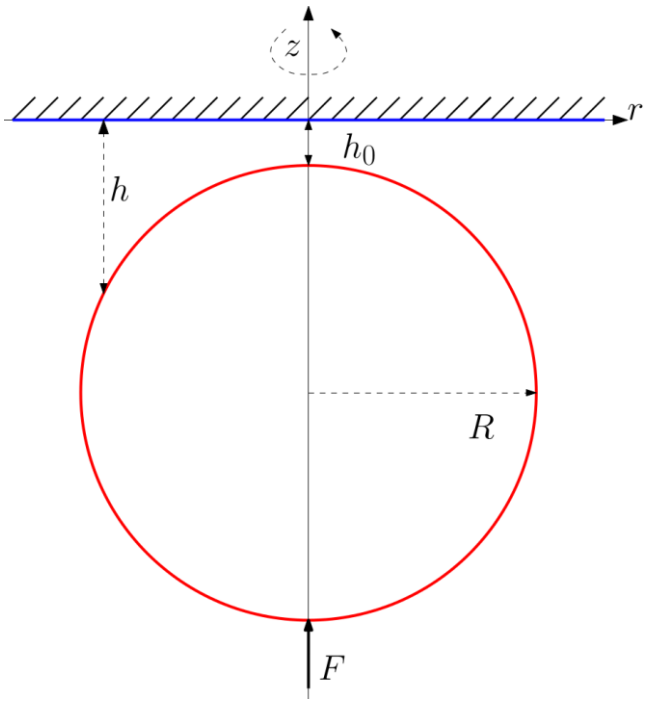

Fig A4.4: Rigid sphere traversing against a rigid wall

Starting with the Reynolds equation, which is the only governing equation for the case under consideration. The problem involves, pushing down a rigid sphere of radius R onto a flat rigid surface and in between the surfaces, there is fluid, which has to be squeezed away.

In the part of the geometry, where film thickness is small, following approximation for the fluid film thickness, can be made,

$$h(r,t) = h_0(t) + \frac{r^2}{2R}. \qquad \text{A4.21}$$

Next, consider the Reynolds equation,

$$\nabla\left(h^3\nabla p\right)=12\eta\frac{\partial h}{\partial t}, \qquad \text{A4.22}$$

and for the axis-symmetric case, it can written as,

$$\frac{\partial}{\partial r}\left(rh^3\frac{\partial p}{\partial r}\right)=12\eta r\frac{\partial h}{\partial t}. \qquad \text{A4.23}$$

Also, we have following constraint on the pressure distribution on the sphere, which has to be satisfied all times,

$$F=\int_0^\infty p\left(r,t\right)2\pi r dr. \qquad \text{A4.24}$$

Non-dimensionalization

Following scheme has been chosen to non-dimensionalize eqs. A4.23 and A4.24.

$$\bar{r}=\frac{r}{R},\ \bar{h}=\frac{h}{R},\ \bar{p}=\frac{pR^2}{F}. \qquad \text{A4.25}$$

This when applied to eq. A4.23,

$$\frac{\partial}{\partial \bar{r}}\left(\bar{r}\left\{\bar{h}_0+\frac{\bar{r}^2}{2}\right\}^3\frac{\partial \bar{p}}{\partial \bar{r}}\right)=\frac{12\eta R^2}{F}\bar{r}\frac{\partial}{\partial t}\left(\bar{h}_0+\frac{\bar{r}^2}{2}\right),$$

choosing, $\bar{t}=\dfrac{Ft}{12\eta R^2}$ to get,

$$\frac{\partial}{\partial \bar{r}}\left(\bar{r}\left\{\bar{h}_0+\frac{\bar{r}^2}{2}\right\}^3\frac{\partial \bar{p}}{\partial \bar{r}}\right)=\bar{r}\frac{\partial}{\partial \bar{t}}\left(\bar{h}_0+\frac{\bar{r}^2}{2}\right). \qquad \text{A4.26}$$

Also, eq. A4.24 can written in non-dimensional form as,

$$\frac{1}{2\pi} = \int_0^{\infty} \bar{p}\left(\bar{r}, \bar{t}\right)\bar{r}d\bar{r} \qquad \text{A4.27}$$

As seen from the non-dimensional analysis, the only quantity with the units of time is $\frac{\eta R^2}{F}$. So, the time of approach scales with $\frac{\eta R^2}{F}$ and is a function of initial and final separations between the surfaces, $\frac{h_{0,1}}{h_{0,2}}$. Therefore the time of approach of sphere against the rigid surface can be written as,

$$\Delta t = \frac{\eta R^2}{F} f\left(\frac{h_{0,1}}{h_{0,2}}\right). \qquad \text{A4.28}$$

This is also the nature of expression obtained from the analytical derivation appended in next section.

Analytical calculation

Consider a rigid sphere of radius R, being pushed onto a flat surface, while squeezing out fluid between the two surfaces. The separation between the lowermost point on the sphere and flat surface is referred to as h_0. The aim of this derivation is to get the time taken by the sphere to be brought down from initial bottommost separation of h_{0i} to final bottom most separation of h_{0f}, while a force F acts on the sphere in the downwards direction.

Thickness of lubrication film

The geometry of the problem has axis-symmetry, therefore r and z represents the coordinates. Henceforth, we have film thickness given as, $h = h(r,t)$. We can write an expression of h in terms of h_0 and r, as follows,

$$h = h_0 + \left[R - \left(R^2 - r^2 \right)^{1/2} \right],$$

$$\Rightarrow h = h_0 + R\left[1 - \left(1 - \frac{r^2}{R^2} \right)^{1/2} \right],$$

$$\Rightarrow h \approx h_0 + R\left[1 - \left(1 - \frac{1}{2}\frac{r^2}{R^2} - \frac{1}{8}\left(\frac{r^2}{R^2} \right)^2 - \frac{1}{16}\left(\frac{r^2}{R^2} \right)^4 - .... \right) \right],$$

$$\Rightarrow h = h_0 + \frac{r^2}{2R}\left[1 + \frac{1}{4}\left(\frac{r^2}{R^2} \right) + \frac{1}{8}\left(\frac{r^2}{R^2} \right)^4 + ... \right],$$

In the lubrication region, $r << R$, hence the above expression can be approximated as,

$$\Rightarrow h = h_0 + \frac{r^2}{2R} \qquad \text{A4.29}$$

Reynold's equation

The Reynolds equation for general coordinate system is given by,

$$\nabla\left[h^3 \nabla p \right] = 12\eta \frac{\partial h}{\partial t} \qquad \text{A4.30}$$

For an axis-symmetric case, the Reynold's equation is given as,

$$\frac{\partial}{\partial r}\left[r h^3 \frac{\partial p}{\partial r} \right] = 12\eta r \frac{\partial h}{\partial t} \qquad \text{A4.31}$$

where,

$p = p(r,t)$ is the fluid pressure in a vertical column of fluid film,

η is the fluid viscosity.

Solution

The Reynold's equation can be integrated to obtain an expression of pressure as a function of fluid film thickness.

Integrating once,

$$\frac{\partial}{\partial r}\left[rh^3\frac{\partial p}{\partial r}\right] = 12\eta r\frac{\partial h}{\partial t},$$
$$\Rightarrow \frac{\partial p}{\partial r} = \frac{6\eta r}{h^3}\frac{\partial h}{\partial t} + \frac{A}{rh^3},$$

To avoid a singularity in pressure gradient at $r = 0$, $A = 0$. Hence, we get,

$$\Rightarrow \frac{\partial p}{\partial r} = \frac{6\eta r}{h^3}\frac{\partial h}{\partial t},$$
$$\Rightarrow \int dp = \left(6\eta\frac{\partial h}{\partial t}\right)\int \frac{r}{h^3}\,dr,$$

using, eq A4.29, we get, $Rdh = rdr$, pugging in above expression,

$$\Rightarrow \int dp = 6\eta R\frac{\partial h}{\partial t}\int \frac{dh}{h^3},$$
$$\Rightarrow p = -\frac{3\eta R}{h^2}\frac{\partial h}{\partial t} + \mathrm{B},$$

For large h, the pressure goes to zero, for it to be satisfied, $B = 0$. Hence,

$$p = -\frac{3\eta R}{h^2}\frac{\partial h}{\partial t}. \qquad \text{A4.32}$$

This pressure, at any point in time balances the net force applied onto the sphere,

$$\Rightarrow F = \int_0^\infty p\left(2\pi r dr\right),$$

$$\Rightarrow F = -\int_0^\infty \frac{3\eta R}{h^2}\frac{\partial h}{\partial t}\left(2\pi r dr\right),$$

$$\Rightarrow F = -\left(6\eta\pi R\frac{\partial h}{\partial t}\right)\int_0^\infty \frac{r dr}{h^2},$$

$$\Rightarrow F = -\left(6\eta\pi R^2\frac{\partial h}{\partial t}\right)\int_{h_0}^\infty \frac{dh}{h^2},$$

$$\Rightarrow F = -\frac{6\eta\pi R^2}{h_0}\frac{\partial h}{\partial t}. \qquad \text{A4.33}$$

Eq. A4.24 can be integrated to obtain the time of approach of the sphere from initial separation of h_{0i} to final separation of h_{0f}.

$$\frac{F}{6\eta\pi R^2}dt = -\frac{dh_0}{h_0}. \qquad \text{A4.34}$$

We will be integrating eq. A4.34 under different loading conditions, which describes the variation of force with the gap between the sphere and substrate.

1) Constant Force

Let the force on the sphere be given by the following function,

$F = nF_{1,max}$,

where,

n is the number of SNARE proteins working together,

$F_{1,max}$ is the maximum force exerted by a single SNARE protein.

Plugging in this expression of F into eq. A4.34 and integrating,

$$\frac{nF_{1,max}}{6\eta\pi R^2}\Delta t = -\int_{h_{0i}}^{h_{0f}} \frac{dh_0}{h_0} = \ln\frac{h_{0i}}{h_{0f}}$$

Hence,

$$\Delta t = \frac{6\eta\pi R^2}{nF_{1,max}} \ln\left(\frac{h_{0i}}{h_{0f}}\right). \qquad \text{A4.35}$$

2) Force changing with gap

Let the force on the sphere be given by the following function,

$$F = nF_{1,max}\left(\frac{h_0}{h^*}\right)^m, \qquad \text{A4.36}$$

where,

n is the number of SNARE proteins working together,

$F_{1,max}$ is the maximum force exerted by a single SNARE protein,

h_0 is the minimum gap between the rigid sphere and rigid substrate,

h^* is the characteristic length scale, chosen so that the force is $F_{1,max}$ at the maximum opening of SNARE.

The maximum opening for a single SNARE bundle is 13nm and measured force at that opening is 17pN. Hence, to F have desired functional properties, h^* must be 13nm.

Plugging in this expression of F into eq. A4.34 and integrating,

$$\frac{nF_{1,max}}{6\eta_0\pi R^2}\Delta t = -\int_{h_{0i}}^{h_{0f}} \frac{d\left(h_0 / h^*\right)}{\left(h_0 / h^*\right)^m} = \frac{1}{m}\left[\left(\frac{h^*}{h_{0f}}\right)^m - \left(\frac{h^*}{h_{0i}}\right)^m\right]$$

$$\Rightarrow \Delta t = \frac{6\eta\pi R^2}{mnF_{1,max}}\left[\left(\frac{h^*}{h_{0f}}\right)^m - \left(\frac{h^*}{h_{0i}}\right)^m\right]. \qquad \text{A4.37}$$

A4.3Rigid sphere against compliant substrate

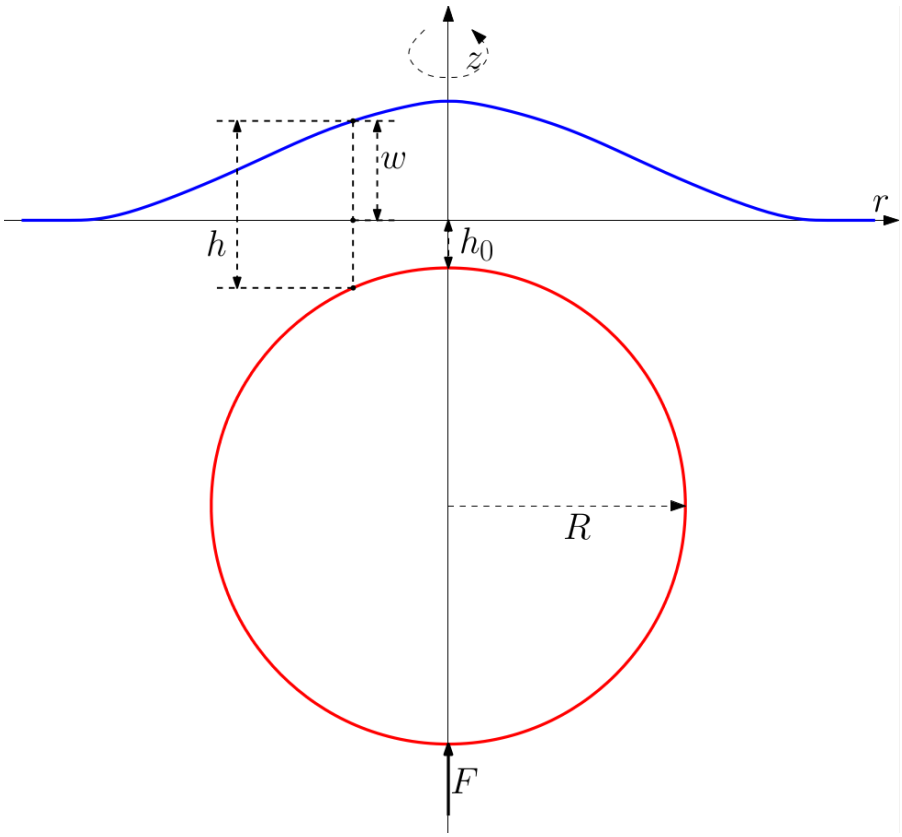

Fig A4.5: Rigid sphere traversing against a flat lipid membrane

Consider a rigid sphere of radius R , being pushed against a initially flat lipid membrane. During this process, the fluid between the two surfaces is squeezed out. The squeezing requires a radially outward pressure gradient for the fluid flow. This pressure field causes the membrane to deform and hence it is an interplay between the pressure field and membrane deformation.

The aim of this derivation is to get the governing equations for the motion of sphere, while a force F pushes it towards the flat lipid membrane.

Governing equations

This problem can be simplified a lot by exploiting the feature of axisymmetry. Under the assumption of axis-symmetry, mathematically this problem involves solving a partial differential equation (PDE) along with the system of ordinary differential equations (ODE's) which govern the deformation of the lipid membrane.

We begin with explaining the two sets of equations used in this analysis.

1) Hydrodynamics

The equation governing the hydrodynamics of the problem is called Reynolds equation. In its most general form, it can be written as,

$$\nabla\left[h^3\nabla p\right]=12\eta\frac{\partial h}{\partial t}. \qquad \text{A4.38}$$

Under the axis-symmetric assumption, it can be written as,

$$\frac{\partial}{\partial r}\left[rh^3\frac{\partial p}{\partial r}\right]=12\eta r\frac{\partial h}{\partial t} \qquad \text{A4.39}$$

along with,

$$h(r,t)=-h_0(t)+\frac{r^2}{2R}+w(r,t), \qquad \text{A4.40}$$

where,

$h(r,t)$, is the film thickness at some time t and at some radial coordinate r,

$p(r,t)$, is the pressure in the fluid film,

η, is the fluid viscosity,

$h_0(t)$, is the separation between the lowermost point on the sphere and far field flat surface,

$w(r,t)$, is the vertical deformation of the surface.

Along with PDE in eq. A4.39, from force balance on the rigid sphere, following constraint equation can be obtained,

$$F = \int_0^\infty p(r,t)\, 2\pi r dr, \qquad \text{A4.41}$$

where, F is the applied force on the rigid sphere, pushing it towards the flat lipid membrane.

Since, the eq. A4.39 is a second order in space and first order in time, it comes along with two boundary conditions,

a) $\left.\frac{\partial p(r,t)}{\partial r}\right|_{r=0} = 0$, due to the symmetry of geometry, A4.42 (a-b)

b) $p(r,t)|_{r\to\infty} \to 0$, in the far field the pressure in fluid film should go to zero,

and the following initial condition,

$p(r,t=0) = 0$, initially there is no deformation in the system. A4.43

2) Lipid membrane deformation

The lipid membrane deformation is governed by a 4th order differential equation,

$$\frac{\kappa}{2}\nabla^4 w - T_0\nabla^2 w = -p(r)\ , \qquad \text{A4.44}$$

where,

κ, is the bending rigidity of the lipid membrane and has a value of $\sim 20k_BT$,

T_0, is the far field pretension in the lipid membrane,

$w(r)$, is the deformation of the lipid membrane, and

$p(r)$, is the pressure acting on the lipid membrane at a given location.

Eq. A4.44 resembles a plate equation with a pretension in it.

Non-dimensionalization

Normalizing this system of equations in accordance to the following scheme,

$$\bar{r} = \frac{r}{R}, \quad \bar{z} = \frac{z}{R}, \quad \bar{H} = RH, \quad \bar{w} = \frac{w}{R}, \quad \bar{h_0} = \frac{h_0}{R},$$

$$\bar{F} = \frac{FR}{\kappa},$$

$$\bar{T_0} = \frac{T_0R^2}{\kappa},$$

A4.45(a-j)

$$\bar{p} = \frac{pR^3}{\kappa},$$

$$\bar{t} = \frac{\kappa t}{\eta R^3}.$$

Non-dimensionalizing the hydrodynamics equations to get,

$$\frac{\partial}{\partial \bar{r}}\left[\bar{r}\bar{h}^3\frac{\partial \bar{p}}{\partial \bar{r}}\right]=12\bar{r}\frac{\partial \bar{h}}{\partial \bar{t}}, \qquad \text{A4.46}$$

along with,

$$\bar{h}\left(\bar{r},\bar{t}\right)=-\bar{h}_0\left(\bar{t}\right)+\frac{\bar{r}^2}{2}+\bar{w}\left(\bar{r},\bar{t}\right), \qquad \text{A4.47}$$

and following constraint equation,

$$\bar{F}=2\pi\int_0^{\infty}\bar{p}\left(\bar{r},\bar{t}\right)\bar{r}d\bar{r}\,. \qquad \text{A4.48}$$

The boundary conditions are normalized to,

a) $\left.\frac{\partial \bar{p}(\bar{r},\bar{t})}{\partial \bar{t}}\right|_{\bar{r}=0}=0,$ A4.49(a-b)

b) $\bar{p}(\bar{r},\bar{t})|_{\bar{r}\to\infty}\to 0.$

The initial condition becomes,

$$\bar{p}(\bar{r},\bar{t}=0)=0. \qquad \text{A4.50}$$

Non-dimensionalizing the lipid membrane deformation equation to get,

$$\nabla^4\bar{w}-2\bar{T}_0\nabla^2\bar{w}=-2\bar{p}\left(\bar{r}\right). \qquad \text{A4.51}$$

Equation A4.51 can be solved exactly analytically using Green's function to get,

$$\bar{w}(\bar{r}) = \frac{1}{\bar{T}_0}\left[K_0\left(\sqrt{2\bar{T}_0}\bar{r}\right)\int_0^{\bar{r}} I_0\left(\sqrt{2\bar{T}_0}\bar{\xi}\right)\bar{p}\left(\bar{\xi}\right)\bar{\xi}\,d\bar{\xi} + I_0\left(\sqrt{2\bar{T}_0}\bar{r}\right)\int_{\bar{r}}^{\infty} K_0\left(\sqrt{2\bar{T}_0}\bar{\xi}\right)\bar{p}\left(\bar{\xi}\right)\bar{\xi}\,d\bar{\xi}\right]$$

A4.52

Numerical solution

This problem is solved in a displacment controlled manner, which means $\bar{h}_0$ is incremented in time according to a specified rate, $\frac{\partial \bar{h}_0}{\partial \bar{t}}$, then pressure is obtained numerically and subsequently the deformation of the lipid membrane.

The numerical solution of the problem has been broken down into two parts. The former involves the state when the lipid membrane is significantly deformed and in the later part the deformation of the lipid membrane is negligible compared to h_0. In the following section each stage is described along with its numerical implementation.

1) lipid membrane significantly deformed $\left(\bar{h}_0 \approx \bar{w}|_{\bar{r}=0}\right)$

The system of equations governing the fluid flow eqs A4.46-A4.50 and A4.52 are solved using a numerical scheme, which is implicit, to obtain the pressure as a function of location along the radial direction while incrementing in time.

The numerical implementation is described as follows,

a) eq A4.46 can be expanded to get,

$$\left[\bar{h}^3 + 3\bar{r}\bar{h}^2\frac{\partial\bar{h}}{\partial\bar{r}}\right]\frac{\partial\bar{p}}{\partial\bar{r}} + \bar{r}\bar{h}^3\frac{\partial^2\bar{p}}{\partial\bar{r}^2} = 12\bar{r}\left(-\frac{\partial\bar{h}_0}{\partial\bar{t}} + \frac{\partial\bar{w}}{\partial\bar{t}}\right)$$

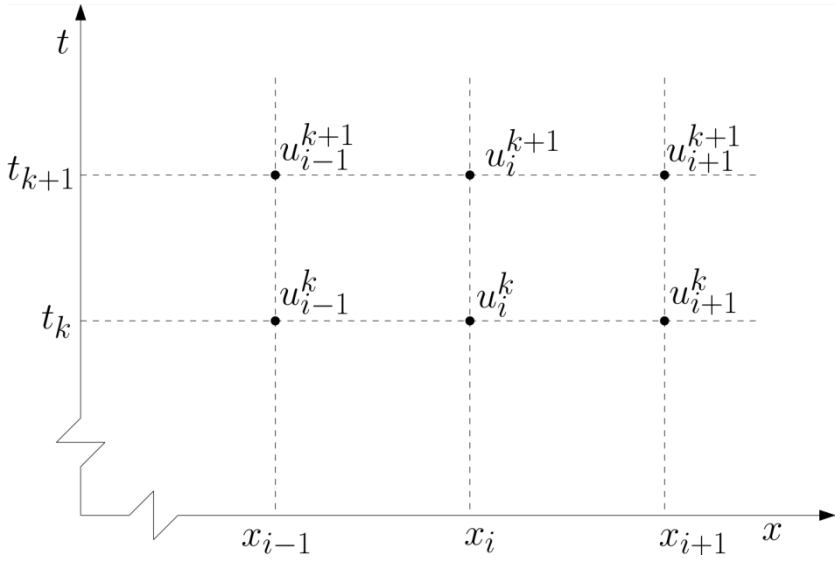

Fig A4.6 : Discretization scheme

b) to solve for pressure field at time $\bar{t}^{k+1}$, the above equation can discretized at a location $\bar{r}_i\,(i = 1,2,3....N)$, while using the following definition of the derivatives,

$$\left(\frac{\partial\bar{p}}{\partial\bar{r}}\right)_i^{k+1} = A_{i,i-1}\bar{p}_{i-1}^{k+1} + A_{i,i}\bar{p}_i^{k+1} + A_{i,i+1}\bar{p}_{i+1}^{k+1}, \text{ and}$$

$$\left(\frac{\partial^2\bar{p}}{\partial\bar{r}^2}\right)_i^{k+1} = B_{i,i-1}\bar{p}_{i-1}^{k+1} + B_{i,i}\bar{p}_i^{k+1} + B_{i,i+1}\bar{p}_{i+1}^{k+1},$$

to obtain,

$$\left[\left(\bar{h}^3+3\bar{r}\bar{h}^2\frac{\partial\bar{h}}{\partial\bar{r}}\right)_i^{k+1}A_{i,i-1}+\left(\bar{r}\bar{h}^3\right)_i^{k+1}B_{i,i-1}\right]\bar{p}_{i-1}^{k+1}$$
$$+\left[\left(\bar{h}^3+3\bar{r}\bar{h}^2\frac{\partial\bar{h}}{\partial\bar{r}}\right)_i^{k+1}A_{i,i}+\left(\bar{r}\bar{h}^3\right)_i^{k+1}B_{i,i}\right]\bar{p}_i^{k+1} \qquad \text{A4.53}$$
$$+\left[\left(\bar{h}^3+3\bar{r}\bar{h}^2\frac{\partial\bar{h}}{\partial\bar{r}}\right)_i^{k+1}A_{i,i+1}+\left(\bar{r}\bar{h}^3\right)_i^{k+1}B_{i,i+1}\right]\bar{p}_{i+1}^{k+1}$$
$$=12\bar{r}_i\left[\left(\frac{\partial\bar{h}_0}{\partial t}\right)^{k+1}+\frac{\bar{w}_i^{k+1}-\bar{w}_i^k}{\Delta t}\right].$$

For these equations, $i=2,3,\ \ldots N-1$.

Also,

$$\left(\frac{\partial\bar{h}}{\partial\bar{r}}\right)_i^{k+1}=A_{i,i-1}\bar{h}_{i-1}^{k+1}+A_{i,i}\bar{h}_i^{k+1}+A_{i,i+1}\bar{h}_{i+1}^{k+1},$$

along with,

$$\bar{h}_i^{k+1}=-\bar{h}_0^{k+1}+\frac{\bar{r}_i^2}{2}+\bar{w}_i^{k+1}.$$

c) Using the boundary condition eq A4.49b, $\bar{p}_N=0$.

d) Using the boundary condition eq. A4.49a, to rewrite as,

$$\frac{\bar{r}_2}{\bar{r}_1}\frac{\bar{p}_1}{\left(\bar{r}_1-\bar{r}_2\right)}+\frac{\bar{r}_1}{\bar{r}_2}\frac{\bar{p}_2}{\left(\bar{r}_2-\bar{r}_1\right)}+\bar{p}_0\frac{\bar{r}_2+\bar{r}_1}{\bar{r}_2\bar{r}_1}. \qquad \text{A4.54}$$

e) The rate of change of $\bar{h}_0$, $\frac{\partial\bar{h}_0}{\partial\bar{t}}$ is specified. For the present simulation it has been assumed to be, $\frac{\partial\bar{h}_0}{\partial\bar{t}}=-\frac{\bar{F}_{max}}{6\pi}\bar{h}_0\left(\frac{\bar{h}_0}{\bar{h}^*}\right)^m$. A4.55

This is based on the result from the rigid substrate case when the SNARE forces decay in accordance with the $\bar{F} = \bar{F}_{max}\left(\frac{\bar{h}_0}{\bar{h}^*}\right)^m$. This dependence of $\frac{\partial \bar{h}_0}{\partial \bar{t}}$ on $\bar{h}_0$ can be tuned my changing the exponent m.

f) $\bar{h}_0$ is incremented at each time step, by the amount specified according to $\frac{\partial \bar{h}_0}{\partial \bar{t}}$,

$$\bar{h}_0^{k+1} = \bar{h}_0^k + \left(\frac{\partial \bar{h}_0}{\partial \bar{t}}\right)^k \Delta t .$$

g) For a specified $\bar{h}_0$, the equations A4.53 and A4.54 solved iteratively and a solution is obtained.

h) From the converged solution of pressure, Force on the sphere is numerically evaluated using the discretized form of eq. A4.48,

$$\bar{F} = 2\pi\Delta r \sum_{i=1}^{N-1} \bar{p}_i \bar{r}_i . \qquad \text{A4.56}$$

This is simulated until the point that the deformation in the middle of the plasma membrane, $\bar{w}|_{\bar{r}=0}$ is negligible compared to $\bar{h}_0$.

Upto this point in the simulation force $\bar{F}$ and location of tip of the sphere $\bar{h}_0$, is measured at each time step. Using this data, a fitting of the form, $\bar{F} = \bar{F}_{max}\left(\frac{\bar{h}_0}{\bar{h}^*}\right)^x$ is done to obtain the exponent x.

2) lipid membrane deformation is negligible $\left(\bar{h}_0 \gg \bar{w}|_{\bar{r}=0}\right)$

In part 1 of the simulation scheme, the deformation at $\bar{r}=0$ is compared with $\bar{h}_0$, and once it is below a threshold value, then it can be ignored. This assumption can simplify the expression of $\bar{h}$ as,

$$\bar{h}\left(\bar{r},\bar{t}\right) \approx -\bar{h}_0\left(\bar{t}\right) + \frac{\bar{r}^2}{2}.$$

This assumption makes the convergence in the iterative solver faster. The numerical scheme remains the same as described in part A4.1).

A4.4 Small deformation of a flat lipid membrane

Consider a flat circular membrane, of radius l spanned in the polar coordinates of r and z. The governing equations for this membrane are given by,

$$\frac{\dot{Q}}{\dot{\xi}} = -\frac{Q}{r}\cos\varphi + 2H\left[d + \kappa H^2 + \kappa\left(2H + \frac{\sin\varphi}{r}\right)\frac{\sin\varphi}{r}\right] - p,$$

$$\frac{\dot{H}}{\dot{\xi}} = -\frac{Q}{\kappa},$$

$$\frac{\dot{\varphi}}{\dot{\xi}} = -2H - \frac{\sin\varphi}{r}, \qquad \text{A4.57(a-e)}$$

$$\frac{\dot{r}}{\dot{\xi}} = \cos\varphi,$$

$$\frac{\dot{z}}{\dot{\xi}} = \sin\varphi,$$

where, $\dot{\xi} = \frac{S}{r}$.

The boundary conditions associated with this membrane are,

1) at $S = 0,$

$$\varphi = 0,$$
$$Q = 0, \qquad \text{A4.58(a-c)}$$
$$r = 0,$$

these boundary conditions comply with the symmetry at the center of the geometry.

2) at $S = l,$

$$\varphi = 0,$$
$$z = 0, \qquad \text{A4.58(d-f)}$$
$$T = -d - \kappa H^2 - \kappa H \frac{\sin\varphi}{r} = T_0,$$

these boundary conditions mimic the far field boundary conditions of a flat lipid bilayer membrane in a finite sized geometry.

Non-dimensionalization

Normalizing this system of equations in accordance to the following scheme,

$$\bar{S} = \frac{S}{R}, \quad \bar{r} = \frac{r}{R}, \quad \bar{z} = \frac{z}{R}, \quad \bar{H} = RH, \quad \bar{\xi} = \frac{\xi}{R},$$

$$\bar{Q} = \frac{QR^2}{\kappa}, \ \bar{d} = \frac{dR^2}{\kappa}, \bar{T} = \frac{TR^2}{\kappa}, \qquad \text{A4.59(a-i)}$$

$$\bar{p} = \frac{pR^3}{\kappa}, \bar{t}^S = \frac{t^S R^3}{\kappa}.$$

In the above scheme, the quantity R is the radius of the synaptic vesicle and κ is the bending rigidity of the lipid bilayer membrane. On applying this non-dimensionalization scheme to the system of eqs. A4.57(a-e) and boundary conditions eqs. A4.58(a-f), we get,

$$\frac{\dot{\bar{Q}}}{\dot{\bar{\xi}}} = -\frac{\bar{Q}}{\bar{r}}\cos\varphi + 2\bar{H}\left[\bar{d} + \bar{H}^2 + \left(2\bar{H} + \frac{\sin\varphi}{\bar{r}}\right)\frac{\sin\varphi}{\bar{r}}\right] - \bar{p},$$

$$\frac{\dot{\bar{H}}}{\dot{\bar{\xi}}} = -\bar{Q},$$

$$\frac{\dot{\varphi}}{\dot{\bar{\xi}}} = -2\bar{H} - \frac{\sin\varphi}{\bar{r}}, \qquad \text{A4.60(a-f)}$$

$$\frac{\dot{\bar{r}}}{\dot{\bar{\xi}}} = \cos\varphi,$$

$$\frac{\dot{\bar{z}}}{\dot{\bar{\xi}}} = \sin\varphi,$$

where, $\dot{\bar{\xi}} = \frac{\bar{S}}{\bar{r}}$.

The boundary conditions modify as follows,

1) at $\bar{S} = 0$,

$$\varphi = 0,$$
$$\bar{Q} = 0, \qquad \text{A4.61(a-c)}$$
$$\bar{r} = 0,$$

2) at $\bar{S} = \bar{l}$,

$$\varphi = 0,$$
$$\bar{z} = 0, \qquad \text{A4.61(d-f)}$$
$$\bar{T} = -\bar{d} - \bar{H}^2 - \bar{H}\frac{\sin\varphi}{\bar{r}} = \bar{T}_0.$$

<u>Udeformed membrane</u>

For an unperturbed membrane, in its undeformed configuration, the loading should be zero ($\bar{p} = 0$), and the system variables are given by,

$$\bar{Q} = 0, \bar{H} = 0, \varphi = 0, \bar{r} = \bar{S} \text{ and } \bar{z} = 0, \qquad \text{A4.62(a-f)}$$

with $\bar{d} = -\bar{T}_0$.

Perturbed solution

Let's choose the following first order perturbation scheme about the undeformed configuration,

$$\bar{Q} = 0 + \bar{Q}_1,$$

$$\bar{H} = 0 + \bar{H}_1, \qquad \text{A4.63(a-f)}$$

$$\bar{\varphi} = 0 + \bar{\varphi}_1,$$

$$\bar{r} = \bar{S} + \bar{r}_1,$$

$$\bar{z} = 0 + \bar{z}_1,$$

$$\bar{d} = -\bar{T}_0 + \bar{d}_1.$$

Now we can derive the boundary conditions in terms of the perturbed variables as follows,

The boundary conditions modify as follows,

1) at $\bar{S} = 0$,

$$\begin{aligned} &\varphi = 0 \Rightarrow \varphi_1 = 0 \\ &\bar{Q} = 0 \Rightarrow \bar{Q}_1 = 0 \\ &\bar{r} = 0 \Rightarrow \bar{r}_1 = 0 \end{aligned} \qquad \text{A4.64(a-c)}$$

2) at $\bar{S} = \bar{l}$,

$$\begin{aligned} &\varphi = 0 \Rightarrow \varphi_1 = 0 \\ &\bar{z} = 0 \Rightarrow \bar{z}_1 = 0, \\ &-\bar{d} - \bar{H}^2 - \bar{H}\frac{\sin\varphi}{\bar{r}} = \bar{T}_0 \Rightarrow \bar{T}_0 - \bar{d}_1 - \bar{H}_1^2 - \bar{H}_1\frac{\varphi_1}{\bar{S}+\bar{r}} = \bar{T}_0 \Rightarrow \bar{d}_1 = 0. \end{aligned} \qquad \text{A4.65(d-f)}$$

Hence, $\bar{d} = -\bar{T}_0$.

Perturbing the governing equations

We start with perturbing the equations one by one and get a linearized form of equations.

1) $$\frac{\dot{\bar{Q}}}{\dot{\bar{\xi}}} = -\frac{\bar{Q}}{\bar{r}}\cos\varphi + 2\bar{H}\left[\bar{d} + \bar{H}^2 + \left(2\bar{H} + \frac{\sin\varphi}{\bar{r}}\right)\frac{\sin\varphi}{\bar{r}}\right] - \bar{p}$$

$$\Rightarrow \dot{\bar{Q}} = -\dot{\bar{\xi}}\frac{\bar{Q}}{\bar{r}}\cos\varphi + 2\bar{H}\dot{\bar{\xi}}\left[\bar{d} + \bar{H}^2 + \left(2\bar{H} + \frac{\sin\varphi}{\bar{r}}\right)\frac{\sin\varphi}{\bar{r}}\right] - \bar{p}\dot{\bar{\xi}}$$

$$\Rightarrow \dot{\bar{Q}} = -\frac{\bar{Q}\bar{S}}{\bar{r}^2}\cos\varphi + 2\bar{H}\frac{\bar{S}}{\bar{r}}\left[\bar{d} + \bar{H}^2 + \left(2\bar{H} + \frac{\sin\varphi}{\bar{r}}\right)\frac{\sin\varphi}{\bar{r}}\right] - \bar{p}\frac{\bar{S}}{\bar{r}}$$

$$\Rightarrow \bar{r}^3\dot{\bar{Q}} = -\bar{Q}\bar{S}\bar{r}\cos\varphi + 2\bar{H}\bar{S}\left[\left(\bar{d} + \bar{H}^2\right)\bar{r}^2 + \left(2\bar{H}\bar{r} + \sin\varphi\right)\sin\varphi\right] - \bar{p}\bar{r}^2\bar{S}$$

plugging in the perturbed functions into the above expression and solving step by step,

$\left(\bar{d} + \bar{H}^2\right) = -\bar{T}_0 + \bar{H}_1^2 \approx -\bar{T}_0$,

$\bar{r}^2\left(\bar{d} + \bar{H}^2\right) = \left(\bar{S}^2 + 2\bar{r}_1\bar{S} + \bar{r}_1^2\right)\left(-\bar{T}_0\right) \approx -\left(\bar{S}^2 + 2\bar{r}_1\bar{S}\right)\bar{T}_0$,

$\left(2\bar{H}\bar{r} + \sin\varphi\right)\sin\varphi = \left[2\bar{H}_1\left(\bar{r}_1 + \bar{S}\right) + \varphi_1\right]\varphi_1 \approx 0$,

$\left[\bar{r}^2\left(\bar{d} + \bar{H}^2\right) + \left(2\bar{H}\bar{r} + \sin\varphi\right)\sin\varphi\right] = -\left(\bar{S}^2 + 2\bar{r}_1\bar{S}\right)\bar{T}_0$,

$2\bar{H}\bar{S}\left[\left(\bar{d} + \bar{H}^2\right)\bar{r}^2 + \left(2\bar{H}\bar{r} + \sin\varphi\right)\sin\varphi\right] = 2\bar{H}_1\bar{S}\left[-\left(\bar{S}^2 + 2\bar{r}_1\bar{S}\right)\bar{T}_0\right] \approx -2\bar{H}_1\bar{T}_0\bar{S}^3$,

$-\bar{p}\bar{r}^2\bar{S} \approx -p\left(\bar{S}^2 + 2\bar{r}_1\bar{S}\right)\bar{S}$,

$$-\bar{Q}\bar{S}\bar{r}\cos\varphi = -\bar{Q}_1\bar{S}\left(\bar{r}_1+\bar{S}\right)\cos\varphi_1 \approx -\bar{Q}_1\bar{S}^2,$$

hence, the R.H.S. of equation simplifies to,

$$-\bar{Q}\bar{S}\bar{r}\cos\varphi + 2\bar{H}\bar{S}\left[\left(\bar{d}+\bar{H}^2\right)\bar{r}^2+\left(2\bar{H}\bar{r}+\sin\varphi\right)\sin\varphi\right] - \bar{p}\bar{r}^2\bar{S} = -\bar{Q}_1\bar{S}^2 - 2\bar{H}_1\bar{T}_0\bar{S}^3 - p\left(\bar{S}^2+2\bar{r}_1\bar{S}\right)\bar{S}.$$

On the other hand, L.H.S. can be written as,

$$\bar{r}^3\dot{\bar{Q}} = \left(\bar{r}_1+\bar{S}\right)^3\dot{\bar{Q}}_1 \approx \bar{S}^3\dot{\bar{Q}}_1.$$

Combining both L.H.S. and R.H.S., to get,

$$\bar{S}^3\dot{\bar{Q}}_1 = -\bar{Q}_1\bar{S}^2 - 2\bar{H}_1\bar{T}_0\bar{S}^3 - p\left(\bar{S}^2+2\bar{r}_1\bar{S}\right)\bar{S},$$

$$\Rightarrow \dot{\bar{Q}}_1 = -\frac{\bar{Q}_1}{\bar{S}} - 2\bar{H}_1\bar{T}_0 - p\left(1+2\frac{\bar{r}_1}{\bar{S}}\right). \qquad \text{A4.66a}$$

2) $$\frac{\dot{\bar{H}}}{\dot{\bar{\xi}}} = -\bar{Q}$$

$$\Rightarrow \dot{\bar{H}}\bar{r} = -\bar{S}\bar{Q},$$

plugging in the perturbed functions,

$$\Rightarrow \dot{\bar{H}}_1\left(\bar{r}_1+\bar{S}\right) = -\bar{S}\bar{Q}_1$$
$$\Rightarrow \dot{\bar{H}}_1\bar{S} = -\bar{S}\bar{Q}_1$$

$$\Rightarrow \dot{\bar{H}}_1 = -\bar{Q}_1 \qquad \text{A4.66b}$$

3) $$\frac{\dot{\varphi}}{\dot{\bar{\xi}}} = -2\bar{H} - \frac{\sin\varphi}{\bar{r}},$$

$$\Rightarrow \dot{\varphi} = -2\bar{H}\dot{\bar{\xi}} - \frac{\sin\varphi}{\bar{r}}\dot{\bar{\xi}},$$
$$\Rightarrow \dot{\varphi} = -2\bar{H}\frac{\bar{S}}{\bar{r}} - \frac{\sin\varphi}{\bar{r}}\frac{\bar{S}}{\bar{r}},$$
$$\Rightarrow \bar{r}^2\dot{\varphi} = -2\bar{H}\bar{S}\bar{r} - \sin\varphi\bar{S},$$

plugging in the perturbed functions,

$$\Rightarrow \left(\bar{r}_1 + \bar{S}\right)^2 \dot{\varphi}_1 = -2\bar{H}_1\bar{S}\left(\bar{r}_1 + \bar{S}\right) - \sin\varphi_1\bar{S},$$
$$\Rightarrow \bar{S}^2\dot{\varphi}_1 = -2\bar{H}_1\bar{S}^2 - \varphi_1\bar{S},$$

$$\Rightarrow \dot{\varphi}_1 = -2\bar{H}_1 - \frac{\varphi_1}{\bar{S}}, \qquad \text{A4.66c}$$

4) $$\frac{\dot{\bar{r}}}{\dot{\bar{\xi}}} = \cos\varphi,$$

$$\Rightarrow \dot{\bar{r}} = \dot{\bar{\xi}}\cos\varphi,$$
$$\Rightarrow \dot{\bar{r}} = \frac{\bar{S}}{\bar{r}}\cos\varphi,$$
$$\Rightarrow \bar{r}\,\dot{\bar{r}} = \bar{S}\cos\varphi,$$

plugging in the perturbed functions,

$$\Rightarrow \left(\bar{r}_1 + \bar{S}\right)\left(\dot{\bar{r}}_1 + 1\right) = \bar{S}\cos\varphi_1,$$
$$\Rightarrow \bar{r}_1 + \bar{S} + \bar{S}\,\dot{\bar{r}}_1 = \bar{S},$$

$$\Rightarrow \dot{\bar{r}}_1 = -\frac{\bar{r}_1}{\bar{S}}, \qquad \text{A4.66d}$$

5) $$\frac{\dot{\bar{z}}}{\dot{\bar{\xi}}} = \sin\varphi,$$

$$\Rightarrow \dot{\bar{z}} = \dot{\bar{\xi}} \sin\varphi,$$

$$\Rightarrow \dot{\bar{z}} = \frac{\bar{S}}{\bar{r}} \sin\varphi,$$

$$\Rightarrow \bar{r}\dot{\bar{z}} = \bar{S} \sin\varphi,$$

plugging in the perturbed functions,

$$\Rightarrow \left(\bar{r}_1 + \bar{S}\right)\dot{\bar{z}}_1 = \bar{S} \sin\varphi_1,$$

$$\Rightarrow \dot{\bar{z}}_1 = \varphi_1, \qquad \text{A4.66e}$$

Hence, we have following system of equations,

$$\dot{\bar{Q}}_1 = -\frac{\bar{Q}_1}{\bar{S}} - 2\bar{H}_1\bar{T}_0 - p\left(1 + 2\frac{\bar{r}_1}{\bar{S}}\right)$$

$$\dot{\bar{H}}_1 = -\bar{Q}_1$$

$$\dot{\varphi}_1 = -2\bar{H}_1 - \frac{\varphi_1}{\bar{S}}, \qquad \text{A4.66(a-e)}$$

$$\dot{\bar{r}}_1 = -\frac{\bar{r}_1}{\bar{S}},$$

$$\dot{\bar{z}}_1 = \varphi_1,$$

Along with following boundary conditions,

1) at $\bar{S} = 0,$

$$\varphi = 0 \Rightarrow \varphi_1 = 0$$
$$\bar{Q} = 0 \Rightarrow \bar{Q}_1 = 0 \qquad \text{A4.65(a-c)}$$
$$\bar{r} = 0 \Rightarrow \bar{r}_1 = 0$$

2) at $\bar{S} = \bar{l},$

$$\varphi = 0 \Rightarrow \varphi_1 = 0$$
$$\bar{z} = 0 \Rightarrow \bar{z}_1 = 0, \qquad \text{A4.65(d-e)}$$

<u>Combined equation and comaprison with plate equation</u>

Reviewing the governing equations,

$$\dot{\bar{Q}}_1 = -\frac{\bar{Q}_1}{\bar{S}} - 2\bar{H}_1\bar{T}_0 - p\left(1 + 2\frac{\bar{r}_1}{\bar{S}}\right)$$

$$\dot{\bar{H}}_1 = -\bar{Q}_1$$

$$\dot{\varphi}_1 = -2\bar{H}_1 - \frac{\varphi_1}{\bar{S}}, \qquad \text{A4.66(a-e)}$$

$$\dot{\bar{r}}_1 = -\frac{\bar{r}_1}{\bar{S}},$$

$$\dot{\bar{z}}_1 = \varphi_1.$$

Start with plugging in the eq. A4.66e into eq. A4.66c,

$$\ddot{\bar{z}}_1 = -2\bar{H}_1 - \frac{\dot{\bar{z}}_1}{\bar{S}} \Rightarrow \bar{H}_1 = -\frac{1}{2}\left(\ddot{\bar{z}}_1 + \frac{\dot{\bar{z}}_1}{\bar{S}}\right), \qquad \text{A4.67}$$

plugging eq. A4.67 into eq. A4.66b,

$$\bar{Q}_1 = -\dot{\bar{H}}_1 \Rightarrow \bar{Q}_1 = \frac{1}{2}\left(\dddot{\bar{z}}_1 + \frac{\ddot{\bar{z}}_1}{\bar{S}} - \frac{\dot{\bar{z}}_1}{\bar{S}^2}\right), \qquad \text{A4.68}$$

plugging eqs. A4.67 and A4.68 into eq. A4.66a,

$$\dot{\bar{Q}}_1+\frac{\bar{Q}_1}{\bar{S}}+2\bar{H}_1\bar{T}_0=-p\left(1+2\frac{\bar{r}_1}{\bar{S}}\right),$$

$$\Rightarrow\frac{1}{2}\left(\ddddot{\bar{z}}_1+\frac{\dddot{\bar{z}}_1}{\bar{S}}-2\frac{\ddot{\bar{z}}_1}{\bar{S}^2}+2\frac{\dot{\bar{z}}_1}{\bar{S}^3}\right)+\frac{1}{2}\left(\frac{\dddot{\bar{z}}_1}{\bar{S}}+\frac{\ddot{\bar{z}}_1}{\bar{S}^2}-\frac{\dot{\bar{z}}_1}{\bar{S}^3}\right)-\bar{T}_0\left(\ddot{\bar{z}}_1+\frac{\dot{\bar{z}}_1}{\bar{S}}\right)=-p\left(1+2\frac{\bar{r}_1}{\bar{S}}\right),$$

$$\Rightarrow\frac{1}{2}\left(\ddddot{\bar{z}}_1+2\frac{\dddot{\bar{z}}_1}{\bar{S}}-\frac{\ddot{\bar{z}}_1}{\bar{S}^2}+\frac{\dot{\bar{z}}_1}{\bar{S}^3}\right)-\bar{T}_0\left(\ddot{\bar{z}}_1+\frac{\dot{\bar{z}}_1}{\bar{S}}\right)=-p\left(1+2\frac{\bar{r}_1}{\bar{S}}\right),$$

$$\Rightarrow\frac{1}{\bar{S}}\frac{\partial}{\partial\bar{S}}\left[\bar{S}\frac{\partial}{\partial\bar{S}}\left\{\frac{1}{\bar{S}}\frac{\partial}{\partial\bar{S}}\left(\bar{S}\frac{\partial\bar{z}_1}{\partial\bar{S}}\right)\right\}\right]-2\bar{T}_0\left[\frac{1}{\bar{S}}\frac{\partial}{\partial\bar{S}}\left(\bar{S}\frac{\partial\bar{z}_1}{\partial\bar{S}}\right)\right]=-2p\left(1+2\frac{\bar{r}_1}{\bar{S}}\right),$$

$$\Rightarrow\nabla_{\bar{S}}^4\bar{z}_1-2\bar{T}_0\nabla_{\bar{S}}^2\bar{z}_1=-2p\left(1+2\frac{\bar{r}_1}{\bar{S}}\right). \qquad \text{A4.69}$$

Comparing this with the governing equation in the literature for a plate with pretension,

$$\nabla_{\bar{r}}^4\bar{w}-\bar{\sigma}_0\nabla_{\bar{r}}^2\bar{w}=\bar{q}, \qquad \text{A4.70}$$

where, $\bar{w}$ is the deflection in the plate,

$\bar{\sigma}_0$ is the pretension in the plate,

$\bar{q}$ is the load per unit area on the plate, and

$\bar{r}$ is the r coordinate of the system.

It can be shown that eqs. A4.69 and A4.70 are same equations. In order to do that, consider eq. A4.66d,

$$\dot{\bar{r}}_1=-\frac{\bar{r}_1}{\bar{S}}\Rightarrow\frac{\partial\bar{r}_1}{\partial\bar{S}}=-\frac{\bar{r}_1}{\bar{S}}\Rightarrow\ln\bar{r}_1+\ln\bar{S}=c\Rightarrow\bar{r}_1\bar{S}=\mathrm{c}_1,$$

along with the boundary condition in eq. A4.65c, $\bar{r}_1\left(\bar{S}=0\right)=0$

$$\Rightarrow\bar{r}_1\bar{S}=0\Rightarrow\bar{r}_1=0. \qquad \text{A4.71}$$

This also helps to conclude from eq. A4.67 d,

$$\bar{r} = \bar{S} \ . \qquad \text{A4.72}$$

Hence, eq. A4.69 can be written down as,

$$\nabla^4_{\bar{r}} \bar{z}_1 - 2\bar{T}_0 \nabla^2_{\bar{r}} \bar{z}_1 = -2p. \qquad \text{A4.73}$$

On comapring eqs. A4.70 and A4.73,

$\bar{\sigma}_0 = 2\bar{T}_0$ and $\bar{q} = -2\bar{p}$.

A4.5 Solution of Small deformation lipid membrane equation

The non-dimensionalised small deformation equation for an axis-symmetric flat lipid membrane can be written as,

$$\nabla^4 w(r) - 2T_0 \nabla^2 w(r) = -2p(r) \qquad \text{A4.74}$$

where,

$w(r)$, is the vertical deformation of the membrane at a given location r,

T_0, is the far field tension in the membrane, and

$p(r)$, is the pressure acting on the membrane at some given location r.

Making following replacements,

$\sigma^2 = 2T_0$ and $q(r) = -2p(r)$,

to get,

$$\nabla^4 w(r) - \sigma^2 \nabla^2 w(r) = q(r). \qquad \text{A4.75}$$

Making one more substitution of $\varphi(r) = \nabla^2 w(r)$ A4.76

to get,

$$\nabla^2 \varphi(r) - \sigma^2 \varphi = q(r). \qquad \text{A4.77}$$

For now, assuming that the pressure distribution is localized on a ring of radius r_0.

Hence, we have,

$q(r) = \delta(r - r_0)$,

and it has the following integral result,

$$2\pi\int_0^\infty r\delta(r-r_0)\,dr = 1. \qquad \text{A4.78}$$

Solving for $\varphi(r)$

We solve eq A4.77for $\varphi(r)$ and eventually solve for $w(r)$. Eq A4.77 can be solved two different ways, method 1 involves use of Hankel Transform and method 2 is standard ODE solving.

Method 1

Taking Hankel transform of eq A4.77,

$$-\xi^2\tilde{\varphi}(\xi)-\sigma^2\tilde{\varphi}(\xi)=\tilde{q}(\xi)=\int_0^\infty q(\rho)J_0(\rho\xi)\rho d\rho \ ,$$

where, $\tilde{f}(\xi)=\int_o^\infty f(r)J_0(r\xi)rdr$ denotes the Hankel transform of a function $f(r)$.

Further simplification gives,

$$\Rightarrow \tilde{\varphi}(\xi)=-\frac{1}{\sigma^2+\xi^2}\int_0^\infty q(\rho)J_0(\rho\xi)\rho d\rho \ .$$

Taking inverse Hankel transform and rearranging the order of integrals to get,

$$\Rightarrow \varphi(r)=-\int_0^\infty \frac{\xi J_0(r\xi)}{\sigma^2+\xi^2}\left[\int_0^\infty q(\rho)J_0(\rho\xi)\rho d\rho\right]d\xi,$$

$$\Rightarrow \varphi(r)=-\int_0^\infty \rho q(\rho)\left[\int_0^\infty \frac{\xi J_0(r\xi)J_0(\rho\xi)}{\sigma^2+\xi^2}d\xi\right]d\rho.$$

The integral in the [ ] brackets is a standard integral and can be written as follows,

$$\int_0^\infty \frac{\xi J_0(r\xi)J_0(\rho\xi)}{\sigma^2+\xi^2}d\xi=\begin{cases} I_0(\rho\sigma)K_0(r\sigma) & 0<\rho<r \\ K_0(\rho\sigma)I_0(r\sigma) & r<\rho \end{cases}.$$

Implementing this result in the integral, we get,

$$\Rightarrow \varphi(r) = -\int_0^r \rho q(\rho) I_0(\rho\sigma) K_0(r\sigma) d\rho - \int_r^\infty \rho q(\rho) K_0(\rho\sigma) I_0(r\sigma) d\rho,$$

$$\Rightarrow \varphi(r) = -K_0(r\sigma)\int_0^r \rho q(\rho) I_0(\rho\sigma) d\rho - I_0(r\sigma)\int_r^\infty \rho q(\rho) K_0(\rho\sigma) d\rho.$$

Now, plugging in the fact that q is a delta function to get a solution for φ

$$\Rightarrow \varphi(r) = -\frac{1}{2\pi}\begin{cases} I_0(r\sigma) K_0(r_0\sigma) & r < r_0 \\ K_0(r\sigma) I_0(r_0\sigma) & r > r_0 \end{cases}. \qquad \text{A4.79}$$

Method 2

Because of the delta function at $r = r_0$, in the region $r \in [0,\infty)$ excluding $r = r_0$, the solution of the eq A4.77 can be written down in terms of two arbitrary constants as follows,

$$\varphi(r) = \begin{cases} A\, I_0(\sigma r) & r < r_0 \\ B\, K_0(\sigma r) & r > r_0 \end{cases}. \qquad \text{A4.80}$$

From the inspection of eq A4.77, it can be observed that, the delta function on the right hand side originates from the $\nabla^2\varphi(r)$ term, rather than $\varphi(r)$ term.

Integrating, both sides of eq A4.77, in the interval $r \in [r_0 - \varepsilon, r_0 + \varepsilon]$,

$$\int_{r_0-\varepsilon}^{r_0+\varepsilon} \left(\nabla^2\varphi - \sigma^2\varphi\right) r dr = \int_{r_0-\varepsilon}^{r_0+\varepsilon} q r dr,$$

$$\Rightarrow \int_{r_0-\varepsilon}^{r_0+\varepsilon} \left[\frac{1}{r}\frac{\partial}{\partial r}\left(r\frac{\partial\varphi}{\partial r}\right) - \sigma^2\varphi\right] r dr = \int_{r_0-\varepsilon}^{r_0+\varepsilon} r\delta(r - r_0) dr,$$

$$\Rightarrow \left(r\frac{\partial\varphi}{\partial r}\right)_{r_0-\varepsilon}^{r_0+\varepsilon} - \underbrace{\sigma^2\varphi\big|_{r_0-\varepsilon}^{r_0+\varepsilon}}_{\approx O(\epsilon)} = \frac{1}{2\pi},$$

$$\Rightarrow (r_0 + \varepsilon)\left(\frac{\partial\varphi}{\partial r}\right)\Big|_{r=r_0+\varepsilon} - (r_0 - \varepsilon)\left(\frac{\partial\varphi}{\partial r}\right)\Big|_{r=r_0-\varepsilon} - 0 = \frac{1}{2\pi},$$

$$\Rightarrow r_0\left[\left(\frac{\partial\varphi}{\partial r}\right)\Big|_{r=r_0+\epsilon} - \left(\frac{\partial\varphi}{\partial r}\right)\Big|_{r=r_0-\varepsilon}\right] = \frac{1}{2\pi}. \qquad \text{A4.81}$$

Apart from this, we have continuity condition for $\varphi(r)$ at $r = r_0$,

$$\varphi|_{r=r_0+\epsilon} = \varphi|_{r=r_0-\epsilon}. \qquad \text{A4.82.}$$

Using the expression of φ from eq A4.80 into the eqs A4.81 and A4.82, to get following set of equations,

$$r_0\left[-B\,K_1(\sigma r_0) - A\,I_1(\sigma r_0)\right] = \frac{q_0}{2\pi}, \qquad \text{A4.83}$$

$$A\,I_0(\sigma r_0) = B\,K_0(\sigma r_0). \qquad \text{A4.84}$$

Solving eqs A4.83 and A4.84 for A and B,

$$A = -\frac{1}{2\pi\sigma r_0}\left[\frac{K_0(\sigma r_0)}{I_0(\sigma r_0)K_1(\sigma r_0) + K_0(\sigma r_0)I_1(\sigma r_0)}\right],$$
$$B = -\frac{1}{2\pi\sigma r_0}\left[\frac{I_0(\sigma r_0)}{I_0(\sigma r_0)K_1(\sigma r_0) + K_0(\sigma r_0)I_1(\sigma r_0)}\right].$$

Using the Wronskian property of modified Bessel functions,

$$I_0(\sigma r_0)K_1(\sigma r_0) + K_0(\sigma r_0)I_1(\sigma r_0) = \frac{1}{\sigma r_0},$$

into the expressions for A and B, to get,

$$A = -\frac{1}{2\pi}K_0(\sigma r_0),$$
$$B = -\frac{1}{2\pi}I_0(\sigma r_0).$$

Going back to eq A4.80, and plugging in the values of A and B to get,

$$\varphi(r) = -\frac{1}{2\pi}\begin{cases} I_0(\sigma r)K_0(\sigma r_0) & r < r_0 \\ K_0(\sigma r)I_0(\sigma r_0) & r > r_0 \end{cases}. \qquad \text{A4.85}$$

Solving for $w(r)$

Both methods of solving yielded the same result, as seen in eqs A4.79 and A4.85.

Next step, is to solve for $w(r)$, in the equation,

$$\nabla^2 w(r) = \varphi(r) = -\frac{1}{2\pi}\begin{cases} I_0(\sigma r) K_0(\sigma r_0) & r < r_0 \\ K_0(\sigma r) I_0(\sigma r_0) & r > r_0 \end{cases}$$

$$\Rightarrow \frac{\partial^2 w}{\partial r^2} + \frac{1}{r}\frac{\partial w}{\partial r} = -\frac{1}{2\pi}\begin{cases} I_0(\sigma r) K_0(\sigma r_0) & r < r_0 \\ K_0(\sigma r) I_0(\sigma r_0) & r > r_0 \end{cases}. \qquad \text{A4.86}$$

The homogeneous solution of eq A4.86 is,

$w(r) = C\ln r + D$.

For a closed form w, $C = 0$ and for the asymptotic solution of $w \to 0$, $D = 0$. Hence, the solution of eq A4.86 only comprises of the particular solution.

Since, $I_0(\sigma r)$ and $K_0(\sigma r)$ are solutions to the following differential equation,

$$\frac{\partial^2 y}{\partial r^2} + \frac{1}{r}\frac{\partial y}{\partial r} - \sigma^2 y = 0 \Rightarrow \frac{\partial^2 y}{\partial r^2} + \frac{1}{r}\frac{\partial y}{\partial r} = \sigma^2 y,$$

hence,

$$\frac{\partial^2 I_0(\sigma r)}{\partial r^2} + \frac{1}{r}\frac{\partial I_0(\sigma r)}{\partial r} = \sigma^2 I_0(\sigma r) \quad \text{and} \quad \frac{\partial^2 K_0(\sigma r)}{\partial r^2} + \frac{1}{r}\frac{\partial K_0(\sigma r)}{\partial r} = \sigma^2 K_0(\sigma r).$$

Using the above fact to obtain the particular solution,

$$\Rightarrow w(r) = -\frac{1}{2\pi\sigma^2}\begin{cases} I_0(\sigma r) K_0(\sigma r_0) & r < r_0 \\ K_0(\sigma r) I_0(\sigma r_0) & r > r_0 \end{cases}. \qquad \text{A4.87}$$

This solution of $w(r)$ in eq A4.87 is the Green's function of the eq A4.75 and can be written in the standard Green's function representation as,

$$G(r\,|\,\xi) = -\frac{1}{2\pi\sigma^2}\begin{cases} I_0(\sigma r)K_0(\sigma\xi) & r<\xi \\ K_0(\sigma r)I_0(\sigma\xi) & r>\xi \end{cases}, \qquad \text{A4.88}$$

and hence,

$$w(r) = 2\pi\int_0^{\infty} G(r\,|\,\xi)q(\xi)\xi d\xi,$$

$$w(r) = -\frac{1}{\sigma^2}\left[K_0(\sigma r)\int_0^{r} I_0(\sigma\xi)q(\xi)\xi d\xi + I_0(\sigma r)\int_r^{\infty} K_0(\sigma\xi)q(\xi)\xi d\xi\right].$$

Plugging in, the values of $q(\xi) = -2p(\xi)$ and $\sigma^2 = 2T_0$,

$$w(r) = \frac{1}{T_0}\left[K_0\left(\sqrt{2T_0}r\right)\int_0^{r} I_0\left(\sqrt{2T_0}\xi\right)p(\xi)\xi d\xi + I_0\left(\sqrt{2T_0}r\right)\int_r^{\infty} K_0\left(\sqrt{2T_0}\xi\right)p(\xi)\xi d\xi\right].$$

A4.89

Implementation in a numerical scheme

For a numerical scheme when the pressure $p(r_i)$ is provided at some discrete data point r_i. Apart from that the domain is also finite, hence the second integral instead of going to ∞ goes to some large value, l. Under these conditions, the deformation $w(r_i)$ can be written as,

$$w(r_i) = \frac{\Delta r}{T_0}\left[K_0\left(\sqrt{2T_0}r_i\right)\sum_{j=0}^{j=i}\left\{I_0\left(\sqrt{2T_0}r_j\right)p\left(r_j\right)r_j\right\} + I_0\left(\sqrt{2T_0}r_i\right)\sum_{j=i+1}^{j=n}\left\{K_0\left(\sqrt{2T_0}r_j\right)p\left(r_j\right)r_j\right\}\right].$$

A4.90

Chapter 5

During synaptic vesicle fusion, SNARE family proteins play an extremely important role. The SNARE complex is anchored to the membranes of the synaptic vesicle and neuron base. They mediate the vesicle fusion starting from docking the vesicle, fusing the lipid membranes and eventually leading to the fusion pore formation. The role of SNARE proteins and the intermediate stages of this fusion are a topic of debate in the neuroscience community. It is believed that SNARE complexes work in collaboration to bring down the synaptic vesicle. The questions on an ideal arrangement of SNARE complexes, number of SNARE complexes and role of membrane tension are still unclear.

In the present work, we have used a Molecular Dynamics (MD) scheme to extract details of synaptic vesicle fusion. The MD scheme used in this work is known as Coarse Grained MD (CGMD). CGMD simulations are an important tool in analyzing complex systems. The behavior of multiple particles can be aggregated to be represented by one single particle. This simplification offers a huge computational advantage by making simulations faster. A reduction in computational expense allows researchers to carry out simulations for longer physical times and for spatially larger systems compared to All Atom (AA) simulations. Due to its capability to run simulations for longer time durations, we were able to simulate synaptic vesicle fusion over a span of nano-seconds. During these simulations we were able to demonstrate the occurrence of synaptic vesicle membrane fusing with neuron plasma membrane and leading to the fusion pore formation.

The CG scheme presented in this work is still under development. With this scheme we aim to understand the dynamics of during the synaptic vesicle fusion. We aim to study the arrangement of SNARE complexes between the two membranes. This arrangement plays an important role as it is an outcome of SNARE to SNARE interaction. Moving further, we will want to answer the most debatable question in the neuroscience community on how many SNAREs are needed to carry out a successful synaptic vesicle fusion. We also want to understand the role of high in-plane tension in synaptic vesicle membrane. This in-plane tension is a result of the osmotic pressure across the lipid membrane of synaptic vesicle, due to the presence of neurotransmitters inside it. The lipid membrane tension is believed to increase the probability of fusion pore formation. In this work we present qualitative results on the effect of in-plane tension in the lipid membrane.

5.1 Abstract

Synaptic vesicle fusion is a key step in the neurotransmission process. SNARE proteins mediate the docking of synaptic vesicles at the plasma membrane and eventually leading to the fusion pore formation which releases the neurotransmitter into the synaptic cleft. In the present work we propose a CGMD model of two juxtaposed lipid membranes undergoing a fusion pore formation. We study the influence of varying number of SNARE complexes and the tension in the lipid membranes on the vesicle fusion. We find that the strength of interaction between the transmembrane domain and the hydrophobic core of the lipid membrane is an important factor in orchestrating the fusion pore formation.

5.2 Introduction

Neurotransmission at the junction of two neurons is mediated by the SNARE (Soluble NSF Attachment Protein Receptor) machinery [1], [2]. SNARE complexes are present in between the synaptic vesicle and plasma membrane of neuron base, linking the two membrane structures. The membranes are held close to each other with the help of clamping force provided by SNARE complexes [3]. This clamping force is believed to be the driving force for the synaptic vesicle fusion and subsequently the fusion pore formation [4]. The mechanism of the fusion pore formation is still an unanswered question as it is difficult to witness the process in vitro, due to its extremely small time and length scales. The process is believed to proceed through two major steps before the release of neurotransmitter in the synaptic cleft: 1) the docking of the synaptic vesicle at the neuron base [5] 2) and opening of the fusion pore [6]. The synaptic vesicles filled with neurotransmitters are continuously replenished near the neuron base and are docked with the help of SNARE complexes. This docked assembly then awaits an action potential [7] to trigger the next step of synaptic vesicle fusion, i.e. pore formation [4], [8].

The SNARE complex driving the synaptic vesicle fusion is made up of four helices, which are derived from 3 different proteins [9]. These proteins are classified as v-SNARE and t-SNAREs. Synaptobrevin (Syb) is the v-SNARE (v stands for vesicle) protein anchored to the membrane of synaptic vesicle membrane with the help of a hydrophobic Trans-Membrane Domain (TMD). Syb contributes one helix in the SNARE complex [10]. On the other hand the Syntaxin (Syx) and SNAP-25 are attached to the plasma membrane of the neuron and are referred to as t-SNAREs (t

stands for target) [11]. Similar to Syb, Syx is attached to the neuron membrane by embedding a hydrophobic TMD. SNAP-25 on other hand is anchored to the hydrophilic surface of the neuron membrane by an adsorbed palmitoyl chain [12]. The Syx and SNAP-25 contribute one and two helices respectively in the SNARE complex formation. When the neurotransmitter filled synaptic vesicle is in the vicinity of the neuron base, the t-SNAREs acts as an acceptor site for the v-SNARE. The zippering of the four helices into a tight bundle leads into the formation of SNARE complex [3][13]. This zippering is driven by interactions of the amino acid residues on each of the contributing helices. This provides the necessary force for docking the synaptic vesicle and bringing the two lipid membranes in proximity of each other. When the action potential is received at the neuron base, fusion pore formation is triggered. Some studies claim that the linker domain of the Syb and Syx becomes structured at this instant [11], [14], [15]. A linker domain is the part of the SNARE proteins which connects the TMD and the part of helix which contributes to SNARE complex. The linker domain is present in Syx and Syb. It has been found to be unstructured before the arrival of action potential, but becomes structured on its arrival.

The two lipid membrane structures [16] involved in this process are synaptic vesicle and plasma membrane of the neuron. The basic constituent of this membrane is a lipid molecule. These molecules are amphithatic in nature. This results in self-assembly in an aqueous environment, such that the hydrophilic portion of the molecule is exposed to water, while the hydrophobic part is hidden away from it. The synaptic vesicles are approximately spherical shaped structures with a radius of $\sim 20nm$ [17]. Due to the presence of neurotransmitter inside the vesicle, a huge amount of osmotic pressure

acts across its lipid membrane. Literature suggests that the osmotic pressure is high enough to keep the membrane of vesicle near the rupture strength [18], [19]. On the other hand the lipid membrane at the neuron base has a very small curvature relative to the synaptic vesicle and can be assumed almost flat. The SNARE proteins Syx and Syb are held to the lipid membrane with the help hydrophobic interaction between the tails of the lipid membranes and the TMD provides the necessary anchoring force.

The details of the mechanism leading to synaptic vesicle fusion and pore formation are still unclear and debatable. The system has been studied using experimental and simulation techniques to develop a better understanding. Molecular simulations present themselves as an ideal technique to visualize synaptic vesicle fusion [7], [20]–[23]. But the huge computational cost associated with molecular simulations poses a limit on length of simulations and spatial details of the system. In such cases coarse graining techniques can be a low computational cost alternative. Coarse Grained Molecular Dynamics (CGMD) simulations offer an opportunity to carry out long duration simulations by cutting down on molecular details. The molecular simulation models for lipid membranes present in literature lie in an extremely wide range of, single bead representation of lipid molecule to a full atomic detail model. In the coarse-grained category, the membrane model with the implicit solvent scheme comes along with a big reduction in computational costs. The presence of water molecules is sufficed by a hydrophobic interaction between the hydrophobic tails. The three bead lipid model by Cooke et al. is chosen for the present work [24]. The SNARE coarse grained model is based on the work by Fortoul et al. [25]. In this model, each amino acid residue is represented by a single bead. An Elastic Network Model (ENM) creates

the helical backbone of the SNARE proteins and Miyajawa-Jernigan (MJ) force field defines the interaction between the amino acid residues. This CG model of SNARE proteins is calibrated against All Atom (AA) simulations and force measurements made in single SNARE laser tweezer experiments. The CG models of lipid membrane and SNARE proteins have been developed in LAMMPS. The hydrophobic interaction between the lipid membranes and TMD is found to be an important tuning parameter for the simulation and with the right choice of hydrophobic interaction the simulations have shown the formation of fusion pore.

In the following section the outline of simulation scheme is described.

5.3 Model

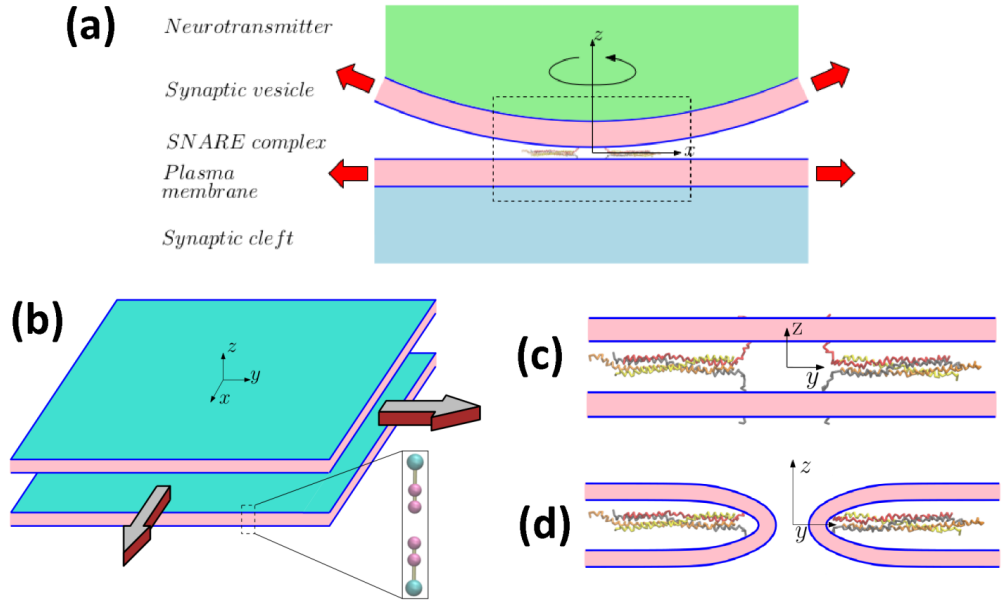

Fig 5.1: Schematic for SNARE mediated synaptic vesicle fusion a) side view of pre-fusion geometry b) simplified membrane geometry c) a side view close up of pre-fusion geometry d) post-fusion and fusion pore formation.

A synaptic vesicle fusion machinery consists of a synaptic vesicle, SNARE complex and plasma membrane of neuron. The SNARE complex is present in between the two lipid membrane structures as shown in Fig 5.1a. The neurotransmitter filled synaptic vesicle is docked at the plasma membrane with the help of zippered SNARE complex. In this state the SNARE complex awaits an action potential to fuse the vesicle and plasma membranes. The number of SNARE complexes present in between the two membranes is a debatable topic in neuroscience community. The electrical conductance studies carried out by Han et al. [8] proposes that 5-8 SNARE complexes are present around the fusion pore. Work of Sinha et al. [26] on fluorescence response from single fusing synaptic vesicle indicates the presence of only two SNARE complexes at the fusion site. Titration analysis by Mohrmann et al. [27] comes up with a conclusion that at least three SNARE complexes are needed for a successful fusion event. The work of Fortoul et al. [25] using coarse grained simulation studies reports the requirement of 4-6 SNARE complexes for synaptic vesicle fusion. The discrepancies in the number of SNARE complexes necessary for fusion is reviewed by Bogaart et al. [28] and is reported to be in the range of 1-11. This variation in number is due to the experimental technique used to obtain this number. The common theme in the reported research on number of SNARE complexes proposes that the expected fusion site is usually located between a ring of SNARE complexes. All the SNARE complexes collaboratively mediated the fusion pore formation.

To simplify the analysis, the fusion site can be visualized as two plane lipid membranes held in proximity of each other by the help of a ring of SNARE complexes. In the present work, the two membranes have been assumed to span the xy

plane as shown in Fig 5.1b. Periodic boundary conditions are imposed in both x and y direction as indicated by arrows in Fig 5.1b. In the initial configuration of the lipid membranes are placed at a given separation from each other as shown in Fig 5.1c. A specified number of SNARE complexes are placed in the gap between the membranes. These SNARE complexes extend their TMD into the two membranes, Syb in vesicle membrane and Syt in plasma membrane respectively. This system is implemented in LAMMPS with a NVE ensemble along with a Langevin thermostat to maintain the temperature of the system at 300K. The expected outcome of this simulation is the formation of fusion pore as shown in Fig 5.1d. In the next section, we present the details of the implemented molecular model.

5.3.1 Lipid membrane

In the present work, the 3 bead lipid model by Cooke et al. [24] is implemented for the lipid membranes. In this model, a single lipid molecule is represented by 3 beads. The head bead represents the hydrophilic head, whereas the rest of the two beads represent the hydrophobic tail. This 3 bead chain is connected with two FENE bonds (V_{FENE}^{lipid}) as shown in Fig 5.2, for which the potential is described in eq. 5.1,

$$V_{FENE}^{lipid}(r) = -\frac{1}{2} K_{FENE}^{lipid} r_{\infty}^{2} \log\left[1-\left(\frac{r}{r_{\infty}}\right)^{2}\right] \qquad 5.1$$

with $K_{FENE}^{lipid} = 30\dfrac{\varepsilon^{lipid}}{\left(\sigma^{lipid}\right)^{2}}$ and $r_{\infty} = 1.5\sigma^{lipid}$.

where, r is the distance between two beads connected by FENE bonds,

K_{FENE}^{lipid} is the potential coefficient,

r_{∞} is the maximum extension allowed in the bond,

ε^{lipid} is the LJ energy parameter for lipid molecule

σ^{lipid} is the LJ the size parameter for lipid molecule.

An additional bond is added to maintain the orientation of the molecule. This is represented by a harmonic spring ($V_{harmonic}^{lipid}$) and it acts between the first (head) bead and the third (second tail) bead as shown in Fig 5.2. The potential of this bond is given by eq. 5.2

$$V_{harmonic}^{lipid}(r) = -\frac{1}{2} K_{harmonic}^{lipid} \left(r - r_0\right)^2 \qquad 5.2$$

with, $K_{harmonic}^{lipid} = 10 \frac{\varepsilon^{lipid}}{\left(\sigma^{lipid}\right)^2}$ and $r_0 = 4\sigma^{lipid}$.

$K_{harmonic}^{lipid}$ is the potential coefficient,

r_0 is the length of the spring.

To simulate the implicit solvent a modified short distance repulsive and long distance attractive potential (V_{tail}^{lipid}) is implemented for tail beads as shown in eq. 5.3. This potential keeps hydrophobic core of the lipid membrane together and maintains the bilayer structure.

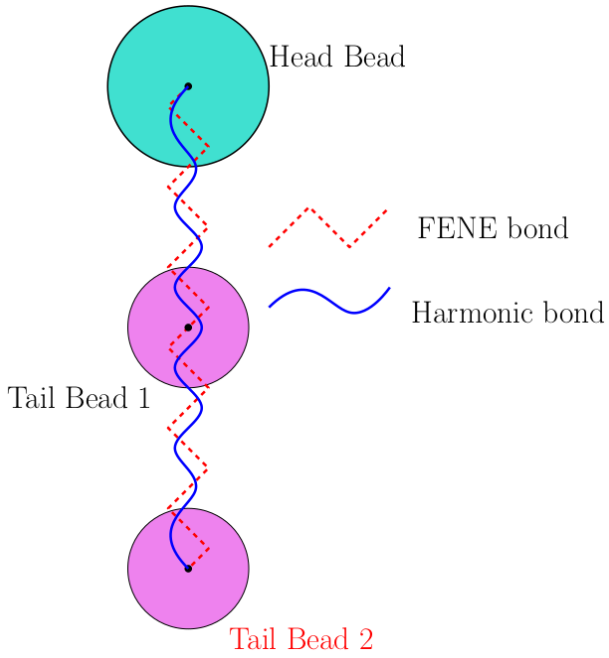

Fig 5.2: FENE and harmonic bonds in a lipid molecule

$$V_{tail}^{lipid}(r)=\begin{cases}4\varepsilon^{lipid}\left[\left(\dfrac{\sigma^{lipid}}{r}\right)^{12}-\left(\dfrac{\sigma^{lipid}}{r}\right)^{6}\right] & r\le r_c,\\ -\varepsilon^{lipid}\cos^2\left(\dfrac{\pi(r-r_c)}{2w_c}\right) & r_c<r\le r_c+w_c,\\ 0 & r_c+w_c<r\end{cases} \qquad 5.3$$

with, $w_c=1.6\sigma^{lipid}$ which is chosen from the parameter space (Fig A5.3) provided by Cooke et al [24].

Here $r_c=2^{1/6}\sigma^{lipid}$, is the location of the minimum of the LJ 6-12 potential.

The interaction between a head and tail bead, and two head beads is governed by Weeks-Charles-Andersen potential ($V_{repulsion}^{lipid}$) as defined by eq. 5.4. This potential provides the necessary soft repulsion between the beads to avoid them collapsing into each other.

$$V_{repulsion}^{lipid}(r) = \begin{cases} 4\varepsilon^{lipid}\left[\left(\frac{\sigma^{lipid}}{r}\right)^{12} - \left(\frac{\sigma^{lipid}}{r}\right)^{6}\right] + \varepsilon^{lipid} & r \le r_c, \\ 0 & r_c < r \end{cases} \quad 5.4$$

The parameters for the lipid membrane model are chosen to reflect the bending stiffness similar to biological membranes. For the values ε^{lipid} = 0.542 kCal/mol and σ^{lipid} = 9.7 nm, the bending rigidity, κ of the membrane is calculated using the simulation experiment described by Hu et al. [29] and shown in Fig 5.3. This value is found out to be 11.8 k_BT and is in agreement with the work in literature using other molecular simulation [30]–[32] as well as experimental techniques [33]–[37]. The details of the bending modulus study are appended in section A5.2.

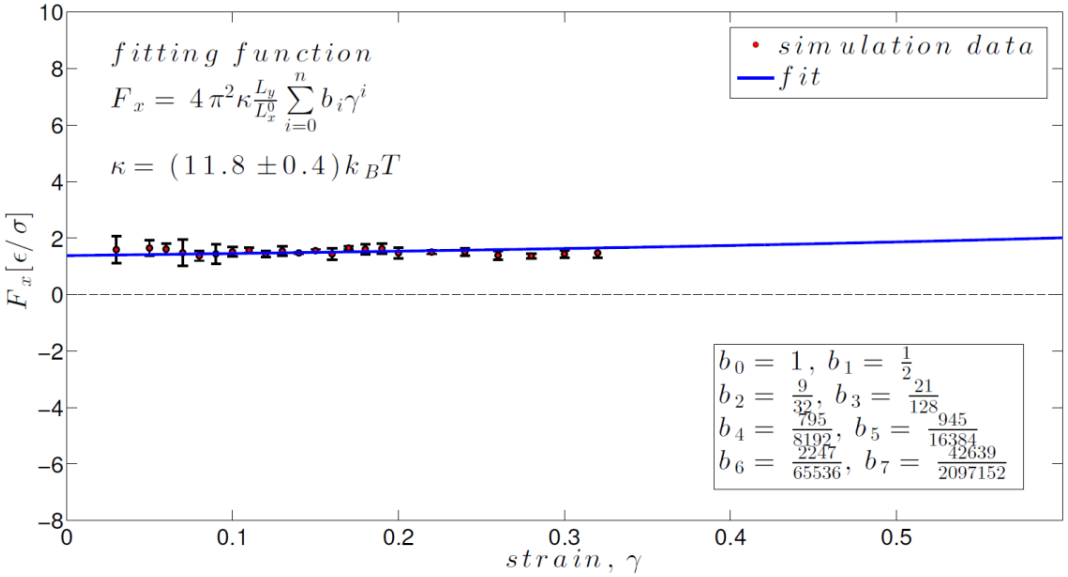

Fig 5.3: Bending stiffness calculation of lipid membrane using the methodology proposed by Hu et al. [29]. F_x **is the force exerted by the lipid membrane on the yz face of the simulation box and is scaled with** $\frac{\epsilon^{lipid}}{\sigma^{lipid}}$**, the coefficients** b_i**'s are the**

coefficients in the expansion, L_x and L_y are the length of the membrane along x and y directions, k_B is the Boltzman Constant and T is the temperature.

5.3.2 SNARE coarse grained model

In the present work the SNARE coarse grained model is based of the work of Fortoul et al. [25]. The CG SNARE model presented in Fortoul et al. was extended to include the Trans-Membrane Domains (TMD) and Linker Domain (LD) of the Syb and Syx. The methodology for extending Syb and Syx is described in section A5.3. This model represents each residue with a single bead placed at the location of α carbon. The representative beads retain the identity by having the equivalent van der Waals radius and mass as that of the residue. The residues interact with other residues in the same SNARE complex by two interactions which are described below.

5.3.2.1 Bonded interactions

The intra-helical interactions between the residue beads are defined using an Elastic Network Model (ENM) [38], [39]. These interactions maintain the helical structure of individual proteins. The location of residue beads along the helices is based on an x-ray structure of the proteins. A cutoff distance R_c is chosen. Two residue beads from same helix and within this cutoff distance are connected by a harmonic spring. The spring potential is given by,

$$V_{harmonic}^{SNARE} = -\frac{1}{2} K_{harmonic}^{SNARE} \left(r - r_0\right)^2, \qquad 5.5$$

where, $K_{harmonic}^{SNARE} = 0.0963 N/m$ and r_0 is the distance between two beads when the individual helices are in relaxed and nearly straight. The value of $K_{harmonic}^{SNARE}$ is carefully chosen after comparing the fluctuation spectrum of individual helices of All Atom (AA) and CG model of individual helices.

5.3.2.2 Non-bonded interactions

The next set of interactions incorporates the chemical specificity of residues which governs the SNARE complex formation. This interaction acts between the residue beads from same helix and the residues on the other helices which are part of the same SNARE complex. The interaction energy of between residues is a scaled version of the contact energy values provided by Miyazawa et al. [40]–[42]. The scaling used in the present work is based on Kim et al. [43] formulation,

$$\varepsilon_{ij}^{SNARE} = \lambda\left(e_{ij} - e_0\right), \qquad 5.6$$

where, ε_{ij}^{SNARE} is the interaction energy, e_{ij} is the contact energy, λ is a scaling factor and e_0 is an offset parameter. The beads within a cutoff distance R_{C_MJ} of each other are assumed to be in contact and the interaction between the beads is governed by a modified 6-12 LJ potential (V_{ij}^{SNARE}) as shown eq. 5.7. The choice of potential is based on the value of ε_{ij}^{SNARE} .

$$V_{ij}^{SNARE} = \begin{cases} 4\left|\varepsilon_{ij}^{SNARE}\right|\left[\left(\frac{\sigma_{ij}^{SNARE}}{r}\right)^{12} - \left(\frac{\sigma_{ij}^{SNARE}}{r}\right)^{6}\right] & \varepsilon_{ij}^{SNARE} < 0 \\ 4\left|\varepsilon_{ij}^{SNARE}\right|\left[\left(\frac{\sigma_{ij}^{SNARE}}{r}\right)^{12} - \left(\frac{\sigma_{ij}^{SNARE}}{r}\right)^{6}\right] + 2\varepsilon_{ij}^{SNARE} & \varepsilon_{ij}^{SNARE} > 0 \; and \; r < r_{ij}^{0} \\ -4\left|\varepsilon_{ij}^{SNARE}\right|\left[\left(\frac{\sigma_{ij}^{SNARE}}{r}\right)^{12} - \left(\frac{\sigma_{ij}^{SNARE}}{r}\right)^{6}\right] & \varepsilon_{ij}^{SNARE} > 0 \; and \; r \geq r_{ij}^{0} \end{cases} \quad 5.7$$

where, r_{ij}^{0} is the distance at which the minimum of the LJ potential occurs, $\sigma_{ij}^{SNARE} = A\left(\frac{\sigma_i^{SNARE} + \sigma_j^{SNARE}}{2}\right)$ is the size parameter of mixed interactions between two residues and σ_i^{SNARE} is the van der Waal radius of a residue bead, A is a tuning parameter to match the bundle width with the experimental acquired value. For the present work $A = 0.8$. The parameter λ in eq 5.6 controls the strength of inter-helical interactions. Its value was chosen so as to match the SNARE unzippering behavior in comparison to the experimental results of single molecule unzippering by Gao et al. [13]. The calibration is done by matching the peak value of force (17.2 pN) reported in the experiments.

In the next step the interaction between the SNARE residue and lipid beads is defined. The interaction between the hydrophobic residue beads and lipid tails ($V_{i,tail}^{lipid-SNARE}$) is defined in eq. 5.8. It is modeled similar to the interaction between the tail beads of a lipid molecule.

$$V_{i,tail}^{lipid-SNARE}(r)=\begin{cases}4\varepsilon_{i,tail}^{lipid-SNARE}\left[\left(\dfrac{\sigma_{i,tail}^{lipid-SNARE}}{r}\right)^{12}-\left(\dfrac{\sigma_{i,tail}^{lipid-SNARE}}{r}\right)^{6}\right] & r\le r_c,\\ -\varepsilon_{i,tail}^{lipid-SNARE}\cos^2\left(\dfrac{\pi(r-r_c)}{2w_c}\right) & r_c<r\le r_c+w_c,\\ 0 & r_c+w_c<r\end{cases} \quad 5.8$$

where, $\varepsilon_i^{lipid-SNARE}=\sqrt{\varepsilon^{lipid}*\varepsilon_{ii}^{SNARE}}$ and $\sigma_i^{lipid-SNARE}=A\left(\dfrac{\sigma^{lipid}+\sigma_i^{SNARE}}{2}\right)$.

In the equation above, $\varepsilon_i^{lipid-SNARE}$ and $\sigma_i^{lipid-SNARE}$ are the energy and size parameter respectively for mixed interaction between the lipid and SNARE beads. The value of $A=0.8$ is same as in the case of V_{ij}^{SNARE}.

5.4 Results

The CGMD scheme described in the previous sections is used to simulate lipid membrane fusion without mediation from SNARE proteins. The purpose of these simulations was to test the ability of the CGMD lipid model to simulate membrane fusion. The membrane fusion models proposed in the literature relies on the presence of explicit solvent, whereas in the present work an implicit solvent scheme is implemented. In the next section we present the results for membrane fusion under the effect of an indent and in the following sections we will show the results from the membrane fusion mediated by SNARE proteins [44].

5.4.1 Membrane fusion under the effect of a rigid indenter

The geometry of the simulation can be described as follows and also shown in Fig. 5.4,

1) All the simulation were carried out in planar periodic box, with periodicity in x and y directions
2) There are two planar membranes facing each other, the top membrane is supposed to represent synaptic vesicle membrane and the bottom membrane represents plasma membrane of neuron. The in-plane stress in the membrane can be altered by changing the density of lipid molecules in either membrane.
3) The length of the membranes in x-direction (L_x) is significantly longer than in y-direction (L_y).

$$\frac{L_x}{L_y} \approx 10$$

4) For all the simulations described in LAMMPS, fix indent is used to create an indenter which then pushes the membranes towards each other.
5) All the indenters are cylindrical, with axis aligned along y axis (into the plane)
6) The diameter of indenter is specified as 2nm. This is based on the assumption that the size of bump induced in the lipid membrane due the anchored SNARE proteins is of the order of few nanometers
7) All the simulation snapshots are on the xz plane, x is horizontal axis, z is vertical axis and y is coming out of the page.

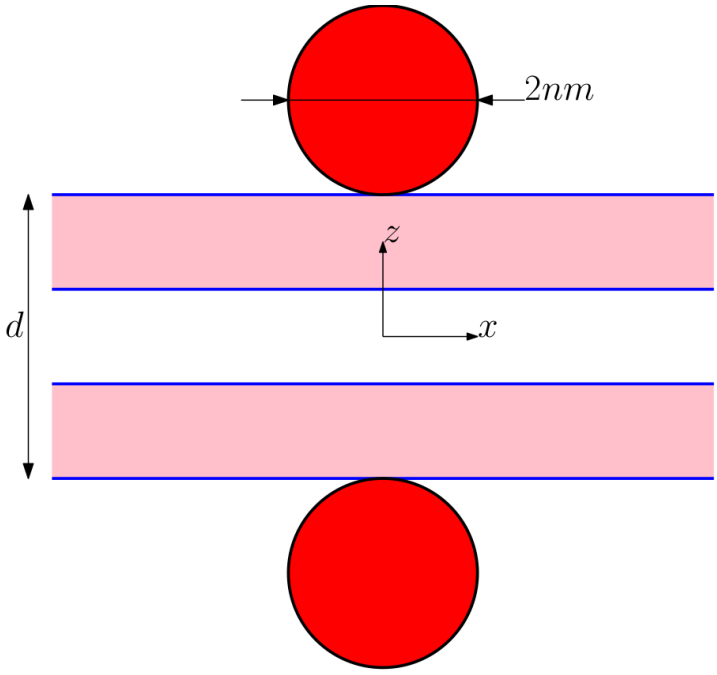

Fig. 5.4: Schematic of membrane fusion under the effect of indenters

In the next step, we conducted two set of simulations with the above setup to induce fusion between the two membranes. The first set of simulation did not have any initial in-plane membrane tension and in the second set of simulations, an initial in-plane tension was imposed in the membranes.

1. **No in-plane membrane tension**

   During these simulations, the separation between the indenters was varied and occurrence of hemi-fusion instances was observed as shown Fig 5.5. Hemi-fusion [45], [46] has been identified as an intermediate state of the apposing lipid membranes where, the lipid monolayers facing the other lipid membrane merge with each other while the rest of the lipid membrane (one monolayer on

each side of the lipid membrane) stay intact. It is believed that, in later stages of fusion process the hemi-fused diaphragm ruptures and leads to the formation of fusion pore [45]–[48].

The gap between the surfaces of the cylindrical indenters, d , as shown in Fig. 5.5 was varied and above some critical separation no hemi-fusion was observed. For this case, when the separation between the indenters was more than ~3.6 nm, hemifusion ceases to take place. The absence of tension is also a crucial factor in the formation of hemi-fusion. In the next section we will see how the in-plane membrane tension affects the membrane conformation when they are placed close to each other.

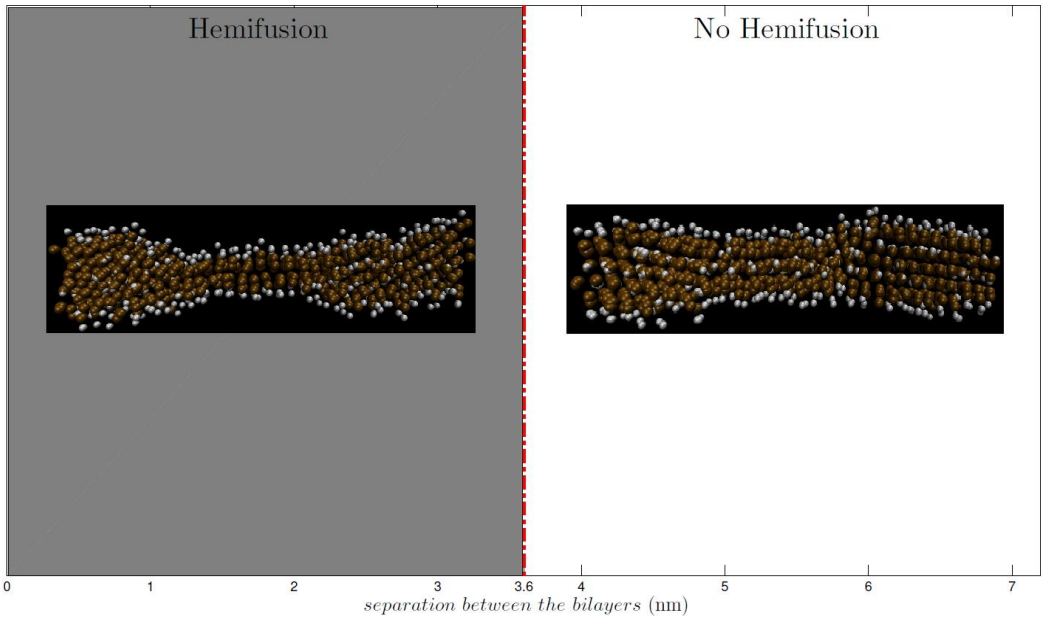

Fig 5.5: Critical separation between the membranes for hemifusion to occur.

2. **In-plane tension present**

For this set of simulation, the tension in the membranes was varied, by varying the number of lipid molecules, while holding the lengths of membranes to be constant. This is done for both lipid bilayers. The separation between the indenters was chosen so that the hemi-fusion was expected to take place.

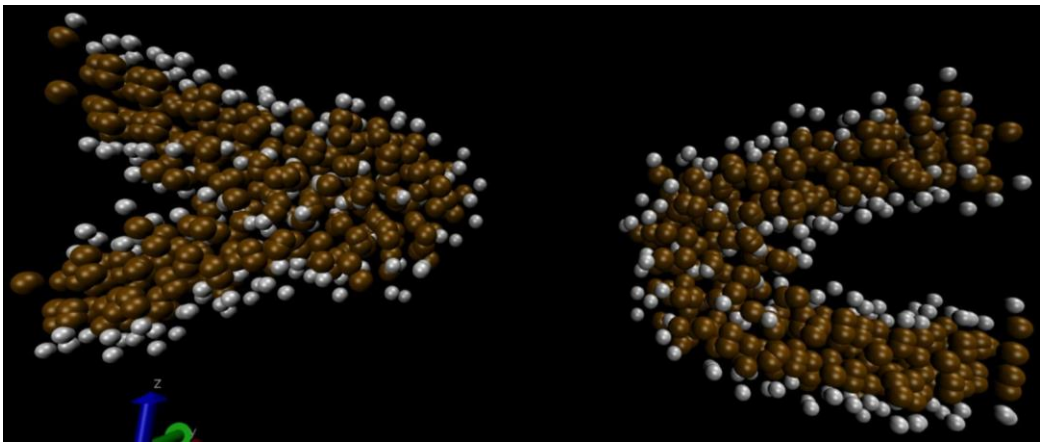

Fig 5.6: Fusion pore formation in membranes under in-plane tension

Few interesting observations, from the variation of tension simulations are,

1. As the tension in the membranes was increased, the length of the hemi-fused diaphragm increased. This is because, the density of lipid molecules increases as the length of the hemi-fused diaphragm and the lipid molecules in two tense membranes are now in one single membrane.
2. For sufficiently large tensions the membranes rupture during the indentation, and the broken ends of the membrane end up joining between the synaptic vesicle membrane and plasma membrane. This leads to the formation of fusion pore, as shown in Fig. 5.6.

This simulation study demonstrated the capability of the CGMD lipid membrane scheme to demonstrate fusion. For the next set of simulations, we have combined the CGMD schemes of lipid membrane and modified SNARE proteins.

5.4.2 SNARE mediated synaptic vesicle fusion

The fusion pore formation during synaptic vesicle fusion is an expected outcome of the process. It is believed that fusion pore formation is a result of collaborative effort of SNARE complexes. It has been proposed the arrival of action potential at the synapse triggers conformational changes in the LD of Syx and Syb [14], [15]. This makes the complete helix of both Syb and Syx to straighten and provides extra force on the opposing membranes to get close to each other and at the same time increases the level on in-plane tension in the membrane of synaptic vesicle and neuron base. In Fig. 5.7 we show the results of our initial tudies of these simulations, which led into a successful fusion pore formation. Fig 5.7 (a) shows the side view (yz plane) of the fused membranes and fig 5.7 (b) shows the fusion pore from the top going through both the membranes Fig 5.8 (a) shows a closer look at the fusion pore and it can be clearly seen that lipid molecules are oriented horizontally around the fusion pore. To dig deeper into the fusion pore structure, two slices around the fusion pore were analyzed. Fig 5.8 (b) shows the red slice and fig 5.8 (c) shows the green slice, viewed along x axis and y axis respectively. In both views it can be clearly seen that the lipid molecules rearrange to form a fusion pore structure.

This scheme can be used to characterize the parameters which will enable the fusion pore formation. In our simulations the interaction between the lipid molecules and the SNARE beads is one of the key interactions in the process of fusion pore formation. This interaction is hydrophobic and is similar to the interaction between the hydrophobic beads of the lipid molecule. If this interaction is weak then the membranes tend to detach from the TMDs of the SNARE complexes. On the other hand if the interaction is too strong the lipid molecules tend to aggregate around TMDs of the SNARE complexes. This aggregation hinders the interaction of the lipid molecules in the opposing lipid monolayers of synaptic vesicle and neuron plasma membrane.

Further simulation studies need to be conducted with the current scheme to find the right parameters. These simulation studies will be done to analyze the effect of number of SNARE complexes, in-plane tension in the membranes, self-arrangement of SNARE complexes around the expected fusion site and subsequently the fusion pore formation.

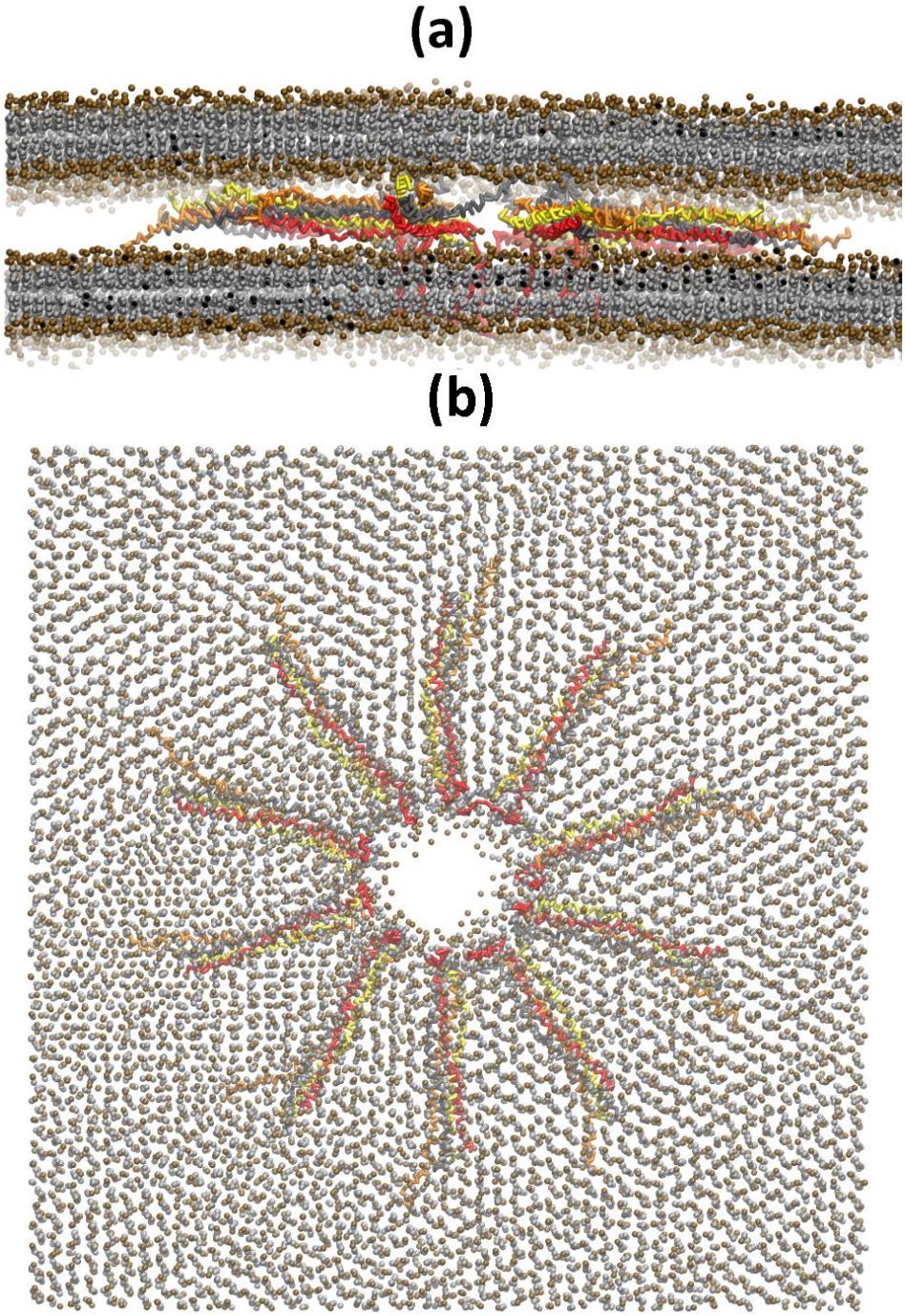

Fig 5.7: SNARE protein mediated synaptic vesicle fusion a) side view (yz plane) b) top view (xy plane)

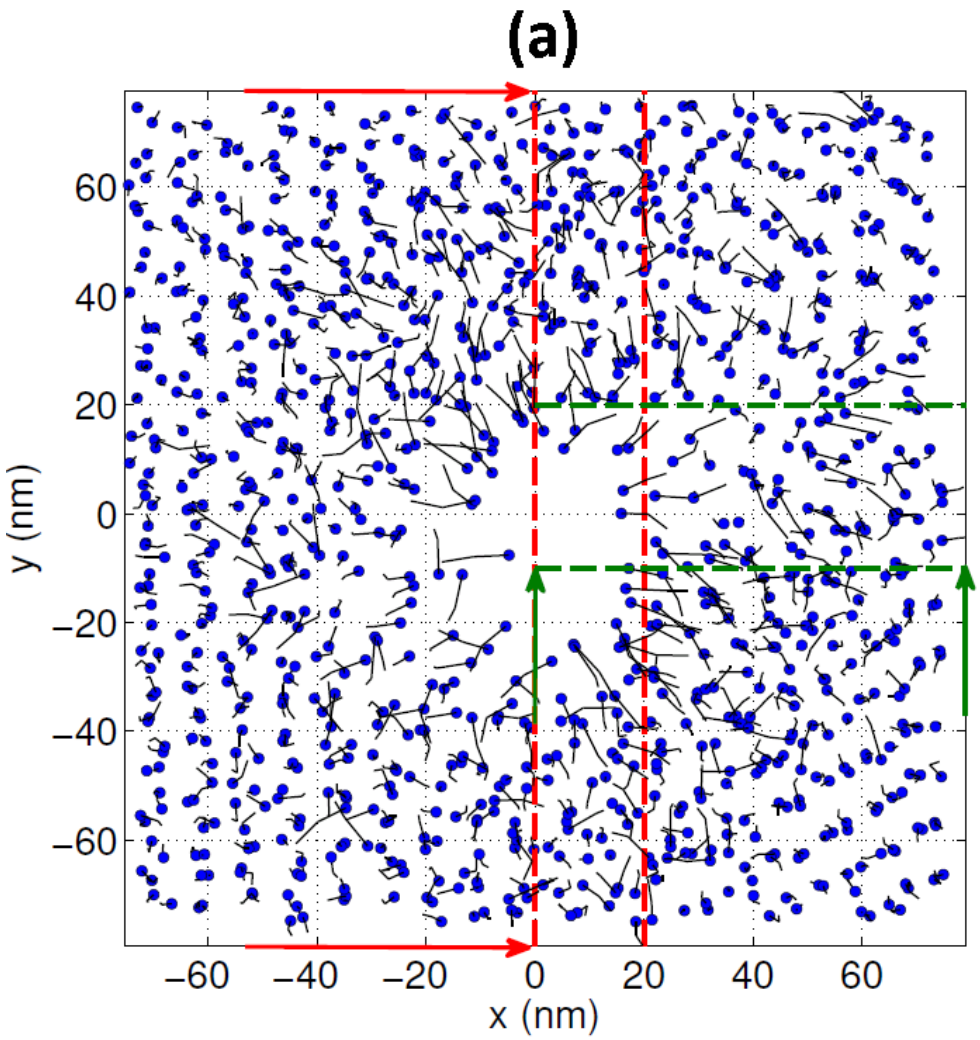
(a)
60
40
20
0
−20
−40
−60
y (nm)
−60
−40
−20
0
20
40
60
x (nm)

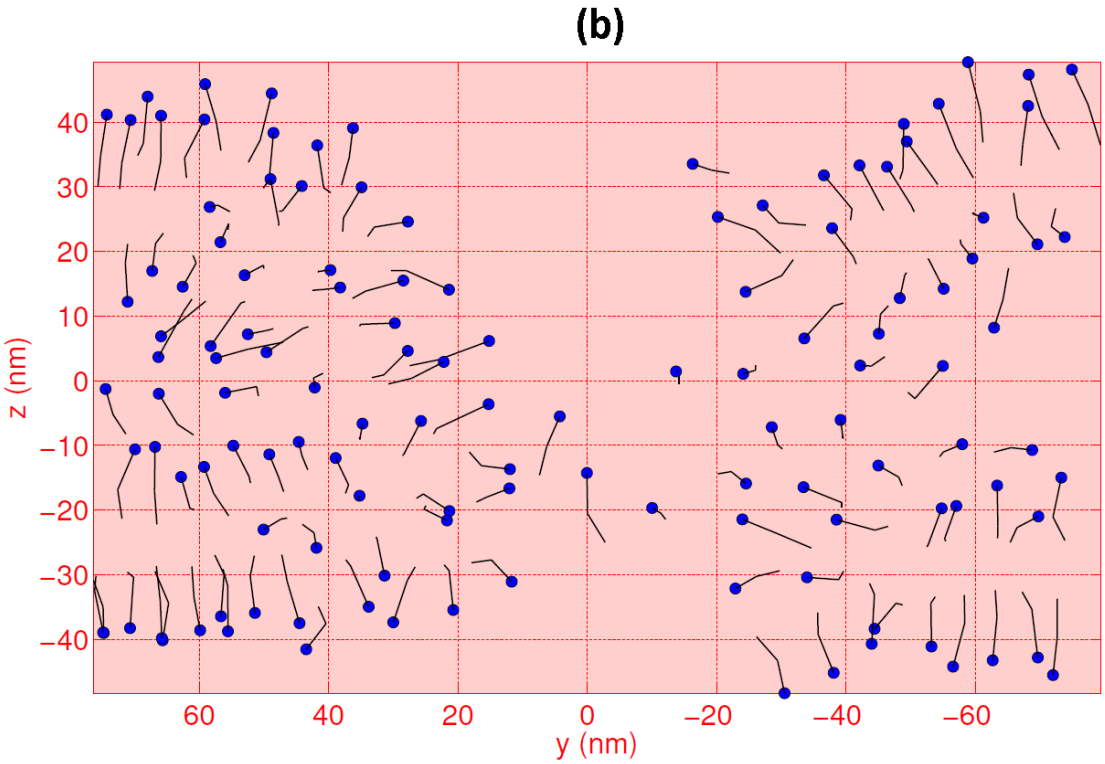
(b)
40
30
20
10
0
−10
−20
−30
−40
z (nm)
60
40
20
0
−20
−40
−60
y (nm)

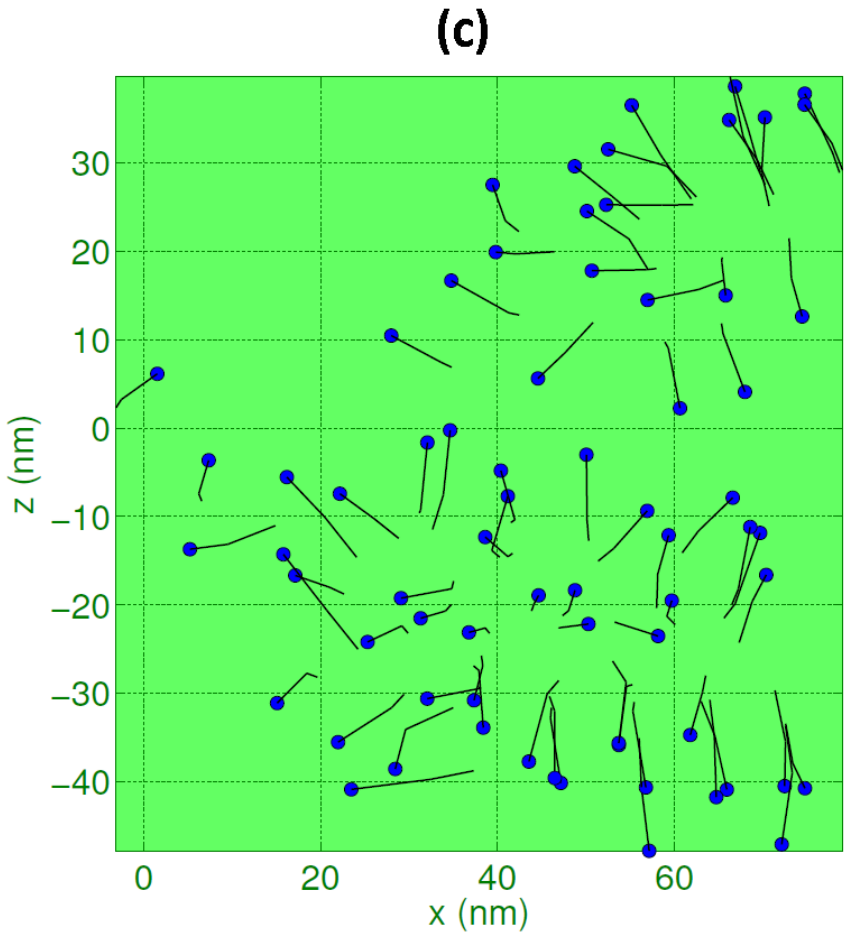

Fig 5.8: (a) A closer look at the fusion pore from the top vesicle side (xy plane) (b) View of the red slice of the fused membranes along x axis (c) View of the green slice of the fused membranes along y axis

5.5 Summary and Conclusion

The CG simulations presented in this work has been demonstrated to show the fusion pore formation. The CG lipid membrane model is computationally efficient due to its implicit solvent scheme and reduces the computational cost of simulations. This scheme has been demonstrated to show lipid membrane fusion and subsequent fusion pore formation. The CG SNARE model includes the chemical specificity of the real

SNARE proteins. This CG model is calibrated to exhibit behavior similar to real SNARE complex obtained from experimental studies conducted on single SNARE reconstitution. The SNARE proteins Syb and Syx are extended to include LD and TMD. These extended proteins are embedded inside the lipid membranes to anchor the SNARE complexes. The work on choosing the right parameters to have a stable lipid membrane and SNARE complex assembly is still under progress. The most crucial amongst those parameters is the interaction between the TMD of SNARE complex and the hydrophobic core of the lipid membranes. At the beginning of the simulation the SNARE complexes are arranged in a circular pattern. The simulation scheme has the capability to vary the number and arrangement of SNARE complexes between the membranes and vary the tension in the lipid membranes.

The fine-tuned simulation scheme can be used to answer some of the following questions related to synaptic vesicle fusion,

1. The number of SNARE complex needed to carry out a successful synaptic vesicle fusion.
2. Self-organization of SNARE complexes around the fusion pore.
3. Collaborative effect of SNARE complexes to lead to the fusion pore formation.
4. Role of in-plane tension in the lipid membranes towards the fusion pore formation.
5. Role of LD domains in pushing the opposing lipid membranes closer to each other to initiate the fusion process.

Bibliography

[1] C. Ungermann, “Functions of SNAREs in intracellular membrane fusion and lipid bilayer mixing,” *J. Cell Sci.*, vol. 118, no. 17, pp. 3819–3828, 2005.

[2] J. Han, K. Pluhackova, and R. A. Böckmann, “The multifaceted role of SNARE proteins in membrane fusion,” *Frontiers in Physiology*, vol. 8, no. JAN. 2017.

[3] X. Lou and Y.-K. Shin, “SNARE zippering,” *Biosci. Rep.*, vol. 36, no. 3, pp. e00327–e00327, 2016.

[4] J. Rizo and C. Rosenmund, “Synaptic vesicle fusion,” *Nat. Struct. Mol. Biol.*, vol. 15, no. n7, pp. 665–674, 2008.

[5] J. Pevsner, S. C. Hsu, J. E. A. Braun, N. Calakos, A. E. Ting, M. K. Bennett, and R. H. Scheller, “Specificity and regulation of a synaptic vesicle docking complex,” *Neuron*, vol. 13, no. 2, pp. 353–361, 1994.

[6] T. Söllner, M. K. Bennett, S. W. Whiteheart, R. H. Scheller, and J. E. Rothman, “A protein assembly-disassembly pathway in vitro that may correspond to sequential steps of synaptic vesicle docking, activation, and fusion,” *Cell*, vol. 75, no. 3, pp. 409–418, 1993.

[7] H. von Gersdorff and G. Matthews, “Dynamics of synaptic vesicle fusion and membrane retrieval in synaptic terminals.,” *Nature*, vol. 367, no. 6465, pp. 735–739, 1994.

[8] X. Han, “Transmembrane Segments of Syntaxin Line the Fusion Pore of Ca2+-Triggered Exocytosis,” *Science (80-.).*, vol. 304, no. 5668, pp. 289–292, 2004.

[9] L. Shi, Q.-T. Shen, A. Kiel, J. Wang, H.-W. Wang, T. J. Melia, J. E. Rothman, and F. Pincet, “SNARE Proteins: One to Fuse and Three to Keep the Nascent

Fusion Pore Open," *Science (80-.).*, vol. 335, no. 6074, pp. 1355–1359, 2012.

[10] J. F. Ellena, B. Liang, M. Wiktor, A. Stein, D. S. Cafiso, R. Jahn, and L. K. Tamm, "Dynamic structure of lipid-bound synaptobrevin suggests a nucleation-propagation mechanism for trans-SNARE complex formation," *Proc. Natl. Acad. Sci.*, vol. 106, no. 48, pp. 20306–20311, 2009.

[11] A. Stein, G. Weber, M. C. Wahl, and R. Jahn, "Helical extension of the neuronal SNARE complex into the membrane," *Nature*, 2009.

[12] S. Gonzalo and M. E. Linder, "SNAP-25 palmitoylation and plasma membrane targeting require a functional secretory pathway.," *Mol. Biol. Cell*, vol. 9, no. March, pp. 585–597, 1998.

[13] Y. Gao, S. Zorman, G. Gundersen, Z. Xi, L. Ma, G. Sirinakis, J. E. Rothman, and Y. Zhang, "Single reconstituted neuronal SNARE complexes zipper in three distinct stages," *Science (80-.).*, vol. 337, no. 6100, pp. 1340–1343, 2012.

[14] D. H. Kweon, C. S. Kim, and Y. K. Shin, "Regulation of neuronal SNARE assembly by the membrane," *Nat Struct Biol*, vol. 10, no. 6, pp. 440–447, 2003.

[15] M. Bowen and A. T. Brunger, "Conformation of the synaptobrevin transmembrane domain," *Proc. Natl. Acad. Sci.*, vol. 103, no. 22, pp. 8378–8383, 2006.

[16] M. Deserno, "Fluid lipid membranes – a primer," *See https//www.cmu.edu/biolphys/deserno/pdf/membrane_theory.pdf*, pp. 1–29, 2007.

[17] B. Zhang, Y. H. Koh, R. B. Beckstead, V. Budnik, B. Ganetzky, and H. J. Bellen, "Synaptic vesicle size and number are regulated by a clathrin adaptor

protein required for endocytosis," *Neuron*, vol. 21, no. 6, pp. 1465–1475, 1998.

[18] D. R. M. P. Mordecai P. Blaustein MD, Joseph P. Y. Kao PhD), "Cellular Physiology and Neurophysiology," *Mosby, Elsevier*, pp. 311–324, 2012.

[19] L. Qu, Y. Akbergenova, Y. Hu, and T. Schikorski, "Synapse-to-synapse variation in mean synaptic vesicle size and its relationship with synaptic morphology and function," *J. Comp. Neurol.*, vol. 514, no. 4, pp. 343–352, 2009.

[20] V. Knecht and S.-J. Marrink, "Molecular Dynamics Simulations of Lipid Vesicle Fusion in Atomic Detail," *Biophys. J.*, vol. 92, no. 12, pp. 4254–4261, Jun. 2007.

[21] R. Jahn and D. Fasshauer, "Molecular machines governing exocytosis of synaptic vesicles.," *Nature*, vol. 490, no. 7419, pp. 201–7, Oct. 2012.

[22] S. J. M. and and A. E. Mark, "The Mechanism of Vesicle Fusion as Revealed by Molecular Dynamics Simulations," 2003.

[23] N. Calakos and R. H. Scheller, "Synaptic vesicle biogenesis, docking, and fusion: a molecular description.," *Physiol. Rev.*, vol. 76, pp. 1–29, 1996.

[24] I. R. Cooke, K. Kremer, and M. Deserno, "Efficient tunable generic model for fluid bilayer membranes," Feb. 2005.

[25] N. Fortoul, P. Singh, C. Y. Hui, M. Bykhovskaia, and A. Jagota, "Coarse-grained model of SNARE-mediated docking," *Biophys. J.*, vol. 108, no. 9, pp. 2258–2269, 2015.

[26] R. Sinha, S. Ahmed, R. Jahn, and J. Klingauf, "Two synaptobrevin molecules are sufficient for vesicle fusion in central nervous system synapses," *Proc. Natl.*

Acad. Sci., vol. 108, no. 34, pp. 14318–14323, 2011.

[27] R. Mohrmann, H. de Wit, M. Verhage, E. Neher, and J. B. Sorensen, "Fast Vesicle Fusion in Living Cells Requires at Least Three SNARE Complexes," *Science (80-.).*, vol. 330, no. 6003, pp. 502–505, 2010.

[28] G. Van Den Bogaart and R. Jahn, "Counting the SNAREs needed for membrane fusion," *J. Mol. Cell Biol.*, vol. 3, no. 4, pp. 204–205, 2011.

[29] M. Hu, P. Diggins, and M. Deserno, "Determining the bending modulus of a lipid membrane by simulating buckling.," *J. Chem. Phys.*, vol. 138, no. 21, p. 214110, Jun. 2013.

[30] M. Hu, J. J. Briguglio, and M. Deserno, "Determining the Gaussian curvature modulus of lipid membranes in simulations.," *Biophys. J.*, vol. 102, no. 6, pp. 1403–10, Mar. 2012.

[31] V. A. Harmandaris and M. Deserno, "A novel method for measuring the bending rigidity of model lipid membranes by simulating tethers," *J. Chem. Phys.*, vol. 125, no. 20, 2006.

[32] S. Kawamoto, T. Nakamura, S. O. Nielsen, and W. Shinoda, "A guiding potential method for evaluating the bending rigidity of tensionless lipid membranes from molecular simulation," *J. Chem. Phys.*, vol. 139, no. 3, p. 034108, Jul. 2013.

[33] R. Dimova, "Recent developments in the field of bending rigidity measurements on membranes," *Advances in Colloid and Interface Science*, vol. 208. pp. 225–234, 2014.

[34] M. Kummrow and W. Helfrich, "Deformation of giant lipid vesicles by electric

fields," *Phys. Rev. A*, vol. 44, no. 12, pp. 8356–8360, Dec. 1991.

[35] L. R. Arriaga, I. López-Montero, F. Monroy, G. Orts-Gil, B. Farago, T. Hellweg, J. Dufourcq, and P. Bothorel, "Stiffening effect of cholesterol on disordered lipid phases: a combined neutron spin echo + dynamic light scattering analysis of the bending elasticity of large unilamellar vesicles.," *Biophys. J.*, vol. 96, no. 9, pp. 3629–37, May 2009.

[36] K. I. Pakkanen, L. Duelund, K. Qvortrup, J. S. Pedersen, and J. H. Ipsen, "Mechanics and dynamics of triglyceride-phospholipid model membranes: Implications for cellular properties and function," *Biochim. Biophys. Acta - Biomembr.*, vol. 1808, no. 8, pp. 1947–1956, 2011.

[37] G. Niggemann, M. Kummrow, and W. Helfrich, "The Bending Rigidity of Phosphatidylcholine Bilayers: Dependences on Experimental Method, Sample Cell Sealing and Temperature," *J. Phys. II*, vol. 5, no. 3, pp. 413–425, Mar. 1995.

[38] Z. Zhang, J. Pfaendtner, A. Grafmüller, and G. A. Voth, "Defining coarse-grained representations of large biomolecules and biomolecular complexes from elastic network models," *Biophys. J.*, vol. 97, no. 8, pp. 2327–2337, 2009.

[39] J.-W. Chu and G. A. Voth, "Coarse-Grained Modeling of the Actin Filament Derived from Atomistic-Scale Simulations," *Biophys. J.*, vol. 90, no. 5, pp. 1572–1582, 2006.

[40] S. Miyazawa and R. L. Jernigan, "Estimation of effective interresidue contact energies from protein crystal structures: quasi-chemical approximation," *Macromolecules*, vol. 18, no. 3, pp. 534–552, May 1985.

[41] S. Miyazawa and R. L. Jernigan, “Residue – Residue Potentials with a Favorable Contact Pair Term and an Unfavorable High Packing Density Term, for Simulation and Threading,” *J. Mol. Biol.*, vol. 256, no. 3, pp. 623–644, Mar. 1996.

[42] S. Miyazawa and R. L. Jernigan, “Self-consistent estimation of inter-residue protein contact energies based on an equilibrium mixture approximation of residues.,” *Proteins*, vol. 34, no. 1, pp. 49–68, Jan. 1999.

[43] Y. C. Kim and G. Hummer, “Coarse-grained Models for Simulations of Multiprotein Complexes: Application to Ubiquitin Binding,” *J. Mol. Biol.*, vol. 375, no. 5, pp. 1416–1433, 2008.

[44] J. C. Shillcock and R. Lipowsky, “Tension-induced fusion of bilayer membranes and vesicles.,” *Nat. Mater.*, vol. 4, no. 3, pp. 225–8, Mar. 2005.

[45] L. V. Chernomordik and M. M. Kozlov, “Membrane hemifusion: Crossing a chasm in two leaps,” *Cell*, vol. 123, no. 3. pp. 375–382, 2005.

[46] G. H. Zan, C. Tan, M. Deserno, F. Lanni, and M. Lösche, “Hemifusion of giant unilamellar vesicles with planar hydrophobic surfaces: a fluorescence microscopy study,” *Soft Matter*, vol. 8, no. 42, p. 10877, 2012.

[47] M. Nishizawa and K. Nishizawa, “Molecular dynamics simulation analysis of membrane defects and pore propensity of hemifusion diaphragms.,” *Biophys. J.*, vol. 104, no. 5, pp. 1038–48, Mar. 2013.

[48] L. V Chernomordik and M. M. Kozlov, “Mechanics of membrane fusion.,” *Nat. Struct. Mol. Biol.*, vol. 15, no. 7, pp. 675–83, 2008.

Appendix A5

A5.1 Brownian Dynamics Calculations

Consider a particle of mass m, suspended in a liquid (friction constant Γ) and moving at speed $\vec{v}$. During this motion, particle has two different forces acting on it, which are,

1. a frictional force of magnitude, $-\Gamma\vec{v}$
2. a random force coming from the bombardment of water particles around this particle, $\vec{R}(\mathrm{t})$ and has the following properties,

   a) $\left\langle \vec{R}(\mathrm{t}) \right\rangle = 0$, means that the force can be random in direction

   b) $\left\langle \vec{R}(\mathrm{t}) \bullet \vec{R}(\mathrm{t}') \right\rangle = c\delta(\mathrm{t}-\mathrm{t}')$, means that the force at two different instants, is not correlated,

   where, c is the parameter which we are going to obtain from this analysis.

So, the equation of motion can be written as,

$$\frac{d\vec{r}}{dt} = \vec{v} \ , \qquad \text{A5.1}$$

$$m\frac{d\vec{v}}{dt} = -\Gamma\vec{v} + \vec{R}(\mathrm{t}) \ . \qquad \text{A5.2}$$

Next, we solve for the velocity, $\vec{v}$ from eq. A5.2. Since, it is an ODE, the solution can be obtained in two parts, a homogeneous solution, $\vec{v}_h$ and a particular solution, $\vec{v}_p$.

a) Homogeneous solution

$$m\frac{d\vec{v}}{dt} = -\Gamma\vec{v}$$

$$\Rightarrow \vec{v} = \vec{v}_0 e^{-\frac{\Gamma}{m}t}$$

where, $\vec{v}_0$ is the velocity of the particle at time $t = 0$.

b) Particular solution

$$m\frac{d\vec{v}_p}{dt} = -\Gamma\vec{v}_p + \vec{R}(\mathrm{t}),$$

assuming that the particular solution is of the type, $\vec{v}_p = e^{-\frac{\Gamma}{m}t}\vec{w}(\mathrm{t})$ and plug it in the above equation to get,

$$m\left(-\frac{\Gamma}{m}e^{-\frac{\Gamma}{m}t}\vec{w}(\mathrm{t}) + e^{-\frac{\Gamma}{m}t}\frac{d\vec{w}(\mathrm{t})}{dt}\right) = -\Gamma e^{-\frac{\Gamma}{m}t}\vec{w}(\mathrm{t}) + \vec{R}(\mathrm{t})$$

$$\Rightarrow \vec{w}(\mathrm{t}) = \frac{1}{m}\int_0^t e^{\frac{\Gamma}{m}\tau}\vec{R}(\tau)\,\mathrm{d}\tau$$

Our complete solution looks like,

$$\vec{v}(\mathrm{t}) = \vec{v}_0 e^{-\frac{\Gamma}{m}t} + \frac{1}{m}e^{-\frac{\Gamma}{m}t}\int_0^t e^{\frac{\Gamma}{m}\tau}\vec{R}(\tau)\,\mathrm{d}\tau \qquad \text{A5.3}$$

In the next step we calculate the kinetic energy of the particle, which is given by,

$$K.E. = \frac{1}{2} m \left\langle \vec{v} \bullet \vec{v} \right\rangle$$

$$= \frac{1}{2} m \left\langle \begin{array}{l} \left|\vec{v}_0\right|^2 e^{-2\frac{\Gamma}{m}t} + \frac{2}{m} e^{-2\frac{\Gamma}{m}t} \int_0^t e^{\frac{\Gamma}{m}\tau} \vec{v}_0 \bullet \vec{R}(\tau)\,\mathrm{d}\tau \\ + \frac{1}{m^2} e^{-2\frac{\Gamma}{m}t} \left(\int_0^t e^{\frac{\Gamma}{m}\tau} \vec{R}(\tau)\,\mathrm{d}\tau \bullet \int_0^t e^{\frac{\Gamma}{m}\tau'} \vec{R}(\tau')\,\mathrm{d}\tau' \right) \end{array} \right\rangle$$

$$= \frac{1}{2} m \left[\begin{array}{l} \left|\vec{v}_0\right|^2 e^{-2\frac{\Gamma}{m}t} + \frac{2}{m} e^{-2\frac{\Gamma}{m}t} \int_0^t e^{\frac{\Gamma}{m}\tau} \vec{v}_0 \bullet \left\langle \vec{R}(\tau) \right\rangle \mathrm{d}\tau \\ + \frac{1}{m^2} e^{-2\frac{\Gamma}{m}t} \left(\int_0^t \int_0^t e^{\frac{\Gamma}{m}(\tau+\tau')} \left\langle \vec{R}(\tau) \bullet \vec{R}(\tau') \right\rangle \mathrm{d}\tau\,\mathrm{d}\tau' \right) \end{array} \right],$$

using the properties of the $\vec{R}(\mathrm{t})$,

$$= \frac{1}{2} m \left[\begin{array}{l} \left|\vec{v}_0\right|^2 e^{-2\frac{\Gamma}{m}t} + \frac{2}{m} e^{-2\frac{\Gamma}{m}t} \int_0^t e^{\frac{\Gamma}{m}\tau} \vec{v}_0 \bullet \underbrace{\left\langle \vec{R}(\tau) \right\rangle}_{=0} \mathrm{d}\tau \\ + \frac{1}{m^2} e^{-2\frac{\Gamma}{m}t} \left(\int_0^t \int_0^t e^{\frac{\Gamma}{m}(\tau+\tau')} \underbrace{\left\langle \vec{R}(\tau) \bullet \vec{R}(\tau') \right\rangle}_{=c\delta(\tau-\tau')} \mathrm{d}\tau\,\mathrm{d}\tau' \right) \end{array} \right]$$

$$= \frac{1}{2} m \left[\left|\vec{v}_0\right|^2 e^{-2\frac{\Gamma}{m}t} + \frac{c}{m^2} e^{-2\frac{\Gamma}{m}t} \left(\int_0^t e^{2\frac{\Gamma}{m}\tau}\,\mathrm{d}\tau \right) \right]$$

$$= \frac{1}{2} m \left[\left|\vec{v}_0\right|^2 e^{-2\frac{\Gamma}{m}t} - \frac{c}{2\Gamma m} e^{-2\frac{\Gamma}{m}t} \left(1 - e^{2\frac{\Gamma}{m}t} \right) \right]$$

$$= \frac{1}{2} m \left[\left|\vec{v}_0\right|^2 e^{-2\frac{\Gamma}{m}t} - \frac{c}{2\Gamma m} e^{-2\frac{\Gamma}{m}t} + \frac{c}{2\Gamma m} \right]$$

for long timespan as $t \to \infty$

$$K.E. \to \frac{c}{4\Gamma} .$$

For a particle in a $3D$ space, the average $K.E.$ of the particle is $= \frac{3}{2} kT$. This gives the value of c as,

$$c = 6\Gamma kT \qquad \text{A5.4}$$

Therefore, we have,

$$\left\langle \vec{R}(\mathrm{t}) \bullet \vec{\mathrm{R}}(\mathrm{t}') \right\rangle = 6\Gamma kT\,\delta(\mathrm{t}-\mathrm{t}') . \qquad \text{A5.5}$$

But, in the numerical scheme Dirac delta functions cannot be implemented because of the discrete time stepping. Thus it has to be replaced by a combination of Heaviside function as shown in Fig A5.1,

$$\delta(\mathrm{t}-\mathrm{t}') \approx \frac{1}{\Delta t}\left\{ H\left[t - \left(t' - \frac{\Delta t}{2} \right) \right] - H\left[t - \left(t' + \frac{\Delta t}{2} \right) \right] \right\}$$

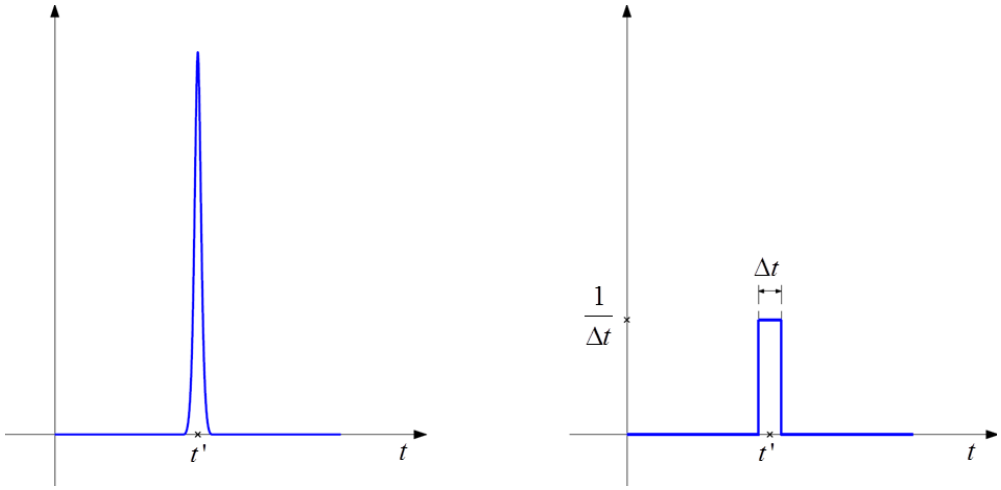

Fig A5.1: Approximating Dirac delta function with Heaviside function

Plugging this in eq. A5.5,

$$\left\langle \vec{R}(t)\bullet\vec{R}(t')\right\rangle = 6\Gamma kT\left\{H\left[t-\left(t'-\frac{\Delta t}{2}\right)\right]-H\left[t-\left(t'+\frac{\Delta t}{2}\right)\right]\right\} \quad \text{A5.6}$$

Dimensional consistency

In eq. A5.6 checking the dimension of both sides.

$$\text{L.H.S.} \Rightarrow \left[\left\langle \vec{R}(t)\bullet\vec{R}(t')\right\rangle\right] = \left[M^2L^2T^{-4}\right]$$

$$\left[\Gamma\right] = \left[MT^{-1}\right]$$

$$\left[kT\right] = \left[ML^2T^{-2}\right]$$

$$\text{R.H.S.} \Rightarrow \left[\frac{6\Gamma kT}{\Delta t}\right] = \left[M^2L^2T^{-4}\right]$$

From the dimensional comparison it can said that the magnitude of the random vector $\vec{R}(t)$ is $\sqrt{\frac{6\Gamma kT}{\Delta t}}$.

Thus, we can write the vector as $\vec{R}(t) = \sqrt{\frac{6\Gamma kT}{\Delta t}}\hat{n}$, where $\hat{n}$ is a random unit vector in $3D$ space.

Coefficient of Diffusion calculation

Again consider eq. A5.2 and dropping the inertial term of acceleration,

$$0 \approx -\Gamma\vec{v} + \vec{R}(\mathrm{t})$$

$$\Rightarrow \vec{v} = \frac{\vec{R}(\mathrm{t})}{\Gamma} = \frac{1}{\Gamma}\sqrt{\frac{6\Gamma kT}{\Delta t}}\hat{n} = \sqrt{\frac{6kT}{\Gamma\Delta t}}\hat{n}$$

$$\Rightarrow \frac{\Delta\vec{x}}{\Delta t} = \sqrt{\frac{6kT}{\Gamma\Delta t}}\hat{n}$$

$$\Rightarrow \Delta\vec{x} = \sqrt{\frac{6kT\Delta t}{\Gamma}}\hat{n}$$

From this above relation, we can say that the magnitude of the random step,

$$l = \sqrt{\frac{6kT\Delta t}{\Gamma}}.$$

Also, it is well known that,

$$\left\langle \vec{r}(\mathrm{t})\bullet\vec{r}(\mathrm{t}) \right\rangle = Nl^2 = 6Dt$$

where, N is the number of steps taken by the particle in the $3D$ space in time $t = N\Delta t$.

Substituting the values in the above relation, we finally have,

$$\cancel{N}\,\frac{6kT\,\cancel{\Delta t}}{\Gamma} = 6D\,\cancel{N}\,\cancel{\Delta t}$$

$$\Rightarrow D = \frac{kT}{\Gamma} \qquad \text{A5.7}$$

<u>Coefficient of Diffusion calculation: Alternative way</u>

We can also get the value of coefficient of diffusion, D from the rms distance calculation. As we know that,

$$\left\langle \vec{r}(\mathrm{t})\bullet\vec{r}(\mathrm{t}) \right\rangle = 6Dt. \qquad \text{A5.8}$$

Begin with, eq. A5.3 and integrate it to get the position of the particle as a function of time.

$$\vec{v}(\mathrm{t}) = \vec{v}_0 e^{-\frac{\Gamma}{m}t} + \frac{1}{m} e^{-\frac{\Gamma}{m}t} \int_0^t e^{\frac{\Gamma}{m}\tau} \vec{R}(\tau)\,\mathrm{d}\tau$$

$$\Rightarrow \frac{d\vec{r}}{dt} = \vec{v}_0 e^{-\frac{\Gamma}{m}t} + \frac{1}{m} e^{-\frac{\Gamma}{m}t} \int_0^t e^{\frac{\Gamma}{m}\tau} \vec{R}(\tau)\,\mathrm{d}\tau$$

$$\Rightarrow \vec{r} = \vec{r}_0 + \int_0^t \vec{v}_0 e^{-\frac{\Gamma}{m}\tau} d\tau + \frac{1}{m} \int_0^t e^{-\frac{\Gamma}{m}\tau} \left(\int_0^\tau e^{\frac{\Gamma}{m}\tau'} \vec{R}(\tau')\,\mathrm{d}\tau' \right) d\tau$$

$$\Rightarrow \vec{r} = \vec{r}_0 + \frac{m\vec{v}_0}{\Gamma} \left(1 - e^{-\frac{\Gamma}{m}t} \right) + \frac{1}{m} \int_0^t e^{-\frac{\Gamma}{m}\tau} \left(\int_0^\tau e^{\frac{\Gamma}{m}\tau'} \vec{R}(\tau')\,\mathrm{d}\tau' \right) d\tau \qquad \text{A5.9}$$

Using eq. A5.9, we can get the r.m.s distance squared from time $t = 0$ as follows,

$$\left\langle \left(\vec{r} - \vec{r}_0\right) \bullet \left(\vec{r} - \vec{r}_0\right) \right\rangle$$

$$= \left\langle \begin{array}{l} \dfrac{m^2 \left|\vec{v}_0\right|^2}{\Gamma^2} \left(1 - e^{-\frac{\Gamma}{m}t} \right)^2 + \dfrac{2}{\Gamma} \left(1 - e^{-\frac{\Gamma}{m}t} \right) \int_0^t e^{-\frac{\Gamma}{m}\tau} \left(\int_0^\tau e^{\frac{\Gamma}{m}\tau'} \vec{v}_0 \bullet \vec{R}(\tau')\,\mathrm{d}\tau' \right) d\tau \\ + \dfrac{1}{m^2} \left(\int_0^t e^{-\frac{\Gamma}{m}\tau} \left(\int_0^\tau e^{\frac{\Gamma}{m}\tau'} \vec{R}(\tau')\,\mathrm{d}\tau' \right) d\tau \right) \bullet \left(\int_0^t e^{-\frac{\Gamma}{m}\tau''} \left(\int_0^{\tau''} e^{\frac{\Gamma}{m}\tau'''} \vec{R}(\tau''')\,\mathrm{d}\tau''' \right) d\tau'' \right) \end{array} \right\rangle$$

$$= \frac{m^2 \left|\vec{v}_0\right|^2}{\Gamma^2} \left(1 - e^{-\frac{\Gamma}{m}t} \right)^2 + \frac{2}{\Gamma} \left(1 - e^{-\frac{\Gamma}{m}t} \right) \int_0^t e^{-\frac{\Gamma}{m}\tau} \left(\int_0^\tau e^{\frac{\Gamma}{m}\tau'} \vec{v}_0 \bullet \left\langle \vec{R}(\tau') \right\rangle \mathrm{d}\tau' \right) d\tau$$

$$+ \frac{1}{m^2} \left(\int_0^t e^{-\frac{\Gamma}{m}\tau} \left(\int_0^t e^{-\frac{\Gamma}{m}\tau''} \left(\int_0^\tau e^{\frac{\Gamma}{m}\tau'} \left(\int_0^{\tau''} e^{\frac{\Gamma}{m}\tau'''} \left\langle \vec{R}(\tau') \bullet \vec{R}(\tau''') \right\rangle \mathrm{d}\tau''' \right) \mathrm{d}\tau' \right) d\tau'' \right) d\tau \right)$$

Using the properties of the random force

$\vec{R}(\tau)$,

$$= \frac{m^2\left|\vec{v}_0\right|^2}{\Gamma^2}\left(1-e^{-\frac{\Gamma}{m}t}\right)^2 + \frac{2}{\Gamma}\left(1-e^{-\frac{\Gamma}{m}t}\right)\int_0^t e^{-\frac{\Gamma}{m}\tau}\left(\int_0^\tau e^{\frac{\Gamma}{m}\tau'}\vec{v}_0\bullet\overbrace{\left\langle\vec{R}(\tau')\right\rangle}^{=0}\mathrm{d}\tau'\right)d\tau$$

$$+\frac{1}{m^2}\left(\int_0^t e^{-\frac{\Gamma}{m}\tau}\left(\int_0^t e^{-\frac{\Gamma}{m}\tau''}\left(\int_0^\tau e^{\frac{\Gamma}{m}\tau'}\left(\int_0^{\tau''} e^{\frac{\Gamma}{m}\tau'''}\underbrace{\left\langle\vec{R}(\tau')\bullet\vec{R}(\tau''')\right\rangle}_{=c\delta(\tau'-\tau''')}\mathrm{d}\tau'''\right)\mathrm{d}\tau'\right)d\tau''\right)d\tau\right)$$

$$= \frac{m^2\left|\vec{v}_0\right|^2}{\Gamma^2}\left(1-e^{-\frac{\Gamma}{m}t}\right)^2 + \frac{1}{m^2}\left(\int_0^t e^{-\frac{\Gamma}{m}\tau}\left(\int_0^t e^{-\frac{\Gamma}{m}\tau''}\left(\int_0^\tau e^{\frac{2\Gamma}{m}\tau'}cH(\tau''-\tau')\mathrm{d}\tau'\right)d\tau''\right)d\tau\right)$$

$$= \frac{m^2\left|\vec{v}_0\right|^2}{\Gamma^2}\left(1-e^{-\frac{\Gamma}{m}t}\right)^2 + \frac{c}{m^2}\left(\int_0^t e^{-\frac{\Gamma}{m}\tau}\left(\int_0^\tau e^{\frac{2\Gamma}{m}\tau'}\left(\int_0^t e^{-\frac{\Gamma}{m}\tau''}H(\tau''-\tau')d\tau''\right)\mathrm{d}\tau'\right)d\tau\right)$$

$$= \frac{m^2\left|\vec{v}_0\right|^2}{\Gamma^2}\left(1-e^{-\frac{\Gamma}{m}t}\right)^2 + \frac{c}{m^2}\left(\int_0^t e^{-\frac{\Gamma}{m}\tau}\left(\int_0^\tau e^{\frac{2\Gamma}{m}\tau'}\left(\int_{\tau'}^t e^{-\frac{\Gamma}{m}\tau''}d\tau''\right)\mathrm{d}\tau'\right)d\tau\right)$$

$$= \frac{m^2\left|\vec{v}_0\right|^2}{\Gamma^2}\left(1-e^{-\frac{\Gamma}{m}t}\right)^2 + \frac{c}{m^2}\left(\int_0^t e^{-\frac{\Gamma}{m}\tau}\left(\int_0^\tau e^{\frac{2\Gamma}{m}\tau'}\left(\frac{m}{\Gamma}\left(e^{-\frac{\Gamma}{m}\tau'}-e^{-\frac{\Gamma}{m}t}\right)\right)\mathrm{d}\tau'\right)d\tau\right)$$

$$= \frac{m^2\left|\vec{v}_0\right|^2}{\Gamma^2}\left(1-e^{-\frac{\Gamma}{m}t}\right)^2 + \frac{c}{m\Gamma}\left(\int_0^t e^{-\frac{\Gamma}{m}\tau}\left(\int_0^\tau\left(e^{\frac{\Gamma}{m}\tau'}-e^{\frac{2\Gamma}{m}\tau'-\frac{\Gamma}{m}t}\right)\mathrm{d}\tau'\right)d\tau\right)$$

$$= \frac{m^2 \left|\vec{v}_0\right|^2}{\Gamma^2}\left(1-e^{-\frac{\Gamma}{m}t}\right)^2 + \frac{c}{m\Gamma}\left(\int_0^t e^{-\frac{\Gamma}{m}\tau}\,\frac{m}{\Gamma}\left(e^{\frac{\Gamma}{m}\tau}-1-\frac{e^{-\frac{\Gamma}{m}t}}{2}\left(e^{\frac{2\Gamma}{m}\tau}-1\right)\right)d\tau\right)$$

$$= \frac{m^2 \left|\vec{v}_0\right|^2}{\Gamma^2}\left(1-e^{-\frac{\Gamma}{m}t}\right)^2 + \frac{c}{2\Gamma^2}\left(\int_0^t\left(2-2e^{-\frac{\Gamma}{m}\tau}-e^{-\frac{\Gamma}{m}t-\frac{\Gamma}{m}\tau}\left(e^{\frac{2\Gamma}{m}\tau}-1\right)\right)d\tau\right)$$

$$= \frac{m^2 \left|\vec{v}_0\right|^2}{\Gamma^2}\left(1-e^{-\frac{\Gamma}{m}t}\right)^2 + \frac{c}{2\Gamma^2}\left(\int_0^t\left(2-2e^{-\frac{\Gamma}{m}\tau}-e^{-\frac{\Gamma}{m}t+\frac{\Gamma}{m}\tau}+e^{-\frac{\Gamma}{m}t-\frac{\Gamma}{m}\tau}\right)d\tau\right)$$

$$= \frac{m^2 \left|\vec{v}_0\right|^2}{\Gamma^2}\left(1-e^{-\frac{\Gamma}{m}t}\right)^2 + \frac{c}{2\Gamma^2}\left(2t-\frac{2m}{\Gamma}\left(1-e^{-\frac{\Gamma}{m}t}\right)-\frac{m}{\Gamma}e^{-\frac{\Gamma}{m}t}\left(e^{\frac{\Gamma}{m}\tau}-1\right)+\frac{m}{\Gamma}e^{-\frac{\Gamma}{m}t}\left(1-e^{-\frac{\Gamma}{m}t}\right)\right)$$

$$= \frac{m^2 \left|\vec{v}_0\right|^2}{\Gamma^2}\left(1-e^{-\frac{\Gamma}{m}t}\right)^2 + \frac{c}{2\Gamma^3}\left(2\Gamma t-2m+2me^{-\frac{\Gamma}{m}t}-m+me^{-\frac{\Gamma}{m}t}+me^{-\frac{\Gamma}{m}t}-me^{-\frac{2\Gamma}{m}t}\right)$$

$$= \frac{m^2 \left|\vec{v}_0\right|^2}{\Gamma^2}\left(1-e^{-\frac{\Gamma}{m}t}\right)^2 + \frac{c}{2\Gamma^3}\left(2\Gamma t-3m+4me^{-\frac{\Gamma}{m}t}-me^{-\frac{2\Gamma}{m}t}\right)$$

Under the condition as $t \to \infty$,

$$\lim_{t\to\infty}\left\langle\left(\vec{r}-\vec{r}_0\right)\bullet\left(\vec{r}-\vec{r}_0\right)\right\rangle$$

$$= \lim_{t\to\infty}\frac{m^2 \left|\vec{v}_0\right|^2}{\Gamma^2} + \frac{c}{2\Gamma^3}\left(2\Gamma t-3m+4me^{-\frac{\Gamma}{m}t}-me^{-\frac{2\Gamma}{m}t}\right)$$

$$= \frac{m^2 \left|\vec{v}_0\right|^2}{\Gamma^2} + \frac{ct}{\Gamma^2} - \frac{3cm}{2\Gamma^3}$$

Plugging in the value of $c = 6\Gamma kT$,

$$= \frac{m^2 \left|\vec{v}_0\right|^2}{\Gamma^2} + \frac{6kTt}{\Gamma} - \frac{9kTm}{\Gamma^2}$$
$$= \text{constant} + \frac{6kTt}{\Gamma}$$

Comparing with eq. A5.8, we can say that,

$$D = \frac{kT}{\Gamma},$$

which is exactly the same result obtained in eq. A5.7.

A5.2 Brownian Dynamics Calculations: Bead with spring calculation

Consider a particle of mass m, suspended in a liquid (friction constant Γ) and moving at speed $\vec{v}$ and attached is a spring from origin with unstretched length as 0.

During this motion, particle has three different forces acting on it, which are,

1. a frictional force of magnitude, $-\Gamma\vec{v}$,
2. a spring force of magnitude, $-K\vec{r}$,
3. a random force coming from the bombardment of water particles around this particle, $\vec{R}(\mathrm{t})$ and has the following properties,

   a) $\left\langle \vec{F}(\mathrm{t}) \right\rangle = 0$, means that the force can be random in direction

   b) $\left\langle \vec{F}(\mathrm{t}) \bullet \vec{F}(\mathrm{t}') \right\rangle = c\delta(\mathrm{t}-\mathrm{t}')$, means that the force at two different instants, is not correlated,

   where, c is the parameter which we are going to obtain from this analysis.

So, the equation of motion can be written as,

$$m\frac{d^2\vec{r}}{dt^2} = -\Gamma\frac{d\vec{r}}{dt} - K\vec{r} + \vec{F}(\mathrm{t}) \ , \qquad \text{A5.10}$$

Next, we solve for the velocity, $\vec{v}$ from eq. A5.2. Since, it is an ODE, the solution can be obtained in two parts, a homogeneous solution, $\vec{v}_h$ and a particular solution, $\vec{v}_p$.

a) <u>Homogeneous solution</u>

$$m\frac{d^2\vec{r}_h}{dt^2} = -\Gamma\frac{d\vec{r}_h}{dt} - K\vec{r}_h$$

$$\Rightarrow \vec{r}_h = \vec{A}e^{\frac{t\left(-\Gamma-\sqrt{-4Km+\Gamma^2}\right)}{2m}} + \vec{B}e^{\frac{t\left(-\Gamma+\sqrt{-4Km+\Gamma^2}\right)}{2m}}$$

b) Particular solution

Using the method of variation of parameters, the particular solution can be obtained which satisfies the following differential equation,

$$m\frac{d\vec{v}_p}{dt} = -\Gamma\vec{v}_p - K\vec{r}_p + \vec{F}(\mathrm{t})$$

Assuming that the particular solution is of the type,

$$\vec{r}_p = \vec{w}_1(\mathrm{t})r_1(\mathrm{t}) + \vec{w}_2(\mathrm{t})r_2(\mathrm{t}),$$

where, $r_1(\mathrm{t}) = e^{\frac{t\left(-\Gamma-\sqrt{-4Km+\Gamma^2}\right)}{2m}}$ and $r_2(\mathrm{t}) = e^{\frac{t\left(-\Gamma+\sqrt{-4Km+\Gamma^2}\right)}{2m}}$.

The particular solution is then given by,

$$\vec{r}_p(\mathrm{t}) = e^{\frac{t\left(-\Gamma-\sqrt{-4km+\Gamma^2}\right)}{2m}} \int_0^t -\frac{e^{\frac{\Gamma\tau_1}{m}+\frac{\left(-\Gamma+\sqrt{-4km+\Gamma^2}\right)\tau_1}{2m}}}{\sqrt{-4km+\Gamma^2}}\vec{F}(\tau_1)\,d\tau_1$$
$$+ e^{\frac{t\left(-\Gamma+\sqrt{-4km+\Gamma^2}\right)}{2m}} \int_0^t \frac{e^{\frac{\Gamma\tau_2}{m}+\frac{\left(-\Gamma-\sqrt{-4km+\Gamma^2}\right)\tau_2}{2m}}}{\sqrt{-4km+\Gamma^2}}\vec{F}(\tau_2)\,d\tau_2$$

Therefore, we have our complete solution as,

$$\vec{r}(\mathrm{t}) = \vec{A}e^{\frac{t\left(-\Gamma-\sqrt{-4Km+\Gamma^2}\right)}{2m}} + \vec{B}e^{\frac{t\left(-\Gamma+\sqrt{-4Km+\Gamma^2}\right)}{2m}}$$
$$+ e^{\frac{t\left(-\Gamma-\sqrt{-4km+\Gamma^2}\right)}{2m}} \int_0^t -\frac{e^{\frac{\Gamma\tau_1}{m}+\frac{\left(-\Gamma+\sqrt{-4km+\Gamma^2}\right)\tau_1}{2m}}\vec{F}(\tau_1)}{\sqrt{-4km+\Gamma^2}}\,d\tau_1$$
$$+ e^{\frac{t\left(-\Gamma+\sqrt{-4km+\Gamma^2}\right)}{2m}} \int_0^t \frac{e^{\frac{\Gamma\tau_2}{m}+\frac{\left(-\Gamma-\sqrt{-4km+\Gamma^2}\right)\tau_2}{2m}}\vec{F}(\tau_2)}{\sqrt{-4km+\Gamma^2}}\,d\tau_2$$

and also, the velocity is given by,

$$\vec{v}(\mathrm{t}) = \vec{A}\frac{\left(-\Gamma-\sqrt{-4Km+\Gamma^2}\right)}{2m}e^{\frac{t\left(-\Gamma-\sqrt{-4Km+\Gamma^2}\right)}{2m}} + \vec{B}\frac{\left(-\Gamma+\sqrt{-4Km+\Gamma^2}\right)}{2m}e^{\frac{t\left(-\Gamma+\sqrt{-4Km+\Gamma^2}\right)}{2m}}$$
$$+ \frac{\left(-\Gamma-\sqrt{-4Km+\Gamma^2}\right)}{2m}e^{\frac{t\left(-\Gamma-\sqrt{-4km+\Gamma^2}\right)}{2m}} \int_0^t -\frac{e^{\frac{\Gamma\tau_1}{m}+\frac{\left(-\Gamma+\sqrt{-4km+\Gamma^2}\right)\tau_1}{2m}}\vec{F}(\tau_1)}{\sqrt{-4km+\Gamma^2}}\,d\tau_1$$
$$+ \frac{\left(-\Gamma+\sqrt{-4Km+\Gamma^2}\right)}{2m}e^{\frac{t\left(-\Gamma+\sqrt{-4km+\Gamma^2}\right)}{2m}} \int_0^t \frac{e^{\frac{\Gamma\tau_2}{m}+\frac{\left(-\Gamma-\sqrt{-4km+\Gamma^2}\right)\tau_2}{2m}}\vec{F}(\tau_2)}{\sqrt{-4km+\Gamma^2}}\,d\tau_2$$

For the sake of simplicity, let us assume that we have following set of initial conditions,

$$\vec{r}(\mathrm{t}=0) = 0$$
$$\vec{v}(\mathrm{t}=0) = 0$$

Using these, we have,

$$A = B = 0,$$

resulting in,

$$\vec{r}(\mathrm{t}) = e^{\frac{t\left(-\Gamma-\sqrt{-4km+\Gamma^2}\right)}{2m}} \int_0^t -\frac{e^{\frac{\Gamma\tau_1}{m}+\frac{\left(-\Gamma+\sqrt{-4km+\Gamma^2}\right)\tau_1}{2m}}}{\sqrt{-4km+\Gamma^2}} \vec{F}(\tau_1)\, d\tau_1$$
$$+ e^{\frac{t\left(-\Gamma+\sqrt{-4km+\Gamma^2}\right)}{2m}} \int_0^t \frac{e^{\frac{\Gamma\tau_2}{m}+\frac{\left(-\Gamma-\sqrt{-4km+\Gamma^2}\right)\tau_2}{2m}}}{\sqrt{-4km+\Gamma^2}} \vec{F}(\tau_2)\, d\tau_2$$

and,

$$\vec{v}(\mathrm{t}) = \frac{\left(-\Gamma-\sqrt{-4Km+\Gamma^2}\right)}{2m} e^{t\frac{\left(-\Gamma-\sqrt{-4km+\Gamma^2}\right)}{2m}} \int_0^t -\frac{e^{\frac{\Gamma\tau_1}{m}+\frac{\left(-\Gamma+\sqrt{-4km+\Gamma^2}\right)\tau_1}{2m}}}{\sqrt{-4km+\Gamma^2}} \vec{F}(\tau_1)\, d\tau_1$$
$$+ \frac{\left(-\Gamma+\sqrt{-4Km+\Gamma^2}\right)}{2m} e^{t\frac{\left(-\Gamma+\sqrt{-4km+\Gamma^2}\right)}{2m}} \int_0^t \frac{e^{\frac{\Gamma\tau_2}{m}+\frac{\left(-\Gamma-\sqrt{-4km+\Gamma^2}\right)\tau_2}{2m}}}{\sqrt{-4km+\Gamma^2}} \vec{F}(\tau_2)\, d\tau_2$$

At this point, let's assume,

$$\alpha = \frac{\Gamma+\sqrt{-4Km+\Gamma^2}}{2m}$$
$$\beta = \frac{\Gamma-\sqrt{-4Km+\Gamma^2}}{2m}$$
$$D = \sqrt{-4Km+\Gamma^2}$$

this simplifies our expression of position and velocity vectors as,

$$\vec{r}(\mathrm{t}) = -\frac{e^{-\alpha t}}{D} \int_0^t e^{\alpha\tau_1} \vec{F}(\tau_1) d\tau_1 + \frac{e^{-\beta t}}{D} \int_0^t e^{\beta\tau_2} \vec{F}(\tau_2) d\tau_2 ,$$

$$\vec{v}(\mathrm{t}) = \frac{\alpha e^{-\alpha t}}{D} \int_0^t e^{\alpha\tau_1} \vec{F}(\tau_1) d\tau_1 - \frac{\beta e^{-\beta t}}{D} \int_0^t e^{\beta\tau_2} \vec{F}(\tau_2) d\tau_2 .$$

Calculating Kinetic Energy

We get the average K.E. of the particle using the following expression,

$$K.E. = \frac{1}{2} m \left\langle \vec{v} \bullet \vec{v} \right\rangle$$

$$= \frac{1}{2} m \left\langle \left(\frac{\alpha e^{-\alpha t}}{D} \int_0^t e^{\alpha \tau_1} \vec{F}(\tau_1) d\tau_1 - \frac{\beta e^{-\beta t}}{D} \int_0^t e^{\beta \tau_2} \vec{F}(\tau_2) d\tau_2 \right) \right.$$
$$\left. \bullet \left(\frac{\alpha e^{-\alpha t}}{D} \int_0^t e^{\alpha \tau_1'} \vec{F}(\tau_1') d\tau_1' - \frac{\beta e^{-\beta t}}{D} \int_0^t e^{\beta \tau_2'} \vec{F}(\tau_2') d\tau_2' \right) \right\rangle$$

$$= \frac{m}{2D^2} \left\langle \begin{array}{l} \alpha^2 e^{-2\alpha t} \int_0^t \int_0^t e^{\alpha(\tau_1 + \tau_1')} \vec{F}(\tau_1) \bullet \vec{F}(\tau_1') d\tau_1' d\tau_1 \\ -2\alpha\beta e^{-(\alpha+\beta)t} \int_0^t \int_0^t e^{\beta \tau_2} \vec{F}(\tau_2) \bullet \vec{F}(\tau_1) d\tau_2 d\tau_1 \\ +\beta^2 e^{-2\beta t} \int_0^t \int_0^t e^{\beta(\tau_2 + \tau_2')} \vec{F}(\tau_2) \bullet \vec{F}(\tau_2') d\tau_2' d\tau_2 \end{array} \right\rangle$$

$$= \frac{m}{2D^2} \left(\begin{array}{l} \alpha^2 e^{-2\alpha t} \int_0^t \int_0^t e^{\alpha(\tau_1 + \tau_1')} \overbrace{\left\langle \vec{F}(\tau_1) \bullet \vec{F}(\tau_1') \right\rangle}^{= c\delta(\tau_1 - \tau_1')} d\tau_1' d\tau_1 \\ -2\alpha\beta e^{-(\alpha+\beta)t} \int_0^t \int_0^t e^{\alpha\tau_1 + \beta\tau_2} \overbrace{\left\langle \vec{F}(\tau_2) \bullet \vec{F}(\tau_1) \right\rangle}^{= c\delta(\tau_1 - \tau_2)} d\tau_2 d\tau_1 \\ +\beta^2 e^{-2\beta t} \int_0^t \int_0^t e^{\beta(\tau_2 + \tau_2')} \overbrace{\left\langle \vec{F}(\tau_2) \bullet \vec{F}(\tau_2') \right\rangle}^{= c\delta(\tau_2 - \tau_2')} d\tau_2' d\tau_2 \end{array} \right)$$

$$= \frac{mc}{2D^2}\left(\begin{array}{l} \alpha^2 e^{-2\alpha t}\int_0^t\int_0^t e^{\alpha\left(\tau_1+\tau_1'\right)}\delta(\tau_1-\tau_1')d\tau_1'd\tau_1 \\ -2\alpha\beta e^{-(\alpha+\beta)t}\int_0^t\int_0^t e^{\alpha\tau_1+\beta\tau_2}\delta(\tau_1-\tau_2)d\tau_2 d\tau_1 \\ +\beta^2 e^{-2\beta t}\int_0^t\int_0^t e^{\beta\left(\tau_2+\tau_2'\right)}\delta(\tau_2-\tau_2')d\tau_2'd\tau_2 \end{array} \right)$$

$$= \frac{mc}{2D^2}\left(\alpha^2 e^{-2\alpha t}\int_0^t e^{2\alpha\tau_1}d\tau_1 - 2\alpha\beta e^{-(\alpha+\beta)t}\int_0^t e^{(\alpha+\beta)\tau_1}d\tau_1 + \beta^2 e^{-2\beta t}\int_0^t e^{2\beta\tau_2}d\tau_2 \right)$$

$$= \frac{mc}{2D^2}\left[\frac{\alpha^2}{2\alpha}e^{-2\alpha t}\left(e^{2\alpha t}-1\right) - \frac{2\alpha\beta}{(\alpha+\beta)}e^{-(\alpha+\beta)t}\left(e^{(\alpha+\beta)t}-1\right) + \frac{\beta^2}{2\beta}e^{-2\beta t}\left(e^{2\beta t}-1\right) \right]$$

$$= \frac{mc}{2D^2}\left[\frac{\alpha}{2}\left(1-e^{-2\alpha t}\right) - \frac{2\alpha\beta}{(\alpha+\beta)}\left(1-e^{-(\alpha+\beta)t}\right) + \frac{\beta}{2}\left(1-e^{-2\beta t}\right) \right]$$

Under the condition that time scale we are considering very large, $t \to \infty$

$$K.E. \to \frac{mc}{2D^2}\left[\frac{\alpha+\beta}{2} - \frac{2\alpha\beta}{(\alpha+\beta)} \right]$$

$$= \frac{mc}{2\left(\Gamma^2-4Km\right)}\left[\frac{\Gamma}{2m} - \frac{2K}{\Gamma} \right]$$

$$= \frac{c}{4\Gamma}$$

It is also known that,

$$K.E. = \frac{3}{2}kT,$$

which gives us,

$$c = 6\Gamma kT.$$

This is exactly the same thing obtained from the case where was no spring involved in the picture. It means that irrespective of the spring's absence or presence, the $K.E.$ is going to be $\frac{3}{2}kT$, as long as we choose the value of $c = 6\Gamma kT$.

Calculating Potential Energy

We get the average P.E. of the particle using the following expression,

$$P.E. = \frac{1}{2}K\left\langle \vec{r}\bullet\vec{r}\right\rangle$$

$$= \frac{1}{2}K\left\langle \begin{array}{l} \left(-\frac{e^{-\alpha t}}{D}\int_0^t e^{\alpha\tau_1}\vec{F}(\tau_1)d\tau_1 + \frac{e^{-\beta t}}{D}\int_0^t e^{\beta\tau_2}\vec{F}(\tau_2)d\tau_2 \right) \\ \bullet\left(-\frac{e^{-\alpha t}}{D}\int_0^t e^{\alpha\tau_1'}\vec{F}(\tau_1')d\tau_1' + \frac{e^{-\beta t}}{D}\int_0^t e^{\beta\tau_2'}\vec{F}(\tau_2')d\tau_2' \right) \end{array} \right\rangle$$

$$= \frac{K}{2D^2}\left\langle \begin{array}{l} e^{-2\alpha t}\int_0^t\int_0^t e^{\alpha\left(\tau_1+\tau_1'\right)}\vec{F}(\tau_1)\bullet\vec{F}(\tau_1')d\tau_1'd\tau_1 \\ -2e^{-(\alpha+\beta)t}\int_0^t\int_0^t e^{\beta\tau_2}\vec{F}(\tau_2)\bullet\vec{F}(\tau_1)d\tau_2 d\tau_1 \\ +e^{-2\beta t}\int_0^t\int_0^t e^{\beta\left(\tau_2+\tau_2'\right)}\vec{F}(\tau_2)\bullet\vec{F}(\tau_2')d\tau_2'd\tau_2 \end{array} \right\rangle$$

$$= \frac{K}{2D^2}\left(\begin{array}{l} e^{-2\alpha t}\int_0^t\int_0^t e^{\alpha\left(\tau_1+\tau_1^{'}\right)}\overbrace{\left\langle \vec{F}(\tau_1)\bullet\vec{F}(\tau_1^{'})\right\rangle}^{=c\delta(\tau_1-\tau_1^{'})}d\tau_1^{'}d\tau_1 \\ -2e^{-(\alpha+\beta)t}\int_0^t\int_0^t e^{\alpha\tau_1+\beta\tau_2}\overbrace{\left\langle \vec{F}(\tau_2)\bullet\vec{F}(\tau_1)\right\rangle}^{=c\delta(\tau_1-\tau_2)}d\tau_2 d\tau_1 \\ +e^{-2\beta t}\int_0^t\int_0^t e^{\beta\left(\tau_2+\tau_2^{'}\right)}\overbrace{\left\langle \vec{F}(\tau_2)\bullet\vec{F}(\tau_2^{'})\right\rangle}^{=c\delta(\tau_2-\tau_2^{'})}d\tau_2^{'}d\tau_2 \end{array}\right)$$

$$= \frac{Kc}{2D^2}\left(\begin{array}{l} e^{-2\alpha t}\int_0^t\int_0^t e^{\alpha\left(\tau_1+\tau_1^{'}\right)}\delta(\tau_1-\tau_1^{'})d\tau_1^{'}d\tau_1 \\ -2e^{-(\alpha+\beta)t}\int_0^t\int_0^t e^{\alpha\tau_1+\beta\tau_2}\delta(\tau_1-\tau_2)d\tau_2 d\tau_1 \\ +e^{-2\beta t}\int_0^t\int_0^t e^{\beta\left(\tau_2+\tau_2^{'}\right)}\delta(\tau_2-\tau_2^{'})d\tau_2^{'}d\tau_2 \end{array}\right)$$

$$= \frac{Kc}{2D^2}\left(e^{-2\alpha t}\int_0^t e^{2\alpha\tau_1}d\tau_1 - 2e^{-(\alpha+\beta)t}\int_0^t e^{(\alpha+\beta)\tau_1}d\tau_1 + e^{-2\beta t}\int_0^t e^{2\beta\tau_2}d\tau_2 \right)$$

$$= \frac{Kc}{2D^2}\left(\frac{1}{2\alpha}e^{-2\alpha t}\left(e^{2\alpha t}-1\right) - \frac{2}{(\alpha+\beta)}e^{-(\alpha+\beta)t}\left(e^{(\alpha+\beta)t}-1\right) + \frac{1}{2\beta}e^{-2\beta t}\left(e^{2\beta t}-1\right)\right)$$

$$= \frac{Kc}{2D^2}\left(\frac{1}{2\alpha}\left(1-e^{-2\alpha t}\right) - \frac{2}{(\alpha+\beta)}\left(1-e^{-(\alpha+\beta)t}\right) + \frac{1}{2\beta}\left(1-e^{-2\beta t}\right)\right)$$

Under the condition that time scale we are considering very large, $t \to \infty$

$$K.E. \to \frac{Kc}{2D^2}\left[\frac{1}{2\alpha} - \frac{2}{(\alpha+\beta)} + \frac{1}{2\beta}\right]$$

$$= \frac{Kc}{2D^2}\left[\frac{(\alpha+\beta)}{2\alpha\beta} - \frac{2}{(\alpha+\beta)}\right]$$

$$= \frac{Kc}{2D^2}\left[\frac{\Gamma}{2K} - \frac{2m}{\Gamma}\right]$$

$$= \frac{Kc}{2(\Gamma^2 - 4Km)}\left[\frac{\Gamma^2 - 4Km}{2K\Gamma}\right]$$

$$= \frac{c}{4\Gamma}$$

plugging in the value of c,

$$= \frac{3}{2}kT$$

So, in case of potential energy it also comes out to be exactly $\frac{3}{2}kT$.

A5.2 Coarse Grained lipid molecule

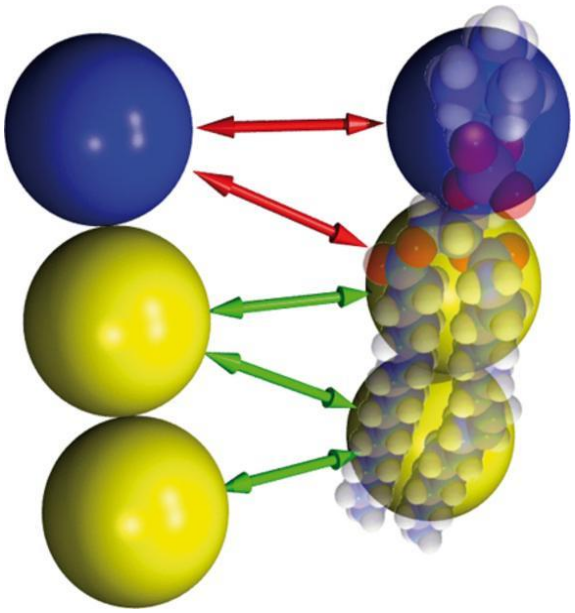

Fig A5.2 : Coarse grained lipid molecule (image ref: [1])

The lipid molecule is represented by a chain of three beads as shown in Fig. A5.2. One bead (shown in blue) is a representative of the hydrophilic part of the lipid molecule. Whereas, the other two beads play the role of the hydrophobic part of the lipid molecule.

The parameter w_c is a tunable parameter, which can be chosen from the parameter space as shown in Fig. A5.3. The choice of the parameters from the plot below determines the stability of bilayer. If the values are chosen outside the prescribed zone, the system tends to be either gas or crystal and doesn't express the right behavior.

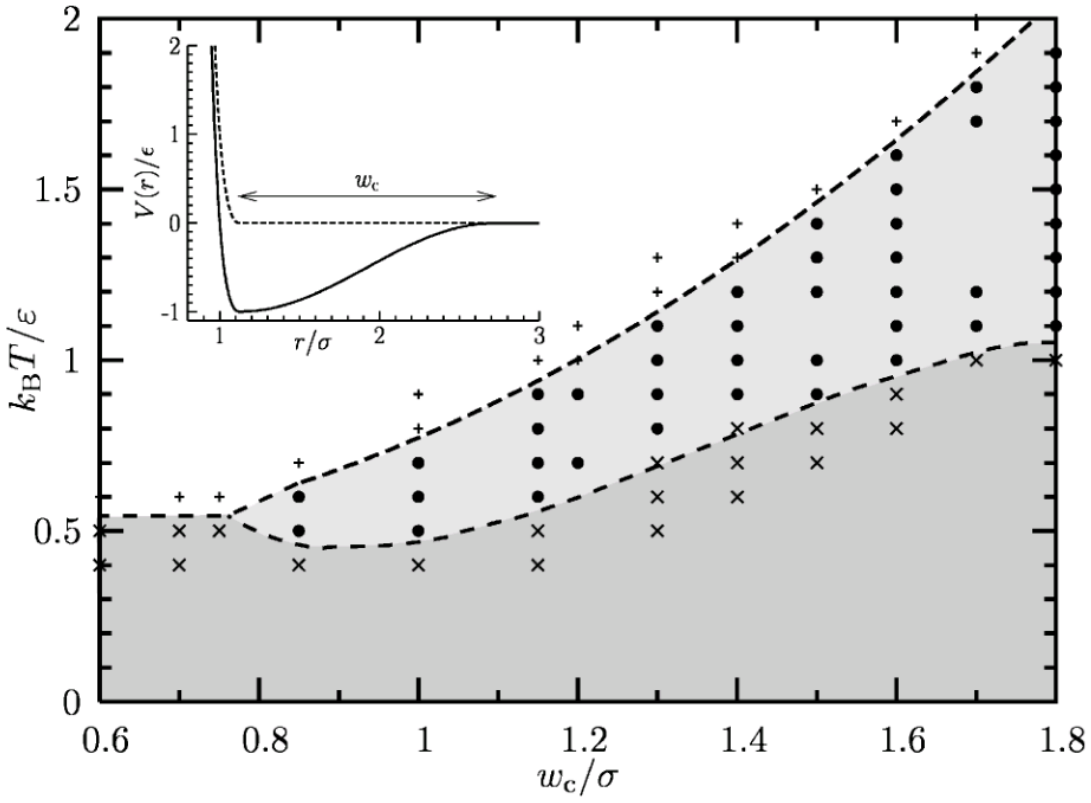

Fig A5.3: Parameter space for attractive potential (image ref: [1])

For this particular simulation the values of parameters are chosen as, $w_c = 1.6\sigma$ and $\frac{k_B T}{\epsilon} = 1.1$.

This above formulation of potentials is implemented in LAMMPS to simulate the lipid membrane formation, under a Langevin thermostat. The details of LAMMPS implementation are discussed in next section.

LAMMPS implementation

The CG molecular model described in the previous section has been implemented in LAMMPS. The simulation is carried out under a Langevin thermostat (LT) under NVE ensemble. LT provides the necessary thermal fluctuations necessary for the proper lipid membrane behavior. The magnitude of these thermal fluctuation inducing

forces (F_T) is determined from "Fluctuation-dissipation" theorem, which relates the viscosity of the solvent (Γ) and system temperature (T) in eq. A5.5,

$$\left\langle \vec{F}_T(\mathrm{t}) \bullet \vec{F}_T(\mathrm{t}') \right\rangle = 6\Gamma k_B T \delta(t - t') .$$

For a numerical scheme this relationship can be simplified as shown in eq. A5.6

$$\vec{F}_T(\mathrm{t}) = \sqrt{\frac{6\Gamma k_B T}{\Delta t}} \hat{n} \ ,$$

where, Δt is the time step for the integration,

and, $\hat{n}$ is a random unit vector in 3D determining the direction of the random force. This random force is a part of the governing equation for the dynamics of the particles in the system, which is essentially the Newton's second law of motion and is a generalized version of eq. A5.10,

$$m\frac{d\vec{v}}{dt} = -\Gamma\vec{v} + \vec{F}\left(\vec{r}(\mathrm{t})\right) + \vec{F}_T(\mathrm{t}), \qquad \text{A5.11}$$

where, m is the mass of the particle,

and, $\vec{F}\left(\vec{\mathrm{r}}(\mathrm{t})\right)$ is the force due to various system interactions involving spring forces, intermolecular interactions etc.

Eq. A5.11 essentially describes the Brownian motion of a particle and can be specialized for the Langevin dynamics by neglecting the inertial term with respect to the force term, which gives us,

$$-\Gamma\vec{v} + \vec{F}\left(\vec{r}(\mathrm{t})\right) + \vec{F}_T(\mathrm{t}) \approx 0 \ . \qquad \text{A5.12}$$

The eq. A5.12 can be solved for the location of the particle in the system under the influence of various system forces, random forces and viscous damping.

In LAMMPS this set of equations is solved for each and every particle at each time step. For the current simulation following parameters were chosen.

Parameter	**value**
Δt	$0.001\,\tau$
Γ	τ^{-1}
neighbor list updation	$50\,\Delta t$

Below is a snippet from the LAMMPS script, with the molecular model incorporated with the before mentioned parameters.

```
# Coarse Grained Lipid
# setting up environment of simulation
units           lj
dimension       3
boundary        p p p
atom_style      full



# defining the pair potential
#                       h-h, h-t & t-t attraction
pair_style      hybrid/overlay lj/cut 1.12246 table linear 10000
```

```
# defining the bonding between the beads
#                    bending bond
bond_style      hybrid harmonic fene

# read the parameters of the system and initial conditions
read_data       input.data

# defining the pair interaction parameters
pair_coeff      1 1 lj/cut 1 0.95 1.06633          # WCA repulsion between h-h beads
pair_coeff      1 2 lj/cut 1 0.95 1.06633          # WCA repulsion between h-t beads
pair_coeff      2 2 lj/cut 1 1 1.12246                    # WCA repulsion between t-t
beads
pair_coeff      2 2 table cosine.table cos         # attractive potential between t-t beads
pair_modify     shift yes                          # shifting the potential and forming WCA
pair interaction

# defining bond parameters
bond_coeff      1 harmonic 5 4
bond_coeff      2 fene 30 1.5 0 0.95
bond_coeff      3 fene 30 1.5 0 1

# specifying run parameters
```

```
group           all type 1 2
neighbor        2.0 multi
neigh_modify    delay 50
timestep        0.001

# specifying the time integration scheme and ensemble
run_style       verlet
fix             1 all langevin 1.100 1.100 1 48279 zero yes
fix             2 all nve
```

In the next section of this works details are provided on the bending rigidity measurement by deforming the lipid bilayer membrane into a buckled structure.

Bending the membrane

The procedure of lipid bilayer membranes bending rigidity calculation involves deforming a periodic membrane inside a box of length less than its natural relaxed length [2], as shown in Fig A5.4.

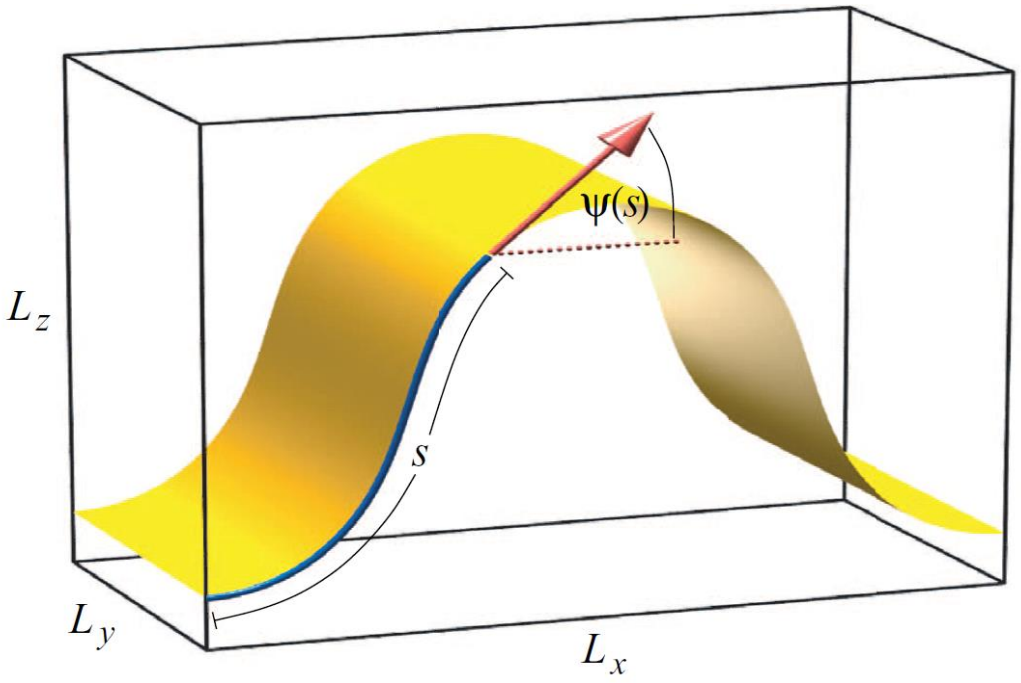

Fig A5.4 : Schematic of membrane bending procedure to determine the bending rigidity [2]

The procedure firstly involves obtaining a relaxed membrane, which is done is LAMMPS by incorporating a NPH ensemble. It is assumed that if membrane is let to fluctuate for a long time under NPH ensemble the membrane is going to attain a relaxed configuration with zero pressure exerted on the walls of the simulation box in both x and y directions. The configuration of membrane is such that most of the deformation occurs in x direction and minimal happens in y-direction. To ensure this, the length of the membrane is chosen to be much longer than the length in y-direction. Also, by doing this, one can analyze the membrane in an analytical fashion and get expressions for forces in and deformations.

After the complete relaxation the natural length L_x^0 of the membrane can be obtained, which is the reference length of the membrane and strain is further defined in terms of this reference length as follows,

$$\gamma = \frac{L_x^0 - L_x}{L_x^0}, \qquad \text{A5.13}$$

where, L_x is the length of the simulation box at some point during the deformation process.

From the analytical analysis, the expression of forces can be obtained as follows,

$$F_x(\gamma) = \kappa \left[\frac{4\pi^2 L_y}{\left(L_x^0\right)^2} \right] \left[1 + \frac{1}{2}\gamma + \frac{9}{32}\gamma^2 + \frac{21}{128}\gamma^3 + \frac{795}{8192}\gamma^4 + \frac{945}{16384}\gamma^5 + \ldots \right] \qquad \text{A5.14}$$

where, F_x , is the force measured on the x-faces of the simulation box,

κ , is the bending rigidity of the lipid bilayer membrane,

γ , is the strain applied on the membrane.

The CG simulation described before, can be used to simulate the lipid membrane bending as described to measure the force on the x-faces of the membrane. The force on the membrane can be measured from the pressure information generated by the simulation output. The method involves measuring the pressure on the simulation in x-direction and converting it to force, by making use of the simulation box area as follows,

$$F_x(\gamma) = P_{xx} L_y L_z \qquad \text{A5.15}$$

In next section, results from the force measurement methodology are shown.

Results

In this section the results of the case where force is measured from pressure measurement. The box dimension for the relaxed membrane are used from [2], with $L_x^0 = 66.75\sigma$ and $L_y = 12\sigma$. The compression is incrementally increased on the box to get different values of strain. At each strain value, the simulation is deployed for a duration of $\sim 10^5 \tau$. Here τ is the characteristic simulation time, given by, $\tau = \sigma\sqrt{\frac{m}{\epsilon}}$.

The force is calculated by averaging over non-overlapping windows of size $\sim 25000\tau$. The mean of all the window averages is used to calculate the representative force values at each strain value.

Below, is the result generated from the simulations in comparison to the result provided in [2]. The bending rigidity of the membrane is found out to be, $\kappa = 11.8 \pm 0.4 k_B T$, which is close to the values reported in literature $12.8 \pm 0.4 \mathrm{k}_B T$ [2], $11.7 \pm 0.2 k_B T$ [3], $12.5 \pm 1.0 k_B T$ [3] and $12.44 \pm 0.26 k_B T$ [4].

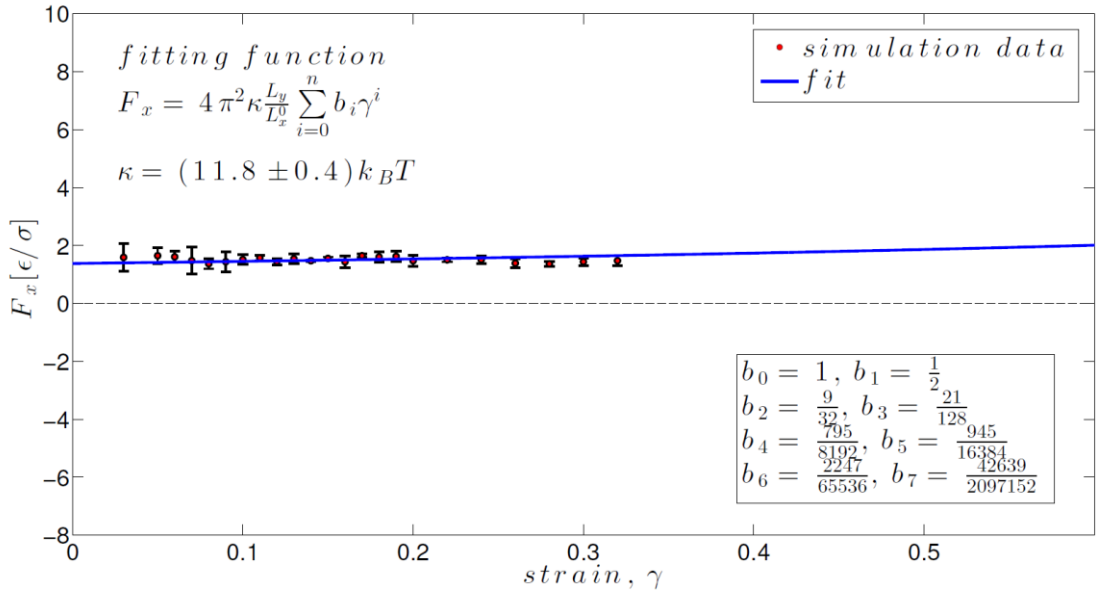

Fig A5.5 : force vs strain

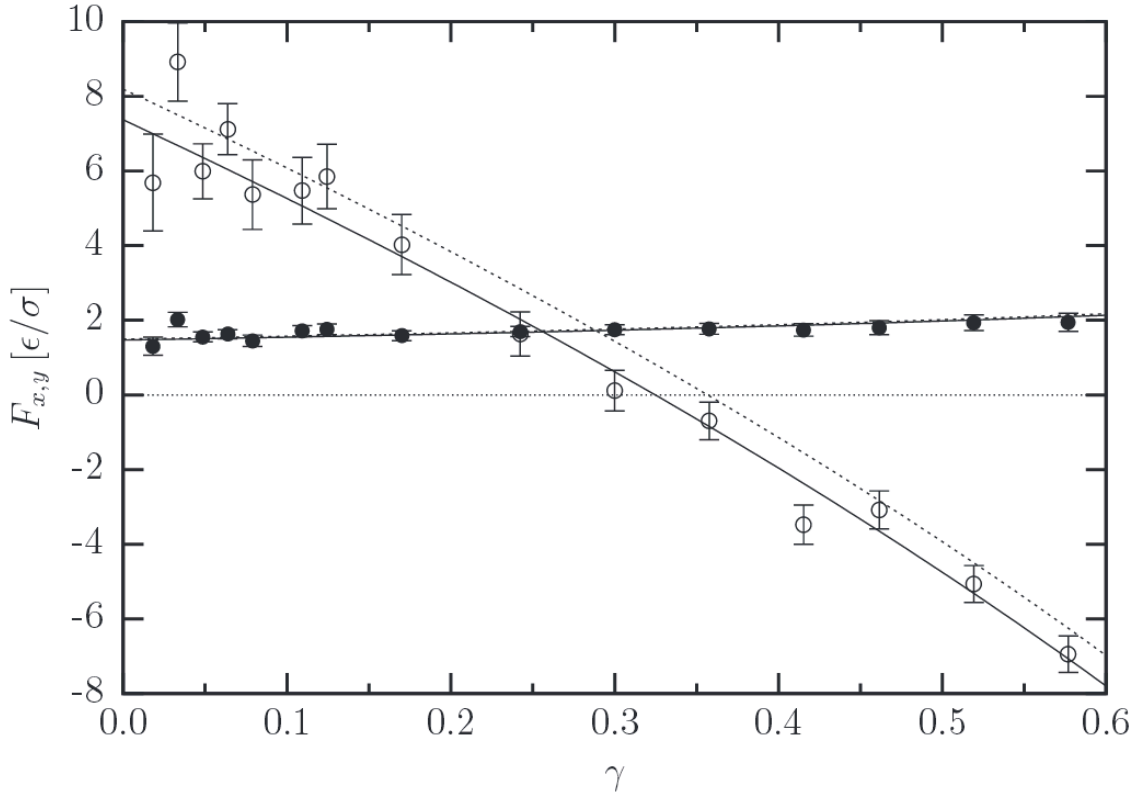

Fig A5.6 : Force vs. strain [2]

A5.3 Coarse Grained SNARE model

The SNARE model presented in this work is based on the CGMD scheme proposed by Fortoul et al. [5]. The CGMD scheme is extended to include the linker and transmembrane domains of the Synaptobrevin (Syb) and Syntaxin (Syx). Below we describe the methodology for the extension of helical structures of Syb and Syx.

A5.3.1 Synaptobrevin (Syb): sequence beyond C-terminus and its structure

Syb is the v-SNARE protein. It contributes one out of four helix in the SNARE bundle. It is believed that Syb is unstructured in the pre-SNARE state (before binding with SNAP-25 and Syx) [6]. Syb is made up of a sequence of 116 amino acids. Following is the breakdown of the sequences relative to the SNARE bundle [7]:

1. 30-85 : SNARE motif
2. 85-95 : Linker domain
3. 95-116 : Transmembrane domain

Fig A5.7 Residue sequence of proteins in Syb [7]

The linker domain (85-95), is partly in the head region (~ 90-93) and partly juxta-positioned right next to head region of lipid membrane [6] (~ 85-89). It is proposed that part of linker domain in the head region of lipid membrane is unstructured. This unstructured domain provides a hinge for the Syb to bend significantly, without

stressing the rest of the - helix. This bend in the Syb has also been observed by Kweon et al. [8] and Bowen et al. [9]. It has been suggested that in the later stages of clamping of SNARE complex, the unstructured domain of the Syb between the linker domain and transmembrane domain goes back to its helical form. This results in an - helix all the way through [7], from sequences 30 to 116 and this later stage - helix formation is believed to be a driving force for the stalk formation and its transition into a membrane fusion pore [10], as outlined in the figure below.

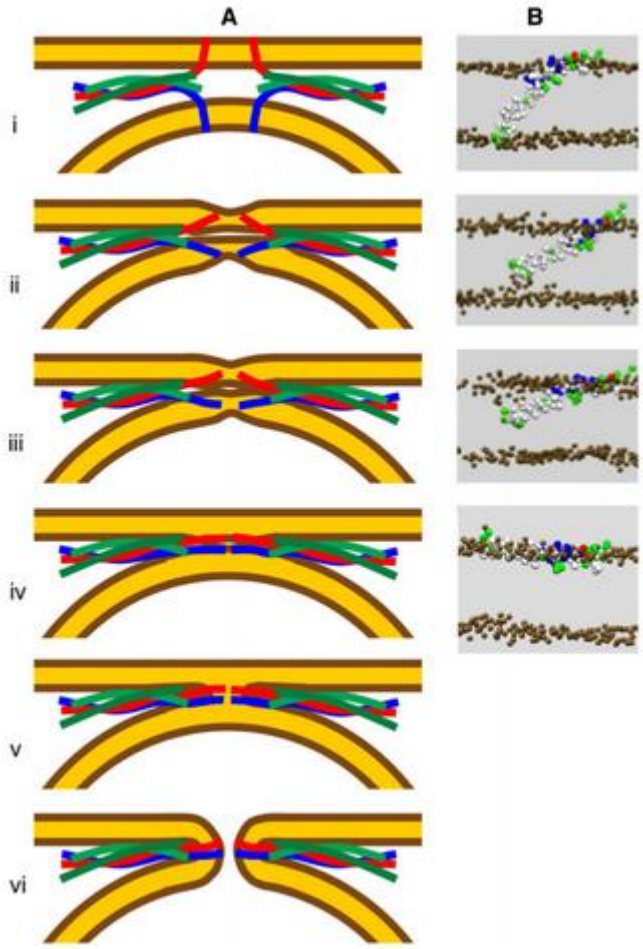

Fig A5.8 Straightening of linker domain [10]

The CGMD SNARE model in Fortoul et al. [5] has the sequences of Syb from 27-89, meaning that,

a) The α helix needs to be extended upto residue 116.
b) The residue sequence ~89-92 needs to be unstructured during the early stage of simulation.
c) During the later part of the simulation the spring network in the linker domain needs to be activated to ensure the α helix throughout.
d) There are ~20 residues in the transmembrane domain, which correspond to an α helix length of 3nm, which agrees well with the thickness of the hydrophobic core lipid bilayer membrane.

A5.3.2 Syntaxin (Syx): sequence beyond C-terminus and its structure

Syx is the t-SNARE protein. It contributes one out of four helix in the SNARE bundle. It is present on the plasma membrane of the neuron, while it binds with SNAP-25, which contributes two helices to the SNARE bundle. Syb is a sequence of 288 amino acids. Following is the breakdown of the sequences relative to the SNARE bundle [7]:

1. 183-256: SNARE motif
2. 257-265: Linker domain
3. 267-288: Transmembrane domain

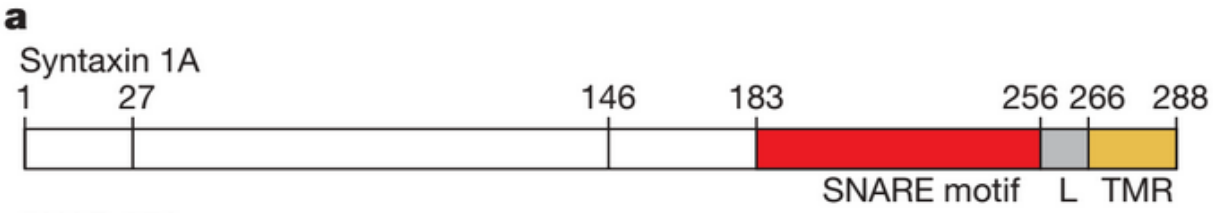

Fig A5.9 Residue sequence of proteins in Syx [7]

In a manner similar to Syb, Syx also has the linker domain (257-265), partly in the head region (~ 261-266) and partly juxta-positioned right next to head region of lipid membrane [11,12] (~ 257-260). It is proposed that part of linker domain in the head region of lipid membrane is unstructured. This unstructured domain provides a hinge for the Syx to bend significantly, without stressing the rest of the - helix.

Lindau et al. [10] concluded that unstructured domain of Syb goes back to its helical form towards the end of SNARE complex clamping. Similar process takes place for the Syx helix too.

The CGMD SNARE model in Fortoul et al. [5] has the sequences of Syx from 189-256, meaning that,

a) The α helix needs to be extended up to 288.
b) Sequence ~261-266 needs to be unstructured during the early stage of simulation,
c) During the later part of the simulation the spring network needs to activated to ensure the - helix throughout the whole Syx
d) There are ~21 residues in the transmembrane domain, which correspond to an α helix length of 3.15nm, which agrees well with the thickness of the hydrophobic core lipid bilayer membrane.

A5.3.3 SNAP25

SNAP-25 has two helices which contribute towards the SNARE bundle, SN1 (5-83), and SN2 (139-204). The unstructured sequence of SNAP-25 [13] between SN1 and SN2 (~85-120) is anchored to the top of the plasma membrane. This domain of SNAP-25 is adsorbed on the surface of the plasma membrane due to palmitoylation of few amino acids. Ideally there should have been an interaction between the two, but for the present work, we are moving ahead without considering this interaction between the unstructured domain of SNAP-25 and lipid membrane.

A5.3.4 Extension of helices of Syb and Syx

The extension of helices was carried out by extending the existing helical structures to append the amino acid sequences corresponding to linker and transmembrane domains of both Syx and Syb. Following steps are involved in the process,

1. Given a helix radius, generate the location of required number of amino acids. These amino acid units are equidistantly placed along the helical trajectory.
2. Obtain the vector along the axis of this generated helix.
3. Obtain the vector along the axis of existing helix.
4. Based on the last atom of existing helix and first atom of the extended helix, find the rest of the two axis for coordinate axis alignment.
5. Generate the rotation matrix to align the extended helix with the existing helix
6. Append the list of transformed coordinates at the end of existing coordinate file
7. Using the list of nearest neighbor location generate an Elastic Network Model.

8. This will provide the natural length of all the springs and the stiffness is same for all the helices.

Bibliography

[1] I. Cooke, K. Kremer, and M. Deserno, "Tunable generic model for fluid bilayer membranes," *Phys. Rev. E*, vol. 72, no. 1, p. 011506, Jul. 2005.

[2] M. Hu, P. Diggins, and M. Deserno, "Determining the bending modulus of a lipid membrane by simulating buckling.," *J. Chem. Phys.*, vol. 138, no. 21, p. 214110, Jun. 2013.

[3] V. A. Harmandaris and M. Deserno, "A novel method for measuring the bending rigidity of model lipid membranes by simulating tethers.," *J. Chem. Phys.*, vol. 125, no. 20, p. 204905, Nov. 2006.

[4] M. Hu, J. J. Briguglio, and M. Deserno, "Determining the Gaussian curvature modulus of lipid membranes in simulations.," *Biophys. J.*, vol. 102, no. 6, pp. 1403–10, Mar. 2012.

[5] Fortoul N, Singh P, Hui CY, Bykhovskaia M, Jagota A. "Coarse-grained model of SNARE-mediated docking." Biophys J. 2015;108(9):2258–69.

[6] Ellena, J. F. *et al.* Dynamic structure of lipid-bound synaptobrevin suggests a nucleation-propagation mechanism for trans-SNARE complex formation. *Proc. Natl. Acad. Sci. U. S. A.* **106,** 20306–20311 (2009).

[7] Stein, A., Weber, G., Wahl, M. C. & Jahn, R. Helical extension of the neuronal SNARE complex into the membrane. *Nature* **460,** 525–528 (2009).

[8] Kweon, D.-H., Kim, C. S. & Shin, Y.-K. Regulation of neuronal SNARE assembly by the membrane. *Nat. Struct. Biol.* **10,** 440–447 (2003).

[9] Bowen, M. & Brunger, A. T. Conformation of the synaptobrevin transmembrane domain. *Proceedings of the National Academy of Sciences* **103,** 8378–8383 (2006).

[10] Lindau, M., Hall, B. A., Chetwynd, A., Beckstein, O. & Sansom, M. S. P. Coarse-grain simulations reveal movement of the synaptobrevin C-terminus in response to piconewton forces. *Biophys. J.* **103,** 959–969 (2012).

[11] Kweon, D.-H., Kim, C. S. & Shin, Y.-K. The Membrane-Dipped Neuronal SNARE Complex: A Site-Directed Spin Labeling Electron Paramagnetic Resonance Study†. *Biochemistry* **41,** 9264–9268 (2002).

[12] Kim, C. S., Kweon, D.-H. & Shin, Y.-K. Membrane topologies of neuronal SNARE folding intermediates. *Biochemistry* **41,** 10928–10933 (2002).

[13] Gonzalo, S., Greentree, W. K. & Linder, M. E. SNAP-25 is targeted to the plasma membrane through a novel membrane-binding domain. *J. Biol. Chem.* **274,** 21313–21318 (1999).

Chapter 6

6.1 Discussion

In the present work we have proposed coarse-grained computational modeling as a tool to analyze biological processes. These models are capable of providing details on various aspects of the systems which might be difficult to obtain experimentally. In this work we have focused on using continuum mechanics and Coarse Grained Molecular Dynamics (CGMD) to model synaptic vesicle fusion.

Synaptic vesicle fusion is a crucial step during the neurotransmission and is the process by which two neighboring neuron cells exchange information with each other. The synaptic vesicles are lipid membrane structures and carry neural information in form of neurotransmitters. A protein of SNARE family, Synaptobrevin (Syb) is attached to the surface of the vesicle. This attachment is due to the Trans-Membrane Domain (TMD) of the Syb which is embedded inside the lipid membrane of the synaptic vesicle. On the target side, two other SNARE family proteins, Syntaxin (Syx) and SNAP25 are attached to the neuron plasma membrane, which is also a lipid membrane structure. Syx is also attached to the neuron plasma membrane by a TMD domain and SNAP25 is adsorbed on the surface of the membrane.

When a neurotransmitter filled synaptic vesicle approaches the neuron plasma membrane, Syx and SNAP25 acts as a receptor site for the Syb attached to the synaptic vesicle. The SNARE motifs of Syb, Syx and SNAP25 start zippering from the free ends and closes towards the anchored end. During this process the synaptic vesicle is positioned closer to the neuron plasma membrane and is known as docking.

The docked vesicle waits for an arrival of an electric impulse known as action potential.

In chapter 2 we have presented a continuum mechanics model for analyzing deformation of lipid membrane structures during the docking. These deformations are an outcome of multiple forces acting on the system which includes SNARE forces, electrostatic repulsion between the membranes, osmotic pressure inside the synaptic vesicle and the in-plane membrane tensions. We obtained the deformed membrane structures for quasi-static variation of the loading on the membranes [1]. The key findings from the continuum model indicates the location of closest approach between the two membranes occur near the protein attachments into the membranes. The in-plane tension in the region surrounded by SNARE complexes is much higher than rest of the membrane. The in-plane tension is an important parameter to monitor as it determines the location of membrane rupture and leads to the fusion pore formation.

In chapter 3 we have used the continuum mechanics and CGMD to answer one of the most debatable questions in the area of neuroscience on how many SNAREs are needed to dock a synaptic vesicle. The SNARE CGMD scheme [2] was developed by Prof. Anand Jagota's research group at Lehigh University. This SNARE model is tuned to show the similar force behavior as demonstrated in experimental work by Gao et al [3]. The model was then used to obtain a force separation curve. This force separation curve was then used to determine an equilibrium configuration of a docked synaptic vesicle. In this docked configuration the distance of closest approach was calculated. This analysis was repeated for different number of SNARE complexes and based on that we proposed that 4-8 SNAREs are needed to dock a synaptic vesicle.

Chapter 4 looks into a hydrodynamics of the synaptic vesicle docking. Docking positions the synaptic vesicle close to the plasma membrane. This requires squeezing out the water present in between the two lipid membranes. The SNARE forces compete against the hydrodynamics force to create a pressure gradient away from the bottom of synaptic vesicle. In the range of separations considered in the analysis, hydrodynamics is the strongest force in comparison to electrostatics and hydration pressure. Here we have used a lubrication theory based continuum mechanics model to obtain the docking time of a synaptic vesicle. In the experiments by Zenisek et al. [4] the docking time of synaptic vesicles has been measured to be ~250 msec. In chapter 4, we have explored various kinds SNARE force behaviors to achieve similar docking times. From our analysis we have concluded that the most crucial feature for the SNARE complex forces is the rate of change of its magnitude with gap closure. Number of SNAREs and in-plane membrane tension are some other parameters in the problem. We found that those parameters do not affect the docking time as strongly as the rate of change of SNARE force with gap.

For the membrane fusion to take place, the lipid membranes need to be in close proximity of each other. The docked synaptic vesicle is staged for the fusion event as it waits for an action potential. Upon its arrival, the SNARE proteins undergo a confirmation change to make Linker Domain (LD) of both Syx and Syb to assume helical shape [5], [6]. This process pushes the lipid membranes further closer leading to the fusion event and subsequently a pore formation to release the neurotransmitter into the synaptic cleft. In Chapter 5, we have presented a CGMD scheme to simulate how two juxtaposed lipid membranes held close to each other by SNARE complexes

undergo fusion. We have used the CG lipid membrane model developed by Cooke et al. [7] and slightly modified CG SNARE model proposed by Fortoul et al. [2]. This scheme has been demonstrated its capability to simulate membrane fusion followed by pore formation. The parameters of this scheme are still under evaluation and subsequently we aim to study the effect of tension on fusion pore formation, required number of SNARE complexes and their self-arrangement.

6.2 Future Work

The continuum mechanics and CGMD scheme present themselves as a powerful tool to analyze and visualize intricate biological systems. The continuum mechanics based model of synaptic vesicle docking can be extended to include the role of lipid membrane interactions, like electrostatics, hydration pressure and hydrodynamics into other membrane processes. One such system is hemifused lipid membrane structures [8]. There is a significant debate about how hemifused diaphragm formation leads into the fusion pore formation. With continuum mechanics we attempted to model such a system to understand the parameters of hemifused diaphragm and their impact on subsequent fusion pore formation. The continuum mechanics models have a limitation in terms of complexity of the governing equations. This theory is ideal for modeling plane strain and axisymmetric systems. Adding further complexity increases the order of governing equations.

Another continuum mechanics tool that we explored during the course of present work is Finite Element Modeling (FEM). The FEM for lipid membrane has potential of exploring problems which are 3 dimensional and are more accurate representation of

the actual biological systems. FEM developed by Klug et al. [9] is an ideal starting point for someone willing to explore this area.

The CGMD scheme presented in this work provides the details of the system which are beyond the capabilities of continuum mechanics models at the cost of computational power. The CGMD scheme can provide molecular details of the fusion process and can be help to visualize the dynamics. This dynamics is otherwise hard to capture in continuum mechanics models. The CG SNARE model can be extended to include the effect of other proteins, for an instance Complexin (Cpx) [10]–[14].

The synaptic vesicle fusion is a kind of problem where molecular details are an important aspect but are only confined to a small portion of the overall system. We propose that continuum mechanics models can be used to understand the system where molecular interactions are not significant. Whereas for the portion which is driven by molecular interactions can be modeled by MD. This kind of multi-scale modeling can certainly help to utilize the robustness of continuum mechanics along with the strength of MD to provide the molecular details.

Bibliography

[1] T. Liu, P. Singh, J. T. Jenkins, A. Jagota, M. Bykhovskaia, and C.-Y. Hui, "A continuum model of docking of synaptic vesicle to plasma membrane," *J. R. Soc. Interface*, vol. 12, no. 102, pp. 20141119–20141119, Dec. 2014.

[2] N. Fortoul, P. Singh, C. Y. Hui, M. Bykhovskaia, and A. Jagota, "Coarse-grained model of SNARE-mediated docking," *Biophys. J.*, vol. 108, no. 9, pp. 2258–2269, 2015.

[3] Y. Gao, S. Zorman, G. Gundersen, Z. Xi, L. Ma, G. Sirinakis, J. E. Rothman, and Y. Zhang, "Single reconstituted neuronal SNARE complexes zipper in three distinct stages," *Science (80-.).*, vol. 337, no. 6100, pp. 1340–1343, 2012.

[4] D. Zenisek, J. A. Steyer, and W. Almers, "Transport, capture and exocytosis of single synaptic vesicles at active zones.," *Nature*, vol. 406, no. 6798, pp. 849–54, Aug. 2000.

[5] D. H. Kweon, C. S. Kim, and Y. K. Shin, "Regulation of neuronal SNARE assembly by the membrane," *Nat Struct Biol*, vol. 10, no. 6, pp. 440–447, 2003.

[6] M. Bowen and A. T. Brunger, "Conformation of the synaptobrevin transmembrane domain," *Proc. Natl. Acad. Sci.*, vol. 103, no. 22, pp. 8378–8383, 2006.

[7] I. R. Cooke, K. Kremer, and M. Deserno, "Efficient tunable generic model for fluid bilayer membranes," Feb. 2005.

[8] D.-H. Kweon, B. Kong, and Y.-K. Shin, "Hemifusion in Synaptic Vesicle Cycle," *Front. Mol. Neurosci.*, vol. 10, 2017.

[9] L. Ma and W. S. Klug, “Viscous regularization and r-adaptive remeshing for finite element analysis of lipid membrane mechanics,” *J. Comput. Phys.*, vol. 227, no. 11, pp. 5816–5835, 2008.

[10] T. Trimbuch and C. Rosenmund, “Should I stop or should I go? The role of complexin in neurotransmitter release.,” *Nat. Rev. Neurosci.*, vol. 17, no. 2, pp. 118–25, 2016.

[11] J. Malsam, D. Parisotto, T. A. M. Bharat, A. Scheutzow, J. M. Krause, J. A. G. Briggs, T. H. Söllner, and T. H. So, “Complexin arrests a pool of docked vesicles for fast Ca2+-dependent release.,” *EMBO J.*, vol. 31, no. 15, pp. 3270–81, 2012.

[12] Y. Lai, J. Diao, D. J. Cipriano, Y. Zhang, R. A. Pfuetzner, M. S. Padolina, and A. T. Brunger, “Complexin inhibits spontaneous release and synchronizes Ca2+-triggered synaptic vesicle fusion by distinct mechanisms,” *Elife*, vol. 3, p. e03756, 2014.

[13] R. J. Hobson, Q. Liu, S. Watanabe, and E. M. Jorgensen, “Complexin maintains vesicles in the primed state in C. elegans,” *Curr. Biol.*, vol. 21, no. 2, pp. 106–113, 2011.

[14] R. T. Wragg, D. Snead, Y. Dong, T. F. Ramlall, I. Menon, J. Bai, D. Eliezer, and J. S. Dittman, “Synaptic Vesicles Position Complexin to Block Spontaneous Fusion,” *Neuron*, vol. 77, no. 2, pp. 323–334, 2013.